DBE TECHNOLOGY GmbH

Investigation on Thermal Expansion Effects in Clay Formations

- TEE -

Final Report

Project leader:	Michael Jobmann
Compiled by:	Mirko Polster
Contributions by:	Michael Jobmann Mirko Polster Matthias Schonebeck

DBE TECHNOLOGY, Peine, February 2007

The reported research work has been funded by the Federal Ministry of Economics and Labour (BMWA = Bundesministerium für Wirtschaft und Arbeit) under the contract No FKZ 02E 9531. However, the authors are responsible for all the content.

Table of Contents

SUMMARY

The present report deals with the research and development activities performed between 01.10.2001 and 31.07.2006 in the framework of the research project:

„Investigation on Thermal Expansion Effects in clay formations“ - TEE -

funded by the Federal Ministry of Economics and Labor in Germany (contract No FKZ 02E 9531). The activities within this project have been performed in relation to in-situ experiments and in close cooperation with ANDRA (Agence nationale pour la gestion des déchets radioactifs) as the manager of two field experiments at Mont Terri Underground Research Laboratory (URL), Switzerland and at the Bure URL in France.

At the Mont Terri URL a heater test named HE-D has been performed to analyze the thermo-hydro-mechanical (THM) rock mass behavior. This test consisted of three phases, two heating phases with different power and duration and one cooling phase in the end. A couple of observation boreholes have been drilled and equipped with sensing devices for temperature, pore water pressure and deformation measurement. The obtained measurement results during the entire test together with laboratory investigations on drill core samples provided a huge data set, which enables for numerical back analysis. Prior to coupled THM back analysis of the HE-D test thermal and hydraulic calibration modeling has been performed, whereas a good fit of calculation and measurements has been achieved and a plausible parameter set has been found. To analyze the mechanical rock behavior a coupled THM modeling has been performed but a good fit could only be achieved for the first 120 days of the experiment. Afterwards the calculated deformations diverge significantly from some of the measurements. Plausible explanations might be given by assumption of a movement along fractures and/or thermally induced water release and/or consolidation (thermo-plasticity effects), however the origin of observed movement is still not completely clarified.

At the Bure URL a vertical mine-by test, the so called REP experiment (response hydromechanique au creusement du puits), has been performed, aimed at characterizing the hydromechanical response of the Callovo-Oxfordian Clay formation due to the ongoing shaft sinking. Analogous to the test at Mont Terri a huge amount of data has been obtained from observation boreholes. This enables for verification of significant effects and processes and validation of parameters within numerical simulations. A comprehensive understanding of the HM-behavior and especially the coupling effects has been achieved during predictive and interpretive modeling. But still the applied hydro-mechanical coupled model was not capable to reproduce all observed effects in a sufficient manner. The HM-coupling seems to be not strong enough to reproduce all in-situ observed effects. The constitutive model improvement and implementation and use of further dependencies is supposed. This comprises consideration of anisotropic elastic and plastic behaviour and a more precise description of the volumetric deformation behavior as well as a dependence of permeability on damage, which were only insufficiently described within the current model.

In general it can be concluded that due to the participation in these two field experiments by direct measurements, laboratory investigations and numerical simulations DBE TECHNOLOGYs understanding of clay rock behavior and corresponding constitutive modeling has been significantly improved. Thus the basis for repository design and layout in a argillaceous host rock was established.

1 INTRODUCTION AND OBJECTIVES

The German Government recommended not only to rely on the salt option for radioactive waste disposal in Germany but also to look at other rock formations that might provide an alternative to salt. Magmatic rock like granite as well as clay rock come into consideration. But due to the less availability of granitic rock in Germany the clay rock has been identified to be the preferred alternative rock formation for investigating its suitability for being the host rock for radioactive waste disposal.

Existing Underground Research Laboratories (URL) in Switzerland and France offer the opportunity to investigate clay rock behavior especially in terms of the thermo-hydro-mechanical impact of heat generating waste. Obtained results from these laboratories will significantly improve the understanding of clay rock behavior and will form the basic knowledge prior to any future site-specific investigations in Germany.

In contrast to the dry salt in a clay host rock water content rises up to about 30%. The coefficient of thermal expansion of water is at least one order of magnitude higher than those of minerals. Thus, a careful evaluation of these effects seems to be an important issue in design, construction and operation of a repository. In case of disposal of heat generating waste in extended emplacement fields containing a large amount of disposal boreholes or drifts this is of uppermost importance.

Main objectives of the research activities are to characterize the THM response of the clay host rock and the effect of thermal expansion on the deformation of underground cavities. This is achieved by means of a combination of measurements and mathematical calculations in a clay environment as a basis for a repository layout for extended borehole or drift disposal of heat generating waste.

At Mont Terri, Switzerland, the so called “Opalinus Clay” which is of Jurassic age, is under detailed investigation by an international consortium (*THURY & BOSSART 1999*, *FOWG & GI 2004*)**.** Among other in-situ tests a heater experiment called HE-D has been performed. One major objective was to investigate the host rock behavior in case of directly being heated without any buffer material between heater and host rock. DBE TECHNOLOGY participated in this experiment by fiber optic temperature and deformation measurements as well as numerical calculations for rock behavior analysis.

At Bure (Meuse/Haute-Marne) in France ANDRA (Agence nationale pour la gestion des déchets radioactifs) is operating an URL in the Callovo-Oxfordian Clay formation (*ANDRA, 1999*). The aim is to provide the necessary data for assessing the feasibility of a deep geological waste repository. This means comparing theoretical repository concepts with the particular conditions encountered in clearly defined geological sites, and demonstrating their safety over the very long term. Among others a vertical mine-by experiment, the so called REP experiment, has been performed, aimed at characterizing the mechanical and hydro-mechanical response of the Callovo-Oxfordian Clay formation due to the ongoing shaft sinking. DBE TECHNOLOGY participated in this experiment by fiber optic deformation measurements in one of the inclined boreholes. The in-situ measurements were to be accompanied by numerical calculations for analyzing the rock behavior.

The following chapters summarize the activities of DBE TECHNOLOGY within both field experiments. Results of the HE-D and REP experiment are given and in particular the lessons learned with regard to repository layout in a clay host rock.

2 SCIENTIFIC STATE OF THE ART

Two different clay formations have been investigated during this project. The Opalinus Clay on the one hand and the Callovo-Oxfordian Clay on the other hand. The Opalinus Clay has been investigated in detail by deep boreholes located at Weiach (*NAGRA, 1988*) and Benken (*NAGRA, 2001*) in Switzerland as well as by underground tests at the Mont Terri rock laboratory (*THURY & BOSSART 1999, FOWG & GI 2004*).

At Mont Terri in Canton Jura, an international research project is being carried out under the auspices of the Swiss Federal Office of Topography. Nagra has been involved in the project for a couple of years. The experiments being carried out in the Rock Laboratory are aimed at investigating the hydrogeological, geochemical and rock mechanical properties of the Opalinus Clay. The behavior of an engineered barrier system constructed in this rock is also being studied. The results represent input for evaluating the feasibility and safety of constructing a geological repository for radioactive waste in a clay host rock (in particular the Opalinus Clay). All investigation results have been compiled in a synthesis report (*NAGRA, 2002*) that forms an integral part of the series of documents produced for the “Entsorgungsnachweis”, the aim of which is to demonstrate the basic feasibility of disposing of spent fuel, vitrified high-level waste and long-lived intermediate-level waste in Switzerland.

Lack of knowledge has been identified for the thermo-hydro-mechanical behavior of the Opalinus Clay in direct vicinity of a heat source. This was one of the reasons for launching a heater experiment called HE-D managed by ANDRA providing the possibility of a participation of DBE TECHNOLOGY within the framework of this project.

The Callovo-Oxfordian Clay is currently investigated at the Bure site in France, located in the Paris basin (*ANDRA, 1999 & 2005c*). Prior to the excavation of the underground rock laboratory a detailed site investigation had been performed by deep boreholes and geophysical surface exploration. Laboratory investigations on drill core samples yield a great amount of rock characterizing parameters to be used as basic input data for mathematical simulation of the rock behavior. At the beginning of the project the excavation activities at the Bure site had just been started.

Prior to reaching the main level of the URL an experimental niche has been excavated for launching the very first in-situ experiments. One of these experiments -REP- (*ANDRA, 2005a,b*) was aimed at characterizing the mechanical and hydro-mechanical response of the Callovo-Oxfordian Clay formation due to the ongoing shaft sinking. DBE TECHNOLOGY participated in this experiment and took on the challenge for geotechnical monitoring of the rock behavior and mathematical analysis by numerical methods.

For geotechnical measurements in both in-situ experiments fiber optic sensing systems have been applied being developed during former R&D projects (*JOBMANN et al. 2000, 2005*). The systems were able to measure temperature and rock deformation and the design had to be adapted prior to their application in the experiments.

For numerical analyses the computer code FLAC3D (*ITASCA, 2002*) could be applied that allows for simulating coupled thermo-hydro-mechanical calculations. This code had been applied for modeling the Opalinus Clay during former experiments and corresponding constitutive laws for argillaceous rock have been developed and implemented as well as verified and validated.

3 LITERATURE REVIEW

Within the following chapter a short compilation of typical mechanical and hydro-mechanical characteristics and features of argillaceous rocks are given. Some constitutive models for description of the behavior are presented as well. Due to complexity of the problem the chapter is not comprehensive but deals with the main topics being addressed in the project. For more detailed studies the literature references are given.

3.1 Some general remarks

Clays are under research in various fields of geosciences (e.g. mineralogy, soil- and rock mechanics, geology, geochemistry) and the type of characterization of the clayey material is different. This often leads to misunderstandings; so for instance for mineralogical-geochemical purpose the mineralogical composition of a sample is important, while origin of the clay or grain size distribution are decisive from geological or geotechnical point of view. For rock mechanical purpose the characterization with regard to the degree of compaction and/or strength is usual: So designations like: (over-)consolidated clays, indurated clays, (soft) claystone up to shale are used for general description of the sample, going along with a change of mechanical behavior from plastic-ductile to brittle. Depending on the amount of silt and limestone the samples are additionally denoted as silty ~ or carbonate-rich ~ up to their classification as mudstone or marlstone. Nevertheless geological and mineralogical aspects like:

- origin and history in terms of pressure and temperature,
- conditions of sedimentation,
- type of minerals (2 or 3-layer minerals, swelling/non swelling etc.)

determine the (hydro-)mechanical behavior as well. A good overview is given in *APLIN, FLEET & MACQUAKER (1999)* and especially on Opalinus Clay in *NAGRA (2002)*.

Figure 3-1 shows the wide range of one mechanical parameter as an illustration (here: uniaxial compressive strength) for various argillaceous rocks in dependence on the natural water content. Due to the correlation of water content to porosity and density this figure also presents the dependence of strength on the degree of compaction.

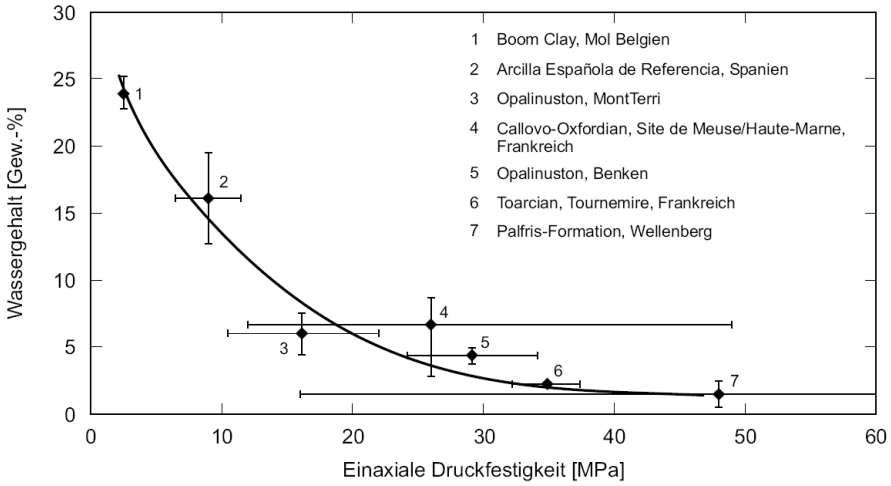

Fig. 3-1:

Water content [$\%_m$] vs. uniaxial compressive strength [MPa] for various argillaceous rocks (*NAGRA, 2002*)

Due to this wide range of the mechanical characteristics a site-specific analysis seems to be necessary. Some features, which may have to be taken into account when considering mechanical behavior of clay rock are:

- anisotropy of elastic properties (Young's Modulus & Poisson's ratio)

- anisotropy of strength properties (failure boundary)
- damage before failure
- distinct hysteresis during cyclic loading
- strain hardening before failure and strain softening after failure (figure 3-2)
- evolution of distinct failure-planes (shear- and tensile failure mode)
- low dilatancy
- time-depending deformation processes (cataclastic flow and/or consolidation)

Figure 3-2 exemplary shows typical stress-strain curves for Opalinus Clay with different water contents. This figure clearly points out that with increasing water content: a) the peak- and residual strength significantly decreases; b) mechanical behavior changes significantly from brittle to ductile and compaction behavior changes form contractant → dilatant for low water contents to nearly volumetric neutral.

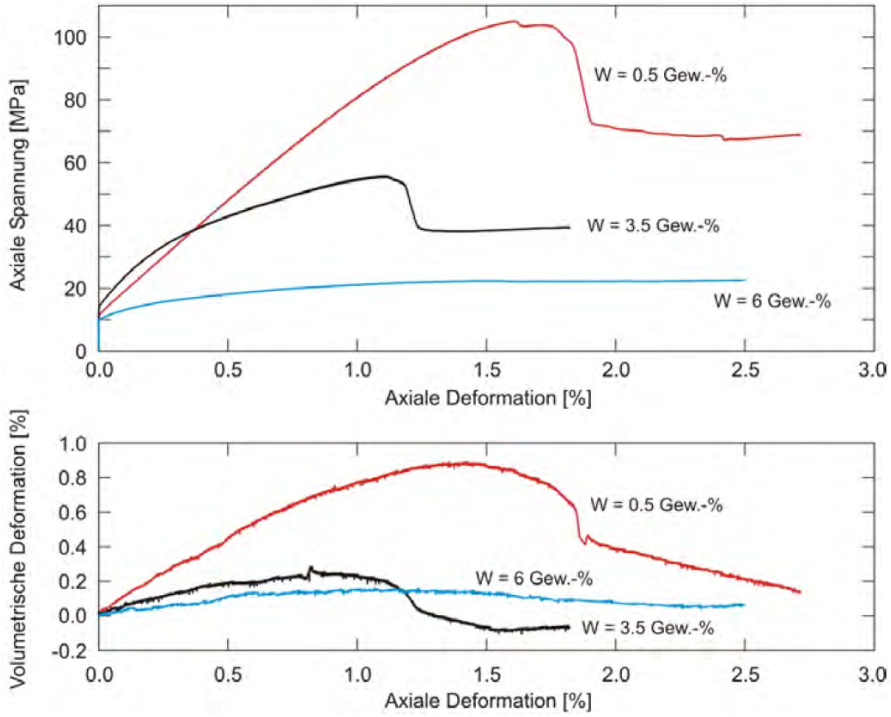

Fig. 3-2:

Stress - strain curves (upper figure) and volumetric vs. axial strain (lower figure) for Opalinus clay gained from triaxial tests at confining pressure σ_3 = 10 MPa (*NAGRA, 2002*)

This abovementioned listing after *KONIETZKY (2003)* refers to the mechanical behavior only. Taking the hydro-mechanical coupling additionally into account (saturated / partially saturated state) a few more effects may have to be considered, as for instance:

- principle of effective stress (pore water pressure effects)
- strong dependence of strength on water content / degree of saturation
- dependence of porosity and permeability on stress state (confining pressure)
- capillary pressure / suction for partially saturated state
- multiphase flow for partially saturated state
- swelling & shrinkage
- changing material behavior after de- and re-saturation cycles.

The additional consideration of thermal influence may require further coupling terms, as for example for description of:

- generation of thermal strains (possibly anisotropic)
- thermal expansion of pore fluid and thermally induced pore pressure generation
- temperature-dependent fluid transport (mobilization of bounded water, change of fluid viscosity, vaporization and precipitation, etc.)

For identification of typical mechanical characteristics as well as intensity of THM-coupling laboratory tests have to be performed. Depending on the degree of peculiarity and on the problem considered they have to be taken into account for constitutive modeling. Figure 3-3 shows a schematic view of THM phenomena interacting in a complex manner.

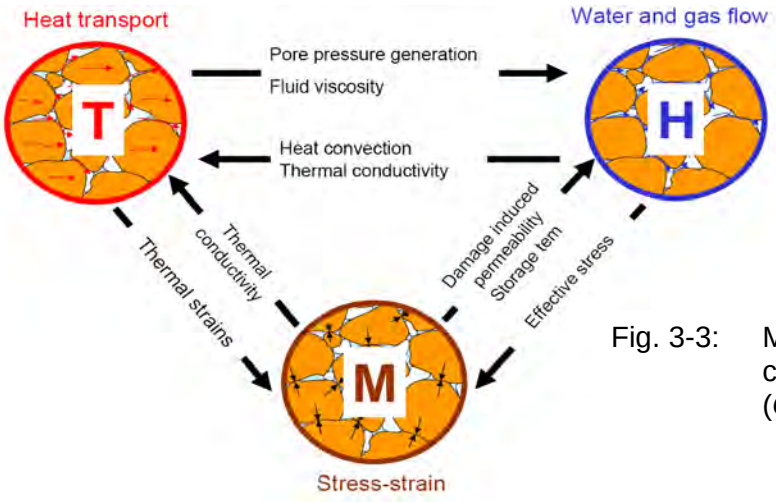

Fig. 3-3: Main phenomena of THM-coupling and their interaction (*GENS et al., 2006*)

Rheologic behavior ("creep") of argillaceous rocks

Due to its importance for prediction of long-term behavior of the host rock the comprehensive understanding of the physical mechanisms of its rheology is necessary. In various laboratory studies and in-situ field observations the rheologic behavior of argillaceous rock has been investigated (c.f. for instance *GHOREYCHI 1998, NAGRA 2002, GASC-BARBIER et al. 2004, ZHANG et al. 2002, 2004a,b*). In accordance to the well-known creep behavior of rock salt the laboratory tests performed on argillaceous rock samples showed a similar evolution of the strain curve with a recognizable transient phase, a phase of steady state deformation rate and for high deviatoric loads a phase of accelerated deformation rate before failure occurs. Similar to rock salt an increase of viscoplastic stain has been observed with increasing deviatoric load, increasing temperature and water content.

Nevertheless the reason for the observed rheologic behavior of argillaceous isn't clarified completely yet. *ZHANG (2004a)* mentioned some different mechanisms, which may be the cause for the rheologic behavior, as for instance: rebalancing of hydraulic pressure, deformation of the mineral skeleton by sliding clay flakes, subcritical propagation of fissures and/or stress-induced transfer of pressure-soluted carbonates. *FABRE & PELLET (2006a)* found some evidence of cataclastic creep (delayed microstructural deterioration) and granular creep (grain sliding and rotation → aggregate deformation) during creep testing and microscopical analysis of different argillaceous rocks. Due to those difficulties in determining the origin of rheologic behavior and separation of creep from other effects like consolidation in the following an over-all designation like "viscoplastic" or "rheologic deformation" instead of the term "creep" or double quotes are used.

ZHANG et al. (2002 & 2004a,b) presented results of creep tests on Callovo-Oxfordian Clay (from URL-Bure) and Opalinus Clay specimens (URL Mt. Terri). Among other things it can be stated that:

- the specimens exhibit pronounced "creep" strains even under low deviatoric loads of < 1.0 MPa confirming that there seems to be no deviatoric threshold for the onset,
- steady state deformation rates (corresponds to "secondary creep phase" with steady "creep" rate) has been observed after a transient phase of weeks to months (months to years for higher stresses > 5 MPa); no cease of rheologic deformation occurred even after more than 18 months.

- high carbonate content and low water content slow down the creep
- the effect of anisotropy on the rheologic behavior can be neglected, because similar creep strain rates have been observed for P (parallel to stratification)- and S-samples (perpendicular to stratification).

Similar results of creep tests on Callovo-Oxfordian samples are reported by *GASC-BARBIER et al. (2004).* Viscoplastic deformation with a steady state deformation rate has been observed even for low deviatoric stress loads (approx. 2 MPa) so that no threshold for the onset of "creep" is assumed. Nevertheless the authors clearly point out that the primary phase is mainly caused by poroelastic effects and a quasi-steady state could be observed > 10 days after start of the load step.

Laboratory tests and in-situ investigations on Opalinus Clay, published by *NAGRA (2002)* showed quasi-steady deformation rates occurring only for high deviatoric loads after a long transient phase. The existence of a secondary creep phase could not be clarified. In contrast to laboratory measurements by *ZHANG (2004a)* a deviatoric threshold for cataclastic deformation is supposed, assured by the facts of a true cohesion of rock and in-situ measurement proving an anisotropic state of rock stress.

FABRE & PELLET (2006a) also observed constant deformation rates (secondary creep phase) in creep tests performed on various argillaceous rock samples. They also assumed the existence of a deviatoric stress threshold, below which only primary "creep" occurs and the strain rates reduce to zero (no constant strain rate exceeded for deviatoric stresses below 17.5 MPa). Furthermore it is mentioned that for deviatoric stresses above a certain value the strain rates accelerate and delayed failure occurs (comparable to tertiary creep phase). This load value has been found close to uniaxial compressive strength and may correspond to stress under maximum contraction.

In contrast to rock salt the argillaceous rock samples show a significant non-zero volumetric deformation behavior during creep testing. In general a transition from compaction to dilation can be observed (c.f. behavior during short-term triaxial testing, figure 3-2). *FABRE & PELLET (2006a)* reported a difference in volumetric behavior depending on the type of rock: so for instance Callovo-Oxfordian samples became dilating as soon as the secondary phase starts, while for some Tournemire clay samples dilation seems to be initiated only at the beginning of the tertiary "creep" phase when crack propagation starts to get unstable.

3.2 Constitutive modeling of argillaceous material

The constitutive models developed (or pre-existing and adopted) for description of the (TH)M behavior of clays and claystones are mainly referring to the sites considered as potential host rock formations for disposal of radioactive waste. Such site-specific formulations can be found for clays with low degree of compaction, like Boom clay or Serrata clay (as for example *LALOUI & MODARESSI, 2002*) as well as for indurated clays and claystones like Opalinus Clay (as for example *GENS et al. 2006, HUNSCHE et al. 2004, BLÜMLING & KONIETZKY 2003*) or Callovo-Oxfordian Clay (as for example *JIA et al. 2006, HOXHA et al. 2004 & 2006a).*

Table 3-1 gives a compilation (not comprehensive) of constitutive models used for description of argillaceous rock. It has to be mentioned that the described constitutive laws are mainly problem-specific formulations, which optionally could be upgraded by additional features or coupling terms and / or adopted and applied to other sites or host rock formations after a re-formulation. The compilation focuses on latest international scientific work, making the development and progress in constitutive modeling obvious.

Particularly within the last decade a broad progress in description of such hard soil / soft rock material has been achieved, turning from pure elasto-plastic approaches (e.g. based on Cam-Clay, Mohr-Coulomb or Hoek-Brown models) to models with an additional consideration of strain hardening / softening behavior, as well as volumetric deformation and rheologic behavior.

A further advancement resulted from consideration of HM-coupling via theory of poromechanics (see for instance the comprehensive description of poroelasticity and poroplasticity by *COUSSY (1995)*). This led to most usual formulation of constitutive laws –especially of the failure surface - by means of the effective stress approach. The determination of the HM-coupling parameters in laboratory tests (paying special attention on drainage and saturation conditions) became common practice (c.f. *HOTEIT et al. 1998*, *BEMER et al. 2004, OZANAM et al. 2004*).

Owing to introduction of multiphase flow approaches further aspects of HM coupling can be taken into consideration for partially saturated conditions, as for instance evolution of capillary pressure according to the retention curve and the resulting effect of suction on the mechanical behavior (e.g. strength). Such approaches are described for example by *ZHANG et al. (2004a), JIA et al. (2006), HOXHA et al. (2006a).*

Within the last few years several authors introduced damage theory based on thermodynamic approaches into constitutive modeling of argillaceous rocks, as for instance *GENS et al. 2006, PELLET et al. 2005*, *CHIARELLI et al. 2003 CONIL et al. 2004*. This allows for a better representation of damage evolution and considerations at a microstructural level. Using this more realistic simulation of physical mechanisms (e.g. stress partitioning to matrix and bonds) some in-situ observed effects (like progressive bond breakage and delayed plastic strain) can be modeled more close to reality. This yields coupling laws based on real physical interrelationships (e.g. evolution of dilation, increase of connected pore space and hydraulic conductivity etc.).
A similar goal is achieved by means of discrete element modeling using particle-method codes, as presented by *DEDECKER (2006)* or *te KAMP et al. (1999, 2003).*

Table 3-1: Compilation of constitutive models for description of argillaceous rocks (not comprehensive)

Model name (or developed by) According references	**General description / features included** (damage, softening / hardening behavior …)	**adopted to** (tested for)
LML *JIA et al. (2006)*	Elasto-plastic model incl. damage, strain hardening & softening, HM-coupling distinguishes partially saturated and saturated state,no mechanical anisotropy	general formulation, adopted to C-O Clay
LAEGO-ENSG *HOXHA et al. (2004 & 2006a)*	Elasto-plastic model incl. damage, strain hardening & softening, HM-coupling based on effective stress approach with different poromechanical behavior for partially saturated and saturated state, no mechanical anisotropy considered	general formulation, adopted to C-O Clay
Laboratoire 3S - IRSN *PELLET et al. (2005)* *FABRE & PELLET (2006b)*	Elasto-viscoplastic model (based on visco-plastic damage law by *Lemaitre*) incl. dam age, strain hardening & softening, anisotropy of damage and time-dependent evolution of damage considered; no HM-coupling considered	general formulation, tested for argillite, marble, anhydrite, etc.
LTVP model *LALOUI & MODARESSI (2002)* *MODARESSI & LALOUI (1997)*	Elasto-plastic deformation model including thermal plasticity (occurrence of thermal hardening and irreversible thermal strains), full THM coupling, no mechanical anisotropy considered	general formulation, tested for Boom Clay, Pontida Clay
Hou – Lux- T (TU Clausthal) *HOU et al. (2002)* *LUX et al. (2005, 2006)* *CZAIKOWSKI & LUX (2006)*	Elasto-plastic – viscoplastic deformation model incl. damage, anisotropic strength behavior, strain hardening & softening, dependency of elastic and plastic (damage- and failure boundary) behavior on water content, creep law (incl. primary, secondary and tertiary creep phase) considers damaged induced (dilatant) and healing induced (contractant) strain rates, full THM-coupling	general formulation, tested for C-O Clay, O. Clay, Konrad Clay
UPC *GENS et al. (2006)*	Composite model considering matrix- and bond behavior (matrix-behavior according to elasto-plastic Hoek-Brown model with strain hardening; bond behavior according damage theory), full THM-coupling, no mechanical anisotropy considered	general formulation, tested for C-O Clay, O. Clay
NAGRA & ITASCA I *BLÜMLING&KONIETZKY (2003)* *KONIETZKY (2003)*	Elasto-plastic – viscoplastic deformation model (modified Mohr-Coulomb law with transversal-isotropic strength behavior, bi-linear formulation incl. strain hardening & softening), HM-coupling; creep after *Salzer* creep law (primary and secondary creep phase incl. hardening)	Opalinus Clay, C-O Clay
NAGRA & ITASCA II *te KAMP et al. (1999, 2003)* *KONIETZKY et al. (2001)*	DEM-modeling (particle flow code PFC), incl. damage (bond failure), strain hardening & softening; HM-coupling considered via effective stress approach (update with calculated pore pressure field from FDM-analysis)	Opalinus Clay
BGR *HUNSCHE et al. (2004)*	Orthorhombic thermo-elastoplastic – viscoplastic deformation model based on Burgers model incl. transversal-isotropic elastic & viscous behavior, no HM-coupling considered	Opalinus Clay

C-O clay = Callovo-Oxfordian Clay (M/HM-argillite) O. Clay = Opalinus Clay

Emphasis of research and constitutive modeling

The research on the THM behavior of argillaceous rock as well as its mathematical formulation and description via constitutive models is an intensively investigated topic in geomechanics on an international scale. Table 3-1 underlines the effort and advancement in constitutive modeling. Nevertheless a comprehensive general formulation is still pending. In the following some trends in constitutive modeling as well as unsolved problems are listed.

I Due to its importance for long-term safety aspects special attention (in laboratory & in-situ tests and modeling) is paid to investigations concerning
- the damage and its hydro-mechanical consequences,
- the time-depending evolution of damage (and prediction of delayed failure) as well as
- the reason for viscoplastic deformation processes (primary, secondary and tertiary phase)

to get a sound understanding of the physical mechanisms prior to constitutive modeling.

II As above mentioned various authors recently presented some approaches introducing damage theory into constitutive modeling. This underlines the trend of turning from a phenomenological description of material behavior at a macroscopic level to a more physical mechanism-based description at a microscopic level. This trend allows for damage-depending formulation of mechanical and hydro-mechanical behavior.

III Because of their structure and texture argillaceous rocks often show a pronounced anisotropic behavior, for instance in terms of stiffness, failure strength, hydraulic or thermal conductivity, etc. Although these characteristics are known, they are often neglected during numerical modeling, mainly caused by a missing implementation into the used code or outstanding mathematical formulation and their numerical implementation, as for instance the mathematical formulation of anisotropic strength.

IV A further challenge in modeling refers to the assessment of the degree of HM-coupling. Especially the M→H coupling and prediction (and partially even back analysis!) of pore pressure evolution is still insufficient (c.f. *SU 2006a & b*). So for instance *LI et al. (2006a & b)* reported a significant discrepancy between pore pressure measurements and the observed extension of the EDZ during gallery excavation at the URL Mol (Belgium) site in comparison to modeling results. The calculation results highly underestimate pore pressure changes in the far-field and EDZ extension within the Boom Clay. This strong degree of HM coupling observed in-situ could not be reproduced by modeling up to now.

Similar observations of a high degree of HM coupling have been gained during excavation work within the Callovo-Oxfordian formation at the URL-Bure; c.f. pore pressure evolution during shaft excavation experiment REP (*ANDRA 2005d, ARMAND & WILEVEAU 2006*) or during drilling of borehole TER1101 within heater experiment TER (*ANDRA, 2006a*).

VI The results of the MODEX-REP test (*SU,* 2006b), which included development and validation of numerical models for description of the HM-behavior of the Callovo-Oxfordian Clay suggested an improvement in modeling of the volumetric strain behavior (short term constitutive model at low and middle deviatoric stress) to remedy the deficiencies in M→H coupling. A further lack of knowledge refers to the effect of desaturation (relative permeability, suction) and the establishment of damage and failure criteria on effective stress and their introduction into numerical modeling.

VII Although the elasto-plastic parts of site-specific developed constitutive models (as for instance described by *NAGRA 2002, BLÜMLING & KONIETZKY 2003*) are able to describe the extension of the EDZ around underground openings quite well, a prediction of the time-depending rock behavior – convergences and especially evolution of damage and failure due to pore pressure induced stress-reorganizations - is almost impossible without correct assessment of HM coupled processes (c.f. *VIETOR et al. 2006*).

3.3 Thermal expansion

HORSEMANN (1994) gave a short review of thermal expansion and thermally induced porewater pressure in clay. The effect of heating on the porewater pressure in argillaceous rocks is very complex. The water content plays a significant role in determining the magnitude of thermal effects. Heating produces thermal expansion of the free water, adsorbed water and mineral phases in the rock and may also produce changes in the thickness of the adsorbed water layers. The volumetric thermal expansion coefficient of free water is temperature- and pressure dependent and can be estimated using the following relationship (*BALDI et al., 1988*):

$$\alpha_w (T,P) = a_0 + (a_1 + b_1 T) \ln (mP) + (a_2 + b_2 T) (\ln (mP))^2 \quad K^{-1} \qquad (3\text{-}1)$$

with

$a_0 = 4.505 \cdot 10^{-4}\ K^{-1}$ $\quad b_1 = -1.200 \cdot 10^{-6}\ K^{-2}$

$a_1 = 9.156 \cdot 10^{-5}\ K^{-1}$ $\quad b_2 = -5.766 \cdot 10^{-8}\ K^{-2}$

$a_2 = 6.381 \cdot 10^{-6}\ K^{-1}$ $\quad m = 1.5 \cdot 10^{-5}\ MPa^{-1}$ (at 15 MPa)

The thermal expansion of several clay minerals has been investigated by *McKINSTRY (1965)* by using a x-ray technique in directions parallel and perpendicular to the layer in the structure. The obtained results are compiled in table 3-1. The standard deviations of the measurements are also given. The mean value of the mineral volumetric thermal expansion coefficient can be described by the following relationship:

Tab. 3-2: Average linear thermal expansion coefficient (reproduced from *McKINSTRY, 1965*)

Mineral	perpendicular $\alpha_1 \cdot 10^{-6}\ K^{-1}$	parallel $\alpha_2 \cdot 10^{-6}\ K^{-1}$	Temp. range
Muscovite	17.8 ± 0.59	3.5 ± 1.3	25 - 600
Phlogopite	17.8 ± 1.40	14.0 ± 3.0	25 - 350
Kaolinite	18.6 ± 1.30	5.2 ± 1.7	25 - 400
Dickite	14.9 ± 0.84	5.9 ± 0.4	25 - 500
Halloysite	10.0 ± 1.50	6.0 ± 2.0	25 - 350
Serpentine	10.2 ± 0.90	6.9 ± 1.7	25 - 500
Pyrophyllite	14.9 ± 1.80	12.2 ± 0.7	25 - 400
Talc	16.3 ± 2.40	3.7 ± 1.4	25 - 700
Chlorite	9.0 ± 2.30	11.1 ± 1.4	25 - 500

$$\alpha_s = (16.8 + 0.004 \cdot (T-T_0)) \cdot 10^{-6}\ K^{-1} \quad \text{with} \quad \alpha_s = \alpha_1 + 2\alpha_2 \qquad (3\text{-}2)$$

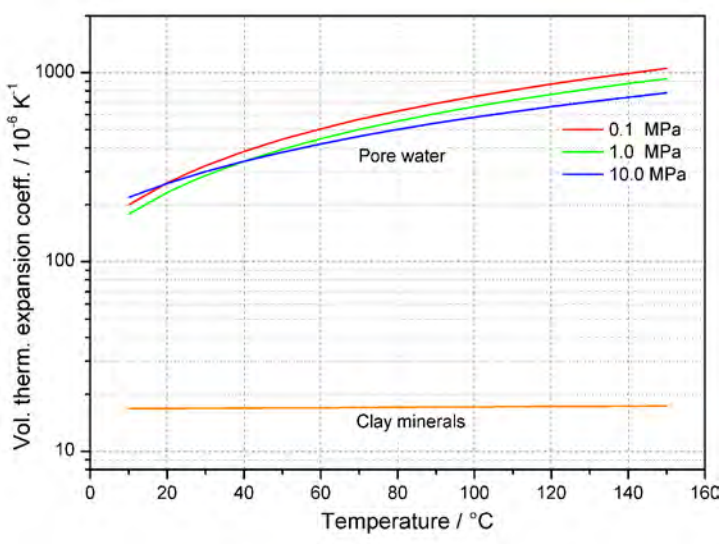

Fig. 3-4: Volumetric thermal expansion coefficient of water and clay minerals

The expansion coefficients calculated using equation (3-1) and (3-2) are plotted in figure 3-4.

The values for water are about one order of magnitude higher than those for minerals indicating the important role of water by describing the thermal expansion effects of claystones. The expansion coefficient of water is slightly dependent on confining pressure as shown in figure 3-4. In addition it should be noted in this context that the thermal properties of adsorbed water probably differs from those of free water (*BALDI et al., 1988, 1991* and *LOW, 1979*) The difference is due to

the strong physico-chemical effects at the contact between water and the mineral surface. The effective thermal expansion coefficient of a claystone sample depends on the void space and the porosity respectively and can be described by using the equation:

$$\alpha_{eff} = \alpha_s \cdot (1-n) + \alpha_w \cdot n \qquad \text{with } n = \text{porosity} \qquad (3\text{-}3)$$

If a heat source is introduced into a permeable porous medium, the expansion of the pore water produces a flux of water which is directed away from the zone of heating. In clays the magnitude of this thermally induced water flux is constrained by the low permeability of the porous medium. Since the thermal expansion of the pore water cannot be easily accommodated by advection, the pore pressures in the vicinity of the heat source rise. In effect, the thermal volume increase is taken up by the local compression of the water and minerals.

Thermally induced pore pressure evolution

Assuming an ideal poroelastic material under undrained oedometric conditions (no volumetric deformation) the pore pressure change due to heating can be given in the following form (c.f. *WILEVEAU & SU 2006*, *ITASCA 2002, COUSSY 1995*):

$$A_p = 3 \cdot \frac{\kappa_0 + 2\,\mu}{b} \cdot \left(\alpha \frac{K}{\kappa_0 + 2\,\mu} - \alpha_0 \frac{K_0}{\kappa_0 + 2\,\mu} \right) \qquad (3\text{-}4)$$

with

A_p change of pressure due to temperature change [MPa / K]
K Bulk-modulus, undrained conditions [MPa]
K_0 Bulk-modulus, drained conditions [MPa]
b Biot coefficient [-]
α linear thermal expansion coefficient [1 / K]

κ_0 parameter [MPa] $\kappa_0 = \frac{E_0 \cdot \nu_0}{(1+\nu_0)(1-2\nu_0)}$ (3-5)

where

ν_0 Poissons ratio, drained [-] $\nu_0 = 0.5 - \frac{3 \cdot G}{(6K_0 + 2G)}$ (3-6)

E_0 Young's modulus, drained [MPa] $E_0 = \frac{2 \cdot G}{1+\nu_0}$ (3-7)

μ parameter (equal to shear modulus) [MPa] $\mu = \frac{E}{2 \cdot (1+\nu)}$ (3-8)

where

E Young's modulus, undrained [MPa] and
ν_0 Poissons ratio, undrained [-]

α_0 parameter with $\alpha_0 = \frac{\alpha - B_S \cdot n \cdot \alpha_f}{1 - B_S \cdot n}$ (3-9)

where

B_s Skempton coefficient [-] $B_S = M \cdot \frac{b}{K} = \frac{K - K_0}{b \cdot K}$ (3-10)

α_f linear thermal expansion coefficient for fluid [1 / K]
n porosity [-]

M Biot modulus [MPa] $M = \frac{K - K_0}{b^2}$ (3-11)

4 HEATER EXPERIMENT AT MONT TERRI (HE-D)

4.1 Location and experimental setting

The study of thermo-hydro-mechanical (THM) processes in argillaceous rock is a part of the ANDRA scientific program dealing with feasibility of a long-life radioactive waste repository in deep geological formation. Tests performed at Mont Terri Rock Laboratory felt within the preliminary phase for thermal experiments to be performed at the Meuse/Haute-Marne Underground Research Laboratory aimed at gaining experience in technical in-situ test preparation and performance as well as host rock behavior analysis. The heater experiment called HE-D is managed by ANDRA and one major objective is to investigate the thermo-hydro-mechanical rock behavior in case of directly being heated without any buffer material between heater and host rock.

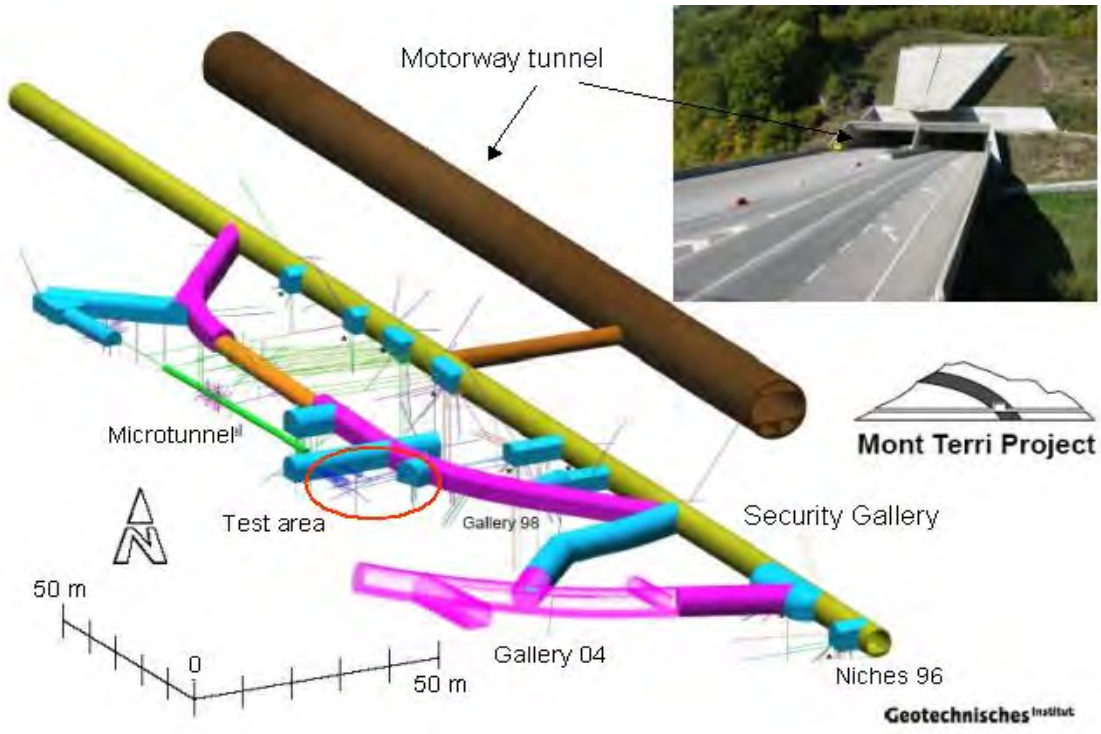

Fig. 4-1: 3D-view of the Mont Terri rock laboratory located next to a motorway tunnel in western Switzerland

The rock laboratory has been excavated next to a motorway tunnel in western Switzerland and covers a couple of experimental niches marked in light blue in figure 4-1. The experiment was carried out in a niche specifically excavated for this purpose, identified as “HE-D Niche”, located in the New Gallery 98 of the rock laboratory. The location of the HE-D Niche was chosen near to the MI Niche in order to drill observation boreholes from both locations parallel and perpendicular to the heater borehole axis. A sketch of the experimental area is shown in figure 4-2. The HE-D Niche was chosen to lie within the shaly facies of the Opalinus Clay, which was assumed to be homogeneous, avoiding the carbonate-rich facies. The WSW axis of the HE-D Niche corresponds to the strike direction of the rock bedding, which dips approximately to the SSE in order to drill the heater borehole parallel to the stratification planes and to avoid crossing bedding planes.

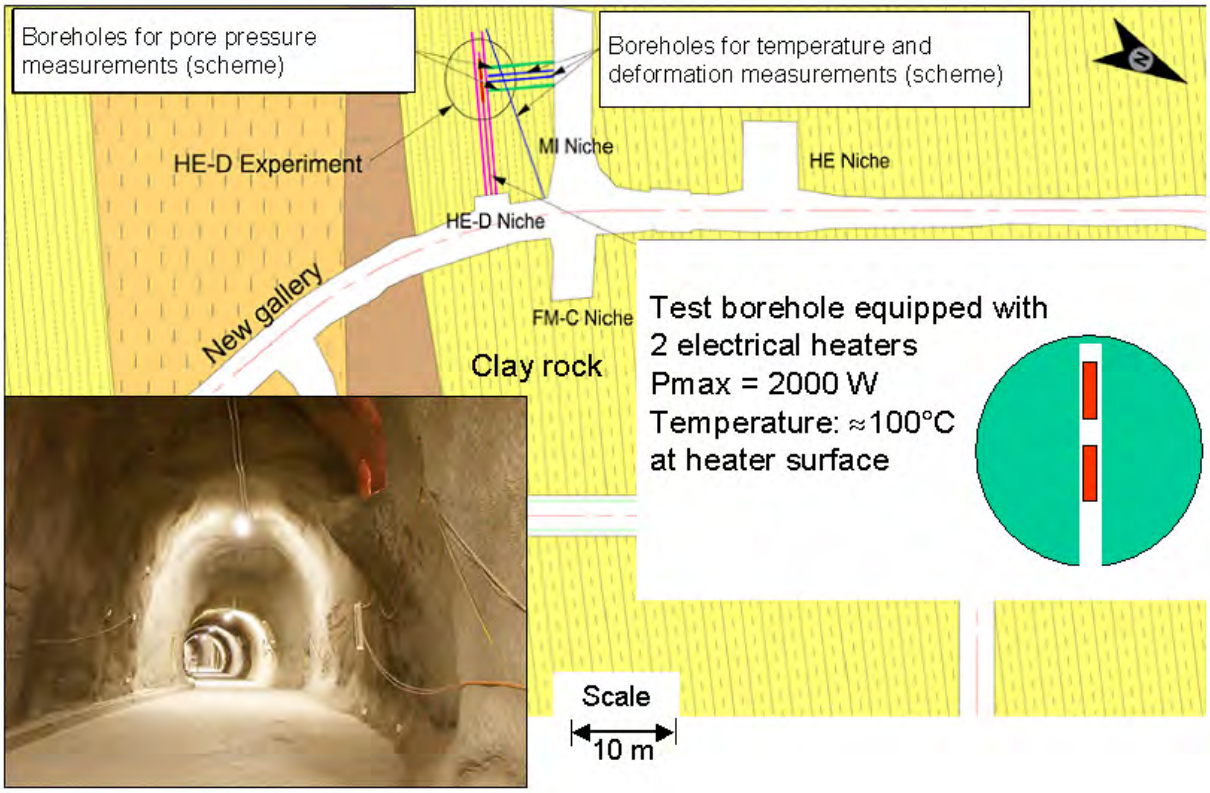

Fig. 4-2: Sketch of HE-D experimental area in Mont Terri rock laboratory

The heater experiment consists of a horizontal heater borehole (c.f. appendix A-3) equipped with two electrical heaters and a couple of observation boreholes drilled in several directions to the heaters (c.f. appendix A-4 to A10). In one of the boreholes called BHE-D06, drilled perpendicular to the heaters, DBE TECHNOLOGY performed deformation and temperature measurements based on fiber optic Bragg grating technology. Rock temperature and displacements were measured at several distances to the heaters as a function of time. This allows for evaluating the temperature induced rock deformation due to the heating process.

4.2 Fiber optic extensometer system

The optical systems have been developed by DBE TECHNOLOGY in co-operation with FOS&S in Belgium. FOS&S (Fiber Optic Sensors & Sensing Systems) is a private held company specialized in the development and commercialization of fiber optical sensing systems. Figure 4-3a shows the principle of the displacement measurement system. The following components can be distinguished:

1. canister with opto-mechanical cells
2. carbon cables
3. fixation points (packers)

The system consists of a number of extensometers outside the borehole which are placed in a canister. Within the borehole, different fixation points have been realized at well defined positions by using packers. From each fixation point, a carbon extension cable goes to the canister where the carbon extension cable is stretched using a spring mechanism, see figure 4-3b. The extensometers in the canisters are connected to the outer ends of the carbon cable. In this way, any movement of the packers will be transduced to the extensometer. As a consequence, the displacement of the connected packer relative to the entrance of the

borehole is measured. The system has the advantage that, to some extent, a reset of the sensors can be applied when the sensor becomes out of range. Furthermore, all sensors are at the same environmental temperature. The used opto-mechanical cell is described in the next chapter.

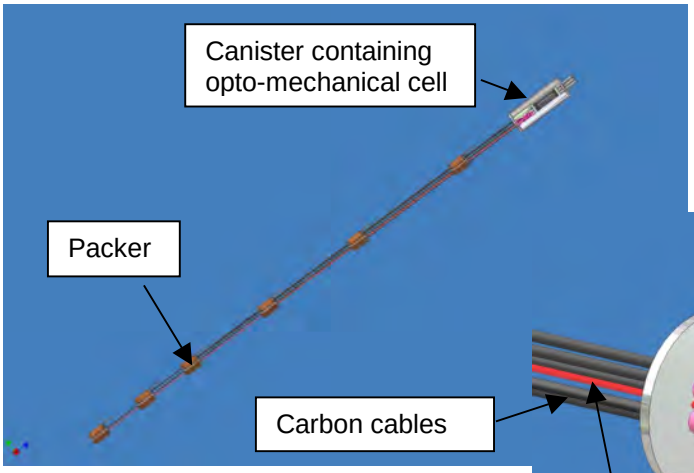

Fig. 4-3a:
Schematic drawing of displacement measurement system

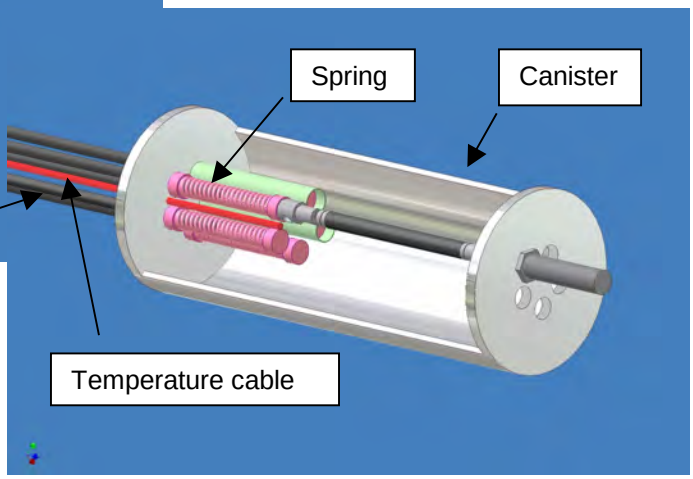

Fig. 4-3b:
Displacement measurement system: Canister with one sensor and spring system

Opto-mechanical cell

A schematic drawing of the opto-mechanical cell is shown in figure 4-4. The cell consists of a metallic tube with a fixation point on each end. Between both fixation points a fiber containing a Fiber Bragg Grating (FBG) is stretched. This FBG is called the strain-FBG. One fixation point of the cell can slide when it is pulled to the outward direction. As a consequence the FBG becomes more or less strained resulting in a wavelength shift. Another parameter influencing the wavelength shift is the temperature. A sensitivity of 10.46 pm/K is expected. In order to compensate for these influences, a second FBG is used, which remains all the time unstrained. This FBG is called the temperature-FBG and allows for monitoring the temperature.

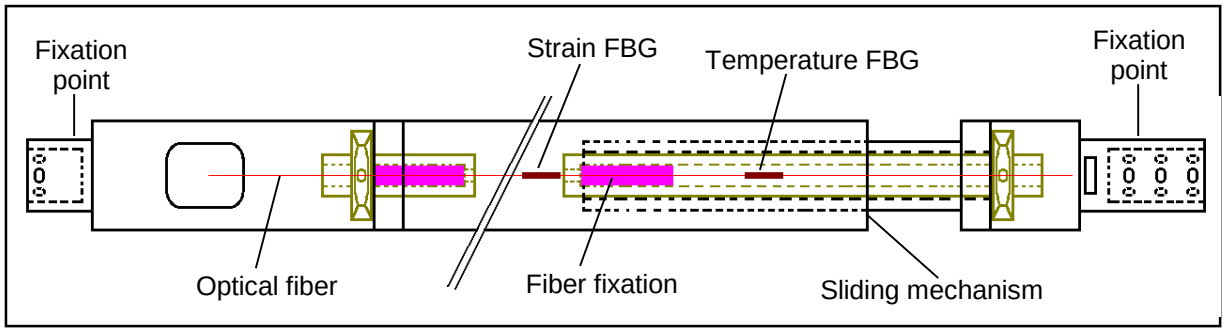

Fig. 4-4: Schematic drawing of opto-mechanical cell

The relative displacement (Δd) of the sliding fixation point can be calculated using the wavelength shift of the strain-FBG ($\Delta\lambda$), the strain sensitivity of the grating (=1.2 pm/µe) and the length of the fiber under stress (L_{FBG}):

$$\Delta d = \Delta\lambda \bullet L_{FBG} \bullet 10^{-6} / 1.2 \qquad (4\text{-}1)$$

with Δd and L_{FBG} expressed in mm and $\Delta\lambda$ expressed in pm. The resolution of the sensor is mainly defined by the resolution of the interrogation unit and is a function of the length of the fiber under stress (L_{FBG}). The resolution of the interrogation unit is typically 1 pm. This corresponds to a displacement resolution (d_{res}) of the opto-mechanical cell of:

$$d_{res} = L_{FBG} \bullet 10^{-6} / 1.2 \qquad (4\text{-}2)$$

The range of the sensor is defined by the maximum strain that the strain-FBG can sustain. Special fabricated FBGs are used which can sustain a strain of up to 5%. In order to assure a reliable working of the sensor, only the half of the maximum strain level is used (2 %). This corresponds to a strain range of:

$$d_{range} = L_{FBG} \bullet 0.02 \qquad (4\text{-}3)$$

Based on equation 4-2 and 4-3 it can be calculated that the resolution is equal to 41.7 $\bullet 10^{-6}$ of the full range. This sensor can be customized very easily. Depending on the requirements requested by the application L_{FBG} can be chosen between 0.1 and 1 m. The thermal expansion coefficient of this carbon tube is 6 $\bullet 10^{-7}$ 1/K.

Carbon extension cable

The carbon extension cable is of the same type as the temperature cable. In order to measure the elongation of the cable, due to for example thermal expansion, one FBG for each carbon cable is used. These FBGs will allow to compensate for any elongation effects of the carbon cable which might affect the accuracy.

Packers

The packers consist of a stainless steel rod and a metallic shield around. The metallic shield can be inflated in the borehole using a hydrostatic system. This allows fixing the packer into the borehole. The PVC/metallic rod has different holes for guiding the fiber (pressure resistant tubings) from the lower cells and the tubings used to inflate the packers.

Fig. 4-5: Packer

Temperature cable

The temperature cable consists of a fiber wherein FBGs have been located on requested positions. The fiber is reinforced by carbon material in order to protect the fiber from environmental influences (figure 4-6). The temperature coefficient is determined by the temperature sensitivity of the grating and the thermal expansion coefficient of the reinforced cable. The sensitivity is equal to 8-10 pm/K. Taking into account the resolution of the instrument, this responds to a temperature resolution of 0.03 K. (*JOBMANN et al., 2005*) The cable has been installed in the same borehole as the strain cable.

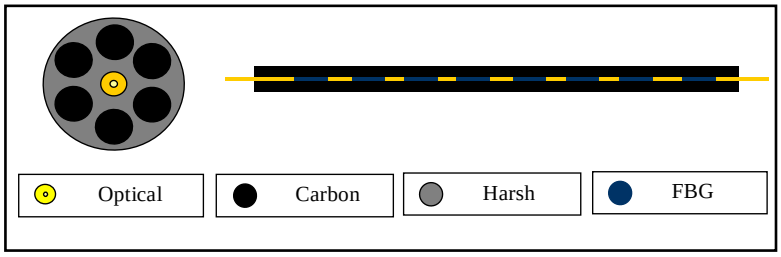

Fig. 4-6: Design of temperature cable

The interrogation system

An optical source illuminates through a coupler and the optical output port of the interrogating system, the Bragg sensors connected to the unit. FC/APCs (Angled Polished Connectors) or E2000 connectors are used. The connectors are beveled avoiding thus multiple reflections between the connector planes. The reflected light by the Bragg sensor is filtered using the Fiber Fabry Perot tunable filter (FFP-TF). The FFP-TF scans the entire wavelength range, typically 40nm (5000GHz). The filter output is detected using a photo-detector, differentiated and zero-crossing processed to achieve picometer resolution. In order to achieve high resolution and high accuracy, a fixed picowave multi-wavelength reference is included in the system. It consists of a reference LED, a fixed Fabry Perot, an isolator and a band-pass filter. They are connected as shown in figure 4-7. The fixed Fabry Perot (FP) is mounted on a thermoelectric heater/cooler (THC) as well as the reference FBG and both are kept at a constant temperature (45°C). The wavelength of the reference FBG serves only to identify a unique FP order of the fixed FP. The fixed FP has very uniformly spaced pass band with better than 1 pm spacing uniformity and has a wavelength difference of 1.5 nm between FP orders. In order not to interfere with the measurements, the light source and the reference LED are alternately switched on and off. In this way, the interrogation system first scans the series of FBGs and stores the peak locations, while the next scan reads the picowave reference that acts as a wavelength scale.

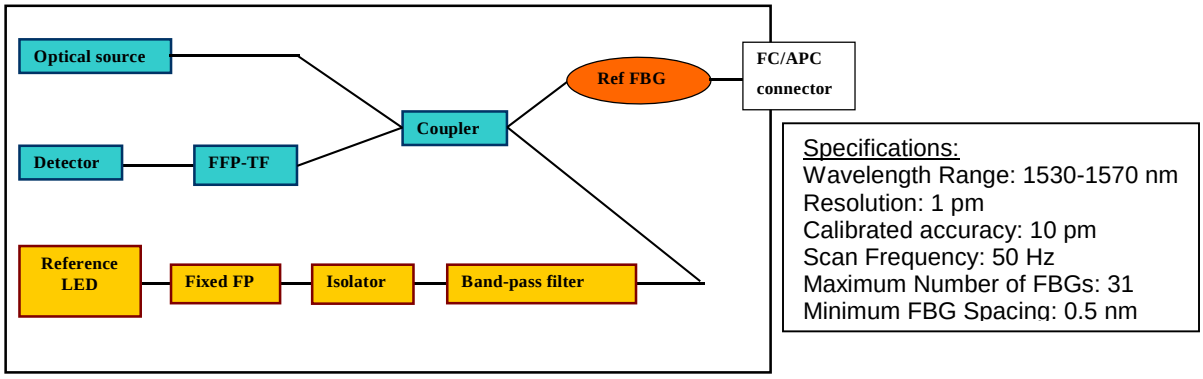

Fig. 4-7: Configuration of interrogation system

Optical source

As optical source, an erbium doped fiber source was used. This source consists of a single mode fiber whose core is doped with the rare earth erbium (Er). The fiber is pumped with a laser diode and due to the energy transitions of the core medium, spontaneous emission occurs around 1550 nm (second telecom window, smallest optical losses) with a spectral width of about 40 nm. This kind of fiber is usually used as an optical amplifier in the telecom industry (ASE or Amplified Spontaneous Emission). The source delivers its constant optical power of 15 mW over its entire spectrum, 1530 nm-1570 nm. No special control is required.

PC Control

The unit is controlled with a PC through a block interface with electrical connectors and cable link to an acquisition card plugged in the PC. The card is a National Instruments NI-DAQ card which is one of the most convenient acquisition card family nowadays suited for achieving and processing analogue and digital signals. The software-driver of the unit is programmed under LabVIEW and performs fine tuning FFP filter scanning, signal acquisition and processing as well as results calculating.

Optical switch

For large scale sensing networks many sensors are to be interrogated. Since the number of sensors that can be multiplexed on one optical line is limited by sensor specifications and design, the WDM unit (Wavelength Division Multiplexing) has to interrogate one after each other as many different optical lines as necessary. This is simply Time Division Multiplexing or TDM combined with WDM. The lines are connected to an optical switch driven by the very same PC driving the interrogation unit. The software switches the lines and stores the results identifying the line interrogated and the sensors interrogated.

Installation at Mont Terri

The installation of the sensing system has been performed in two parts. In December 2003 the optical fibers and the carbon rods have been installed in borehole BHE-D6 (figure 4-8) and in January 2004 the opto-mechanical cell (sensor head) has been added together with the optical source and data acquisition system. During the first period 5 packers have been fixed at different depths which is measured from the wall to the fixation of the carbon cable. The temperature cable installed in parallel to deformation cable measured the temperature at seven different positions. The final configuration and setup is shown on figure 4-9.

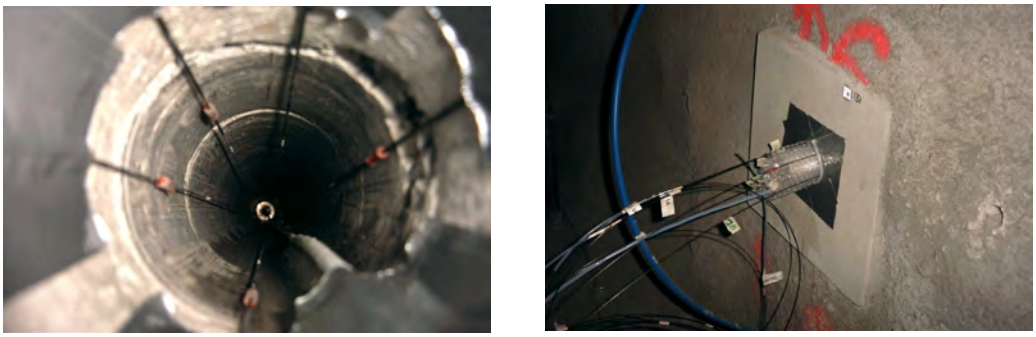

Fig. 4-8: Installation of carbon rods and temperature cable

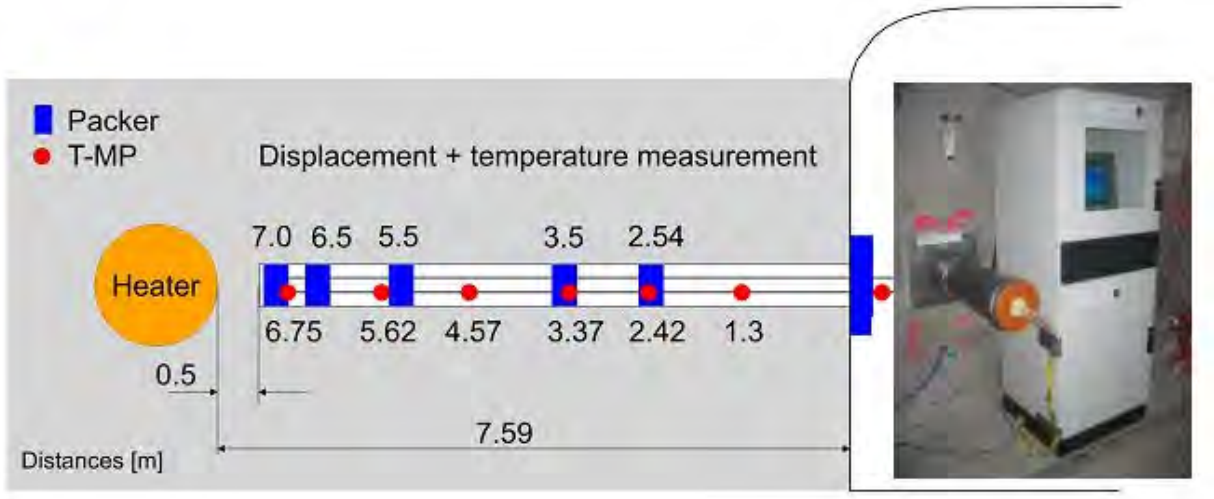

Fig. 4-9: Final configuration of measurement system in BHE-D6

The blue rectangles indicate the position of the packers and thus the deformation measurement points. The red dots are indicating the temperature sensing points. Due to drilling activities in the direct vicinity of the borehole mouth a breaking of the cable has occurred yielding a loss of the first deformation measurement point at 2.54 meter. All other cables could be repaired.

4.3 Measurement results

The deformation and temperature measurements in BHE-D6 started at 14th January 2004 (approx. 83 days before start of heating) and ended at 10th October 2005 (551 days after start of heating). The measurement results of the other observation boreholes gained during HE-D experiment are given in appendix B.

4.3.1 Temperature measurement

Figure 4-10 shows measurement results of all DBE TECHNOLOGY temperature sensors, while figure 4-11 shows only sensors near to MI Niche including the GRS sensors BHE-D07 and BHE-D12. Among other things following facts can be stated:

I The temperature measured in the MI Niche (sensor TM1) changes within a seasonal cycle and possibly due to additional disturbance by working in the niche. Sensor TM1 shows an amplitude of approximately 7 K (13°C … 20°C).

II The influence of ventilation temperature variation can be observed for all sensors. Before start of heating the sensors TM3 – TM7 show a decrease of up to 0.5 K for the last 2 months before heating (and even later), which indicates a temperature equilibration process in the rock due to ventilation temperature. This trend is proven by sensors BHE-D07 and D12 which show a similar response (c.f. figure 4-11 and appendix B-7 and B-12). For this reason all measurement data of BHE-D06 represents a superposition of this equilibration process and the temperature increase due to heating.

III The change of ventilation temperature strongly affects all measurements of sensors next to MI Niche but its influence reduces with increasing distance from the niche wall going along with a later time of onset (figure 4-11).
However, even for sensor TM4 located 3.37 m behind drift wall this ventilation effect overcompensates heating induced temperature increase. This results in a temperature decrease even 40 days before stop of heating.

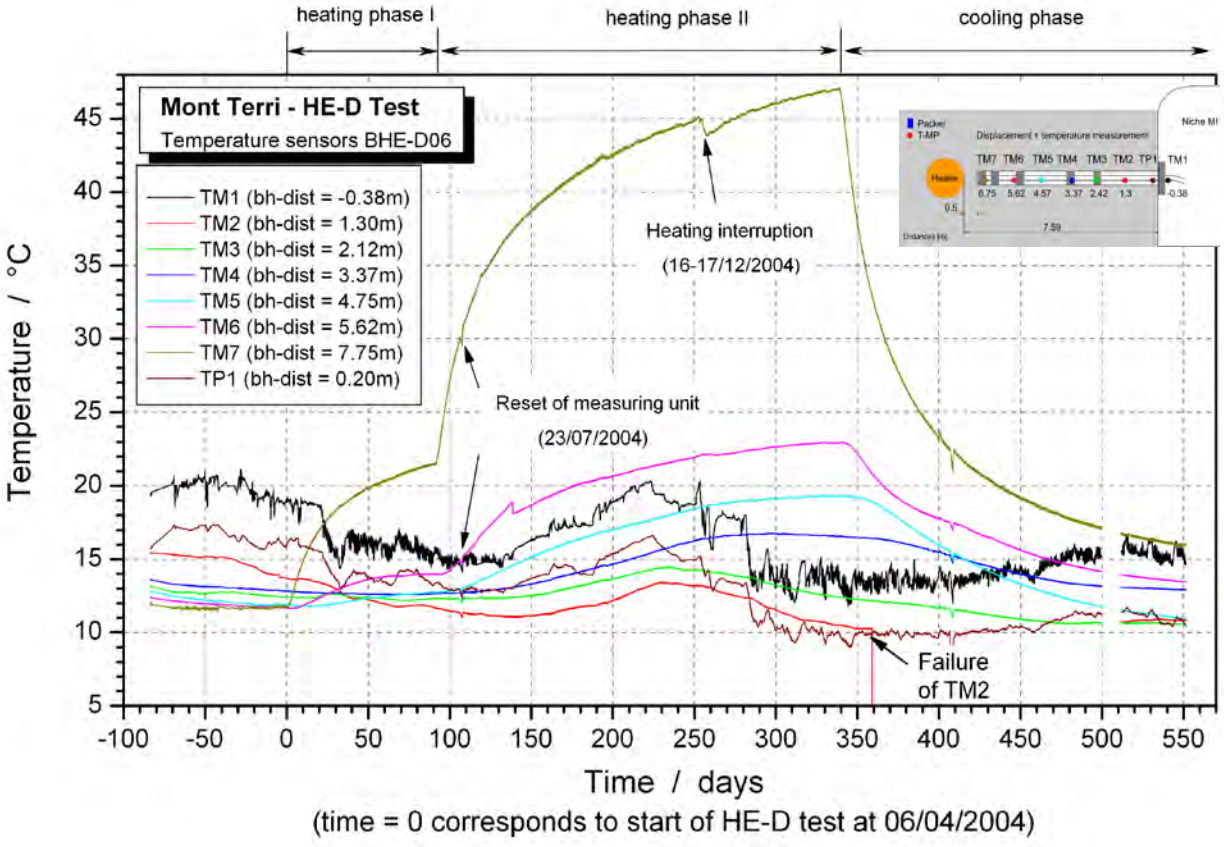

Fig. 4-10: Temperature measurement results in borehole BHE-D06

IV A non uniform temperature distribution before start of heating is evident with an increase of temperature into direction of MI Niche.
V The small drops in temperature occurring at all sensors at the 108th day (23/07/2004) are caused by reset of measuring unit.
VI Sensor TM2 fails during 359th and 512th day. Furthermore a data loss occurred for all sensors between 499th and 512th day.
VII Sensor TM6 show a sharp decrease of about 0.8 K at the 138th day. A possible reason could be the penetration of water into the borehole (water was observed at the borehole mouth at an intervention).

The measurements show that there is a superposition of temperature increase due to heating with local equilibration of rock temperature. Since these effects result in temperature differences of the same order of magnitude it has to be considered for evaluation of sensors next to MI Niche and of course for the following back analysis.

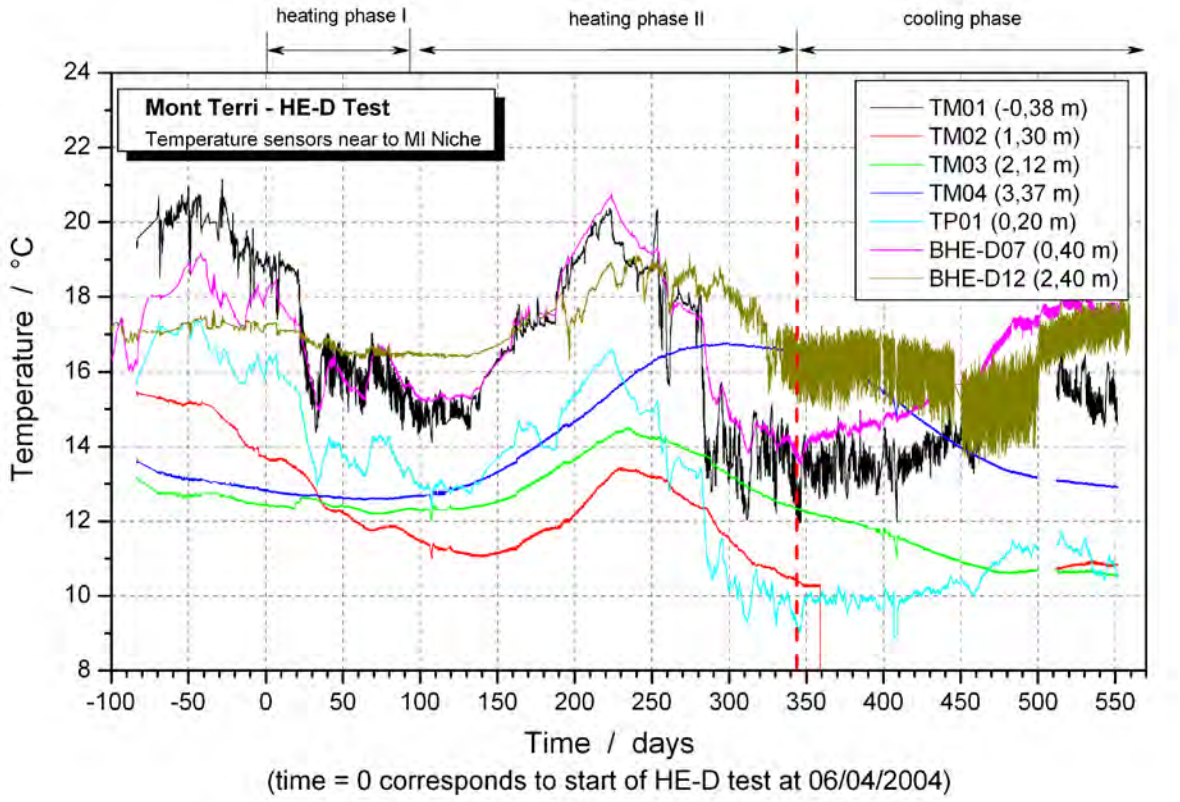

Fig. 4-11: Temperature evolution at sensors next to MI Niche

4.3.2 Displacement measurement

Figure 4-12 shows displacements of packers in borehole BHE-D06 relative to the head plate in MI Niche from start of measurements (83 days before start of heating) until end of HE-D test. The measurements indicate that:

I For all sensors an ongoing expansion of measuring interval is evident. This process can be proven for all sensors (except DP1) even before start of heating. During this period sensors show a similar slope of approx. 8.8 µm/d. This effect is probably caused by a movement somewhere between sensor DP2 and the head plate. A possible reason for this could be the opening of an EDZ-fracture going along with a rigid block-movement of fractured rock towards MI Niche. Such rock convergence mechanism is described by *BOSSART et al. (2002)*. Within their investigations covering the overcoring of resin-filled fractures, an interconnected network of unloading fractures parallel to drift wall (subvertical dipping) has been detected with a horizontal extension of up to 0.7 m behind drift wall

(excavation via pneumatic hammering). Similar values for horizontal extension of EDZ are given by *SCHUSTER et al. (2001)* and *ALHEID et al. (2002)* obtained from geoelectric and seismic methods. *VIETOR et al. (2006)* supposed discontinuous fractures even > 2.5 m away from the tunnel wall, which can be activated by excavation work and account for a large part of deformation. He reported extensometer measurements during excavation work of EZ-A Niche before and after a roof fall which gives evidence of a complete rock block detachment without significant internal deformation.

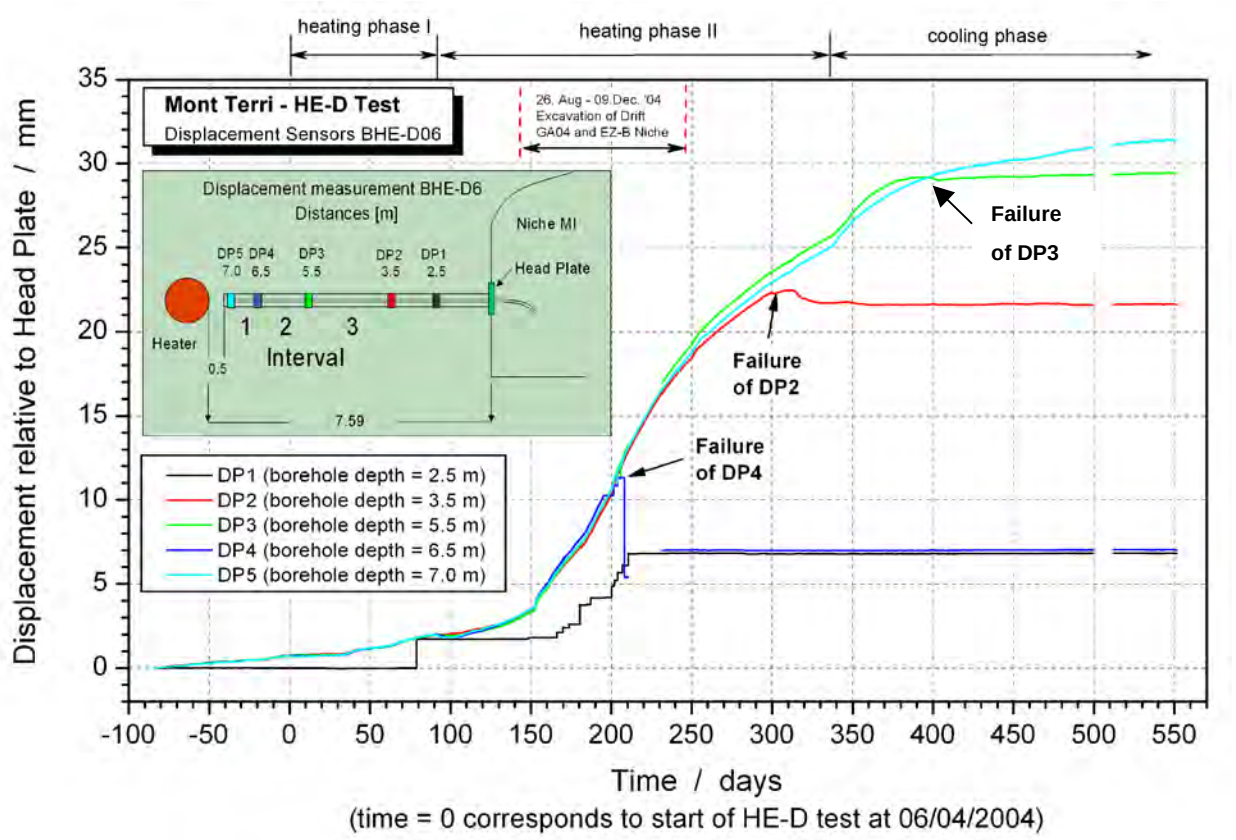

Fig. 4-12: Measured packer displacements relative to head plate

The assumption of a rigid block-movement is also supported by following facts:

- o visual site inspection: open fractures in the shotcrete and host rock had been observed near the head plate
- o extensometer measurements of SOLEXPERTS in borehole BHE-D5, which show significant expansion of first interval PT01 – head (approx. 1.5 m - 0.5 m behind MI Niche wall), c.f. appendix B-6 and C-10
- o inclination measurement at MI Niche wall by SOLEXPERTS.

II Convergences increased rapidly since 152th day. A possible explanation for these movements could be stress redistributions induced by excavation work of Gallery GA04 and EZ-B Niche (26th of August – 9th of December 2004). This assumption is supported by *VIETOR et al. (2006)*, who reported that convergences showed significant correlations to excavation work at the Mont Terri URL, even though the tunnel face was > 20 m away. He supposed not only mechanical stress distributions causing these convergences, but rather pore pressure re-distributions in the far-field and a strong hydro-mechanical coupling.

III Since date of installation the displacement sensor DP1 is out of order due to a damage of fiber-optic cable caused by drilling.

IV Sensors DP4 (200th day), DP2 (300th day) and DP3 (400th day) failed due to exceeding the measurement range. The drift convergences measured in the Mont Terri URL (c.f. tunnel

convergences reported by *NAGRA, 2003*) and the measurement layout calculations did not imply such large deformations as obtained in the MI Niche.

V At the beginning of each heating phase the slope of all curves decrease, while heater-near packers show strongest and quickest reaction. This phase of a negative slope is followed by a positive slope.

Because this above mentioned convergence effect superposes the thermally induced deformations only relative displacements between the packers have been used for interpretation of measurements, assuming that they are not affected by the mentioned effect and therefore representing thermally induced deformation (figure 4-13). Following measurement intervals were used for interpretation of relative packer displacement (from heater to MI Niche):

- interval 1: between packer DP5 (7.0 m borehole-depth) and DP4 (6.5 m)
- interval 2: between packer DP4 (6.5 m borehole-depth) and DP3 (5.5 m)
- interval 3: between packer DP3 (5.5 m borehole-depth) and DP2 (3.5 m)

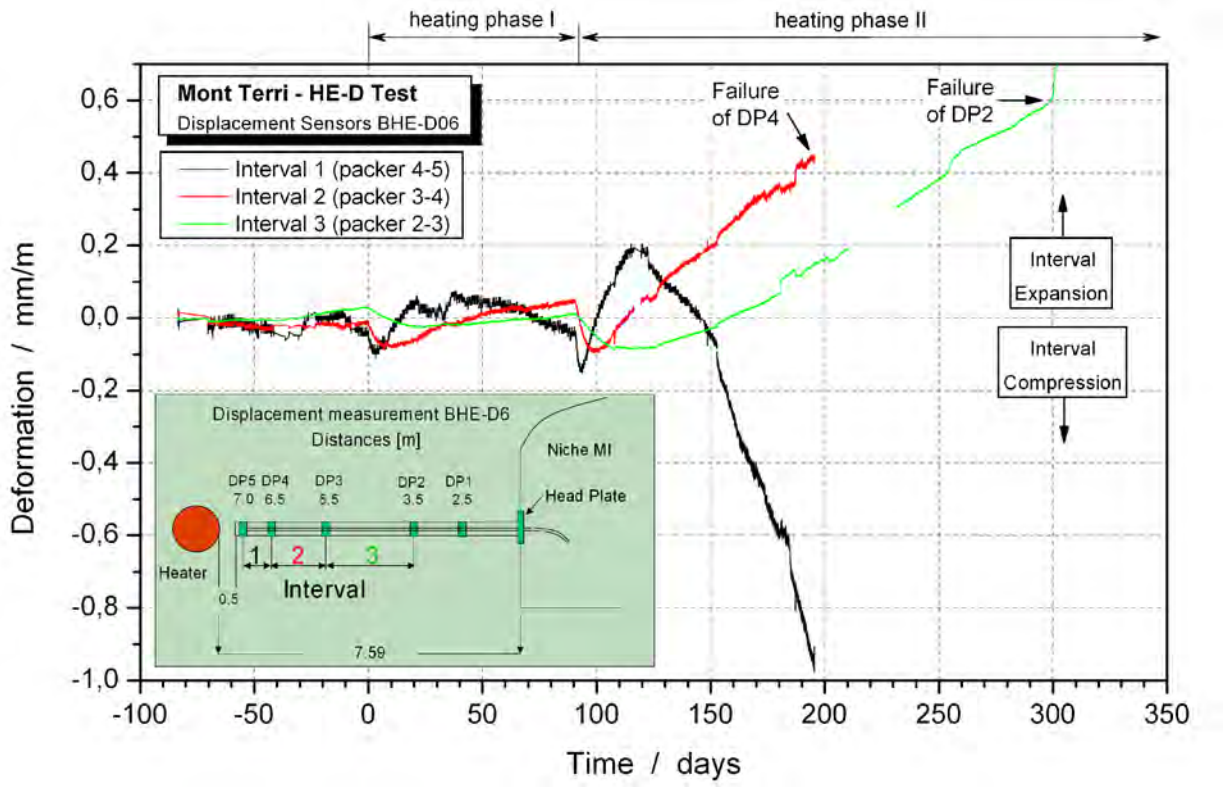

Fig. 4-13: Relative sensor displacements measured in BHE-D06

Following facts can be stated by interpretation of figure 4-13:

I The sensors indicate a deformation of rock even before start of heating. While interval 1, nearest to heater, indicates an expansion due to the stress release caused by drilling of BHE-D0 (about 28–32 days before heating) the interval 3 shows a significant expansion which is assumed to be caused by faster moving of packer 2 towards MI Niche.

II Immediately after start of heating all intervals are subjected to a phase of compression due to increasing rock pressure caused by thermal expansion of the rock close to the heaters. The duration of phase and time of maximum compression depend on the distance to the heater. For interval 1, nearest to heaters, the compression effect is superposed by thermal expansion three days after start of heating and compensated after approx. 8 days. During this time the intervals far from the heaters still show a further compression because they are not affected by thermal expansion up to that time. The same effects of compression and following expansion can be observed for heating phase II with higher slopes caused by higher rock pressure and temperatures.

III Due to the fact, that a steady state heat flow within an interval would cause a constant value of relative displacement the decrease of relative displacement in interval 1 indicates the presence of another effect. This compression effect could be observed during both heating phases, while in heating phase II the compression of the interval is much higher and runs faster than during heating phase I. The origin of movement is still not clarified (movement along fractures? / thermally induced water release? / consolidation or thermo-plasticity effects? / re-arrangement of clay-particles under thermal load?). Deformation measurements by SOLEXPERTS in boreholes BHE-D04 and BHE-D05 (c.f. appendix B-5 & B-6) also showed larger deformation in an area 2 – 4 m away from heater.

4.4 Laboratory investigations on drill core samples

Prior to the heating phase several drill core samples have been taken from the BHE-D06 borehole to perform laboratory investigations on the thermo-physical rock properties (Fig. 4-14). The measurements were aimed at using the results as basic input parameters for the numerical back analysis of the thermal rock behavior. The investigations included the thermal conductivity, thermal diffusivity, specific heat capacity and linear thermal expansion (*BUNTEBARTH 2004, JOBMANN & POLSTER 2005*). For all rock properties the temperature dependence has been investigated completed by measurements of pressure dependence of the thermal conductivity and diffusivity. Special attention has been turned to the effect of anisotropy.

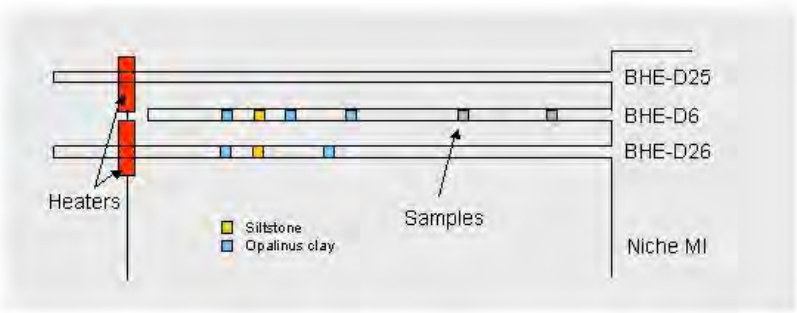

Fig. 4-14:
Location of drill core samples taken from borehole BHE-D06 and BHE-D26

After the end of the experiment two new boreholes have been drilled for additional investigations. From one of these boreholes (BHE-D26) a few drill core samples have been taken to perform additional laboratory investigations on the thermo-physical rock properties (figure 4-14). These investigations have been focused on the thermal conductivity of the clay samples as a function of water content (*BUNTEBARTH, 2006*). It is worth mentioning that at a distance of about 5.20 m from the niche the clay was rather silty yielding a higher value of thermal conductivity than determined for the Opalinus Clay.

4.4.1 Thermal conductivity

The measurements have been performed by using the divided-bar method at an uniaxial pressure of p=2 MPa. One sample with known conductivity and the new sample are compared under steady state heat flow conditions. The thermal conductivity of the new sample λ_p can be determined by the temperature gradient within the sample and the heat flow density Q. The accuracy of the measurements is about 1.5 %.

$$\lambda_p = Q / (\Delta T/ \Delta x)_p = \lambda_p (\Delta T/\Delta x)_w / (\Delta T/\Delta x)_p \qquad (4\text{-}4)$$

index w – heatflowmeter
index p – sample

The thermal conductivity of a porous solid depends on its mineral composition, porosity, pore filling fluid as well as on temperature and pressure environment.

The first measurements were aimed at determining the thermal conductivity as a function of temperature yielding only slight temperature dependence (*BUNTEBARTH, 2004*). Especially in the temperature range covered by the experiment (20°-100°C rock temperature) this dependence could be neglected ($\lambda = \lambda(T) = -9.7 \cdot 10^{-4}\ T[°C] + 1.28$ [W/m·K]). The dependence on pressure is also rather small (figure 4-15) and after reaching a pressure of about 2 MPa the thermal conductivity is more or less constant. The slight increase at low pressures is due to the closing of micro cracks which are not typical for the location but occurred during sampling and preparation. The pressure also reduces device specific contact resistances. In order to be sure to avoid these effects all future measurements have been performed by applying a pressure of 2 MPa.

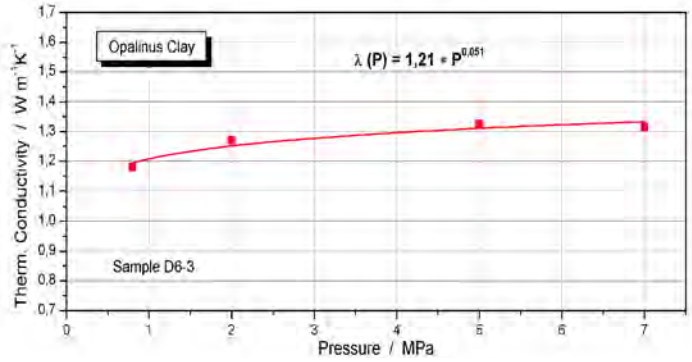

Fig. 4-15: Thermal conductivity vs. normal pressure

A plot of measurement results is shown in figure 4-16. In addition the results from the first measurement campaign have also been plotted for comparison. It is interesting to see that the conductivity values obtained from the new measurements (BHE-D26) are higher than those obtained during the first measurement campaign (BHE-D6) even the locations of sampling are close to each other.

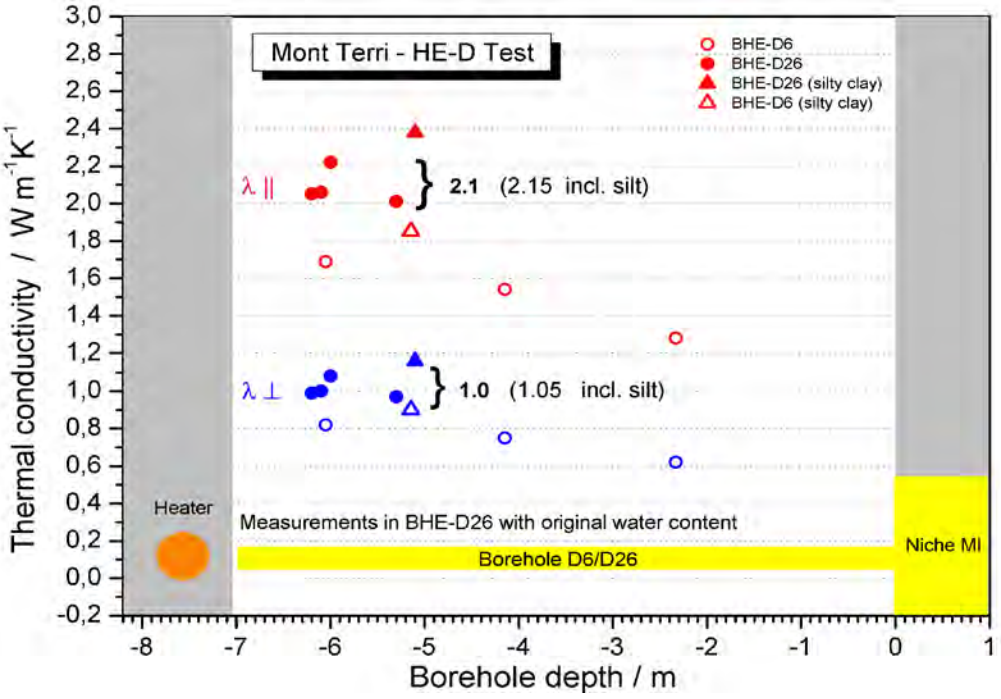

Fig. 4-16: Thermal conductivity of core samples taken from borehole BHE D-26 and D-6 as a function of distance to the MI Niche.

It is assumed that this difference is mainly due to the different used sealing techniques right after sampling. In the first case the samples have been sealed using metallic foil and in the second case the samples have been completely sealed with artificial resin. The later technique has the advantage that all pores at sample boundary have been completely sealed avoiding any vaporization. Thus no fluid has been lost at all prior to the measurements in the laboratory and the original water content could be kept. This hypothesis seems plausible if we look at the dependence of thermal conductivity on water content which in addition has been measured in the lab (figure 4-17).

During the first measurement campaign a decrease of thermal conductivity has been noticed the nearer the samples have been taken from the niche. It is assumed that due to a transition from sandy, carbonate-rich facies to shaly facies towards direction of MI Niche also mineralogical composition changes significantly (c.f. figure 4-2 and 4-19). Thus the lower content of quartz and calcite (λ_{quartz} = 7.8 W/m·K, $\lambda_{calzite}$ = 3.4 W/m·K) and the higher content of clay minerals with significant lower thermal conductivities consequently lead to lower thermal conductivities. This hypothesis is proofed by geologic mapping of the test area.

Further hypotheses for the conductivity difference are local inhomogeneities of facies and mineralogical composition respectively. Different types of clay have been found in the investigated area within clay-rich shaly facies. Two samples for example consist of silty clay that has a significantly higher thermal conductivity (figure 4-16). If no very sharp boundary is assumed between clay types different mineral compositions might occur along the 2 boreholes and thus leading to slightly different thermal conductivities. It is assumed that both effects together might be the reason for the conductivity difference.
In figure 4-17 measurement results of thermal conductivity as a function of water content are plotted for different samples.

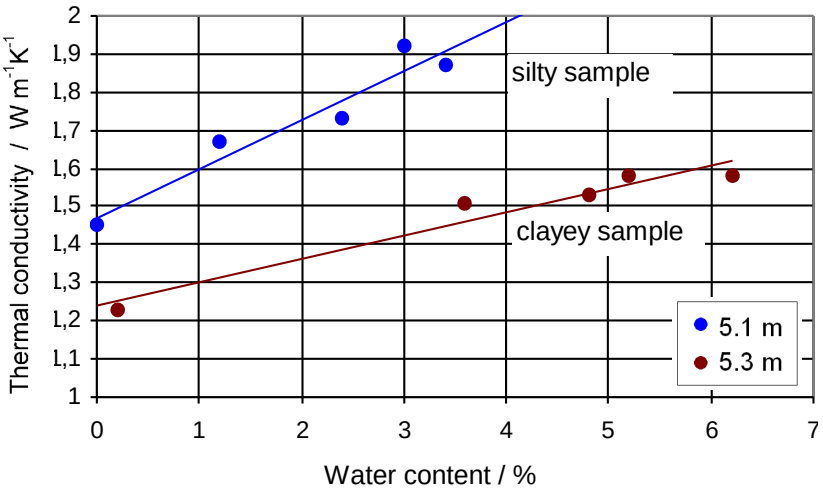

Fig. 4-17: Thermal conductivity of core samples (BHE D-26) as a function of water content

The samples have been saturated up to a water content of 7%. For higher water content the samples got very plastic and a measurement of the thermal conductivity was not possible any more. The measurements have been started at 7% water content. Then the samples have been dried at 97°C for a couple of hours and the remaining water content has been determined and the thermal conductivity been measured. As expected the dependence of thermal conductivity on water content is linear and can be described by the following relationships (mean values):

$$\lambda\ [W\ m^{-1}\ K^{-1}] = 1.36 + 5.25 \cdot w\ [-] \qquad (4\text{-}5)$$

This means that λ increases about 0.053 W $m^{-1}K^{-1}$ per percent water content.

4.4.2 Specific heat capacity

The specific heat capacity of Opalinus Clay has been determined on 2 samples, whereas one sample was tested again after drying. The results are listed in table 4-1. The mean value for a temperature of 20°C is approx. 60% higher than reference value of 800 J $kg^{-1}K^{-1}$ given in *ANDRA (2003)* and 40% higher than mean value of 920 J $kg^{-1}K^{-1}$ given in *NAGRA (2002)*.

Table 4-1: Results of specific heat capacity measurements

Sample	cp (kJ/kg K)	cp (kJ/kg K)
	T=20°C	T=140°C
D6-1	1.23	1.39
D6-2	1.36	1.38
D6-2 dry	1.14	1.39
Mean (without dry)	**1.29**	**1.38**

4.4.3 Thermal expansion

The thermal expansion has been measured on different samples under drained conditions. Figure 4-18 shows as an example the results for sample D6-1. The blue curve shows the typical expansion of a wet sample as a function of temperature. The red curve represents the first derivative making the processes of releasing different water more obvious. So figure 4-18 clearly points out that an assumption of constant thermal expansion coefficient is only valid for temperature below approx. 40°C. For temperatures within a range of 40 to 85°C the release of adhesive bound water compensates the thermal expansion. Above 85°C the beginning release of interlayer water overcompensates thermal expansion so that an overall shrinkage can be observed.

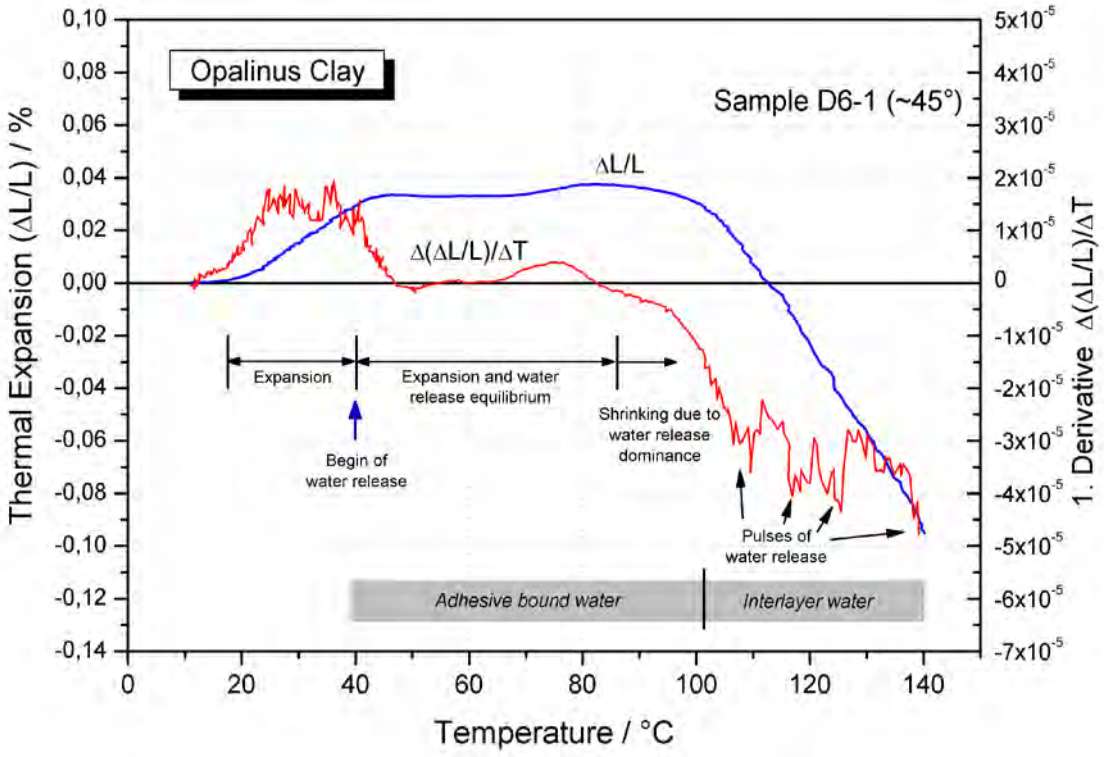

Fig. 4-18: Thermal expansion and shrinkage of Opalinus Clay sample

For all other measurements the characteristic shape of the curves is quite similar clearly indicating that expansion and shrinkage of the clay samples is strongly dominated by the water content. Certainly an anisotropic behavior could not be clearly identified. The linear thermal

expansion coefficient has been calculated to $1 \cdot 10^{-5}$ K^{-1} valid for temperatures up to 50°C. This value is lower than those one given as the reference value $2.5 \cdot 10^{-5}$ K^{-1} (*ANDRA, 2003*). It has been obtained from preliminary laboratory measurements that have been performed up to a temperature of 50°C only under undrained conditions (*GENS, 2000*). The sample with a water content of w = 3.92% has been completely sealed by a latex membrane to avoid any water release. Thus the measured expansion is mainly affected by water expansion within the sample since the expansion coefficient of water is one order of magnitude higher than those of minerals. It can be stated that both measurements provide the range of the expansion coefficient valid for the in-situ heater test.

4.5 Back analysis

The fiber optic in-situ measurements have been accompanied by three dimensional numerical calculations for the purpose of analysis and description of the rock behavior (c.f. *JOBMANN & POLSTER, 2005*). Due to the strong anisotropic rock properties, the geological situation, anisotropic state of stress and the location of the drifts, a full 3D model was necessary to apply. The rock properties determined in the laboratory have been used as basic input parameters for the model calculations. The following chapters will give a detailed model description, an overview of the used constitutive laws and thermo-physical rock properties as well as the modeling results compared to the measurements.

For modeling of the HE-D experiment a back analysis with a stepwise solution has been applied. Due to the fact that the temperature is the driving force for thermo-hydro-mechanical (THM) behavior of the rock, only the temperature evolution has been modeled as a first step. This was to achieve a most realistic temperature field prior to any hydro-mechanical simulation. Different sets of thermal parameters within a range given by results of former (*ANDRA 2003, NAGRA 2002*) or accompanying laboratory investigations (*BUNTEBARTH, 2004*) were used to achieve best fit of measured and calculated temperatures. Measurements of temperature sensors in borehole BHE-D0 (GEXTER, heater borehole), BHE-D06 (DBE TECHNOLOGY) as well as sensors in BHE-D07 - BHE-D17 (GRS) were used for this process (c.f. appendix B)

Afterwards a coupled hydro-mechanical (HM) calculation for calibration of hydraulic behavior has been performed. The data of 2 experiments were used for calibration process:

- pore pressure measurements at the ED-B drift as stated in NAGRA, 2002 and
- pore pressure measurements of HE-D test (boreholes BHE-D07 to BHE-D17, see appendix B-7 to B-17) before start of heating.

The calculations were aimed at determining the initial state of pore pressure that fits most to measured initial conditions. The set of thermal and hydraulic parameters which fits best to the measurement has been used as input for the following coupled THM-calculation. Within this step a fitting of measured and calculated displacements has been achieved while varying different mechanical and hydraulic parameters.

The mathematical calculations have been performed with FLAC^{3D} which is a 3D continuum code based on the finite difference method (*ITASCA, 2002*). It uses an explicit or implicit solution scheme and can be used for thermal, fluid, creep and dynamic analysis. Coupled THM-problems can also be handled. Although a finite difference method is applied, no regularly grid is necessary since FLAC ^{3D} uses the so-called mixed discretization method (*CUNDALL, 1982*). In order to consider anisotropic thermal conductivities an additional module has been developed and implemented into the source code.

4.5.1 Constitutive model

For solving coupled THM-problems FLAC ^{3D} uses following balance equations and transport laws (*ITASCA, 2002*):

- equations of motion and equilibrium,
- equation of energy balance (thermal analysis),
- equation of fluid-mass balance,
- Fourier's Law of heat conduction,
- Darcy's Law of fluid transport in a porous medium.

The thermo-mechanical coupling takes place via the thermal expansion coefficient α_t. A further constitutive equation specifies the fluid response to changes in pore pressure, volumetric stains and temperature within the poro-elastic medium. Pore pressure and temperature influences are involved in the incremental laws to complete the THM-coupling.

Heat flow

For numerical solution of heat-flow problems the code uses the equation of energy balance and transport laws, which are derived from Fourier's Law of heat conduction. The energy-balance equation can be given in following differential expression:

$$-q_i^t + q_v^t = \rho \cdot c_v \frac{\partial T}{\partial t} \qquad (4\text{-}6)$$

with

q_i^t	heat-flux vector [W / m^2]
q_v^t	volumetric heat-source intensity [W / m^3]
ρ	density [kg / m^3]
c_v	specific heat at constant volume [J / kg·K]
T	temperature [°C]
t	time [s]

index t = thermal; index i = three components of vector , i = 1,3

Transport of heat is taken into account by heat conduction. The dependence between heat-flux and temperature gradient (Fourier's Law) for a homogenous isotropic solid can be given in following form:

$$q_i = -\lambda \cdot T_{,i} \qquad (4\text{-}7)$$

with

λ	thermal conductivity [W / m·K]
$T_{,I}$	vectored temperature gradient [K / m]

However, the calculations consider anisotropic thermal conductivities. A consideration of ventilation temperature can be taken into account by a convective boundary condition with:

$$q_n = h\,(T - T_e) \qquad (4\text{-}8)$$

with

h	convective heat-transfer coefficient [W / m^2·K]
T	temperature of boundary surface [°C]
T_e	ventilation temperature [°C]

The (one way-) coupling to the mechanical stress calculation is carried out via the thermal expansion coefficient α_t. Thermal-strain increments ε_{ij} associated with the free expansion corresponding to temperature change ΔT have the form:

$$\Delta\varepsilon_{ij} = \alpha_t \Delta T \delta_{ij} \qquad (4\text{-}9)$$

with

α_t	coefficient of linear thermal expansion [1/K]
ΔT	temperature difference [K]
δ_{ij}	Kronecker delta.

Within a solution of thermal-stress problems a reformulation of the incremental stress-strain relations takes place, which is accomplished by subtraction of the thermal strain increment from the total strain increment.

Fluid flow

For numerical solution of fluid-flow problems the code uses the equation of fluid-mass balance and Darcy's law of fluid transport in a porous medium. The fluid-mass balance equation can be given in following form:

$$-q_i^f + q_v^f = \frac{\partial \zeta}{\partial t} \qquad (4\text{-}10)$$

with

q_i^f specific discharge vector [1 / s] (index f = fluid)
q_v^f volumetric fluid source intensity [1 / s]
ζ variation of fluid volume per unit volume of porous material due to diffusive fluid mass transport
t time [s]
index f = fluid; index i = three components of vector , i = 1,3

The relation between the specific discharge vector and the pore pressure is defined by the transport law after Darcy. For a homogenous isotropic solid and constant fluid density it can be given in the form:

$$q_i^f = -\frac{k}{\rho_f g} \cdot \left[p - \rho_f \, x_j \, g_j \right]_{,i} \qquad (4\text{-}11)$$

with

k hydraulic conductivity [m / s]
ρ_f density of fluid [kg / m^3]
g_i components of gravity vector [m / s^2]
p pore pressure [Pa]

Anisotropic hydraulic conductivities are not considered. Permeability-porosity relations are neglected too. However, the code only considers single-phase flow. Thus, multiphase-flow effects like evolution of capillary pressure according to saturation state are neglected. A dependency of fluid viscosity (and so hydraulic conductivity) on temperature is also neglected.

Changes in the variation of pore pressure p is related linearly to changes in fluid content ξ, volumetric strain ε and temperature T by following fluid constitutive law:

$$\frac{\partial p}{\partial t} = M \left(\frac{\partial \xi}{\partial t} - \alpha \frac{\partial \varepsilon}{\partial t} + \beta \frac{\partial T}{\partial t} \right) \qquad (4\text{-}12)$$

with

M Biot modulus [Pa]
α Biot coefficient [-]
β undrained thermal coefficient [1 / K] with $\beta = 3\left[\alpha_g (\alpha - n) + \alpha_f n\right]$ (4-13)

where α_g linear thermal expansion coefficient for grains [1 / K]
α_f linear thermal expansion coefficient for fluid [1 / K]
n porosity [-]

Using equation (4-12) the pore pressure increment Δp_{ther} caused by a change of temperature ΔT is calculated by

$\Delta p_{ther} = M \beta \Delta T$ for compressible solid constituents (α < 1.0) (4-14)

$\Delta p_{ther} = \frac{K_f}{n} \beta \Delta T$ for incompressible solid constituents (α = 1.0) (4-15)

Mechanical constitutive model

The mechanical behavior is described as an elasto-plastic material law. Within the calculation an additive splitting of the deformation tensor and the tensor of deformation velocities into an elastic part $\dot{\varepsilon}_e$ and a plastic part $\dot{\varepsilon}_p$ is performed.

$$\dot{\varepsilon} = \dot{\varepsilon}_e + \dot{\varepsilon}_p \tag{4-16}$$

In the elastic part of the isotropic constitutive model, strain increments $\Delta\varepsilon$ generate stress increments $\Delta\sigma$ according to the linear and reversible Hook's law. Anisotropic elastic behavior as e.g. stated by ANDRA (2003), NAGRA (2002) or HUNSCHE et al. (2005) is not considered.

$$\Delta\sigma_{ij} = 2G\,\Delta\varepsilon_{ij} + (K - \frac{2}{3}G)\,\Delta\varepsilon_{kk}\,\delta_{ij} \tag{4-17}$$

with

G	shear modulus [N / m^2]
K	bulk modulus [N / m^2]
$\Delta\varepsilon$	volumetric strain increment
δ_{ij}	Kronecker delta.

For describing the plastic material behavior a DRUCKER-PRAGER yielding criterion with tension cut-off is chosen. The failure envelope for this criterion $f(I_2^D, \sigma) = 0$ is defined by:

$f^s = 0$ (shear failure) with $f^s = \sqrt{I_2^D} + q_\phi\,\sigma - k_\phi$ (4-18)

and the tension cut-off

$f^t = 0$ (tension failure) with $f^t = \sigma - \sigma_t$ (4-19)

where σ mean stress with $\sigma = \frac{1}{3}(\sigma_1 + \sigma_2 + \sigma_3)$ (4-20)

I_2^D second invariant of the deviatoric stress.

The material parameters q_ϕ, k_ϕ and σ_t describe the strength properties of material and can be evaluated by means of either compressive and tensile strength or friction parameters. For the numerical calculation an associated flow rule was used. Anisotropic plastic behavior as e.g. stated by *HUNSCHE et al. (2005)* is not considered.

The rate of steady state deformation (secondary creep rate) obtained from creep tests by *ZHANG et al. (2002 & 2004a)* and *NAGRA (2002)* is very low in comparison to transient deformation after loading or plastic deformations *(NAGRA, 2002)*. In addition only limited data on the supposed mechanism of creep and threshold for its onset are available. So for instance *NAGRA (2002)* reported that significant creep occurs first, when deviatoric stress reaches a certain threshold of 7.5 MPa while *ZHANG et al. (2004a)* found no lower threshold for the onset of creep of Opalinus Clay. Hence, viscous behavior ("creep") is neglected within constitutive modeling for numerical calculations. Nevertheless rheologic behavior caused by consolidation is considered (pore pressure gradient → fluid flow / drainage → change in stress state by increase of effective stress → mechanical response) which partly accounts for the observed rheologic behavior. More detailed information about the rheologic behavior of argillaceous rocks is given in chapter 3.
Neglecting a viscous part of the constitutive model can also be justified by the fact that sliding micrometer measurements by SOLEXPERTS show no significant deformation of the MI Niche wall from start of measurement at 9th December 2003 until September 2004.

4.5.2 Model description

The numerical model has been developed with regard to the real geological setting. The geological situation and the corresponding model are outlined in figure 4-19 and 4-20.

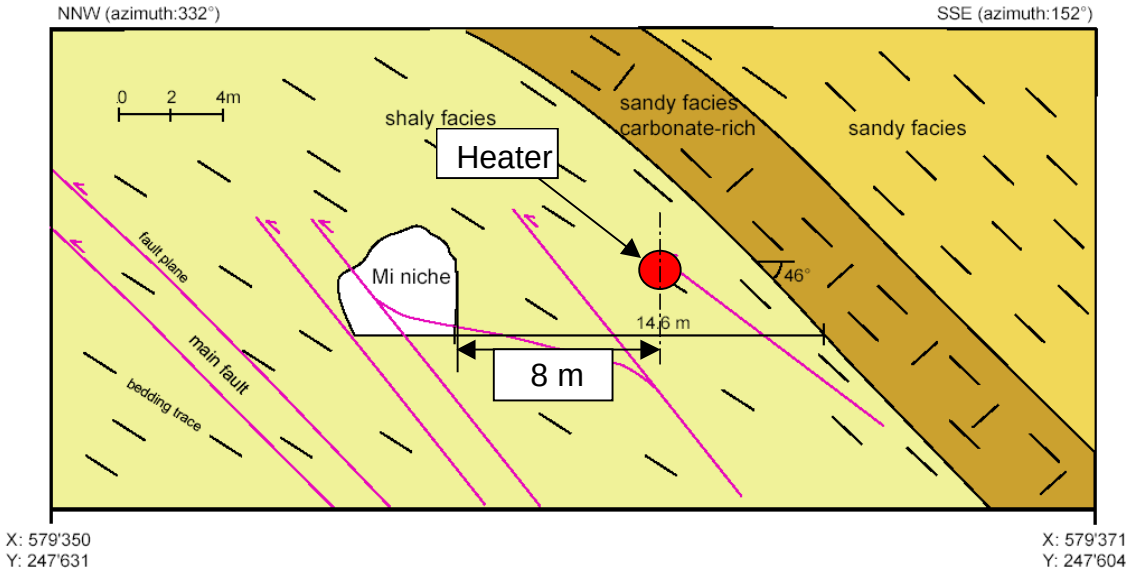

Fig. 4-19: Cross-section normal to the MI Niche axis at 12 m from the niche entrance

The calculations have been performed with a model consisting of about 103.500 Elements and 105.000 nodes (figure 4-20). The volumetric extension of the model has been chosen to be large enough so as to avoid a temperature increase at the model boundaries (assumed to be adiabatic) during the entire experiment and to avoid an influence on the state of stress due to boundary effects. This is the case for a block of 100 m x 100 m x 75 m. The smallest discretization has been realized in the direct vicinity of the heaters with respect to the high temperature gradient in that area using minimum node distances of approx. 5 cm (figure 4-21 and 4-22).

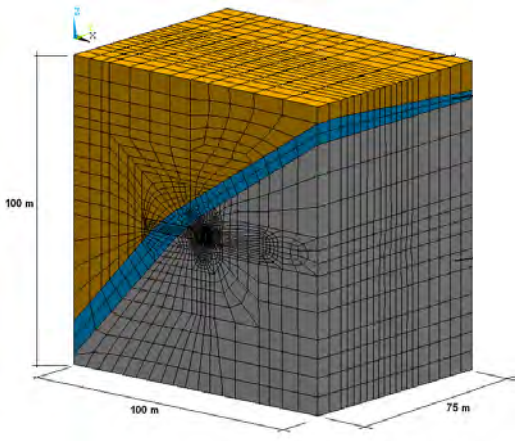

Fig. 4-20: Numerical model and geometry of the test area including discretization

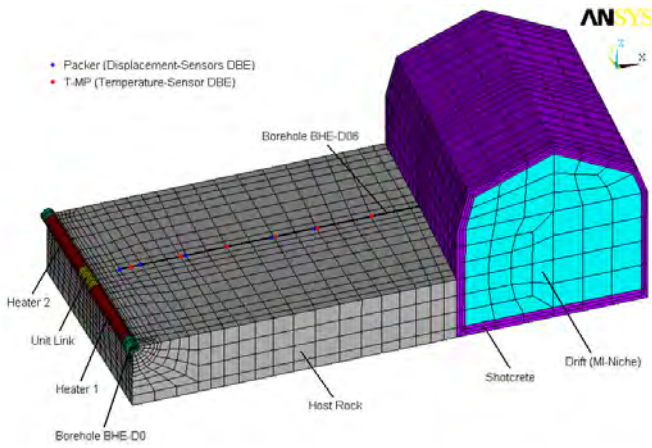

Fig. 4-21: Numerical model, detailed view into the strain cable area

Figure 4-22 shows drifts and boreholes, which are present within the model:
- MI Niche (covered by 20 cm shotcrete; not considered)
- New Gallery (covered by 20 cm shotcrete; not considered)
- HE-D Niche and borehole BHE-D0

The 2 heaters were modeled as cylinders with L = 2.0 m and ∅ = 30 cm directly facing host rock.

Appendix A-1 gives the node locations within the numerical model, which correspond to the real locations of DBE TECHNOLOGY sensors with exception of 3 temperature sensors. Figure 4-23 shows the locations of measurement points, representing DBE TECHNOLOGY and GRS sensors in BHE-D07 – D17. In this figure the locations of GRS sensors are projected into a vertical cross section along borehole BHE-D06. Appendix A-2 gives location of these sensors and of additional temperature and pore pressure sensors in BHE-D01 – D03. Differences of in-situ and modeled location are caused by discretization constraints.

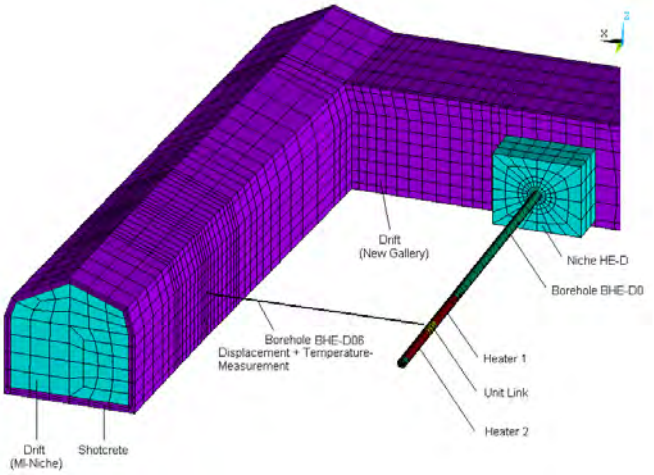

Fig. 4-22: Numerical model, detail of modeled drifts and boreholes

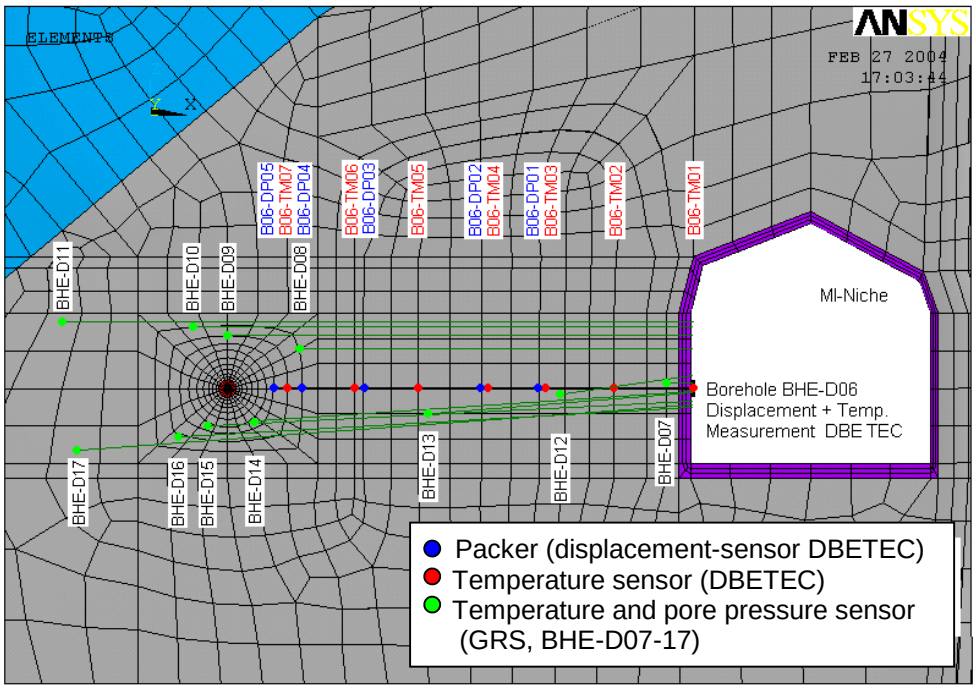

Fig. 4-23: Numerical model, location of sensors (GRS sensors are projected to plane)

4.5.3 Thermal modeling

Key problem for back analysis is a correct input of heat into the model, which has been handled by calibration of the model using measured temperatures at heaters surface (sensors H1T1-H1T3 and H2T1-H2T3 of heater borehole BHE-D0). To achieve a most realistic temperature field different sets of thermal parameters within a range given by results of former (*ANDRA 2003, NAGRA 2002*) or accompanying laboratory investigations (*BUNTEBARTH, 2004*) have been used. Measurements of temperature sensors in borehole BHE-D0 – D03 and BHE-D7 – D17 were used for this process (c.f. appendix B).

Boundary conditions, parameters and calculation sequence

Prior to heating the model was initialized with a constant temperature of 15°C. The heaters are modeled as a homogeneous volumetric heat source. The used source strength is assumed to be constant for each heating phase except heater failure at 16^{th}-17^{th} of December 2004 and 11^{th}-16^{th} of March 2005. Only thermal properties were assigned to the heater, assuming homogeneous isotropic parameters of density = 3 000 kg/m^3, thermal conductivity λ = 10 W/m·K and a specific heat capacity of c_p = 1 000 J/kg·K. The mechanical interaction with host rock was realized by applying the borehole contour with a normal stress of 1.0 MPa (internal boundary condition) as measured at the hydraulic packers. Another boundary condition was set by applying the nodes, representing the measuring ring (middle between both heaters) with a temperature function, calibrated at sensor HED-B00TEM1.

For the excavated volume within the numerical model the thermal properties of air were used assuming a density = 1.12 kg/m^3, a thermal conductivity = 0.0257 W/m·K and a specific heat capacity of 1 007 J/kg·K. Due to temperature measurement results of sensors near MI Niche (figure 4-11) additional calculations have been performed, including an additional convective heat transport (inner boundary condition) assuming a convective heat-transfer coefficient of h = 2 W/m^2·K and a temperature of convective medium T_e according to measurement of sensors TM1 and TP1 (c.f. figure 4-11).

For a first analysis all facies of Opalinus Clay were assumed to have homogeneous thermal material properties with an anisotropic thermal conductivity. The maximum conductivity is assumed to exist in the plane parallel to stratification with a strike of 57° N (parallel to BHE-D0) dipping 45° to south-east (*BOSSART et al., 2002*). Due to laboratory investigations (*BUNTEBARTH, 2004*) an increase of conductivity with raising pressure of approx. 1.8% / MPa has been taken into account. A dependence of conductivity on temperature was neglected.

Because the resulting temperature at the heaters surface depends on source strength, specific heat and thermal conductivity, an adequate evolution of temperature could be achieved by various sets of these parameters. Figure 4-24 represents a nomograph for identification of a parameter set, which can be used as calculation input resulting in appropriate temperature at the heaters surface. The range of investigated parameter sets has been chosen according to results of the laboratory investigations. Furthermore, the figure shows various parameter sets used as input for thermal calculations.

As preliminary result of thermal calibration five selected models are presented as follows. Thermal properties assumed for Opalinus Clay and applied source strength are given in table 4-2. Only model TC1 and TC5 are fulfilling conditions of the nomograph (figure 4-24), while model TC2 represents a set of thermal parameters gained by inversion (CEA-calculation, state: HE-D TD No.7) pointing out significant higher conductivities in comparison to TC1. Model TC3 uses same materials properties as TC2 but reduced source strength. Model TC4 uses parameter set of UPC which also assumes higher thermal conductivities (even perpendicular to bedding) at 100% transition of electrical power to volumetric heating power.

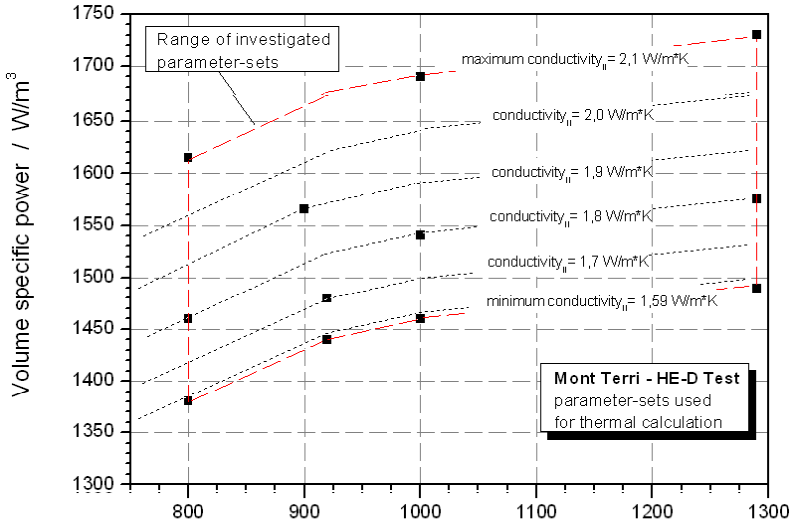

Fig. 4-24: Nomograph for identification of a parameter set (conductivity$_{II}$ = thermal conductivity parallel to stratification)

A convective heat transport (inner boundary condition) for simulation of ventilation effect has been taken into account in model TC5. Material parameters used for this model are valid to model TC1 which additional assumes a convective heat-transfer coefficient of h = 2 W/m^2·K.

The applied calculation sequence is given in table 4-3.

Tab. 4-2: Compilation of parameters used for thermal calibration (selected models)

Model	Density ρ in [kg/m^3]	Thermal Conductivity λ in [W / m K]	Factor of anisotropy A in [-]	Specific heat capacity c_p in [J / kg K]	Source strength of heaters (% of $P_{electric}$) in [W/m^3]
TC1	2 407	//: 1.70 ⊥: 0.81	2.1	920	phase I : 1 480 (65%) phase II: 4 400 (65%)
TC2 ("CEA")	2 445	//: 2.757 ⊥: 1.323	2.08	995	phase I : 2 300 (100%) phase II: 6 900 (100%)
TC3 ("CEA")	2 445	//: 2.757 ⊥: 1.323	2.08	995	phase I : 2 070 (90%) phase II: 6 210 (90%)
TC4 ("UPC")	2 450	//: 2.8 ⊥: 1.6	1.75	840	phase I : 2 300 (100%) phase II: 6 900 (100%)
TC5 including convection	2 407	//: 1.70 ⊥: 0.81	2.1	920	phase I : 1 480 (65%) phase II: 4 400 (65%)

Tab. 4-3: Calculation sequence applied

Date	Time according to start of heating [d]	progress
04/1998	-2190	Excavation of New Gallery and MI Niche
14.01.2004	-83.4	Installation of sensors in BHE-D06 (deformations set to 0)
04.03.2004	-32.7	Drilling of borehole BHE-D0 (1st step)
08.03.2004	-28.8	Drilling of borehole BHE-D0 (2nd step)
06.04.2004	0.0	Begin of heating phase I (P = 650 W)
06.07.2004	90.8	Begin of heating phase II (P = 1950 W)
23.07.2004	108.8	Hydraulic loss in packer 2 (normal stress is set to 0 for heater 2)
16.12.2004	254.7	Switch-off heater
17.12.2004	255.2	Restart heating phase II
11.03.2005	338.6	Power loss (P = 160 W)
16.03.2005	344.0	Restart heating phase II (P = 1950 W)
16.03.2005	344.1	Switch-off heater
	550	End of simulation

Comparison of calculated and measured temperatures

Figures 4-25, 4-26 and 4-27 show selected results of thermal calculations. Figure 4-25 compares calculation results of temperature evolution at heaters surface with measurement value (mean value of H1T1–H1T3 and H2T1–H2T3). Figure 4-26 and 4-27 show a comparison of measurement and calculation for sensor BHE-D15 (close to heater, r = 0.96 m) and for sensor BHE-D11 (r = 2.95 m away from heater). Measurement at both exemplary chosen sensors is assumed to be only little affected by ventilation effects. The temperature evolution for all other sensors analyzed is given in appendix C – G.

Figure 4-25 shows a good fit of measurement and calculation for model TC1 with a deviation of less than 1 K at the end of heating phase I and less than 0.5 K at the end of heating phase II respectively. The peaks in the measured values were caused by problems with power supply (22th of July 2004; 107th day and 16th – 17th of December 2004, 254th and 255th day) and leakage of packer 2 (23th of July, 107th day). The high degree of curve matching indicates a correct input of heat into model TC1.

Models assuming higher source strengths show an overestimation of temperature at heaters surface. Reduction of heat input for model TC2 by 10% leads to a more realistic temperature evolution.

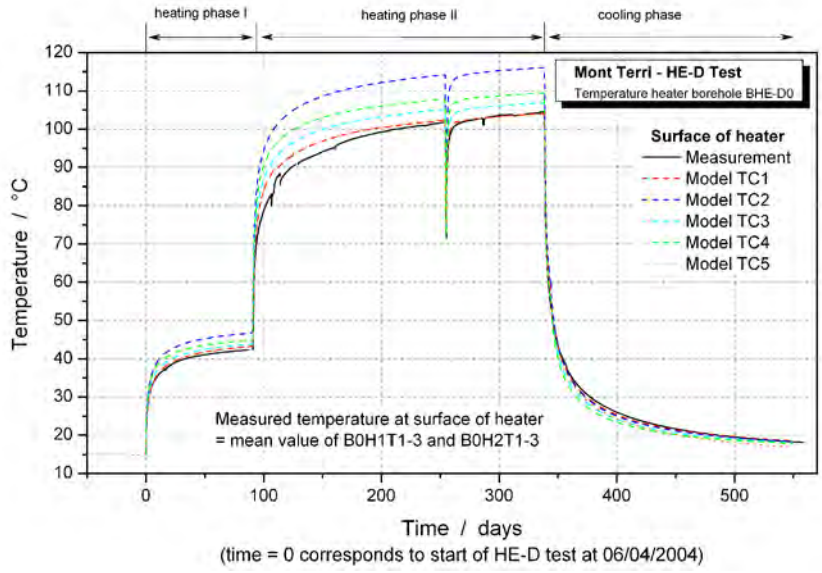

Fig. 4-25: Comparison of measured and calculated temperatures for heater borehole BHE-D0

Due to increased amount of heat the models TC2 – TC4 show an overestimation of temperature at sensors BHE-D15 and D11. Furthermore it can be observed that temperature evolutions – especially in highly transient phases, e.g. caused by changed electrical power – show significant higher slopes due to the higher thermal conductivities. Evaluation of cooling phase – generally more appropriate due to fewer disturbances – shows a rapid decreasing temperature for those models. As a conclusion we assume that the thermal conductivity chosen for models TC2 – TC4 (appendix D to F) seems to be too high.

The additional heat transport via convection of model TC5 leads – with its current implementation of a dominating heat output - to a general decrease in temperature, which superposes conductive temperature equilibration process (figures 4-25 to 4-27). Convection results in a significant cooling of the host rock which induces an additional temperature gradient. This consequently leads to a faster transport of heat away from heater and to a final state of temperature approximately 2 K below the initial state. So on the one hand an excellent fit of measured and calculated temperatures in vicinity to MI Niche could be achieved but on the other hand set boundary conditions lead to significant temperature decrease in the host rock area around the heater (c.f. appendix G vs. appendix C).

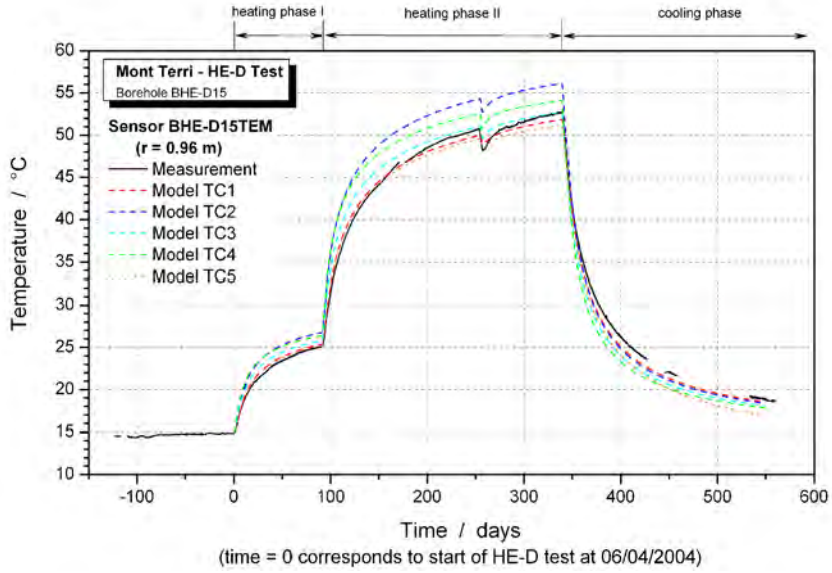

Fig. 4-26: Comparison of measured and calculated temperatures for BHE-D15

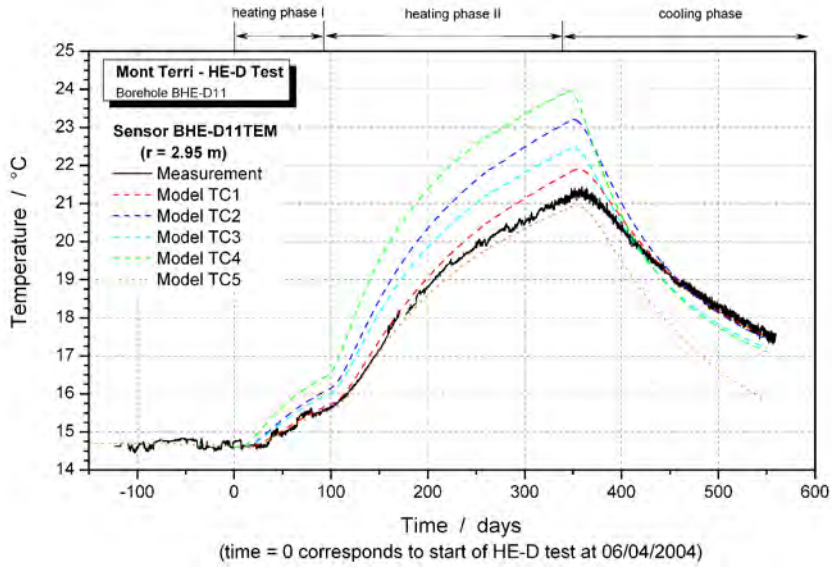

Fig. 4-27: Comparison of measured and calculated temperatures for BHE-D11

A more detailed comparison of temperature measurement and calculation results is given in appendix C – G, where temperature evolutions for models TC1 - TC5 at various sensor locations are given.

4.5.4 Hydraulic modeling

For calibration of hydraulic behavior of Opalinus Clay the results of two in-situ experiments performed at Mont Terri URL had been used:

- Pore pressure and convergence measurements at the ED-B drift
- Pore pressure measurements of GRS sensors within HE-D experiment.

Hydraulic calibration at measurements of ED-B drift excavation

The excavation of ED-B drift was accompanied by pore pressure measurements performed in 3 boreholes (*NAGRA, 2002*). Two measurement campaigns – one directly after drift excavation and one 3 years later – allow for investigation of pore pressure distribution and evolution. Furthermore drift convergence has been measured.

The calculations have been performed with a quasi 2D-model (3D, plain strain) consisting of about 4 400 Elements and 8 900 nodes (figure 4-28). Only the drift geometry with a diameter of 3.5 m was modeled; the shotcrete lining was neglected. For HM coupled calculations the model was initialized with a hydrostatic pore pressure of p = 2 MPa, which was fixed at the outer boundaries and fixed to the value of zero at the drift contour (inflow conditions). Single-phase fluid flow with an initial saturation of S_r = 1 was assumed. Prior to simulation of excavation the model has been initialized with an anisotropic initial state of stress according to given values by *ANDRA (2003)*.

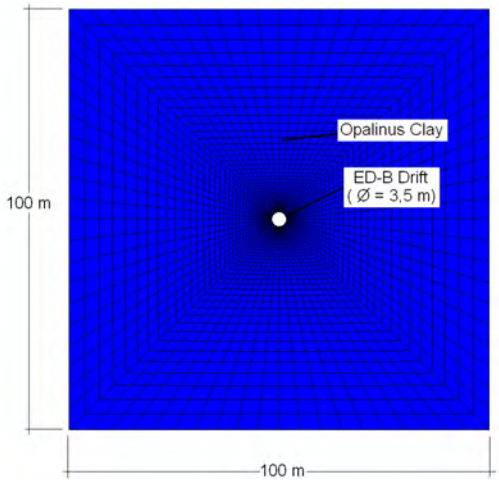

σ_v = 7.25 MPa (neglecting subvert. direction of σ_1)
σ_H = 4.75 MPa (horizontal, N 320° E)
σ_h = 2.0 MPa (horizontal, N 50° E)

Fig. 4-28:
Numerical model used for hydraulic calibration

The excavation of drift was modeled within one step. This leads to an instantaneous evolution of pore pressure due to volumetric deformation. The simulation ends 3 years after excavation. Exemplary for calibration work five models are presented. The mechanical parameters used are listed in table 4-4 and remained constant for all the models. Within this calibration a variation of hydraulic conductivity took place. A further calculation with a reduced Biot-Modulus was performed, accounting for a more compressible pore fluid (simulation of unsaturated conditions).

Tab. 4-4: Compilation of parameters used for HM calibration at ED-B drift excavation

Model	Hydraulic Conductivity k in [m/s]	Biot-Modulus M in [MPa]	Biot-Coefficient α in [-]	Porosity n in [%]	Mechanical parameters (valid for all models)	
HC1	$2 \cdot 10^{-14}$	7 890	0.6	13.7	Youngs Modulus Poissons ratio Compressive strength Tensile strength	4 000 MPa 0.33 10 MPa 1.0 MPa
HC2	$1 \cdot 10^{-13}$	7 890	0.6	13.7		
HC3	$2 \cdot 10^{-12}$	7 890	0.6	13.7		
HC4	$5 \cdot 10^{-13}$	7 890	0.6	13.7		
HC5	$5 \cdot 10^{-13}$	5 000	0.6	13.7		

Figure 4-29 and 4-30 show a comparison of measurement values with calculation results directly after drift excavation and 3 years after excavation respectively. The model HC1 and HC2 assume low hydraulic conductivities and overestimate the excavation induced pore pressure evolution. The low permeability accounts for only a slow decrease of pore pressure so that 3 years later the level of pore pressure is still significant higher than measured.

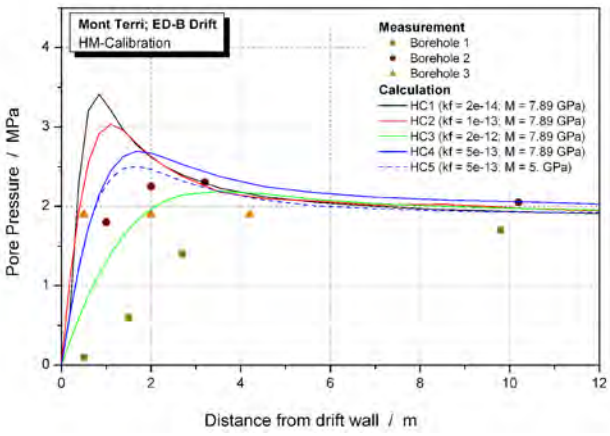

Fig. 4-29: Comparison of measured and calculated pore pressures directly after drift excavation

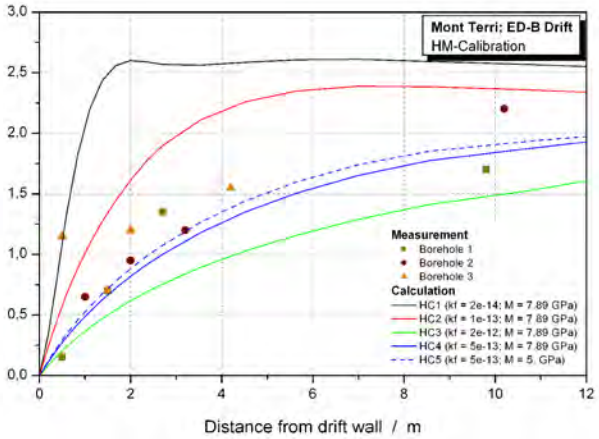

Fig. 4-30: Comparison of measured and calculated pore pressures three years after drift excavation

Even though model HC3 shows an adequate pore pressure distribution for the initial state the pressure decreases faster than measured. Model HC4 with k = $5 \cdot 10^{-13}$ m/s slightly overestimates pore pressures for the initial state and slightly underestimates pore pressures after 3 years. A reduced Biot-Modulus – simulating "not fully saturated" conditions by a higher compressibility of pore fluid – yields a good fit of measured and calculated values.

Figure 4-31 shows convergence measurements for ED-B drift for the first 3 years after excavation (*NAGRA, 2002*). The lower figure shows corresponding calculation results of model HC5. Due to the use of an elasto-plastic model and instantaneous simulation of drift excavation elasto-plastic deformations occur immediately. All following deformations are caused by consolidation of material and induced stress-redistribution. After approx. 1 year the deformation rates decrease and no significant convergence occurs anymore. This stays in contrast with measurement results which show slower decreasing deformation rates indicating presence of "real" rheological material behavior. But these visco-plastic deformations are still small compared to elasto-plastic

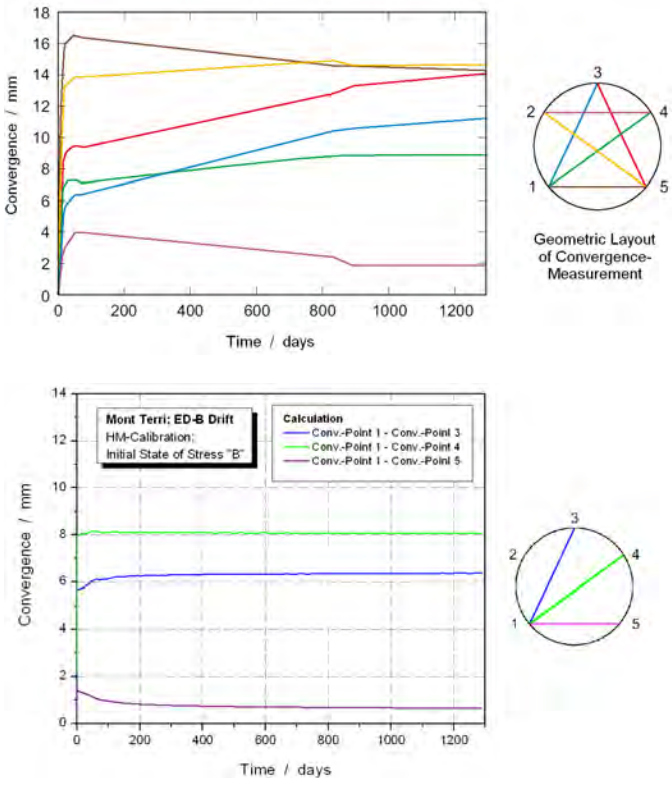

Fig. 4-31: Measured (upper fig., NAGRA, 2002) and calculated convergences (lower fig.) at ED-B drift

response. Nevertheless calculation results show adequate choice of stiffness- and strength parameters. The initial deformation values as well as extension of failure zone (EDZ) and type of failure (figure 4-32) correspond to in-situ investigations of *BOSSART et al. (2002)* and to back analysis results of *BLÜMLING & KONIETZKY (2003)*.

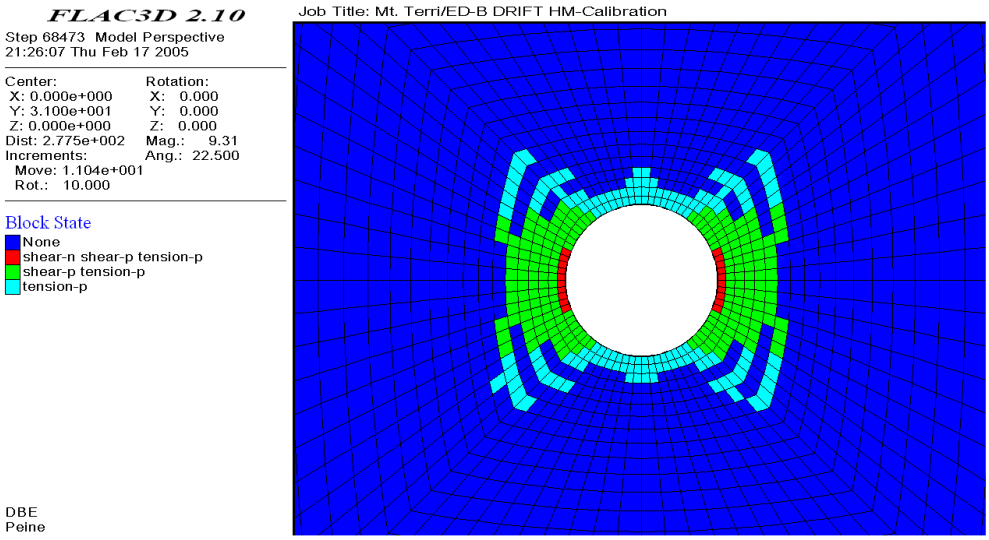

Fig. 4-32: Extension and type of failure zone (EDZ) at ED-B drift
(state: shear = shear-failure; tension = tension-failure; n = now, p = past)

Hydraulic calibration at initial state of HE-D experiment

A further calibration has been performed using pore-pressure measurements of GRS to set up an initial state that fits most to measured initial conditions. It has to be mentioned, that only the point of time just before start of heating has been evaluated. For this time a quasi-stationary state was assumed. Earlier time periods are influenced by disturbance due to drilling and installation of sensors, while at later times only sensors with a good fit of measured and calculated temperature provide possibility of calibration due to the strong interdependency of THM effects caused by heating.

The calculations have been performed with the 3D-model described above. For hydro-mechanical calculations the model was initialized with a hydrostatic pore pressure (p = 2.2 MPa at drift floor), which was fixed at the outer boundaries (inflow conditions) and fixed to the value of zero at all contours of openings. Single-phase fluid flow with an initial saturation of S_r = 1 was assumed. The calculation sequence corresponds to table 4-3. As an example results of 3 HM-calculations with a variation of hydraulic conductivity and Biot-Modulus are presented. For model HC_HED2 the hydraulic conductivity of host rock was assumed to be 5 times higher than for HC_HED1 (reference values), which is within a range for shaly facies of $2 \cdot 10^{-14}$ to $2 \cdot 10^{-12}$ m/s given in *NAGRA (2002)*. Other parameters are compiled in table 4-5. Model HC_HED3 considers a more com-

Tab. 4-5: Compilation of hydraulic parameters used for calibration at HE-D measurement

Opalinus Clay (all facies)		**model HC_HED1**	**model HC_HED2**	**model HC_HED3**
Hydraulic conductivity k intact rock EDZ (0-1.0 m) EDZ (1.0-2.0 m)	[m/s]	$1 \cdot 10^{-13}$ $1 \cdot 10^{-12}$ $5 \cdot 10^{-12}$	$5 \cdot 10^{-13}$ $5 \cdot 10^{-12}$ $1 \cdot 10^{-12}$	$5 \cdot 10^{-13}$ $5 \cdot 10^{-12}$ $5 \cdot 10^{-12}$
Porosity n	[%]	13.7	13.7	13.7
Biot modulus M	[MPa]	7 890	7 890	5 000
Biot coefficient α	[-]	0.6	0.6	0.6

pressible pore fluid (simulation of unsaturated conditions) and a 2 m extension of EDZ with a hydraulic conductivity of $5 \cdot 10^{-12}$ m/s. All calculations consider an increased hydraulic conductivity for EDZ, which has an extension of approximately 2 m. The assumed hydraulic conductivities are still very low in comparison to in-situ investigations reported in *BOSSART et al. (2002)*, but giving enough "contrast" to intact rock by a factor of 10.

Tab. 4-6: Comparison of measured and calculated pore pressures for sensors BHE-D7-D17

pore pressure sensor	measurement [kPa]	model HC_HED1 [kPa]	model HC_HED2 [kPa]	model HC_HED3 [kPa]
BHE-D07	97	18	10	3
BHE-D08	767	1 598	803	658
BHE-D09	254	1 666	802	711
BHE-D10	563	1 843	967	887
BHE-D11	624	2 082	1 318	1 202
BHE-D12	571	171	171	34
BHE-D13	208	973	661	400
BHE-D14	483	1 752	959	847
BHE-D15	831	1 851	1 034	947
BHE-D16	1 065	1 971	1 181	1 097
BHE-D17	931	2 164	1 541	1 447

Table 4-6 presents results of HM-calculations compared to measurement values from 1st April 2004 while figure 4-33 shows distribution of pore pressure at this date in a contour plot for measurements (upper figure) and calculation model HC_HED2 (lower figure).

Results show, that for reference value of hydraulic conductivity the calculated level of pore pressure 6 years after excavation is still significantly higher than measured. The assumption of a hydraulic conductivity increased by a factor of 5 and an increased compressibility of pore fluid leads to a pore pressure distribution more close to in-situ state.

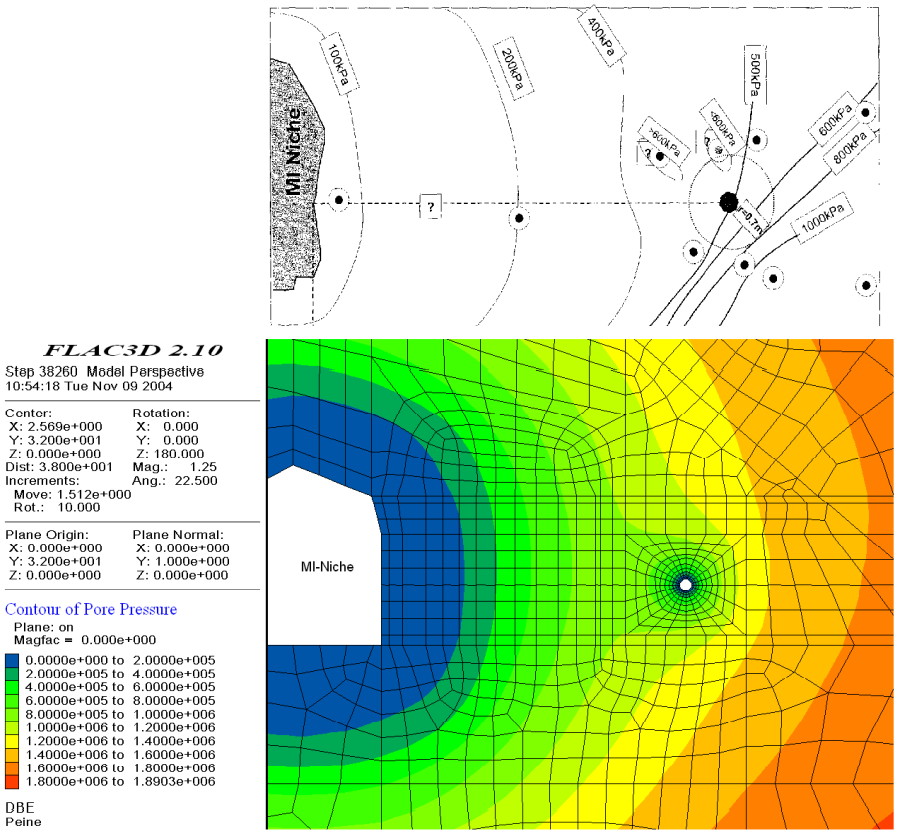

Fig. 4-33: Distribution of pore pressure before start of heating (01. April 2004)
upper figure: measurement (Source: Handout TD No. 4, H. Kull, GRS)
lower figure: calculation, model HC_HED2; pore pressure in [Pa]

4.5.5 Coupled thermo-hydro-mechanical calculations

The sets of thermal and hydraulic material parameters gained from calibration reported above have been used as input values for coupled THM-analysis. Within this step a fitting of measured and calculated pore pressures and displacements has been achieved while varying different mechanical and hydraulic parameters.

Boundary conditions, calculation sequence and used parameters

For coupled THM-calculations the 3D-model as described above has been used. The applied boundary conditions for coupled THM-calculations are equal to those used for thermal and hydraulic calibration. The calculation sequence applied is given in table 4-3. Prior to simulation of excavation history (1st New Gallery and MI Niche, 2nd BHE-D0) the model has been initialized with an anisotropic initial state of stress according to the reference values (ANDRA, 2003):

σ_v = 7.25 MPa (neglecting subvertical direction of σ_1)
σ_H = 4.75 MPa (horizontal, N 320° E, approx. perpendicular to MI Niche axis)
σ_h = 2.0 MPa (horizontal, N 50° E, approx. parallel to MI Niche axis)

As stated above an elasto-plastic material behavior with a DRUCKER-PRAGER yielding criterion with tension cut-off was chosen. All facies of Opalinus Clay were assumed to have homogeneous mechanical properties. Shotcrete lining was not taken into account. An overview of used parameters is given in table 4-7.

Tab. 4-7: Compilation of used parameters

		Model THM1	**Model THM2**
thermal parameters			
Density ρ	[kg / m^3]	2 407	2 450
Specific heat capacity c_p	[J / kg·K]	920	840
Thermal conductivity λ	[W/ m·K]	//: 1.70 ⊥: 0.81	//: 2.80 ⊥: 1.60
Factor of anisotropy A	[-]	2.1	1.75
mechanical parameters			
Poisson ratio ν	[-]	0.33	0.27
Youngs Modulus E	[MPa]	4 000	7 000
Compressive strength $\sigma_{c, uniax}$	[MPa]	10.0	10.0
Tensile strength $\sigma_{t, uniax}$	[MPa]	1.0	1.0
Thermal expansion coefficient rock matrix (unsaturated, drained [*2]) α_t	[1 / K]	$1.5 \cdot 10^{-5}$	$2.6 \cdot 10^{-5}$
Thermal expansion coefficient for grains α_g	[1 / K]	$9 \cdot 10^{-6}$	$2.6 \cdot 10^{-5}$
hydraulic parameters			
Hydraulic conductivity k intact rock EDZ (0-1,0 m) EDZ (1,0-2,0 m)	[m/s]	 $5 \cdot 10^{-13}$ $5 \cdot 10^{-12}$ $1 \cdot 10^{-12}$	 $2.5 \cdot 10^{-13}$ $2.5 \cdot 10^{-13}$ $2.5 \cdot 10^{-13}$
Porosity n	[%]	13.7	13.7
Biot modulus M	[MPa]	7 890	5 000
Biot coefficient α	[-]	0.6	0.6
Undrained thermal coefficient β volumetric (after eq. (4-8)) linear [*1]	[1 / K]	 $9.47 \cdot 10^{-5}$ $3.2 \cdot 10^{-5}$	 $1.2 \cdot 10^{-4}$ $3.9 \cdot 10^{-5}$
Thermal expansion coefficient for fluid α_f	[1 / K]	$2.0 \cdot 10^{-4}$	$2.0 \cdot 10^{-4}$

[*1] isotropic material, [*2] only de-saturated zones around drifts

Exemplary two THM-calculations are presented. Model THM1 (c.f. appendix C) combines calibrated thermal parameters of model TC1 and hydraulic parameters of model HC_HED2 using a linear thermal expansion coefficient of grains $\alpha_g = 9 \cdot 10^{-6}$ 1/K (mean values of laboratory investigation by *BUNTEBARTH (2004)*.

Model THM2 (c.f. appendix F) uses a parameter set which assumes higher thermal conductivities (at η = 100% efficiency; equal to thermal parameters of TC4). The hydraulic conductivity is assumed to be isotropic with a value of $2.5 \cdot 10^{-13}$ m/s. Furthermore the model THM2 is stiffer than model THM1 using an isotropic Young's modulus of 7 GPa. The linear thermal expansion coefficient of grains α_g has been set to the reference value of $2.6 \cdot 10^{-5}$ 1/K. Only heat conduction is considered.

Comparison of calculation and measurement

Results of numerical calculation, using above mentioned parameters are given in appendix C for THM1 and in appendix F for THM2. For both models evolution of temperature for sensors in boreholes BHE-D01 – BHE-D03 and BHE-D06 - D17, evolution of pore pressure in BHE-D03 and BHE-D7-D17 and evolution of interval deformation in borehole BHE-D06 is shown. Due to choice of equal thermal parameters for THM1 and TC1 as well as THM2 and TC4 the calculated temperature field corresponds too. As an example figure 4-34 shows results for THM1. Further details concerning temperature evolution have been reported in chapter 4.5.3 “thermal calibration”.

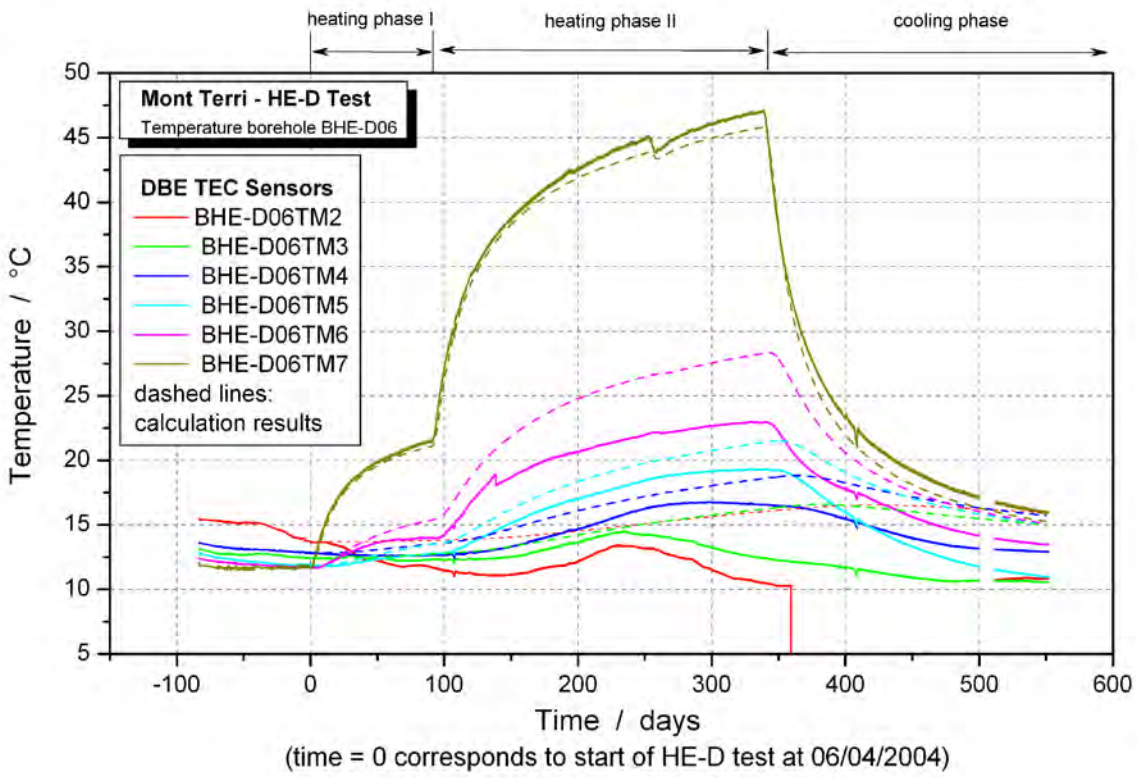

Fig. 4-34: Comparison of measured and calculated temperatures for BHE-D06

Comparison of calculated and measured displacements

Displacement measurements in borehole BHE-D06 are superposed by an effect which causes huge displacements towards MI Niche. This effect is probably caused by block movement of EDZ along fracture network somewhere between head plate and packer DP2 (see chapter 4.3.2). For interpretation of thermally-induced deformations only relative displacements of packers have therefore been evaluated. For this purpose an offset of calculated deformations has been performed, setting up an equal state of deformation at t = 0 days. Results of calculation for model THM1 and THM2 (figure 4-35 and 4-36) show that:

- Until approx. 150th day a good fit of measured and calculated deformations has been achieved for intervals 2 and 3 with a deviation < 0,15 mm/m for THM1 and < 0,04 mm/m for THM2. Values of maximum compression as well as duration of compression phase are in good accordance to measurement, indicating that chosen parameters reflect compressibility (mechanical stiffness and Biot modulus of fluid) of the system in a propper manner. For THM2 with an increased stiffness, heat input and higher thermal expansion coefficient the calculated maxima occur earlier than measured (figure 4-36).

- The slope of expansion phase is significant smaller than measured for THM1, indicating that an undrained linear thermal expansion coefficient of $\alpha_t = 3.2 \cdot 10^{-5}$ 1/K (linear thermal expansion coefficient of grains $\alpha_g = 9 \cdot 10^{-6}$ 1/K) wasn't large enough. Calculation results for model THM2 assuming an increased undrained thermal expansion coefficient of $\alpha_t = 3.9 \cdot 10^{-5}$ 1/K ($\alpha_g = 2.6 \cdot 10^{-5}$ 1/K) show steeper slopes, fitting quite well the phase of expansion for intervals 2 and 3 up to about 150th day. Afterwards for both intervals an effect occurs, causing a further expansion of interval. It is supposed that the excavation of Gallery GA04 and EZ-B Niche is strongly correlated with this effect (see chapter 4.3.2).
- For Interval 1 calculation results also fit well the measured deformations until 22th day. After that the measurement values show a negative slope indicating an activity which causes an ongoing shortening of interval, while the calculated deformation reaches a constant value of expansion. The compression effect is accelerated at about the 35th and 115th day.

Sliding micrometer measurements in boreholes BHE-D04 and BHE-D05 (appendix B-5 and B-6) also indicate a significant expansion of Interval 7 (both boreholes) approx. 2.5 – 3.5 m away from heater towards MI Niche. The measured deformation of intervals in borehole D04 / D05 is about 10 / 5 times higher than calculated. It has to be mentioned, that due to discetization constraints there is a difference in location of the measurement marks within model and in-situ test which only allows for a qualitative comparison.

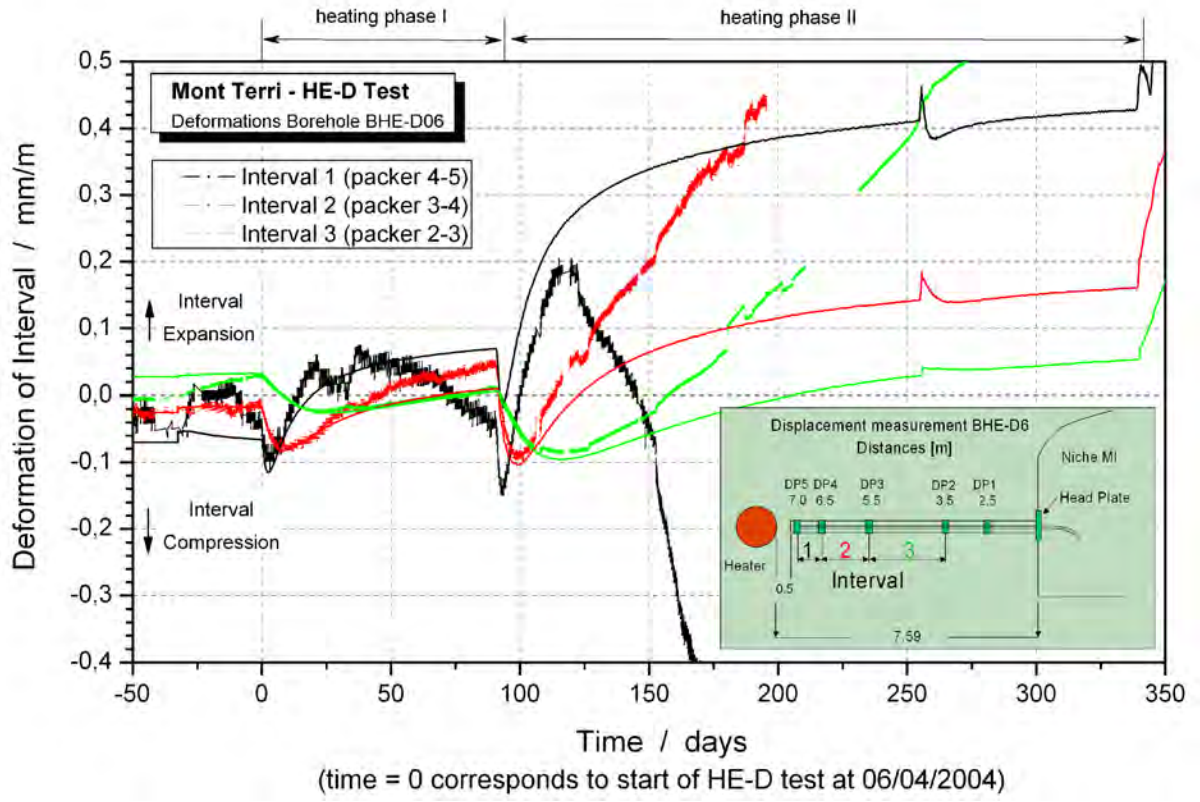

Fig. 4-35: Comparison of measured and calculated deformation for model THM1

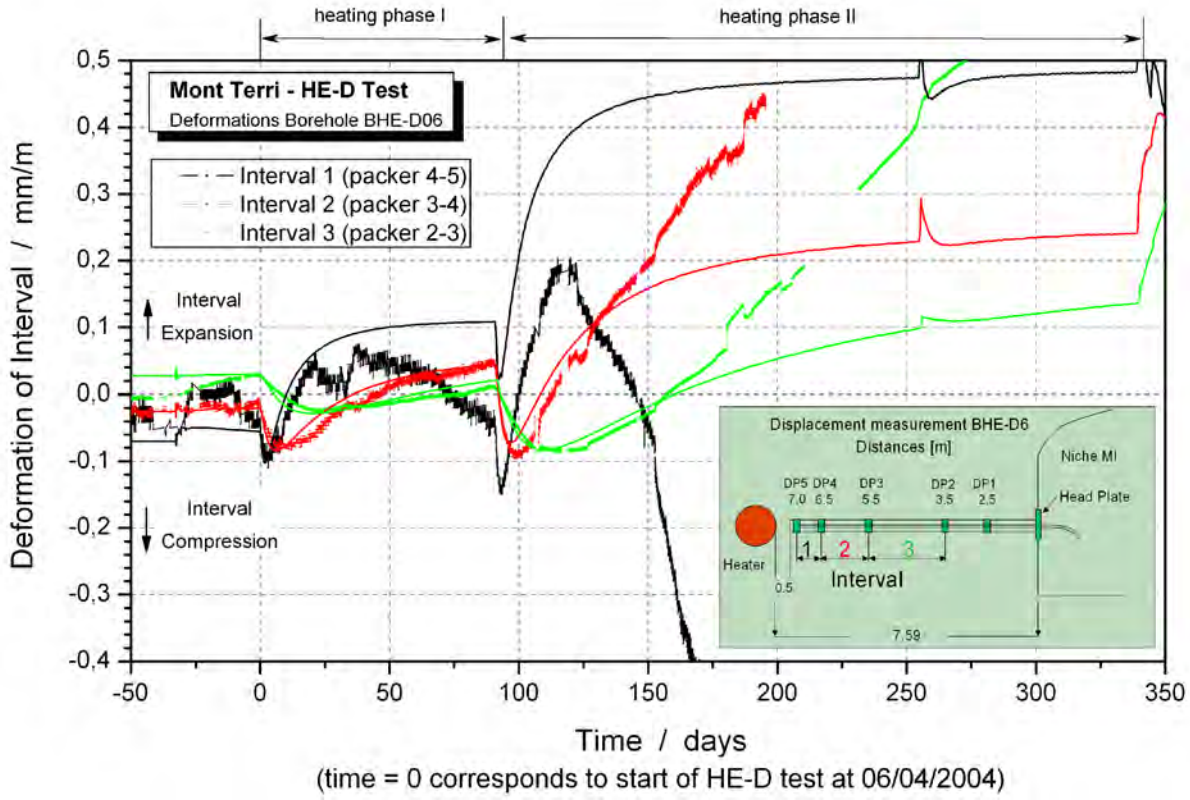

Fig. 4-36: Comparison of measured and calculated deformation for model THM2

Comparison of calculated and measured pore pressures

A comparison of measured and calculated pore pressures is given in appendix C-7 and C-8 for model THM1 and in appendix F-7 and F-8 for model THM2. Following things can be stated:

- For model THM1 a more realistic distribution of pore pressure before start of heating is present (model equals to HC_HED2; see table 4-5 and 4-6). Due to the lower hydraulic conductivity of model THM2 and the neglect of an EDZ with increased permeability the level of pore pressure ranges between 1.5 and 1.9 MPa near to heater being therefore significantly higher than the measured initial state.
- The low permeability which inhibits the pressure decay and the greater heat quantity consequently lead to an overestimation of maximum pore pressures for each heating phase of model THM2. The calculated maximum pore pressures exceed the measured values by a factor of 2 – 3. More realistic results are obtained by model THM1 mainly due to higher hydraulic conductivity assumed.
- The pressure built-up and following decay especially during heating phase I is overestimated by both models. For some sensors still a (slow) pressure built-up occurs in-situ. A possible explanation might be the assumption of single-phase flow at 100% saturation and low compressibility of pore fluid for both models (or still lasting re-saturation process of test zone in slim hole after drilling ?).
- For some sensors (e.g. BHE-D8, D11, D15, D16) model THM1 shows a well corresponding pressure decrease which indicates an adequate choice of hydraulic conductivity.
- The failure of heater packer at 108th day, simulated by release of normal pressure does not lead to pore pressure drops as observed by sensors BHE-D15, D14 and D03.

5 SHAFT EXPERIMENT AT BURE (REP)

5.1 Location and experimental setting

In the Meuse/Haute-Marne Underground Research Laboratory (URL-Bure, figure 5-1) a vertical mine-by experiment, the so called REP experiment, has been performed, aimed at characterizing the mechanical and hydro-mechanical response of the Callovo-Oxfordian Clay formation due to the ongoing shaft sinking (*ANDRA, 2005a and 2005b*).

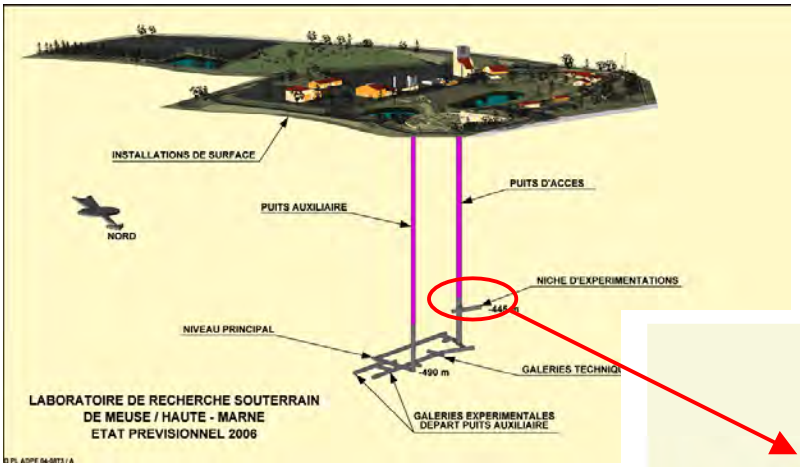

Fig. 5-1:
Sketch of location and layout of the URL at Bure
(figure provided by ANDRA)

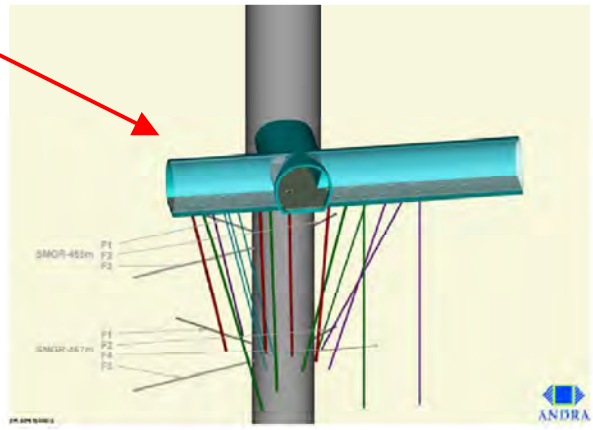

Fig. 5-2:
Design of the shaft experiment REP at experimental niche on the depth level of -445 m
(figure provided by ANDRA)

For this purpose a couple of observation boreholes has been drilled in several direction to the access shaft (c.f. figure 5-2 and appendix H). Prior to further shaft sinking 15 boreholes have been drilled from experimental niche at –445 m depth and equipped for pore pressure and permeability measurement, rock mass deformation measurement and velocity survey. During shaft sinking another 7 boreholes have been drilled in radial direction to the shaft wall at a depth of -455m and –467m (geomechanical measurement section SMGR-1 and SMGR-2).

DBE TECHNOLOGY participates in this experiment by deformation measurements via fiber optic extensometer, based on Fiber Bragg Grating (FBG) technology in the inclined borehole REP2207 (*ANDRA 2004; JOBMANN et al. 2005*). The in-situ measurements are accompanied by numerical calculations to analyze the observed rock behavior.

5.2 Fiber optic extensometer system

Two schematic drawings of the fiber optic deformation measurement system, which has been installed in borehole REP2207 are given in figures 5-3 and 5-4. The system consists of five extensometers outside the borehole which are placed in a canister at the entrance of the borehole (figure 5-5c). Within the borehole, five packers are fixed at well defined positions (figures 5-3 and 5-4). From each fixation point, a carbon extension cable goes to the canister where it is connected with the fiber optic extensometers via a spring mechanism. As a con-

sequence, the displacement of the connected packer relative to the entrance of the borehole is measured. The system has the advantage that a reset of the sensors can be applied when the sensors goes out of range.

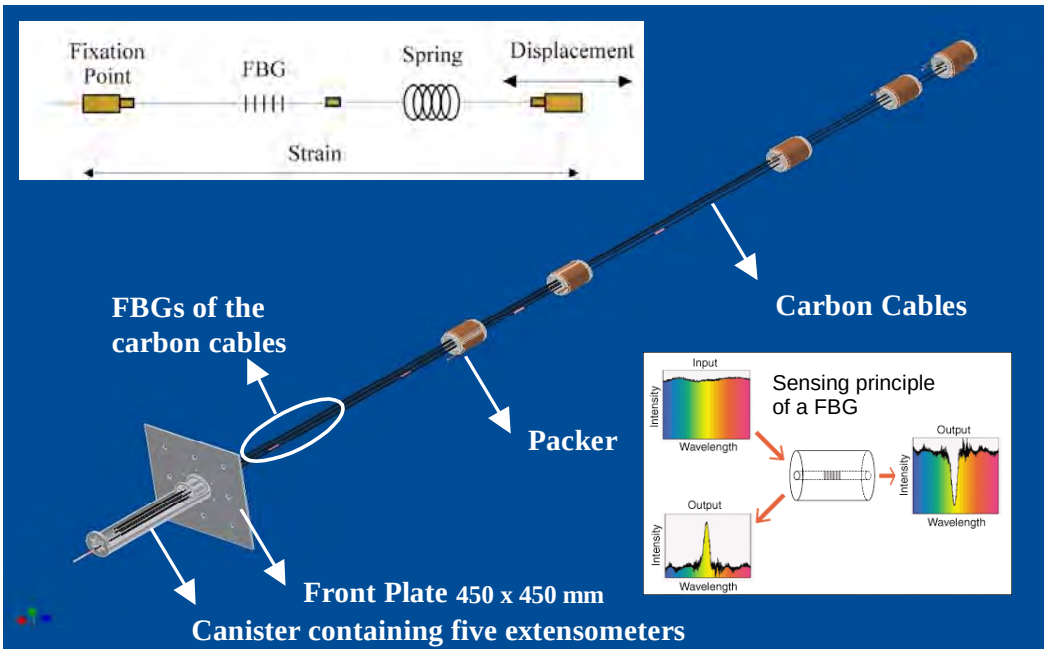

Fig. 5-3: Schematic drawing of the measurement system

Furthermore, two temperature probes have been installed, one in the canister and the other one in the borehole. These are used to compensate the temperature influence on the sensor system. Figure 5-4 shows the instrumental layout of borehole REP2207 giving further details on temperature sensors' and packer location. A more detailed description of the measurement system and its installation is given by *JOBMANN et al. (2005)*.

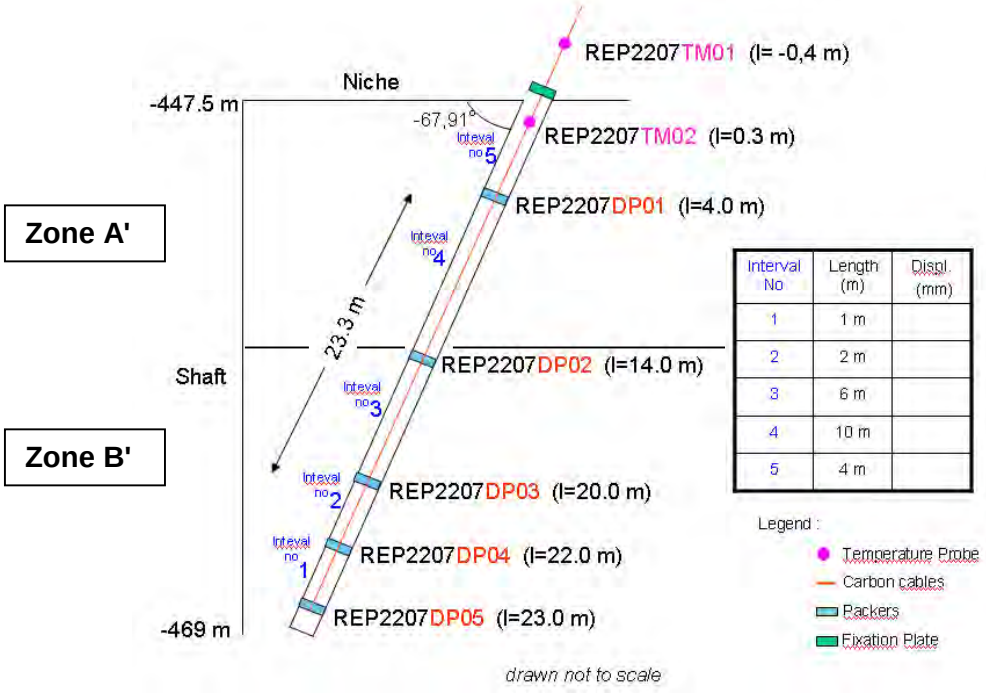

Fig. 5-4: Setup of measurement system in borehole REP2207

Figures 5-5a to 5-5c are photos taken during the system installation in January/05. Figure 5-5a shows the inflatable packer and the carbon cable, figure 5-5b gives an insight into the equipped borehole and figure 5-5c shows the final setup of measurement system in the experimentation niche at –445 m depth.

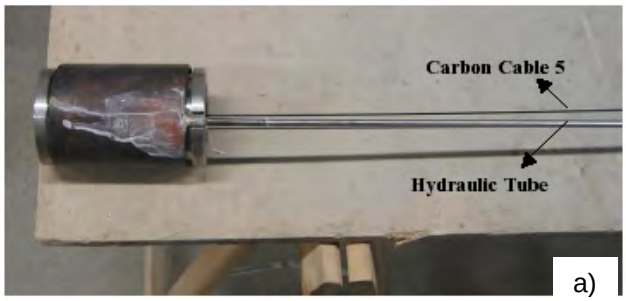

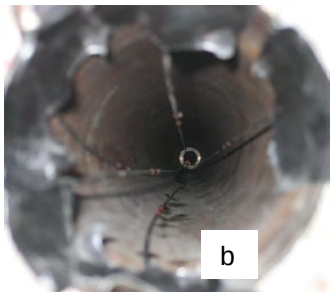

Fig. 5-5:
Details of measurement system for REP2207

5.3 Measurement results

The measurements in borehole REP2207 started at 08th of February 2005 (approx. 29 days before start of REP experiment at 10th of March 2005). The measurements were disturbed by following occurrences:

- 22/02/2005 (-16 d) Repair of the C03 cable (carbon cable to packer DP3)
- 02/03/2005 (-8 d) Change of TM02-2 to TM02-1 (bad results on TM02-2)
- 15/03/2005 (5 d) Movement of the canister (cause unknown)
- 24/05/2005 (70 d) Malfunction of the SLED (Laser in the unit) and repair
- 05/07/2005 (112 d) Re-installation of the unit.

Measurement results of the other observation boreholes are given in appendix I.

5.3.1 Temperature measurement

Figure 5-6 shows measurement results of REP2207 temperature sensors since start of measurements until 15th of November 2005. Due to a strain loss on the grating of TM2-2 only measurements of TM2-1 gives accurate temperatures in borehole REP2207. The temperatures measured 0.3 m inside the borehole range between 20°C (winter/spring) and 24°C (summer). The sensor TM1 inside the canister shows significant higher amplitudes for the first 4 months, ranging from approx. 14°C up to 23.7°C. A possible reason is supposed in changes of ventilation temperature (influence of seasonal cycle, work in niche and shaft, etc.).

Beside a malfunction of sensor TM1 between 38th and 55th day the temperature measurement values for all sensors should be handled with care between 60th and 70th day, because the scattering indicates the begin of malfunction of the system. After re-installation of the system both sensors differ only slightly from each other, which indicates an equilibration of temperature for the host rock area next to the niche.

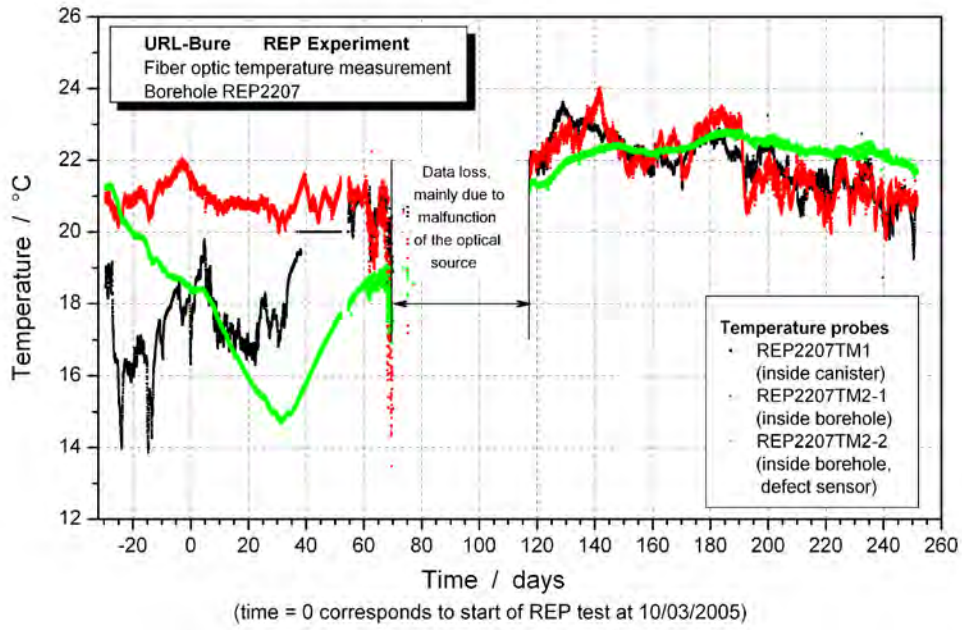

Fig. 5-6: Temperature measurement results in borehole REP2207

5.3.2 Displacement measurement

A schematic presentation of packer movement before and after mine-by is given in figure 5-7. With the ongoing shaft sinking before passing of shaft level a gradual compression of rock mass took place, mainly caused by increasing vertical stress around the shaft. After mine-by a extension of intervals can be observed, mainly caused by release of horizontal stress.

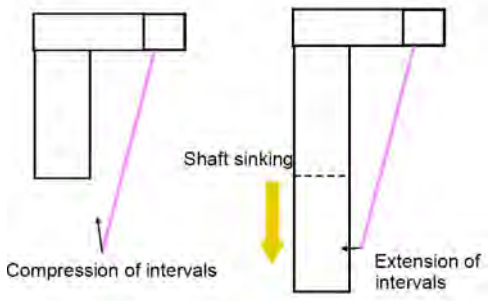

Fig. 5-7:
Packer movement before and after mine-by (*ARMAND et al. 2006*)

Fig. 5-8 shows the displacement of each packer relative to the head plate until 15th of November 2005 (250 days after start of experiment). The arrows in the lower part of the figure mark the different excavation cycles of the REP experiment. The packers DP3, DP4 and DP5 show an elongation of interval even before further shaft sinking of REP experiment. This was probably still a response to niche excavation. However, the movement of packers DP1 and DP2 relative to head plate is almost negligible within this period.

The compression of intervals at the 15th of March (5th day) with a movement of all packers (except DP1) by a value of approx. 0.2 mm towards the niche is caused by the 2nd excavation cycle. This is in line with measurements of the classical extensometer REP2202, which was installed in a similar direction parallel to σ_H (c.f. appendix I-6). The re-distribution of stress is assumed to lead to a higher vertically stressed rock area around the shaft.

Until the next excavation cycle on 27th of March (48th day) distances between packers DP1, DP3-DP5 increase again (figure 5-8). This result differs from REP 2202, where no significant displacements occur within this period.
The ongoing elongation of the distance between packer and head plate continues after re-installation of the system. The reaction of packer DP5 – which was expected to show highest displacement between packer location and head plate – couldn't be clarified up to now.

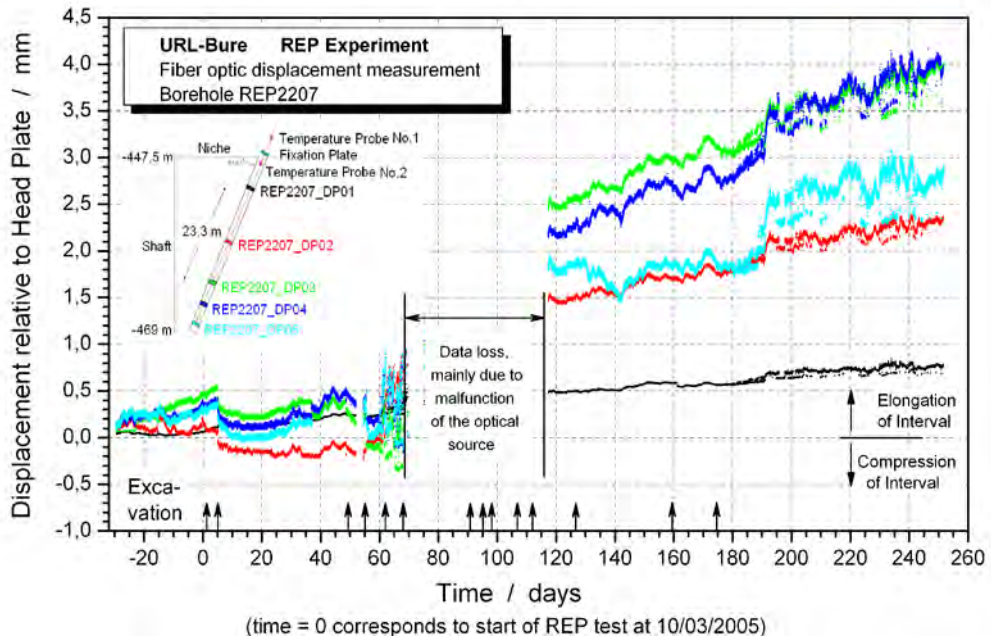

Fig. 5-8: Measured packer displacements relative to head plate

The resulting displacements between packers located in the REP section and the niche as well as displacement rates obtained from extensometer boreholes REP2202 and REP2207 are comparable. The shift in displacements at 190th day as well as the scattering afterwards is still pending clarification.
Figure 5-9 shows the deformation of intervals between the packers. This figure also points out a compressive deformation of ε = 0.08 … 0.1% at the end of REP test (1/2 year after start) for the shaft near interval 1.

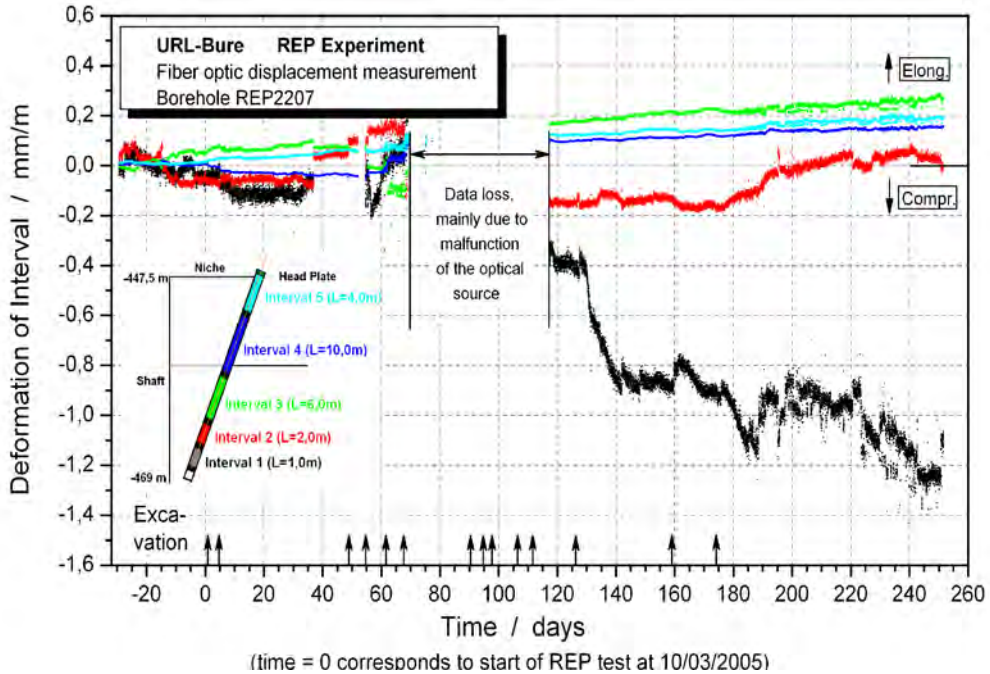

Fig. 5-9: Deformation of intervals measured in REP2207

The other intervals show significant smaller deformations (extension-path) with final elongations up to 0.03% (little compression during mine-by). Intervals used for interpretation of relative packer displacement are given in figure 5-9.

5.4 Predictive modeling

Prior to excavation predictive model calculations have been performed in order to obtain the rock response to be expected during and after shaft excavation. The used rock properties differ a little bit from the reference values given in the Dossier 2005-Référentiel du Site (*ANDRA, 2005c*) since this document was not available at that time.

5.4.1 Constitutive model

For fluid flow and hydro-mechanical coupling the same theory is valid as for modeling of the HE-D in-situ test at Mont Terri (chapter 4.5.1).

Mechanical constitutive model

An elastoplastic-viscoplastic constitutive law was used to describe the mechanical behavior of the host rock formation. The model combines Hook and Mohr-Coulomb (short-term behavior) with a simple Norton Power law (long-term behavior). Within the calculation an additive splitting of the deformation tensor and the tensor of deformation velocities into an elastic part $\dot{\varepsilon}_e$, a plastic part $\dot{\varepsilon}_p$ and an viscous part $\dot{\varepsilon}_v$ was performed.

$$\dot{\varepsilon} = \dot{\varepsilon}_e + \dot{\varepsilon}_p + \dot{\varepsilon}_v \tag{5-1}$$

In the elastic part of the isotropic constitutive model strain increments $\Delta\varepsilon$ generate stress increments $\Delta\sigma$ according to the linear and reversible Hook's law:

$$\Delta\sigma_{ij} = 2G\,\Delta\varepsilon_{ij} + (K - \frac{2}{3}G)\,\Delta\varepsilon_{kk}\,\delta_{ij} \tag{5-2}$$

with G shear modulus, K bulk modulus, $\Delta\varepsilon$ volumetric strain increment and δ_{ij} the Kronecker delta. Anisotropic elastic behavior was not considered. For describing the plastic material behavior a Mohr-Coulomb yielding criterion with tension cut-off was chosen. For post-failure state reduced strength parameters were assigned to account for strain-softening behavior. The failure envelope for this criterion $f(\sigma_1, \sigma_3) = 0$ is defined in terms of effective stresses by:

$f^s = 0$ *(shear failure)* with $f^s = \sigma_1 - \sigma_3\, N_\phi + 2\,c\,\sqrt{N_\phi}$ (5-3)

with $N_\phi = \dfrac{1+\sin(\phi)}{1-\sin(\phi)}$ (5-4)

$\sigma_1 \le \sigma_2 \le \sigma_3$ principal effective stresses
(convention: compressive stresses are negative)
c Cohesion [MPa]
ϕ Angle of inner friction [°]

and $f^t = 0$ *(tension failure)* with $f^t = \sigma_3 - \sigma_t$ (5-5)

with an tension limit of σ_t.

Anisotropic strength behavior was not considered. Furthermore the influence of desiccation and moistening on the strength behavior of material was neglected. For description of viscoplastic behavior a simple Norton power law approach after (*ZHANG et al., 2002*) was chosen neglecting primary and tertiary creep phase. The secondary creep rate is given by:

$$\dot{\varepsilon}^{cr} = \begin{cases} A \cdot \sigma^n & \text{for} \quad \sigma \ge \sigma^{ref} \\ 0 & \text{for} \quad \sigma < \sigma^{ref} \end{cases} \tag{5-6}$$

with: σ von Mises stress,
σ^{ref} Reference stress,
n, A creep parameters (function of mineralogy, water cont., T, …)

For σ^{ref} a creep threshold of σ^{ref} = 4.1 MPa was chosen according to the anisotropic in-situ state of stress. Although laboratory investigations showed that rheological behavior is evident for such low deviatoric stress, a neglecting of this creep threshold would lead to a change in the stress field during simulation. An acceptable first fit of creep tests in *ZHANG et al. (2002)* and *HOTEIT et al. (1998)* is possible using creep parameters of n = 1 and A = $6 \cdot 10^{-12}$ 1/s (zone B' and C') and A = $1.2 \cdot 10^{-12}$ 1/s (zone A'). It has to be stated, that the chosen simple model for description of rheologic behavior may not exactly represent the creep mechanism of claystones, which is still uncertain (c.f. chapter 3). For the predictive modeling no damage criterion has been applied. The used Mohr-Coulomb failure criterion is defined in terms of effective stresses and given by equations (5-3) and (5-5).

5.4.2 Model description

Due to the anisotropic initial state of stress and the design of the experimental niche (not parallel to stress field) a full 3D model was necessary to apply. The numerical model (315 000 zones and 319 000 grid points) has been developed with regard to the real geological setting and geomechanical units according to modeling hypothesis H 1 and H 2 in *ANDRA (2005b)* (c.f. figures 5-10 and 5-11 and appendix J-2).

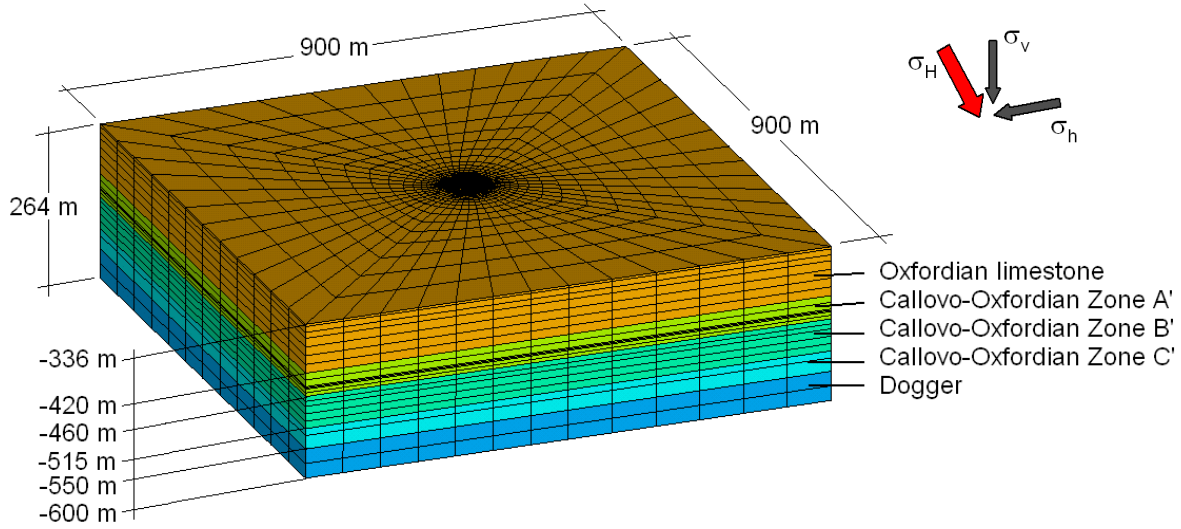

Fig. 5-10: Numerical model geometry and geology

The shaft was modeled with a diameter of excavation ∅ = 6.25 m and a constant thickness of lining with d = 0.52 m. The niche at the -445 m level was modeled with a simplified rectangular cross-section (figure 5-11).

The location of nodes, taken into account for the purpose of evaluation of REP2207 measurement correspond to real packer location in the experiment. For other output points of the numerical model (displacements, pore pressures) the distance to the in-situ sensors' position may differ slightly by < approx. 0.5 m, because discretization has been adopted to the fiber-optic measurement system. The notation and location of the sensors which have been used for comparison with modeling results is given in appendix H. The origin of the used coordinate system corresponds to the centre of the shaft head (z-direction = shaft axis). The y-direction points into North and the x-direction to East (c.f. appendix H-3).

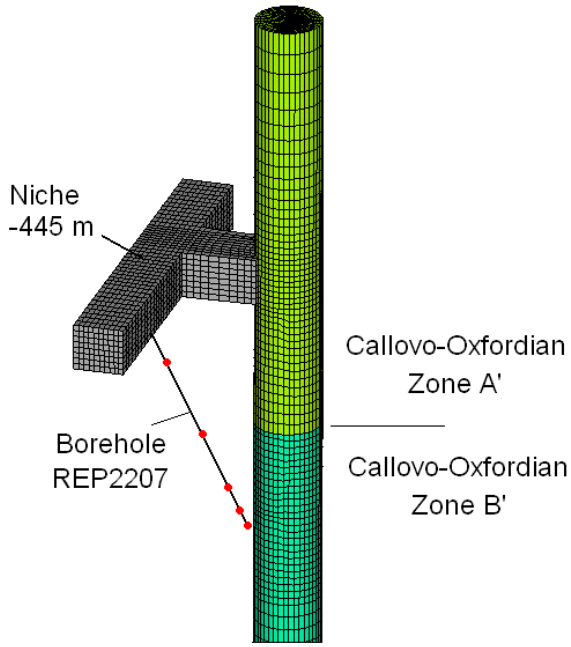

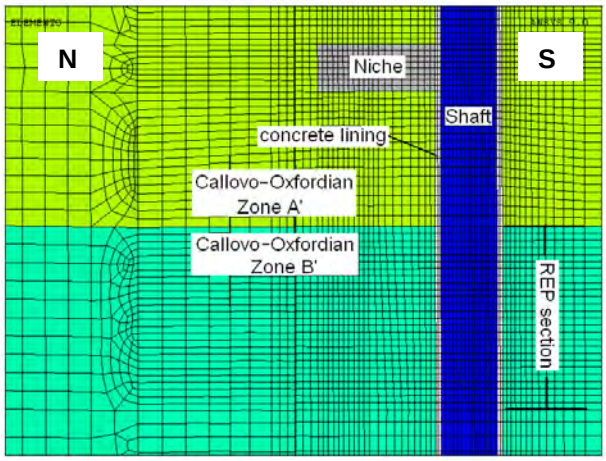

Fig. 5-11: Discretization details
left: Shaft and Niche at -445 m
right: vertical cross section N-S through REP area

Boundary conditions, parameters and calculation sequence

The model was applied with displacement boundary conditions (zero displacement normal to lower and lateral boundaries). The initial state of stress as well as the pore pressure was chosen according to hypothesis H 3 and H 9 in *ANDRA (2005b)*:

Initial pore pressure:	$p = = \gamma_w * z$	$\gamma_w = 10\,000$ N/m^3, hydrostatic
Initial state of stress:	$\sigma_{zz} = \sigma_v = \gamma_1 * z$	for z > -417 m; $\gamma_1 = 24\,700$ N/m^3
	$= \gamma_1 * 417 + \gamma_2 * (z + 417)$	for z < -417 m; $\gamma_2 = 24\,200$ N/m^3
	$\sigma_h = 1.0 * \sigma_v$	direction N62.5°E
	$\sigma_H = 1.3 * \sigma_v$	direction N152.5°E

The pore pressure has been fixed to the hydrostatic value at the boundaries (except upper boundary). After simulation of excavation the pore pressure at the shaft and niche surface was fixed to zero (inflow conditions). The fluid tension limit was set to zero, so that no negative pore pressures (effect comparable to suction) could develop. The temperature was fixed at T = 20°C. Ventilation temperature changes were not taken into account.
For modeling of the support a time depending evolution of stiffness and strength of concrete lining (thickness 0.52 m) has been taken into account (figure 5-12). A temporary support (arches, bolts) was not considered.

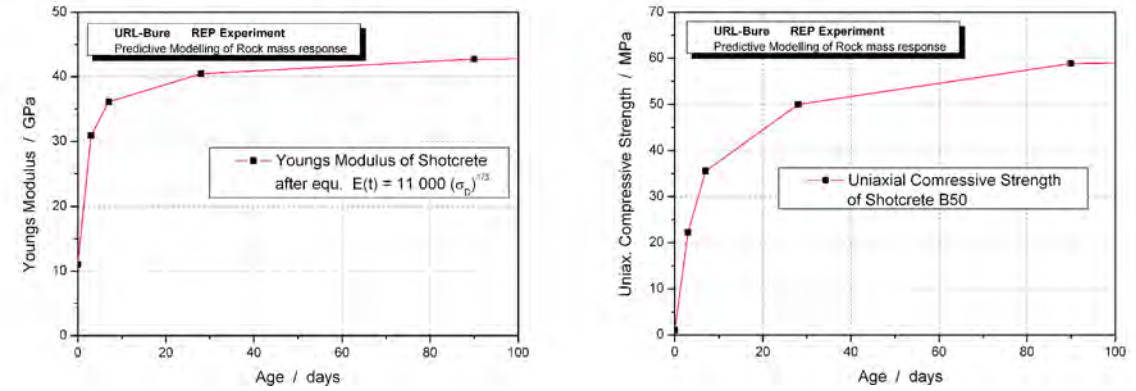

Fig. 5-12: Time depending evolution of stiffness and strength of concrete lining

The rock properties given by *ANDRA (2005a,b,c)* and *ZHANG et al. (2002)* have been used as basic input parameters for the predictive calculations. Table 5-1 shows the used mechanical and hydraulic parameters for description of host rock zone A' and B' & C'.

Tab. 5-1: Compilation of used parameters for predictive modeling

Mechanical Parameters		Zone A'	Zone B' + C'
Youngs' Modulus E	MPa	9 000	
Poisson ratio ν	-	0.3	
Pre-failure behavior			
Angle of Friction ϕ	°	35	19
Cohesion c	MPa	7.2	9.0
Tensile strength Rt	MPa	2.1	2.1
Compressive strength Rc	MPa	25.3	27.8
Post-failure behavior			
Angle of Friction ϕ	°	35	19
Cohesion c	MPa	4.0	4.2
Rheological behavior			
Creep factor A	1 / s	1.2e-12	6e-12
Creep exponent n	-	1	1
Hydraulic parameters			
Hydraulic Conductivity k_f (equiv. Permeability K	m / s m^2	5e-13 (isotropic value) *1 ≅ 5e-20)	
Porosity Φ	%	15.0	
Biot Modulus M	MPa	6 000	
Biot coefficient b	-	0.8	

*1 Due to an error the hydraulic conductivity of zones with post-failure state was set to zero.

The chronology of excavation was chosen according to hypothesis H 7 (c.f. appendix J-3 for an extract) given in *ANDRA (2005b)* beginning at 30th of April 2004 (–315 d). The excavation was modeled by instant removal of excavated zones. The last removal is modeled at begin of September 2005. The excavation work at the main level has not been taken into account.

5.4.3 Comparison of prediction and measurements

Prior to a back analysis or interpretive modeling the predictions have been evaluated in comparison with the in-situ measurements. The shaft convergences, extensometer interval deformation and the pore water pressure evolution have been investigated (c.f. appendix M).

Shaft convergence

Figure 5-13 shows a comparison of predicted and measured convergences in σ_h and σ_H direction for the geotechnical measurement section SMGR-2. For the first month the predicted values are in good agreement with the measured convergences, pointing out a sufficient description of short-term behavior (in especially elastic parameters). The used viscoplastic part of the constitutive law led to an over-estimation of convergences for long periods of time, although the used creep parameters are gained from laboratory investigations and calibrated by back-analysis of creep tests.

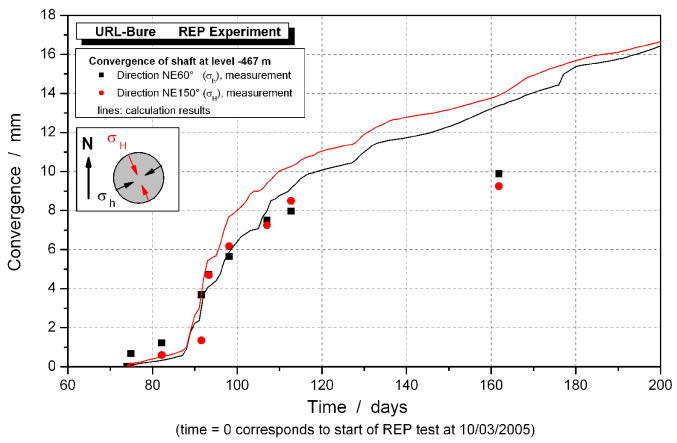

Fig. 5-13: Comparison of measured and predicted shaft convergence

Displacement and strain in the rock

Figure 5-14 gives a comparison of measured and predicted rock displacements for selected intervals of extensometer REP2201 (drilled perpendicular to σ_H, figure 5-14a) and REP2202 (drilled parallel to σ_H, figure 5-14b). Both figures show the displacements between two adjacent packers. The packers are located in the middle (DFO06 – DFO07; 1.5 … 2.7 m away from shaft wall) and at the bottom of each borehole (DFO09 – DFO10; 0.4 … 1.5 m away from shaft wall). Following things can be stated:

I The in-situ observed mechanical response due to shaft sinking is more sensitive than represented by the predictive calculations. For example a compression of the rock between sensors DFO09 and DFO10 can be recognized, even the excavation front is more than 10 m away.

II For the selected intervals DFO06 – DFO07 results of blind prediction are in good agreement with in-situ data. It is worth mentioning that the magnitudes of deformation are quite small. The observed host rock deformation within this area is assumed to be nearly pure elastic. The evolution of REP2202_DFO06 – DFO07 indicates that after a phase of compression during mine-by, mainly due to additional vertical load caused by stress redistribution, the stress releases after mine-by. The interval deformations obtained after mine-by are close to the initial values. The magnitude of deformation corresponds well, giving confidence in chosen elastic parameters.

III A comparison of the relative displacement evolution for intervals close to the shaft shows significant different behavior of this zone, which cannot be reproduced by the model. So for instance a significant compression of interval is measured as the excavation level is approaching. In contrast to this, calculations point out elongations of those intervals for this phase of experiment, mainly caused by unloading.

IV After mine-by and its ongoing unloading a remaining elongation of the interval between REP2202_DFO09 and DFO10 is evident. This effect cannot be reproduced by the simulation, although plastic deformation is considered within this zone.

V The measured displacement between REP2201_DFO09 and DFO10 shows a different behavior. After experiment induced interval compression a sudden movement occurs at the 105th day. This rock reaction was probably caused by a discontinuous movement within this interval. Figure 5-15 shows displacements of all REP2201 packers relative to the head plate, making the movement between the packers more obvious.

VI All sensors show an ongoing elongation of interval, which is assumed to be caused mainly by rheological behavior of the rock and only partly by further shaft sinking.

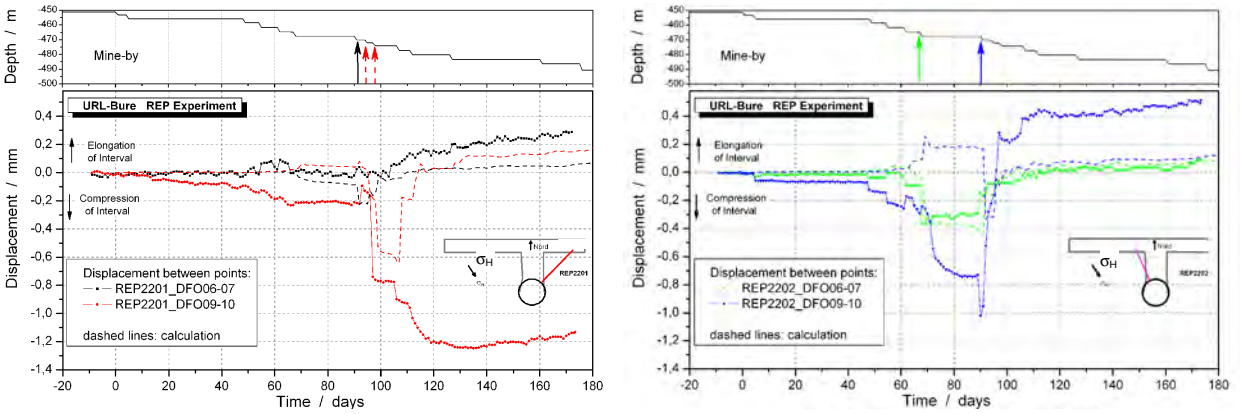

Fig. 5-14: Comparison of measured and predicted displacements for
a) REP2201 (left) and b) REP2202 (right)

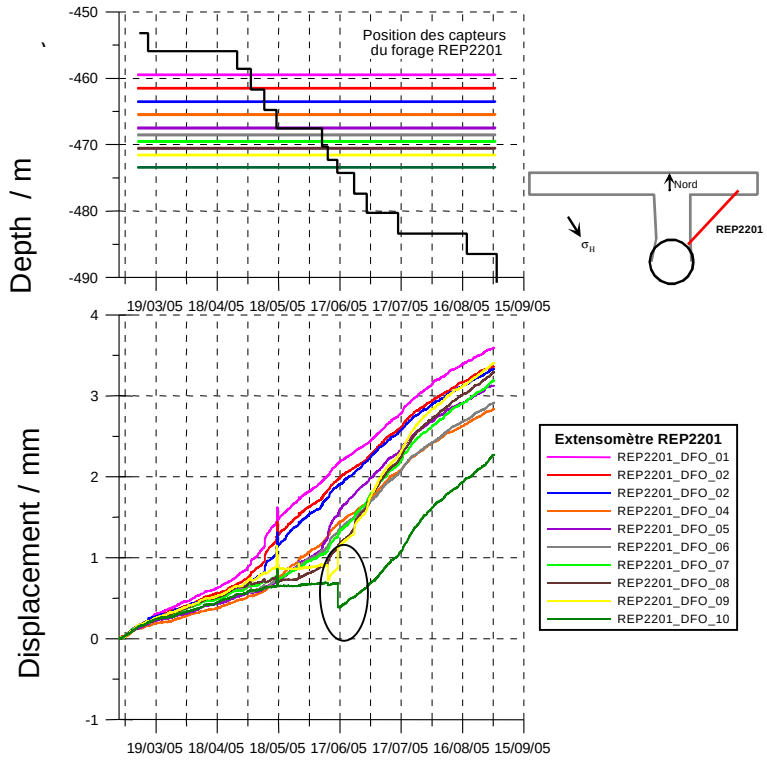

Figure 5-15:

Measurement of Displacements relative to head plate for packers of extensometer REP2201
(*ANDRA 2006a*)

Pore pressure evolution

Due to an error the hydraulic conductivity of post-failure zones (located mainly at the shaft contour) was set to a value of zero. This impermeable zone avoided simulation of drainage by the shaft so that the obtained pore pressure decrease is only caused by changes in volumetric strain and pore pressure equilibration within intact rock mass. For this reason the predicted pore pressures highly overestimate in-situ measurement (figure 5-16a,b).

The significant evolution of pore-overpressures, as obtained after mine-by at the sensors in σ_H direction (REP2102_PRE_05, figure 16b), are not predicted by the simulation as well. Furthermore the initial in-situ state differs by approx. 0.6 … 1.2 MPa from modeling assumption.

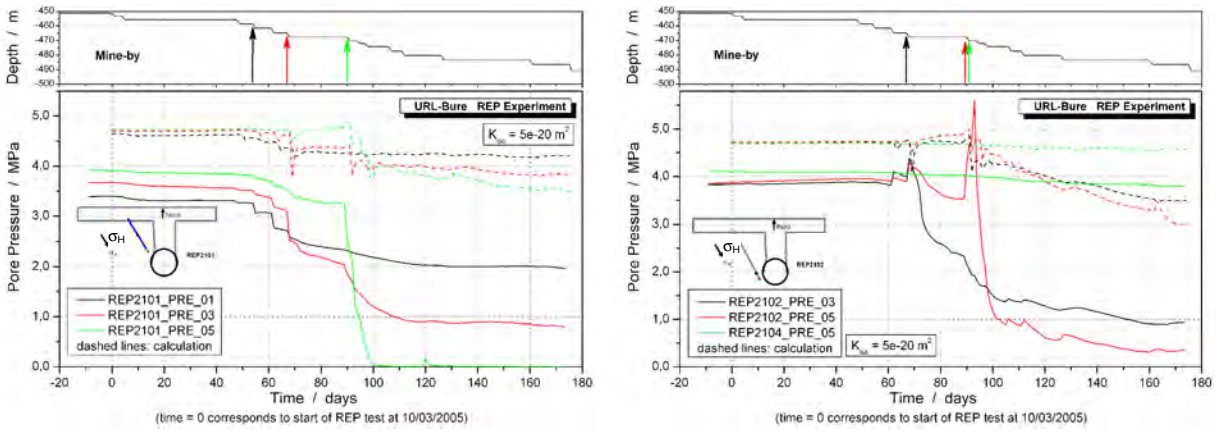

Fig. 5-16: Comparison of measured and predicted pore pressures for
a) REP2101 (left) and b) REP2102 and 2104 (right)

EDZ

Due to absence of a suitable damage criterion for evaluation of EDZ-extension only post-failure zone had been determined during the predictive modeling phase. According to the stress-based failure-criterion given by equations (5-3) and (5-5) the extension of post-failure zone (plasticity) has been determined:

in σ_h direction (N62.5°E): approx. 1.0 m (measured from shaft wall),
in σ_H direction (N152.5°E): approx. 0.7 m (measured from shaft wall).

Therefore the extension of micro-fissuring zone (before peak strength) is assumed to be slightly wider. Please note that discretization of the 3D model around the shaft was quite coarse. Its fine enough for the intended evaluation of rock deformation in the REP2207 extensometer area, but not fine enough to give an exact information on the extension of EDZ and post-failure zone.

5.5 Back analysis

The main differences compared to predictive modeling is the use of a fluid model assuming anisotropy of hydraulic conductivity. Other differences refer to changes of the used parameter set, especially regarding hydraulic conductivity and the rheological rock behavior (*POLSTER & JOBMANN, 2006*). To be more close to the observed in-situ state the initial pore pressure has been reduced to: $p = \gamma_w \bullet (z + 70)$ with $\gamma_w = 10$ kN/m^3.

The creep factor A has been reduced according to equation (5-6) for zone B' by a factor of three, and after a fitting process the hydraulic conductivity has been increased by a factor of 2 compared to the reference values. In addition to that a radius-depending permeability for the near field around the shaft was taken into account. According to a suggestion of ANDRA based on in-situ investigations the following assumption was used:

$$\frac{K}{K_0} = 13.6 \cdot 10^{-0.2323\ d} \qquad (5\text{-}7)$$

with d distance to the shaft wall [m] (d < 4.85 m)

Figure 5-17 shows a graph of equation 5-7 using an initial permeability of K_0 = 5e-20 m^2. The permeability increases towards the shaft by a factor of up to 11.

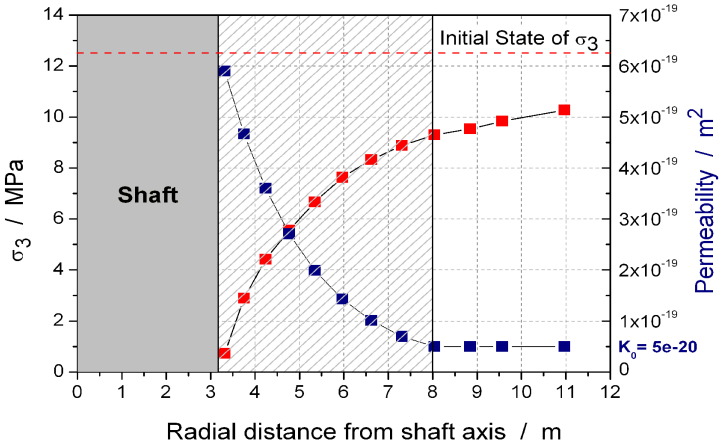

Fig. 5-17:

Assumption for variation of permeability in the near and far field of the shaft.

It is known that the physical background of permeability increase isn't represented by this assumption. Damage and stress related formulations of this dependence are still pending. Nevertheless the effect of permeability change with distance can be taken into account and it's relevance can be checked. The parameter-set used for interpretive modeling is compiled in table 5-2.

Tab. 5-2: Compilation of used parameters for interpretive modeling

Mechanical Parameters		Zone A'	Zone B' + C'
Youngs' Modulus E	MPa	9 000	
Poisson ratio ν	-	0.3	
Pre-failure behavior			
Angle of Friction ϕ	°	35	19
Cohesion c	MPa	7.2	9.0
Tensile strength Rt	MPa	2.1	2.1
Compressive strength Rc	MPa	25.3	27.8
Post-failure behavior			
Angle of Friction ϕ	°	35	19
Cohesion c	MPa	4.0	4.2
Rheological behavior			
Creep factor A	1 / s	1.2e-12	2e-12
Creep exponent n	-	1	1
Hydraulic parameters			
Hydraulic Conductivity k_{II} / $k_{\perp}$ (equiv. Permeability K_{II} / $K_{\perp}$	m / s m^2	1e-12 / 1e-13 ≅ 1e-19 / 1e-20)	
Porosity n	%	15.0	
Biot Modulus M	MPa	6 000	
Biot coefficient b	-	0.8	

5.5.1 Shaft convergence

Figure 5-18 shows a comparison of calculated and measured convergences in σ_h and σ_H direction for the geotechnical measurement section SMGR-2. The reduction of creep factor A leads to a sufficient fitting quality for the obtained time period. Nevertheless it has to be stated that the chosen Norton approach is supposed to overestimate deformations for long term simulations (because the constitutive model does not contain withstanding elements, like conic dashpot or parallel spring; reduction of the secondary creep rate results from von Mises stress decrease).

Due to the assumed anisotropic stress field the model points out higher convergences in σ_H direction (ovalisation of shaft cross section). The shaft convergences observed in-situ are more or less equal for both directions.

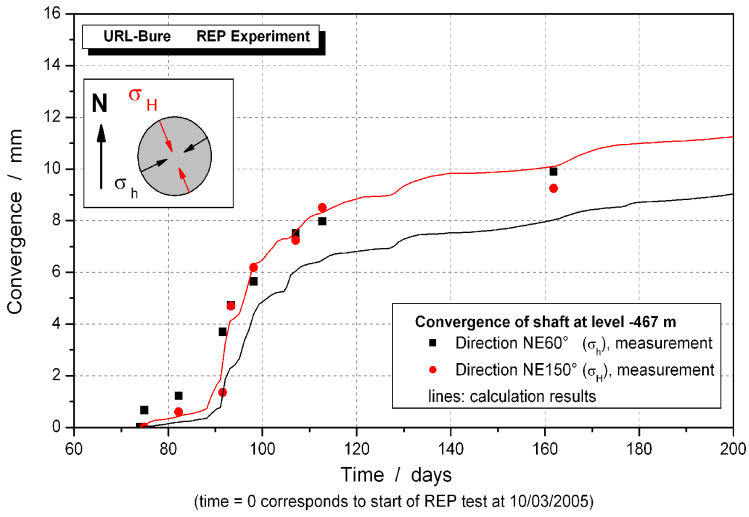

Fig. 5-18:
Comparison of measured and calculated shaft convergences

5.5.2 Displacement and strain in the rock

Due to the fact that the mechanical constitutive model and parameters were not changed for interpretive modeling similar results are obtained by calculation. The calculation results for relative displacements of two adjacent packers is given in figures 5-19 and 5-20. The reduction of creep factor A leads to slight differences compared to predictive modeling for the phase after mine-by (lower deformation rates; e.g. comparison of figures 5-19 and 5-13). The in-situ observed effects for the intervals near to the shaft, as for instance the gradual compression before mine-by (figure 5-19a,b), particularly between shaft near packers DFO09 and DFO10 or the sudden compression between packers REP2201_DFO09 and DFO10 after mine-by (figure 5-19a) can't be reproduced by this model as well. Thus, for comparison of calculation results and measurements same things are valid as stated in chapter 5.4.3.
Figure 5-20a,b present a comparison of packer displacements relative to the head plates for extensometers REP2201 and REP2202, which points out, that calculated and measured packer displacements are similar in terms of general trends.

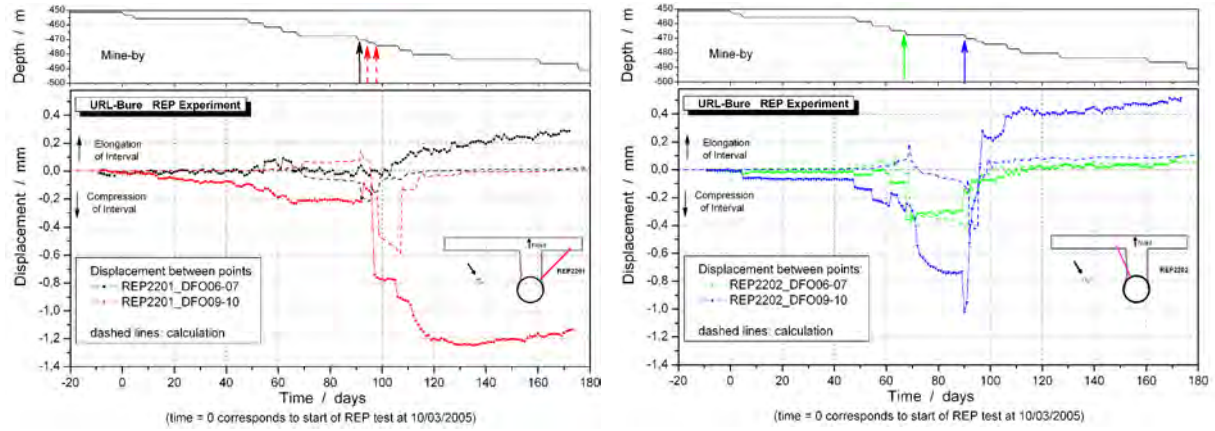

Fig. 5-19: Comparison of measured and calculated displacements for extensometer a) REP2201 (left) and b) REP2202 (right)

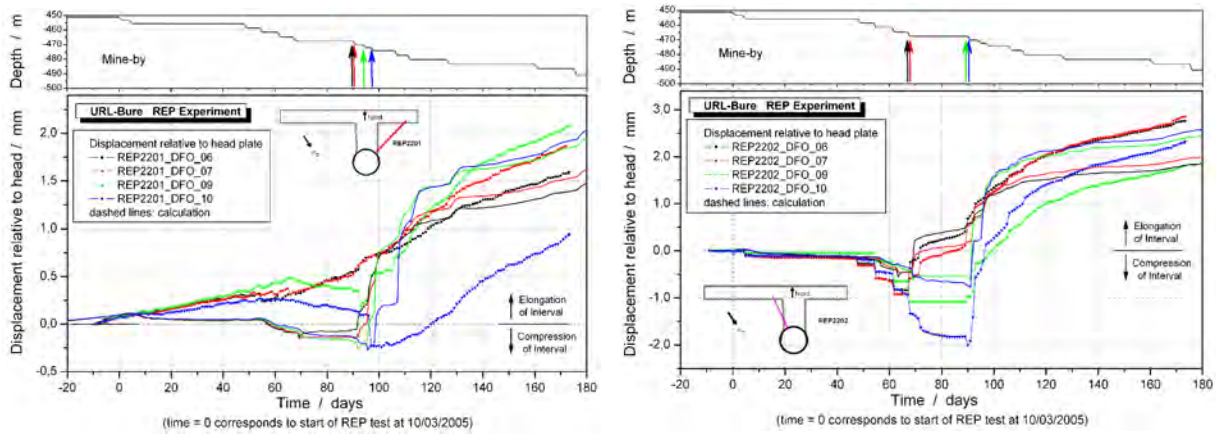

Fig. 5-20: Comparison of measured and calculated displacements relative to head plate for packers of extensometer a) REP2201 (left) and b) REP2202 (right)

Figure 5-21 and 5-22 show modeling results for relative and absolute packer displacements in borehole REP2207. The obtained interval elongation before start of the REP test, as well as after the 2nd excavation cycle since start of the REP experiment is underestimated by the model. This effect has also been observed at borehole REP2201 (figure 5-20a) and indicates the presence of another effect (as e.g. floor heave?).

The magnitudes of interval compression before mine-by are underestimated as well. These differences has also been observed for the other two extensometers (e.g. comparison of figure 5-22 with 5-14 and 5-20b).

A comparison of absolute values of packer displacements and tendencies after re-installation of the unit shows good fitting for packers DP1 and DP4. The packer displacements of DP2 and DP3 are slightly underestimated. The numerical results for movement of DP5 differ strongly from in-situ measurement (figure 5-22). Considering the interval deformations (figure 5-21) it can be obtained, that a compression of the interval 1 closest to shaft (and also for interval 2 between packer DP4 and DP3) is evident. Such trend has also been observed in-situ for shaft near interval of REP2201, however it is highly underestimated by the numerical model.

The deformations of other intervals are acceptably reflected by the model with only slightly lower deformation rates.

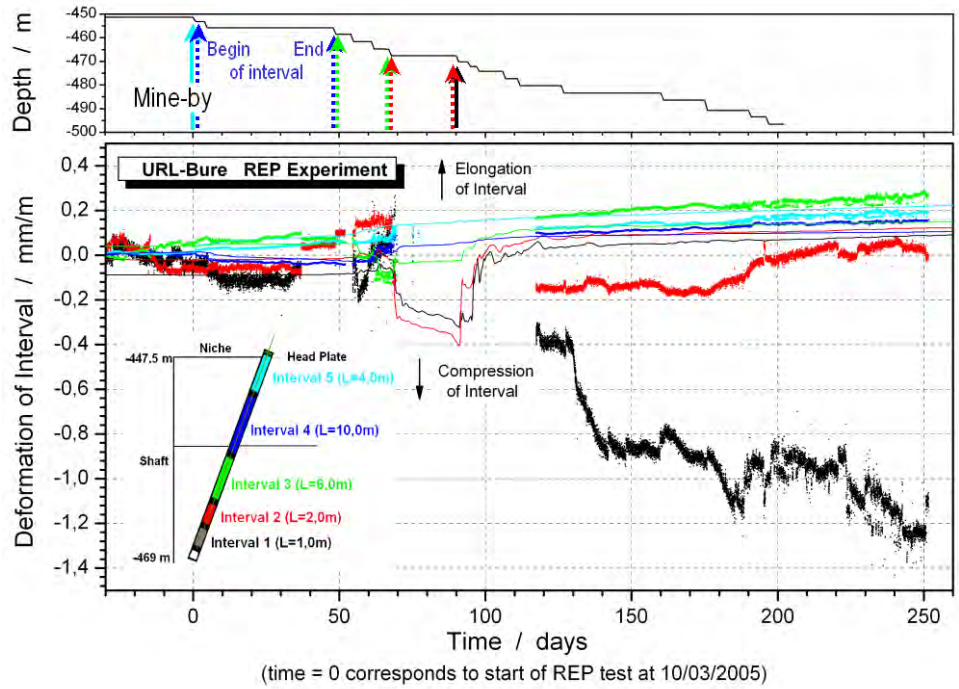

Fig. 5-21: Comparison of measured and calculated interval deformations for extensometer REP2207

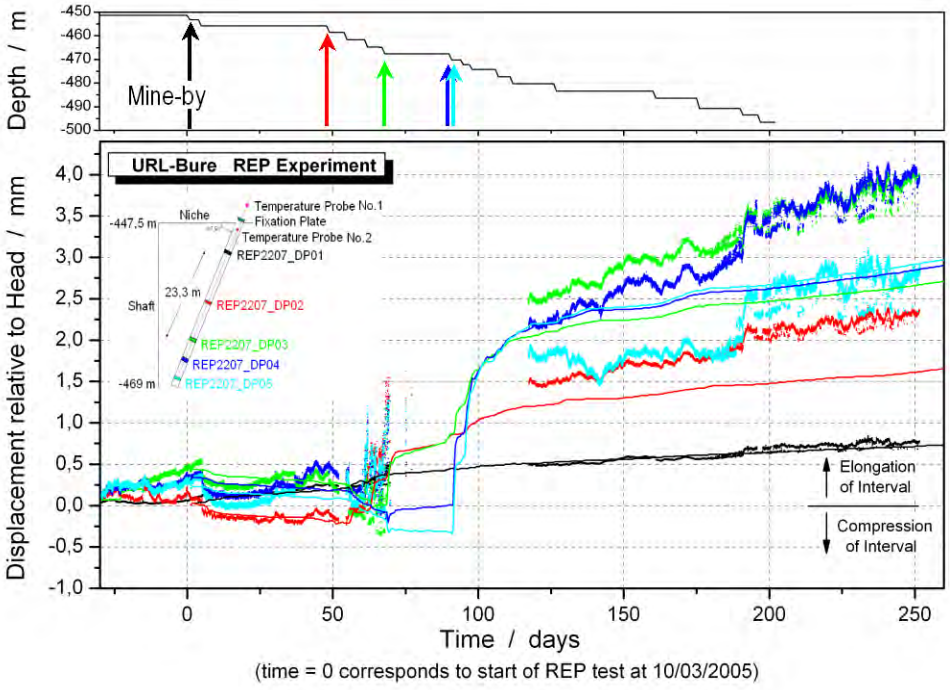

Fig. 5-22: Comparison of measured and calculated displacements relative to head plate for packers of extensometer REP2207

5.5.3 Pore pressure evolution

As stated above a calibration of hydraulic behavior has been performed by means of several calculations with varying hydraulic conductivity. As an example the evolution of pore pressure at 3 sensors of borehole REP2101 is shown in figures 5-23a and 5-23b, for two different assumptions concerning permeability. It can be obtained that the model with higher permeability (figure 5-23b, assuming $K_{0\,\parallel}$ = 1e-19 m^2 / $K_{0\,\perp}$ = 1e-20 m^2) better fits the drainage

behavior of rock mass than the model assuming reference values of permeability as given by *ANDRA (2005b)* (figure 5-23a, assuming $K_{0\,\parallel}$ = 5e-20 m^2 / $K_{0\,\perp}$ = 5e-21 m^2).

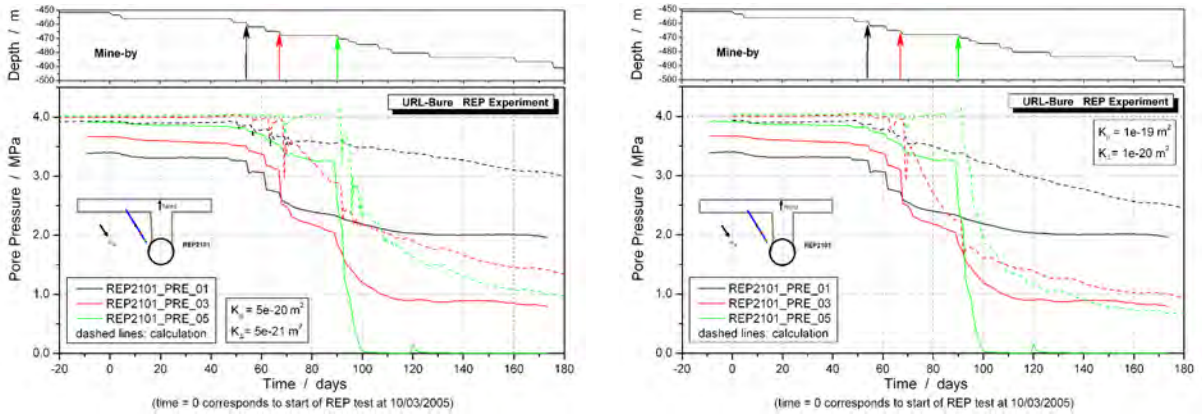

Fig. 5-23: Comparison of measured and calculated pore pressures for REP2101 assuming a) reference values for permeability (left) and b) increased permeability (right)

Figure 5-24a,b show modeling results assuming increased permeability (Table 5-2) for the other selected sensors. The simulated drainage behavior a few days after mine-by that is assumed to be less disturbed by HM response due to further sinking is in good agreement with the in-situ data. Although there is still a slight overestimation, the slopes of pore pressures decrease correspond well, which gives confidence in chosen permeability values.

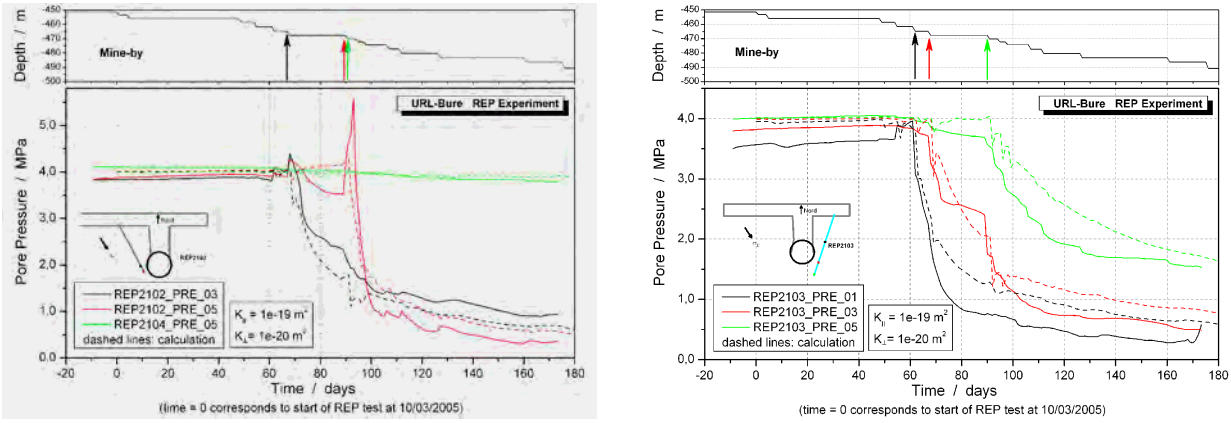

Fig. 5-24: Comparison of measured and calculated pore pressures for a) REP2102, REP2104 (left) and b) REP2103 (right)

The HM response of rock mass due to the shaft sinking is highly underestimated for the most sensors, especially:

- the gradual decrease of pore pressure observed for sensors in direction of σ_H before the excavation passes sensors' level (e.g. figure 5-23b, sensors REP2202_PRE_03 and PRE_05) and
- observed pore over-pressures for sensors in direction of σ_h (e.g. figure 5-24a, sensor REP2202_PRE_05) at the time of mine-by.

The chosen HM-coupling seems to be not sufficient to reproduce all the in-situ observed effects. The presence of further dependencies is supposed (e.g. dependence of permeability on damage), which were not considered or insufficiently described within the model.

5.5.4 EDZ

Failure zone

The extension of post-failure zone (plasticity) has been determined according to the stress-based failure-criterion of the constitutive model given by equations (5-3) and (5-5). Assuming strength parameters as given in table 5-2 failure occurs up to a depth of:

in σ_h direction (N62.5°E): approx. 1.0 m (measured from shaft wall),
in σ_H direction (N152.5°E): approx. 0.7 m (measured from shaft wall).

Damage zone

For evaluation of EDZ-extension the stress-based Hoek-Brown criterion has been applied.

$$\sigma_{1\,\text{admissible}} = \sigma_3 + \sigma_{ci} \cdot \left(\frac{m_b \cdot \sigma_3}{\sigma_{ci}} + S \right)^a \qquad (5\text{-}8)$$

Assuming the lower boundary values for damage as given in *ANDRA (2005c)* with σ_{ci} = 9.6 MPa, m = 1.5, S = 1, a = 0.5 (zone B') the EDZ may reach up to
approx. 2 m (measured from shaft wall), in σ_h direction (N62.5°E) and
approx. 1 m (measured from shaft wall), in σ_H direction (N152.5°E).

Figure 5-25 gives an exemplary evaluation of the damage criterion at a level of -455 m (date: 10/05/05; after excavation cycle 184). The value represents the relationship between actual and maximum admissible stress $\sigma_{1\,\text{actual}}$ / $\sigma_{1\,\text{admissible}}$ (values > 1.0 indicate damage state). Figure 5-25 clearly shows the influence of the anisotropic state of stress on the non-uniform extension of the damaged zone. The calculation results point out that in σ_h direction at the shaft contour von Mises stresses $\sigma_{eqv} \approx 20$ MPa are reached, whereas only approximately half of the value occurs in σ_H direction. The according stress field is given in appendix L.

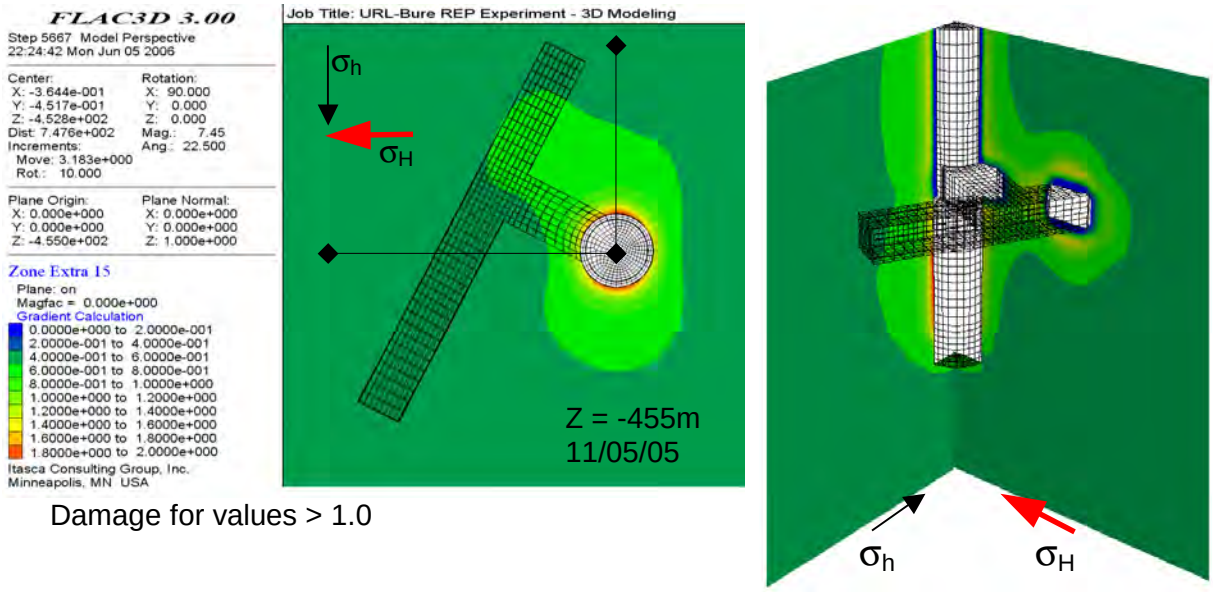

Damage for values > 1.0

Fig. 5-25: Damage criterion [-] after excavation cycle 184 (10/05/2005)
Left: horizontal cross section at -455 m,
Right: cross section along principal stress planes; view from NNE

6 CONCLUSIONS AND LESSONS LEARNED

The following section gives major conclusions regarding the thermo-hydro-mechanical behavior of argillaceous rocks gained from results of the two in-situ experiments named HE-D (Opalinus Clay, Mt. Terri) and REP (Callovo-Oxfordian Clay, Bure). Geotechnical measurements, numerical modeling and their comparison in terms of back analysis allowed for a detailed analysis of rock mass behavior. Unexpected effects and problems occurred during experiment performance as well as some difficulties in numerical simulation of the observed rock mass behavior. This underlines further requirements in constitutive model improvement for description of argillaceous host rock behavior.

6.1 General conclusions

In the following some observations are listed, which were gained during the course of the project. The aspects described below were in part astonishing or unexpectedly strong and describe the "surprising" behavior of argillaceous rock from a phenomenological point of view. Nevertheless those problems have to be taken into account for feasibility studies on construction and operation of a repository in an argillaceous host rock.

The first aspect refers to **problems with drift wall stability** (c.f. chapter 4.3.2: observations at MI-Niche and roof-fall at EZ-A Niche 2005 at Mont Terri, reported by *VIETOR et al., 2006*, figure 6-1). Such problems have been observed even for

- relatively low stress levels (c.f. Mt. Terri with approx. 200 m overburden thickness) and
- comparatively small cross sections (usually shotcrete-lined).

In this context the observed **partly high convergence-rates** are surprising, too. It is most likely that they are caused by progressive opening of pre-existing fractures (within EDZ) far beyond drift wall. *VIETOR et al. (2006)* reported that the surrounding rock within the reach of installed extensometers (≈ 2.5 m) does only account for a small portion of observed convergences. This gives evidence of complete rock block detachments without significant internal deformation. These observations also underline the **influence of low strength of bedding planes and/or rock joints**, which determine failure mechanism and failure strength of rock mass.

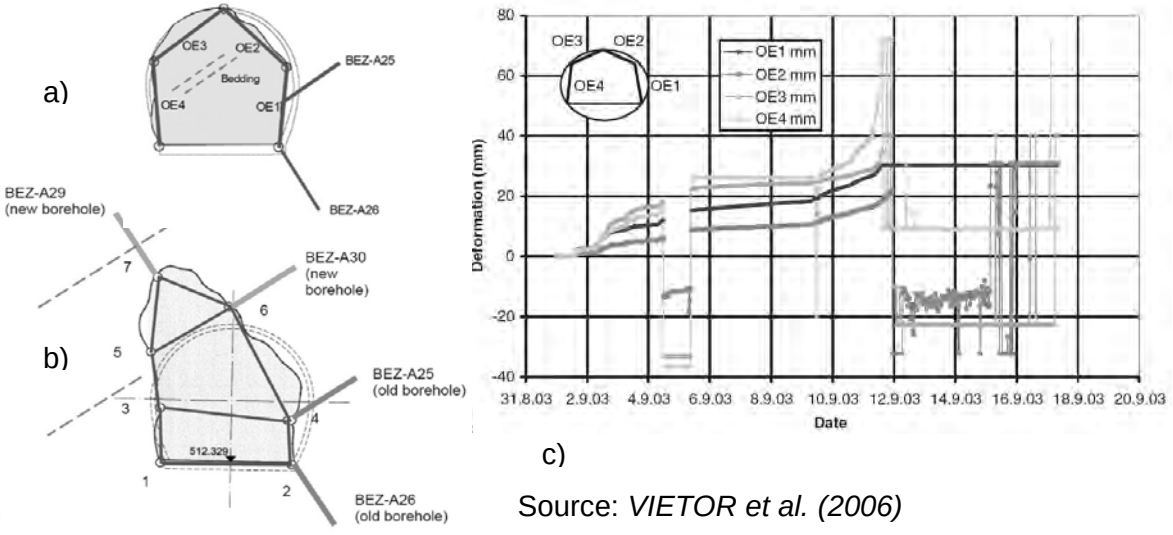

Source: *VIETOR et al. (2006)*

Fig. 6-1: a) Geometry of original profile of EZ-A Niche with position of extensometers
b) Geometry after rock fall at 11th and 12th September 2005 (130 m^3)
c) Evolution of deformation at the tunnel surface

A further aspect in this context refers to the **far-reaching stress re-distributions with effects on mechanics and hydraulics.** Such observations have been gained during HE-D experiment, where excavation work of the gallery GA 04 and EZ-B Niche in a distance of approximately 30 – 40 m most likely affected extensometer measurement.
Moreover, various authors reported observations on hydraulic disturbances in the far-field of excavations (c.f. chapter 3.2 emphasis of research and constitutive modeling).

During both field experiments a **development of significant pore-overpressures** has been observed, which was much higher than expected from the hydraulic point of view.
So during the HE-D heater test a **thermally-induced** increase of pore pressure of about 0.2 MPa/K has been measured (short-term value = quasi undrained conditions). The sensors in the direct vicinity to the heater showed maximum pore pressures around 4.0 MPa (sensors BHE-D03 and BHE-D16 with r = 1.1 and 1.35 m distance to heater axis, c.f. appendix B-4 and B-16). Taking into account the initial pore pressures of 1.5 MPa and 1.0 MPa the maximum applied heating power of 1.95 kW (equal to the volumetric heating power of a German HAW / BSK3 (spent fuel) canister after approximately 9 a / 5 a interim disposal period) led to pore-overpressures of 2.5 MPa and 3.0 MPa, respectively.
During the REP experiment significant **excavation-induced** pore-overpressures have been observed. They occurred only for short time in host rock areas, which were subjected to volumetric compression due to stress-redistribution. The maximum value around Δp = 2.0 MPa has been detected in σ_h direction in a distance of 1.2 m behind the shaft wall after mine-by. Similar observations have been reported in *NAGRA 2002* for the excavation of the Mont Terri ED-B drift (c.f. chapter 4.5.4) as well as during excavation work at the –490 m level of the URL-Bure in the framework of the SUG experiment.

6.2 Conclusions with regard to numerical modeling

Prior to both in-situ experiments predictive calculations have been performed. Later on a refinement of the numerical model during comparative modeling phase took place. The blind prediction was useful to point out the ability of numerical codes to describe the observed host rock behavior. Furthermore it clearly shows deficiencies in the assessment of the significant effects and coupling processes. A comparison of such blind-prediction results for the REP experiment is given in appendix M. It can be stated, that certain aspects of THM modeling are well-understood, so that numerical models are able to predict and/or reproduce observed host rock behavior with high accuracy (see for instance appendix M-1: elastic deformation in the shaft far-field during REP experiment). A low degree of conformance could be observed for the near-field response, when host rock is near damage or failure state, c.f.:

- shaft near extensometer intervals during REP-experiment (appendix M-2) or
- or MI-Niche convergence during HE-D-experiment (appendix B-5 & B-6).

Table 6-1 summarizes aspects of THM modeling and gives a rating to their reproducibility within coupled numerical calculations (quality of host rock behavior description). Especially in case of M→H modeling (hydraulic responses to load changes) the used coupling formulations are often not able to reproduce the observed effects and underestimate the extension of the hydraulically disturbed zone (HDZ, c.f. chapter 3.2 emphasis of research and constitutive modeling and appendix M-4).

Tab. 6-1: Compilation of aspects of THM modeling of argillaceous rock behavior and their numerical reproducibility (quality of prediction)

Reproducibility of host rock behavior / prediction quality	
high	**medium / low**
Mechanical behavior - elastic response in the far-filed - failure mechanisms & depth of failed (pseudo-plastic) zone and damaged zone	***Mechanical behavior*** - rheologic host rock behavior (time-depending evolution of EDZ) - processes involving discontinuum-mechanical effects, for example fracture propagation and –movement
Hydraulic behavior - drainage behavior	***Hydro-Mechanical behavior*** - behavior of argillaceous rock at partially-saturated conditions (2-phase flow) - M→H behavior / degree of coupling excavation-induced changes of pore pressure (often significantly underestimated HDZ)
Thermal behavior - calculation of the temperature field and heat propagation	***Hydro-Thermal (M)behavior*** - evolution of pore pressure due to heating

Table 6.1 underlines a lack of knowledge and necessity of further research – particularly with regard to the importance of the long-term behaviour of a potential host rock for disposal of radioactive waste. Thus, further research should be focused on:

A laboratory and in-situ investigations for theoretical modeling, e.g. aimed at:
- degree of HM-coupling and its mathematical description / choice of parameter,
- mechanism of damage and its consequences on H and HM behavior,
- description of time-dependent damage evolution,
- mechanism of viscoplastic deformation

B numerical modeling, e.g. aimed at:
- incorporating all features, which are relevant for the considered problem, in particular anisotropy of mechanical, hydraulic and thermal parameters
- dependencies of mechanical parameters on water content and degree of saturation
- introduction of damage theory approaches (damage as state variable for description of HM behavior)

6.3 Conclusions on HE-D experiment

For modeling of the HE-D experiment a back analysis of the coupled THM problem with a stepwise solution has been applied. As a first step a thermal calibration has been performed by means of temperature measurements in boreholes BHE-D0 to BHE-D3 and BHE-D07 - D17. Within a given range of material parameters generally based on first laboratory investigations a variation of parameters took place to achieve best fit of measured and calculated temperatures. Finally, a set of thermal material parameters was determined, yielding a good fit of measurement and calculation. Looking at the scattering of the measured thermal conductivities due to different water contents or mineral composition the specific heat capacity of c_p = 920 J / kg·K and the thermal conductivity of λ = 1.7 / 0.81 W / m·K parallel / perpendicu-

lar to stratification seem to be reasonable especially if we consider a disturbed zone around the heater borehole with slightly lower thermal conductivities than the undisturbed clay rock.

Furthermore some sets of parameters were tested, which assume higher thermal conductivities at an input of η = 100% and 90% of the electrical power applied. Consequently these models slightly overestimate measured temperatures. Furthermore it can be observed that temperature evolutions – especially in highly transient phases, e.g. caused by changed electrical power – show significant higher slopes due to the higher thermal conductivities. Evaluation of cooling phase – generally more appropriate due to less disturbance – shows a rapid decreasing temperature for those models. As a conclusion we assume that the thermal conductivity chosen for these sets seems to be too high.

Within a following hydraulic calibration at measurement values from ED-B drift excavation as well as the initial state of the HE-D experiment a set of hydraulic parameters has been found resulting in an initial state of pore pressure that fits to the measurements in BHE-D7 to D17. An adequate distribution of pore pressure before start of heating has been achieved by increasing the hydraulic conductivity in comparison to the reference value of $k = 1 \cdot 10^{-13}$ m/s. A calculation assuming a value of $k = 5 \cdot 10^{-13}$ m/s provides a satisfying fit of measured and calculated pore pressures. A reduction of the Biot-Modulus allowed an increased compressibility of pore fluid to simulate the presence of air-filled void in-situ. This approach becomes necessary, because of the model restriction to a single phase fluid and a saturation of $S_r = 1$. To which extend errors arise from simplifying modeling assumptions, e.g. neglect of multiphase flow (concept of relative permeability) and neglect of damage- and failure dependent permeability cannot be clarified finally.

The calibrated set of thermal and hydraulic parameters which fits best to the measurement has been used as input for the following coupled THM-calculation. Within this step of solution a satisfying fit of measured and calculated displacements has been achieved while varying different mechanical and hydraulic parameters.

Due to a damage of one fiber-optic cable and an ongoing expansion, occurring between sensor 2 and the head plate, only 3 measurement intervals of BHE-D6 could be quoted for the sake of interpretation. After start of each heating phase all intervals are undergoing a phase of compression due to increasing rock pressure followed by a phase of expansion which over-compensates compression. However, interval 1 which is nearest to the heaters shows an additional effect of shortening, which clearly dominates deformation behavior by over-compensating thermal expansion during heating phase II. Since 150th day the intervals 2 and 3 are supposed to be influenced by excavation work, too. This effect is leading to a faster expansion of intervals with a distance of approx. 2.5 – 4.5 m to the heater. This was also detected by sliding micrometer measurement in borehole BHE-D04 and D05.

For both chosen sets of material parameters a good fit of measured and calculated deformations has been achieved for intervals 2 and 3 until 150th day. Afterwards calculated results diverge significantly from measurement. A set of parameters has been tested, which assumes higher thermal conductivities at an input of η = 100% of the electrical power applied and lower hydraulic conductivities but this generally overestimates pore pressures. The pressure built-up and following decrease especially during heating phase I is overestimated by both sets. In heating phase II the model with the calibrated set of parameters shows a good fit of pressure decrease to selected sensor results which indicates an adequate choice of hydraulic conductivity.

The near distance of the temperature sensors to the pore pressure sensors within boreholes BHE-D07 – BHE-D17 allows for an evaluation of a dependency of pore pressure evolution on temperature. Figure 6-2 shows the pore pressure vs. temperature curves for heater near sensors BHE-D15 and D16 (for the other sensors see appendix B-18 and B-19). After the begin of each heating phase an almost linear increase of pore pressure can be noted, which is gradually superposed and later on overcompensated by drainage. Table 6-2 gives the calculated pore pressure gradients for the linear part of the p vs. T curves for the first few days after increase (or switch-off) of heating power. Thus it can be assumed that drainage can be almost neglected and pore pressure changes are mainly caused by thermal expansion itself and its hydro-mechanical response, in particular the thermally induced stresses. The values for the quoted sensors range between 0.02 … 0.5 MPa/K, most of them being around 0.2 MPa/K. Those values obtained in-situ are slightly lower than the calculated value of 0.29 MPa/K gained from theoretical considerations using equation (3-4) and the parameters of model THM1 as given in table 4-7.

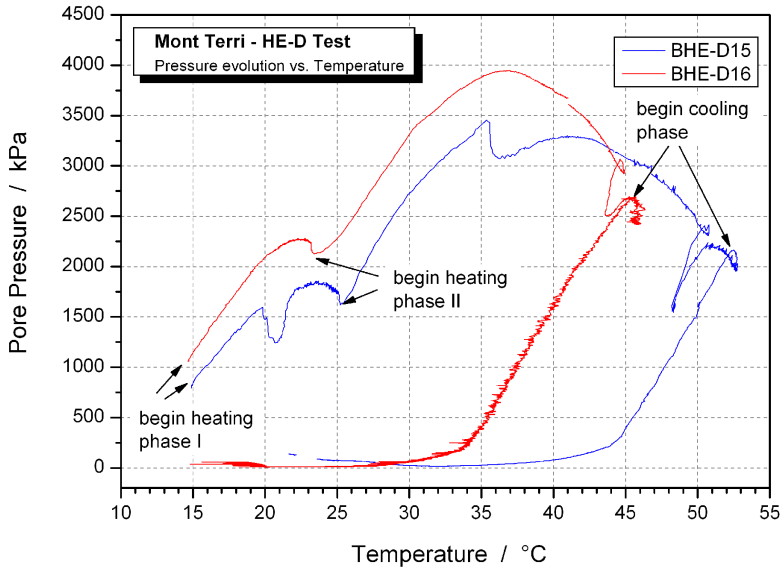

Fig. 6-2: Pore pressure evolution vs. temperature

Tab. 6-2: Temperature-induced pore pressure gradients for GRS sensors

Borehole	Pressure gradient in [MPa / K]		
	heating phase I	heating phase II	cooling
BHE-D08	0.12	0.12	0.18
BHE-D09	0.021	0.21	0.16
BHE-D11	0.39	0.15	0.07
BHE-D13	0.07	0.35	0.46
BHE-D14	0.15	0.15	0.27
BHE-D15	0.16	0.24	0.26
BHE-D16	0.19	0.21	0.24
BHE-D17	0.16	0.17	0.50
mean	**0.16**	**0.20**	**0.27**

n general there seems to be an increase of pressure gradient while experiment advances. This might be due to the fact that thermal expansion coefficient is not as constant as it is used in the model but depends on temperature or temperature range being looked at respectively for both water and minerals (c.f. chapter 3.3). Thus the initial temperature level for starting a new heating phase has an influence on the pore pressure increase/decrease to be expected during further temperature increase/decrease.

6.4 Conclusions on REP experiment

The huge database of in-situ measurements, which were gained from the REP experiment gives the opportunity to investigate the hydro-mechanical response of the Callovo-Oxfordian Clay due to a progressive shaft sinking. Aimed at an advance in comprehensive understanding of HM-behavior and especially the coupling effects as well as an improvement of constitutive models all main effects observed during the experiment should be taken into account.

At the present state the applied hydro-mechanical coupled model was not capable to reproduce all observed effects in a sufficient manner. Summarizing the HM-model analysis following things can be stated:

Hydraulic behavior

I Even if a simple single-phase fluid flow (without consideration of suction) is assumed a sufficient description of drainage behavior after mine-by can be given, if the model takes into account:
- slightly increased initial permeabilities (by a factor of 2 against reference values)
- dependency of permeability on damage and/or stress.

Damage- and stress-related formulations of this dependency are still pending. A radius depending approach was used instead of describing a zone of increased permeability around the shaft.
For set up of an initial pore pressure field close to in-situ state the drainage induced by shaft and niche has to be taken into account.

II The HM response of rock mass due to the shaft sinking is highly underestimated compared with sensors' reaction, especially:
- the gradual decrease of pore pressure observed for sensors in direction of σ_H before the excavation passes sensors' level (e.g. figure 5-23b, sensors REP2202_PRE_03 and PRE_05) and
- the observed rapid pore pressure increase with significant over-pressures for sensors in direction of σ_h (e.g. figure 5-24a, sensor REP2202_PRE_05) at the time of mine-by.

Figure 6-3 shows the calculated pore pressure distribution before and after the 184th excavation cycle. It underlines, that the calculated pore over-pressure in direction of σ_h ($\Delta p < 0.5$ MPa approx. 1…3 m behind the shaft wall) is significant smaller than measured (e.g. Δp = 1.5 MPa at sensor REP2102_PRE_05 in a distance of 1.3 m).

Additional 2D calculations have been performed, using a finer mesh (c.f. appendix K-1 and *POLSTER & JOBMANN, 2006*). Immediately after excavation pore pressures reach up to 5.5 MPa approximately 0.5 m behind shaft wall (appendix K-2). The pressure decreases quickly. At sensors locations similar pressure evolutions are gained as for 3D modeling (exemplary shown for sensors REP2102_PRE_05 and REP2103_PRE_03; appendix K-3 and K-4). Due to the insufficient description of the HM-response no significant differences in pore pressure evolution for the phase of mine-by could be obtained for the three models – even different states of stress were assumed.

It can be concluded that the HM-coupling seems to be not sufficient (strong) enough to reproduce the in-situ observed effects. The existence of further dependencies is supposed (e.g. dependence of permeability on damage; volumetric deformation behavior of rock mass), which were not assumed or insufficiently described within the model.

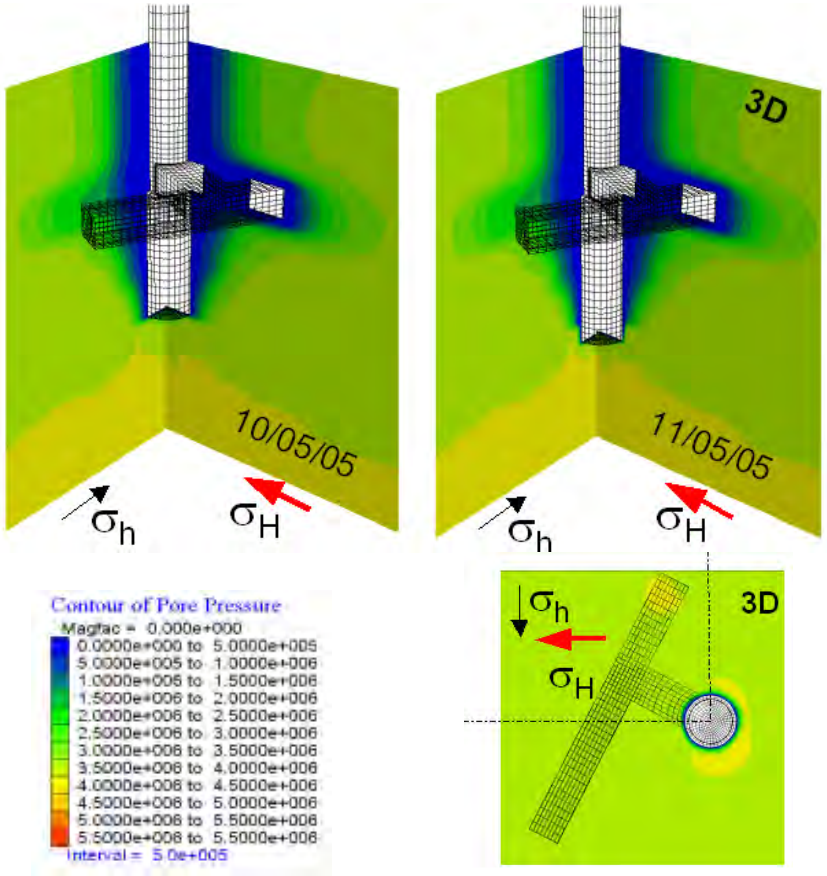

Fig. 6-3: Pore pressure distribution [Pa] before (upper left figure) and after (right figures) excavation cycle 184 (10/05/2005) Lower figure: horizontal cross section at -455 m,

Mechanical behavior

It is a known fact that the transfer of mechanical parameters gained from laboratory investigations on samples to the rock mass may lead to an over- or under-estimation of rock mass behavior. During modeling work the creep parameter A was reduced by a factor of 3, because a 1:1 transfer of the laboratory-based parameter-set led to an overestimation of rheological behavior. After this adjustment a good accordance of measured and calculated shaft convergences has been achieved. However, it has to be mentioned that the chosen Norton Power Law approach describes the rheologic behavior of the rock from a phenomenological point of view, but representing most likely not the mechanism, which is responsible for rheologic behavior of argillaceous material.

For a comprehensive description of HM and especially rheological behavior among other things the influence of water content and desaturation has to be taken into account. Results of creep tests, showing quasi-constant deformation rates of the samples (*ZHANG et al., 2004a*) allow the choice of above mentioned simple creep approach for natural water content. But wetting and desaturation led to significant increase of deformation rate and nearly zero deformation for desaturation, respectively.

A fit of rheological behavior by means of 2D calculation results for shaft convergences would lead to an overestimation of rheological behavior (see appendix K-9). The reason for this is an under-estimation of creep-inducing von Mises stress for the 2D case (*POLSTER & JOBMANN, 2006*).

The elasto-plastic part of the constitutive model seems to be less suitable for a proper description of rock mass behavior close to the shaft contour, which is assumed to be in failure or damaged state. So for instance the rock compression before, during and especially after the phase of mine-by is not sufficiently reproduced by the simulation. An appropriate description of deformation behavior, especially volumetric deformation, for pre- and post-failure state seems to be required for a satisfying HM response simulation of the rock mass. Due to the use of a continuum-code model some in-situ observed deformations (e.g. compression between packers REP2201_DFO09 and DFO10 after mine-by) cannot be reproduced.

Although the model is quite simple it has to be stated, that the obtained results for shaft convergences as well as strains in the far field of the shaft (distance > 1.5 m from shaft wall) are in good agreement with in-situ measurements.

7 REFERENCES

ALHEID, H.-J.; KRUSCHWITZ, S.; SCHUSTER, K.; YARAMANCI, U. (2002) : Charakterisierung der Auflockerungszone um Strecken im Opalinuston mit seismischen und geoelektrischen Verfahren. Zeitschrift Angewandte Geologie, 2/2002

ANDRA (1999) : Geological Statement Report of the Eastern Site. Report No. A RP ADS 99-00506.

ANDRA (2003) : Geological situation at the test area and defined reference values for the Opalinus clay, Internal report.

ANDRA (2004) : Laboratoire de Recherche Souterrain de Meuse / Haute-Marne: Fiber Optic Deformation Measurements - Installation Report. D RP 0DBE 05.001

ANDRA (2005a) : Laboratoire de Recherche Souterrain de Meuse/Haute-Marne: Resultats des mesures apres installation du dispositif experimental – Experimentation REP., D.NT.ADPE.05.0471.

ANDRA (2005b) : Underground Research Laboratory of Meuse/Haute-Marne: Specification for modeling of the REP experiment (2005) – WP3 of the MODEX-REP project, C.SP.ASMG.05-0024.

ANDRA (2005c) : Dossier 2005 - Référentiel du Site Meuse/Haute-Marne, C.RP.ADS 04.0022.

ANDRA (2005d) : Laboratoire de Recherche Souterrain de Meuse/Haute-Marne: Resultats de mesures apres la phase de fonçage du puits entres les cotes -454m et –480m Experimentation REP. Internal Report D.RP.ADPE.05.0855, 10/2005

ANDRA (2006a) : Laboratoire de Recherche Souterrain de Meuse/Haute-Marne: Premiers resultants de l' experimentation TER, Periode de Juillet 2005 a septembre 2006. Internal Report D.RP.ADPE.06.0524, 09/2006

BALDI, G., HUECKEL, T., PELLEGRINI, R. (1988) : Thermal volume changes of the mineral-water system in low-porosity clay soils, Can. Geotech. J. 25, 807-825, Canada.

APLIN, A.-C.; FLEET, A.-J.; MACQUAKER, J.-H. (1999) : Muds and Mudstones: Physical and fluid flow properties. published by the Geological Society London.

ARMAND, G.; WILEVEAU, Y. (2006) : In situ observations and measurements of the Callovo-Oxfordian argillites behaviour during shaft and drifts excavation of the MHM-URL. presentation held at: Seminary in Geomechanics on modelling of hydromechanical behaviour of the Callovo-Oxfordian argillites observed in the MHM-URL, Université Paris XI – Orsay, 07. June 2006

BALDI, G., HUECKEL, T., PELLEGRINI, R. (1988) : Thermal volume changes of the mineral - water system in low-porosity clay soils. Can. Geotech. J. 25 , p. 807-825

BALDI, G., HUECKEL, T., PEANO, A., PELLEGRINI, R. (1991) : Developments in modelling of thermo-hydro-geochemical behavior of Boom clay and clay based buffer materials, Commission of the European Communities, nuclear science and technology, Final Report, Vol. 1+2, ISMES Spa, Bergamo (EUR 13365 EN).

BEMER E., LONGUEMARE P., VINCKÉ O. (2004) : Poroelastic parameters of Meuse/Haute Marne argillites: effect of loading and saturation states. In: Applied Clay Science, 26, pp. 369–366.

BLÜMLING, P. & KONIETZKY, H. (2003) : Development of an excavation disturbed zone in claystone (Opalinus Clay). In: Geotechnical Measurements and Modeling, Natau, Fecker & Pimentel (eds) p. 127-132, Zwets & Zeitlinger, Lisse, ISBN 90 5809 603 3

BOSSART, P.; MEIER, P.;MÖRI, A.; TRICK, T.; MAJOR, J.-C. (2002) : Geological and hydraulic characterization of the excavation disturbed zone in the Opalinus Clay of Mont Terri Rock Laboratory. Engineering Geology 66.

BUNTEBARTH, G. (2004) : Bestimmung thermophysikalischer Eigenschaften an Opalinustonproben. Laboratory investigations on opalinus clay samples, Geophysikalisch-Technisches Büro, Clausthal-Zellerfeld.

BUNTEBARTH, G. (2006) : Bestimmung der Wärmeleitfähigkeit an Opalinuston-Proben, Geophysikalisch-Technisches Büro, Clausthal-Zellerfeld.

CHIARELLI, A. S.; SHAO, J.F.; HOTEIT, N. (2003) : Modeling of elastic-plastic damage behavior of a claystone, International Journal of Plasticity, 19, pp. 23–45

CONIL, N.; DJERAN-MAIGRE, I.; CABRILLAC, R.; SU, K. (2004) : Thermodynamics modeling of plasticity and damage of argillite, C. R. Mecanique 332, pp. 841–848

COUSSY, O. (1995) : Mechanics of porous continua, 2nd ed. (Wiley)

CUNDALL, M. (1982) : Mixed Discretization Procedure for Accurate Solution of Plasticity Problems, Int J. Num. Meth. and Analytical Methods in Geomechanics, Vol. 6, p. 1 29,139.

CZAIKOWSKI, O.; LUX, K.-H. (2006) : Physical modeling and numerical simulation of long-term deformation behavior of indurated clay with special consideration of anisotropic effects and in situ measurements. In: Proceedings of Eurock 2006, Multiphysics coupling and long term behavior in rock mechanics, Liège, Belgium 2006, p. 487-492

DEDECKER, F. (2006) : Evaluation of damage using a three dimensional Adaptive Continuum / Discontinuum Codes. presentation held at the Seminary in Geomechanics on modelling of hydromechanical behaviour of the Callovo-Oxfordian argillites observed in the MHM-URL, Université Paris XI – Orsay, 07. June 2006

FABRE, G.; PELLET, F. (2006a) : Creep and time-dependent damage in argillaceous rocks. In: International Journal of Rock Mechanics & Mining Sciences 43 (2006), p.950-960

FABRE, G.; PELLET, F. (2006b) : Multiscale analysis and analytical modeling of creep and damage in argillaceous rocks. In: Proceedings of Eurock 2006, Multiphysics coupling and long term behavior in rock mechanics, Liège, Belgium 2006, p.403-409

FOWG & GI (2004) : Mont Terri Project - Programme overview and work programme of phase 10 (July 2004 – June 2005), Federal Office for Water and Geology & Geotechnical Institute Ltd., St. Ursanne, 10/2004

GASC-BARBIER, M. ; CHANCHOLE, S. ; BÉREST, P. (2004) : Creep behavior of Bure clayey rock. In: Applied Clay Science 26; pp. 449–458.

GENS, A. (2000) : HE Experiment: Complementary Rock Laboratory Tests – Laboratory Interim Report Phase 3. Unpubl. Mont Terri Report.

GENS, A.; VAUNANT, J.; GARITTE, B.; WILEVEAU, Y. (2006) : Response of a saturated mudstone under excavation and thermal loading. In: Proceedings of Eurock 2006, Multiphysics coupling and long term behavior in rock mechanics, Liège, Belgium 2006, p.35-44

GHOREYCHI, M. (1998) : Comportement differe comptetenu des couplages thermo-hydro-mechaniques des argilites silto-carbonates de l'Est. G.3S Rapport Final No. B RP 0.G.3S 98-007/A

HORSEMANN, S.T. (1994) : The disposal of high level radioactive waste in argillaceous host rocks, identification of parameters, constraints and geological assessment priorities, Publicacion Technica Num. 04/94, ENRESA, Spain.

HOTEIT, N.; OZANAM, O.; SU, K. (1998) : Geomechanical Investigation of an Argillaceous Formation in the East of France. Proceed. International Workshop on Rock Mechanics of Nuclear Waste Repositories, Vail, CO

HOU, Z.; LUX, K.-H. (2002) : Geomechanische Planungskonzepte für untertägige Tragwerke mit besonderer Berücksichtigung von Gefügeschädigung, Verheilung und hydromechanischer Kopplung. Habilitationsschrift, Heft Nr.13 Schriftenreihe der Professur für Deponietechnik und Geomechanik am Institut für Aufbereitung und Deponietechnik, TU Clausthal, 2002

HOXHA, D.; HOMAND, F.; GIRAUD, A.; AUVARAY, C.; SU, K. (2006a) : Poromechanical behavior of Meuse-Haute Marne argillite: laboratory evidences and modeling. In: Proceedings of Eurock 2006, Multiphysics coupling and long term behavior in rock mechanics, Liège, Belgium 2006, p.121-126

HOXHA, D.; GIRAUD, A.; BLAISONNEAU, A.; HOMAND, F.; CHAVANT, C. (2004) : Poroplastic modeling of the excavation and ventilation of a deep cavity. Int. J. Numer. Anal. Meth.Geomech; 28(4), pp.339–364

HOXHA, D.; JIANG, Z.; HOMAND, F.; GIRAUD, A.; SU, K.; WILEVEAU, Y. (2006b) : Impact of THM constitutive behavior on the rock-mass response: case of HE-D experiment in Mont Terri Underground Rock Laboratory. In: Proceedings of Eurock 2006, Multiphysics coupling and long term behavior in rock mechanics, Liège, Belgium 2006, p. 199-204

HUNSCHE, U.; WALTER, F.; SCHNIER, H. (2004) : Evolution and Failure of the Opalinus Clay: relationship between deformation and damage, experimental results and constitutive equation. In: Applied clay science 26 (2004), p. 403-411

HUNSCHE, U.; NAUMANN, M.; SCHULZE, O. (2005) : Application of the Dilatancy Concept on the Behaviour of Opalinus Clay. Clays in Natural & Engineered Barriers. Tours, 03/2005

ITASCA (2002) : FLAC^{3D}. Fast Lagrangian Analysis of Continua in Three Dimensions, Version 2.1., Minnesota, USA.

JIA, Y.; DUVEAU, G.; SHAO, J.F.; SU, K.; WILEVEAU, Y. (2006) : Thermo-hydromechanical modeling in unsaturated hard clay and application to nuclear waste storage. In: Proceedings of Eurock 2006, Multiphysics coupling and long term behavior in rock mechanics, Liège, Belgium 2006, p.505-511

JOBMANN, M.; FISCHER, S.; VOET, M. (2000) : Entwicklung und Erprobung redundanter faseroptischer Meßsysteme mit Selbstkontrolle zur Endlagerüberwachung, Abschlussbericht, Band I+II, DBE, Peine.

JOBMANN, M.; VLEKKEN, J.; VOET, M. (2005) : Operational safety monitoring with fiber optic sensing systems, Final Report, Vol. 1,2,3, DBE TECHNOLOGY, Peine.

JOBMANN, M; POLSTER, M. (2005) : The response of opalinus-clay due to heating: a combined analysis of in-situ measurements, laboratory investigations and numerical calculations. presentation held at 2nd International meeting on clays in natural & engineered barriers for radioactive waste confinement, March 14-18, 2005, Tours, France, paper in prep.

KONIETZKY, H.; te KAMP, L.; BLÜMLING, P.; MAJOR, J.-C. (2001) : Micro-mechanical analysis of excavation disturbed zones around tunnels. In: Computer Methods and Advances in Geomechanics, p. 543-546, Balkema, Rotterdam, ISBN 90 5809 183 X

KONIETZKY, H. (2003) : Tonsteine als Endlagerwirtsgestein. 32. Geomechanik Kolloquium Leipzig, November 2003, pp. 42–52.

KONIETZKY, H.; BLÜMLING, P.; te KAMP, L. (2003) : Opalinuston: Felsmechanische Untersuchungen, Unpubl., NAGRA Interner Bericht.

LALOUI, L.; MODARESSI, H. (2002) : Modeling of the thermo-hydro-plastic behavior of clays. In: Hydromechanical and thermohydromechanical behavior of deep argillaceous rock. Hoteit et al. (eds.), Zwets & Zeitlinger, Lisse, ISBN 90 5809 533 9

LI; X.L.; BASTIAENS, W.; BERNIER, F. (2006a) : The hydromechanical behaviour of the Boom Clay observed during excavations of the connecting gallery at Mol site. In: Proceedings of Eurock 2006, Multiphysics coupling and long term behavior in rock mechanics, Liège, Belgium 2006, p.467-472

LI; X.L.; BERNIER, F.; SILLEN, X. (2006b) : Compared short and long-term hydromechanical behaviour of clays around underground research laboratories in the Callovo-Oxfordian argillites and Boom Clay. Presentation held at: Seminary in Geomechanics on modelling of hydromechanical behaviour of the Callovo-Oxfordian argillites observed in the MHM-URL, Université Paris XI – Orsay, 07. June 2006

LOW, P.F. (1979) : Nature and properties of water in montmorillonite-water systems, Soil. Sci. Soc. Am. J. 43, 651-658, Madison, Wisc.

LUX, K.-H.; DÜSTERLOH, U.; WOLTERS, R.; CZAIKOWSKI, O. (2005) : Gebirgsmechanische Beurteilung von Tongesteinsformationen im Hinblick auf die Endlagerung radioaktiver Abfälle, Bericht im Auftrag des BfS, Technische Universität Clausthal, 03/2005,

LUX, K.-H.; CZAIKOWSKI, O. (2006) : Übertragbarkeit von Stoffgesetzen für Steinsalz auf Tonstein. In: Siebtes Statusgespräch zu FuE-Vorhaben auf dem Gebiet der Entsorgung gefährlicher Abfälle in tiefen geologischen Formationen, Forschungszentrum Karlsruhe, Wissenschaftliche Berichte FZKA-PTE Nr. 9, Juli 2006

McKINSTRY, H.A. (1965) : Thermal expansion of clay minerals, The American Mineralogist, Vol. 50, Pennsylvania.

MODARESSI, H.; LALOUI, L. (1997) : A thermo-visco-plastic constitutive model for clays. In: International Journal for numerical and analytical methods in geomechanics, vol: 21, p. 313-335

NAGRA (1988) : Sondierbohrung Weiach, Geologie, Textband und Anlagenband, Nagra Technischer Bericht (NTB) 86-01, Baden, Schweiz.

NAGRA (2001) : Sondierbohrung Benken, Untersuchungsbericht, Nagra Technischer Bericht (NTB) 00-01, Wettingen, Schweiz.

NAGRA (2002) : Projekt Opalinuston - Synthese der geowissenschaftlichen Untersuchungsergebnisse, Nagra Technischer Bericht (NTB) 02-03, Wettingen, Schweiz.

OZANAM, O.; HOTEIT, N.; BEMER, E.; HEITZ, J.-F. (2002) : Experiment determination of poroelastic parameters of a clayey rock. In : Second Biot Conference on Poromechanics, Grenoble, France, August 2002. Zwets & Zeitlinger, Lisse, Netherlands, pp. 275–280

PELLET, F.; HAJDU, A.; DELERUYELLE, F. & BESNUS, F. (2005) : A viscoplastic constitutive model including anisotropic damage for the time dependent mechanical behavior of rock, International Journal for Numerical and Analytical Methods in Geomechanics, vol : 29 n. 9, pp 941–970.

POLSTER, M.; JOBMANN, M. (2006) : Back analysis of deformation and pore pressure development due to shaft sinking based on 2D and full 3D modelling. presentation held at: Seminary in Geomechanics on modelling of hydromechanical behaviour of the Callovo-Oxfordian argillites observed in the MHM-URL, Université Paris XI – Orsay, 07. June 2006

SCHUSTER, K.; ALHEID, H.-J.; BÖDDENER, D. (2001) : Seismic investigation of the excavation damaged zone in Opalinus Clay. Engineering Geology 61.

SU, K. (2006a) : Development and Validation of Hydromechanical Constitutive Models for Callovo-Oxfordian Argillites : the MODEX-REP Project - Synthesis Part 3; European Commission – MODEX-REP project: contract FIKW-CT-2000-00029

SU, K. (2006b) : MODEX REP project: results and lessons learnt & perspectives. Presentation held at: Seminary in Geomechanics on modelling of hydromechanical behaviour of the Callovo-Oxfordian argillites observed in the MHM-URL, Université Paris XI – Orsay, 07. June 2006

te KAMP, L.; KONIETZKY, H.; BLÜMLING, P.; ANDO, K.; MAJOR, J.-C. (1999) : Micromechanical back-analysis of laboratory tests on rock. In: Numerical Models in Geomechanics – NUMOG VII, p. 411-416, Balkema, Rotterdam, ISBN 90 5809 095 7

te KAMP, L.; KONIETZKY, H.; BLÜMLING, P. (2003) : Conceptual modeling of Opalinus Clay with FLAC and PFC. In: Numerical Modeling in Micromechanics via Particle methods, p. 315-320, Zwets & Zeitlinger, Lisse, ISBN 90 5809 532 0

THURY M. & BOSSART, P. (1999) : The Mont Terri rock laboratory, a new international research project in a Mesozoic shale formation, in Switzerland, Engineering Geology 52, pp 347-359.

VIETOR, T.; BLÜMLING, P.; ARMAND, G. (2006) : Failure mechanisms of the Opalinus Clay around underground excavations. In: Proceedings of Eurock 2006, Multiphysics coupling and long term behavior in rock mechanics, Liège, Belgium 2006, p. 479-484

WILEVEAU, Y. & SU, K. (2006) : TER experiment – installation, first measurements and further interpretation. presentation 2nd technical meeting on TER experiment, 15th of Feb. 2006, Chatenay-Malabry

ZHANG, C.-L.; DITTRICH, J.; MÜLLER, J.; ROTHFUCHS, T. (2002) : Experimental Study of the Hydromechanical Behavior of the Callovo-Oxfordian Argillites, Part of the MODEX-REP Project. GRS – 187.

ZHANG, C.-L.; ROTHFUCHS, T.; MOOG, H.; DITTRICH, J. & MÜLLER, J. (2004a) : Thermo-Hydro-Mechanical and Geochemical behavior of the Callovo-Oxfordian Argillite and the Opalinus Clay. Final Report, GRS – 202

ZHANG, C.-L.; ROTHFUCHS, T.; JOCKWER, N.; KRÖHN, K.-P. ; MIEHE, R.; MOOG, H. (2004b) : Results of Laboratory Investigations on Clays. DisTec2004 International Conference on Waste Disposal, April 26-28, Berlin.

8 APPENDIX INDEX

HE-D EXPERIMENT / URL MONT TERRI

REP EXPERIMENT / URL BURE

Appendix H Sensor locations

Appendix I Measurement results

Appendix J Modeling assumptions

Appendix K Comparison of 2D and 3D-modeling

Appendix L **Stress field after excavation cycle 184**

Appendix L-1 Stress field for cross section along initial principal stress planes; view from NNE (convention: compressive stresses are negative)

Appendix L-2 von Mises stress [Pa], horizontal cross section at –455 m

Appendix L-3 Minimum principle stress σ_3 [Pa], horizontal cross section at –455 m

Appendix L-4 Maximum principle stress σ_1 [Pa], horizontal cross section at –455 m

Appendix M **Blind prediction results**

Appendix M-1 Interval deformation for extensometer REP 2202 DFO07 – DFO06
Comparison between measurement results and blind prediction results of various modeling teams (shaft far-field*, SU 2006b*)

Appendix M-2 Interval deformation for extensometer REP 2202 DFO10 – DFO09
Comparison between measurement results and blind prediction results of various modeling teams (shaft near-field*, SU 2006b*)

Appendix M-3 Shaft convergences, section SMGR2, -467,5 m ; Direction NE 150°
Comparison between measurement results and blind prediction results of various modeling teams (*SU 2006b*)

Appendix M-4 Pore pressure at REP2101_Pre_05
Comparison between measurement results and blind prediction results of various modeling teams (*SU 2006b*)

Sensor	borehole distance	distance to heater axis
Temperature sensors, borehole BHE-D06		
TM01	0.0 m (-0.38 m [*1])	7.74 m (8.12 m [*1])
TM02	1.30 m	6.44 m
TM03	2.54 m (2.42 m [*1])	5.20 m (5.32 m [*1])
TM04	3.5 m (3.37 m [*1])	4.24 m (4.37 m [*1])
TM05	4.57 m	3.17 m
TM06	5.62 m	2.12 m
TM07	6.75 m	0.99 m
Displacement sensors, borehole BHE-D06		
DP01	2.54 m	5.20 m
DP02	3.50 m	4.24 m
DP03	5.50 m	2.24 m
DP04	6.50 m	1.24 m
DP05	7.0 m	0.74 m

[*1] Values in brackets = in-situ values; differing from numerical model

Appendix A-1 Locations of temperature and displacement sensors in BHE-D06

Sensor	Location of sensor (corresponding to coordinate system of ANDRA)			
	x in-situ / model	y in-situ / model	z in-situ / model	distance to heater axis in-situ / model
BHE-D07	-7.13 / -7.22	9.02 / 9.06	0.04 / 0.00	7.13 / 7.22
BHE-D08	-1.06 / 1.25	8.00 / 7.94	0.70 / 0.68	1.27 / 1.42
BHE-D09	0.07 / 0.00	8.50 / 8.41	0.85 / 0.88	0.85 / 0.88
BHE-D10	0.77 / -0.39	8.99 / 9.11	1.01/ 1.04	1.27 / 1.11
BHE-D11	2.71 / -2.64	7.99 / 7.96	1.17 / 1.25	2.95 / 2.92
BHE-D12	-5.29 / 5.68	11.27 / 11.02	-0.09 / 0.00	5.29 / 5.68
BHE-D13	-3.29 / 3.72	11.26 / 11.02	0.58 / -0.42	3.34 / 3.74
BHE-D14	-0.40 / 0.59	12.26 / 11.59	-0.67 / -0.83	0.78 / 1.02
BHE-D15	0.42 / -0.34	11.75 / 11.30	-0.86 / -0.91	0.96 / 0.97
BHE-D16	0.90 / -0.50	11.25 / 11.02	-1.10 / -1.25	1.42 / 1.35
BHE-D17	2.67 / -2.16	12.24 / 11.68	-1.30 / -1.50	2.97 / 2.63
BHE-D01TEM1	0.69 / 0.56	14.11 / 14.00	0.36 / 0.23	0.78 / 0.61
BHE-D01TEM2	0.68 / 0.71	12.61/ 12.57	0.43 / 0.40	0.80 / 0.81
BHE-D01TEM3	0.66 / 0.60	11.12/ 11.20	0.50 / 0.55	0.83 / 0.81
BHE-D01TEM4	0.65 / 0.63	9.62 / 9.53	0.58 / 0.58	0.87 / 0.86
BHE-D01TEM5	0.64 / 0.68	8.12 / 8.17	0.65 / 0.61	0.91 / 0.91
BHE-D01TEM6	0.63 / 0.66	6.62 / 6.71	0.72 / 0.91	0.96 / 1.12
BHE-D02TEM1	-0.75 / -0.94	13.28 / 13.50	-2.36 / -2,40	2.48 / 2.58
BHE-D02TEM2	-0.73 / -0.97	11.83 / 11.67	-1.97 / -1.90	2.10 / 2.13
BHE-D02TEM3	-0.72 / -0.50	10.39 / 10.37	-1.58 / -1.50	1.74 / 1.58
BHE-D02TEM4	-0.71 / -0.79	8.45 / 8.41	-1.06 / -1.00	1.28 / 1.27
BHE-D02TEM5	-0.70 / -0.66	7.49 / 7.38	-0.81 / -0.85	1.07 / 1.08
BHE-D03	0.85 / 0.65	8.87 / 8.73	-0.72 / -0.57	1.11 / 0.86

Appendix A-2 Locations of temperature and pore pressure sensors in BHE-D01 – D3 and D07-D17

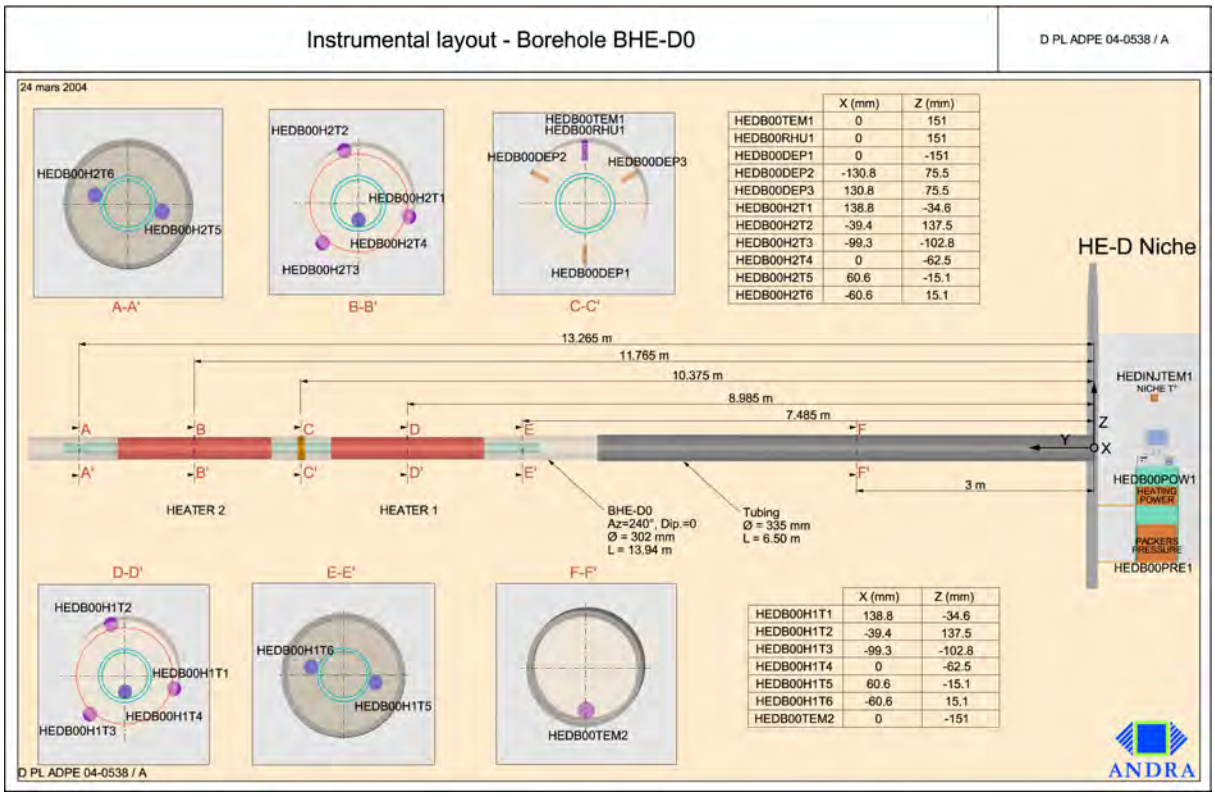

	X (mm)	Z (mm)
HEDB00TEM1	0	151
HEDB00RHU1	0	151
HEDB00DEP1	0	-151
HEDB00DEP2	-130.8	75.5
HEDB00DEP3	130.8	75.5
HEDB00H2T1	138.8	-34.6
HEDB00H2T2	-39.4	137.5
HEDB00H2T3	-99.3	-102.8
HEDB00H2T4	0	-62.5
HEDB00H2T5	60.6	-15.1
HEDB00H2T6	-60.6	15.1

	X (mm)	Z (mm)
HEDB00H1T1	138.8	-34.6
HEDB00H1T2	-39.4	137.5
HEDB00H1T3	-99.3	-102.8
HEDB00H1T4	0	-62.5
HEDB00H1T5	60.6	-15.1
HEDB00H1T6	-60.6	15.1
HEDB00TEM2	0	-151

Appendix A-3 Instrumental layout of borehole BHE-D00 (source: ANDRA)

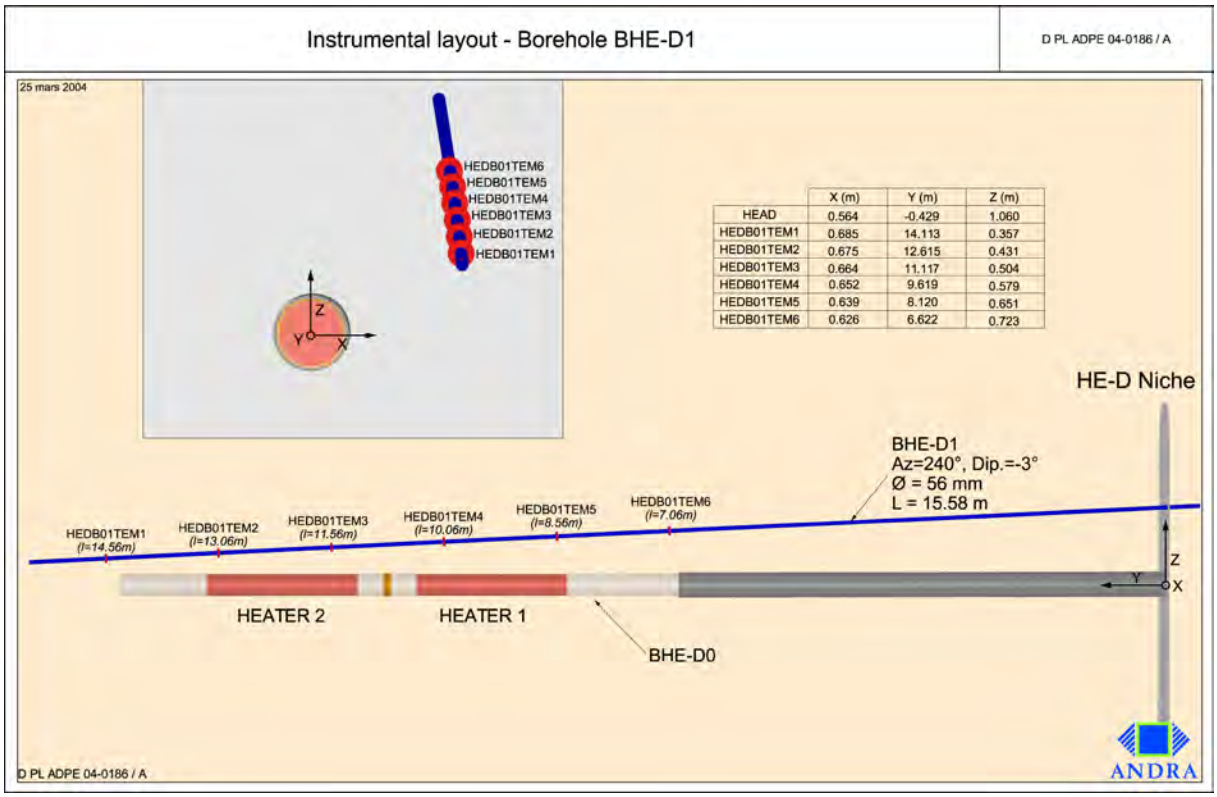

	X (m)	Y (m)	Z (m)
HEAD	0.564	-0.429	1.060
HEDB01TEM1	0.685	14.113	0.357
HEDB01TEM2	0.675	12.615	0.431
HEDB01TEM3	0.664	11.117	0.504
HEDB01TEM4	0.652	9.619	0.579
HEDB01TEM5	0.639	8.120	0.651
HEDB01TEM6	0.626	6.622	0.723

Appendix A-4 Instrumental layout of borehole BHE-D01 (source: ANDRA)

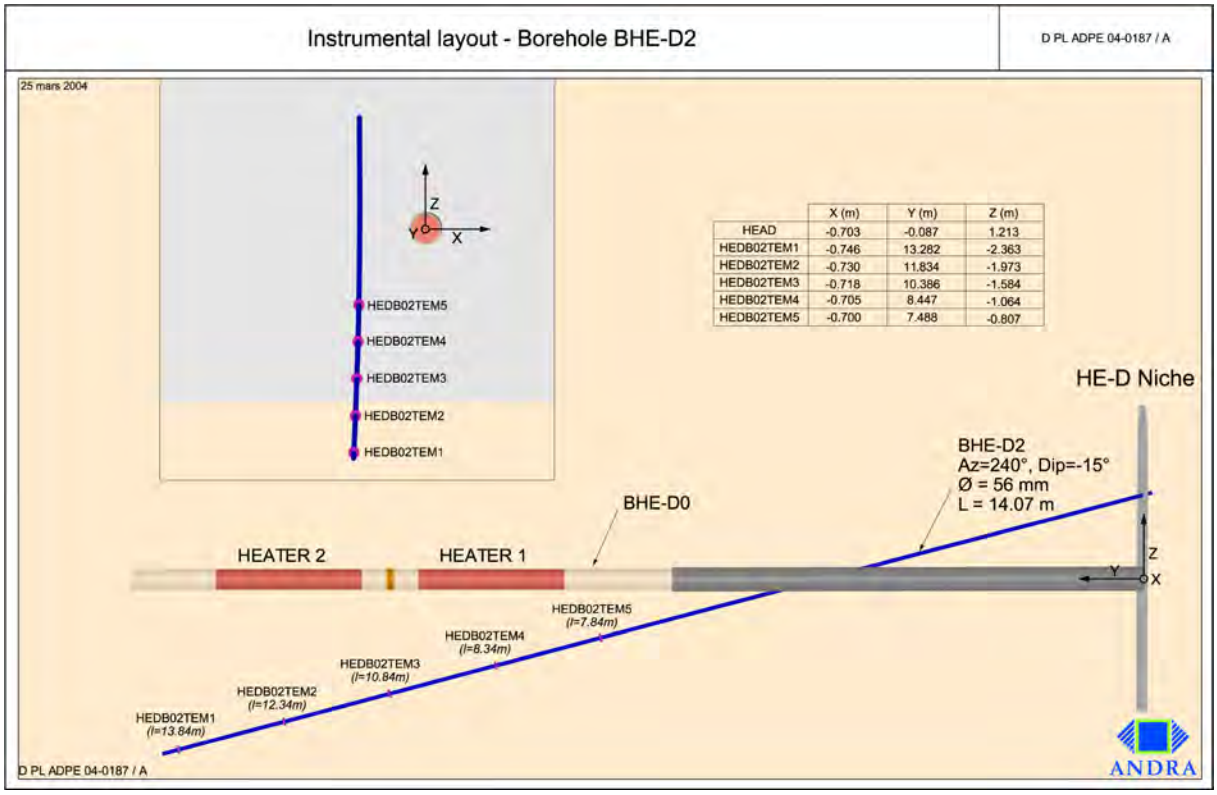

	X (m)	Y (m)	Z (m)
HEAD	-0.703	-0.087	1.213
HEDB02TEM1	-0.746	13.282	-2.363
HEDB02TEM2	-0.730	11.834	-1.973
HEDB02TEM3	-0.718	10.386	-1.584
HEDB02TEM4	-0.705	8.447	-1.064
HEDB02TEM5	-0.700	7.488	-0.807

Appendix A-5 Instrumental layout of borehole BHE-D02 (source: ANDRA)

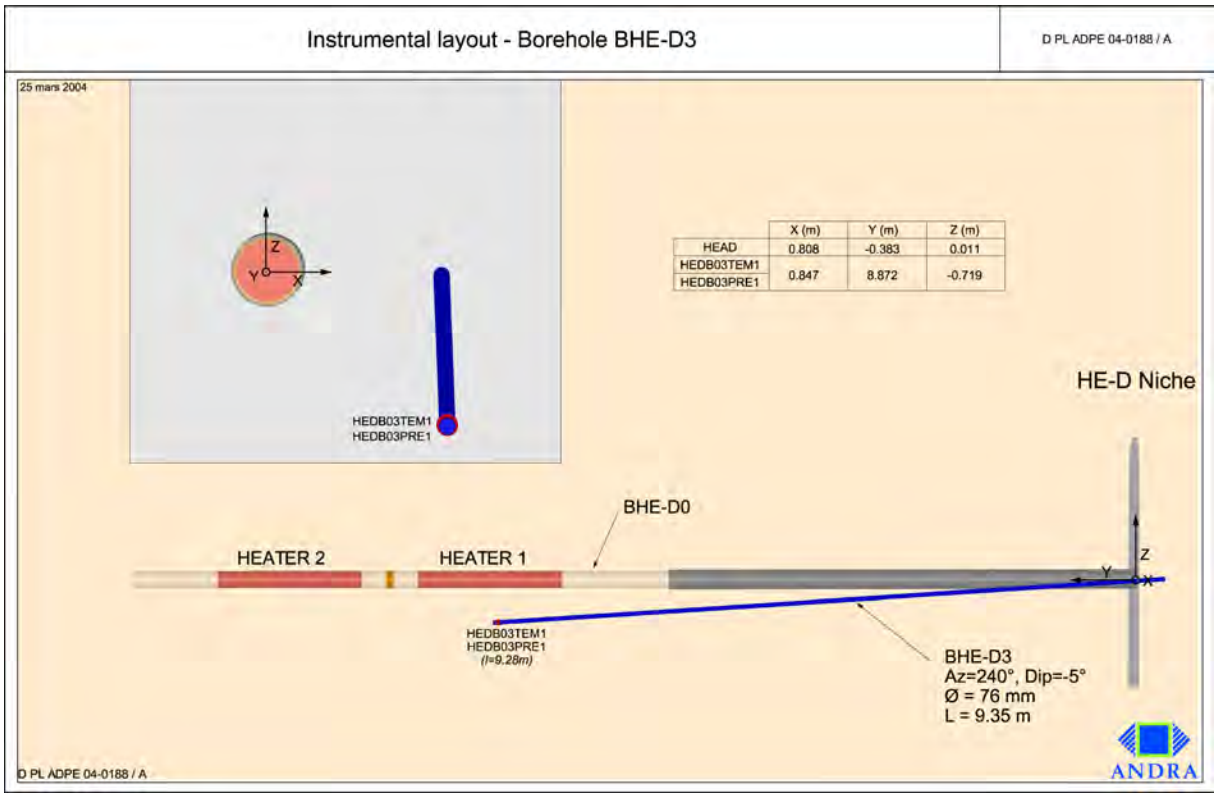

	X (m)	Y (m)	Z (m)
HEAD	0.808	-0.383	0.011
HEDB03TEM1	0.847	8.872	-0.719
HEDB03PRE1			

Appendix A-6 Instrumental layout of borehole BHE-D03 (source: ANDRA)

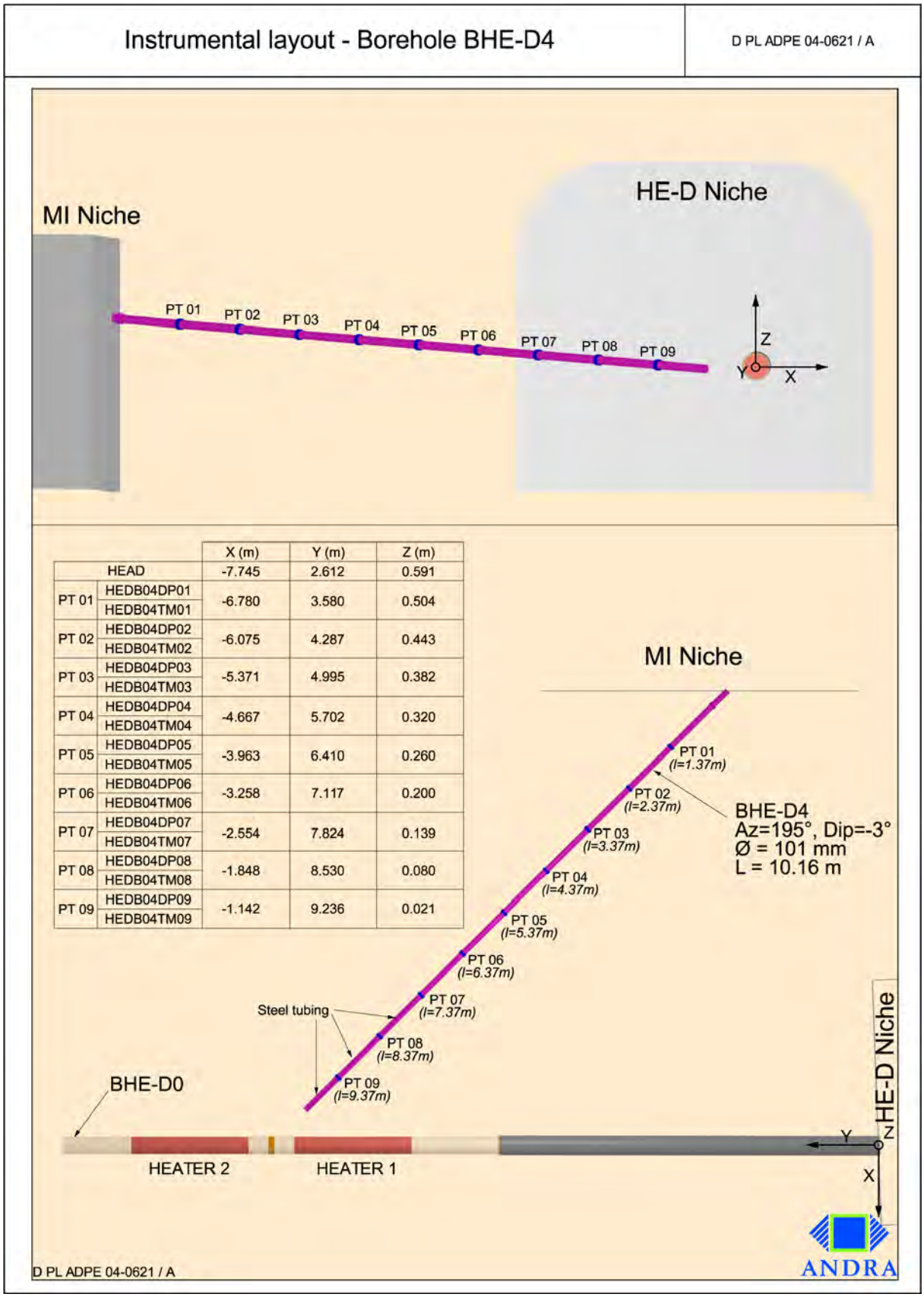

		X (m)	Y (m)	Z (m)
HEAD		-7.745	2.612	0.591
PT 01	HEDB04DP01	-6.780	3.580	0.504
	HEDB04TM01			
PT 02	HEDB04DP02	-6.075	4.287	0.443
	HEDB04TM02			
PT 03	HEDB04DP03	-5.371	4.995	0.382
	HEDB04TM03			
PT 04	HEDB04DP04	-4.667	5.702	0.320
	HEDB04TM04			
PT 05	HEDB04DP05	-3.963	6.410	0.260
	HEDB04TM05			
PT 06	HEDB04DP06	-3.258	7.117	0.200
	HEDB04TM06			
PT 07	HEDB04DP07	-2.554	7.824	0.139
	HEDB04TM07			
PT 08	HEDB04DP08	-1.848	8.530	0.080
	HEDB04TM08			
PT 09	HEDB04DP09	-1.142	9.236	0.021
	HEDB04TM09			

Appendix A-7 Instrumental layout of borehole BHE-D04 (source: ANDRA)

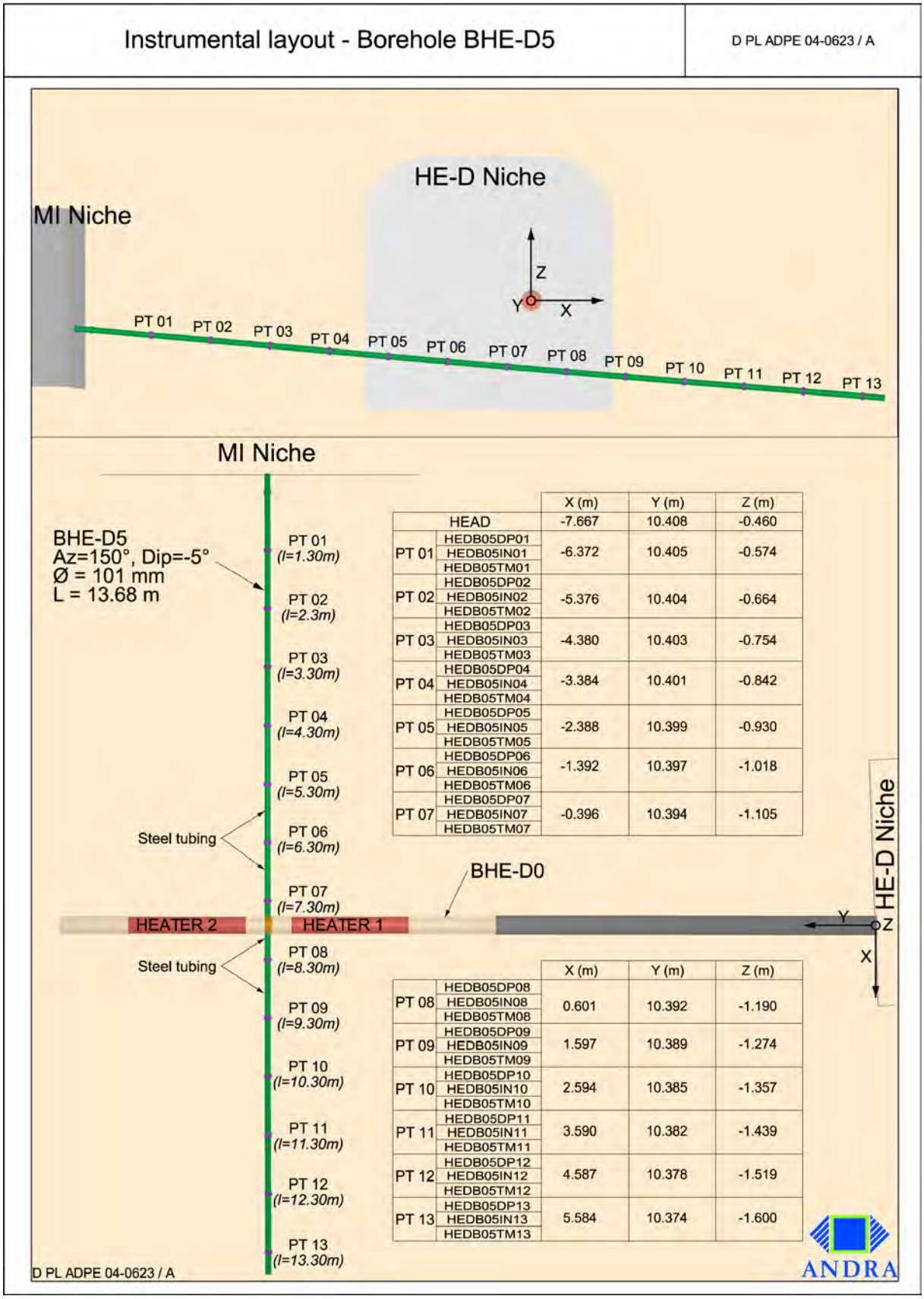

		X (m)	Y (m)	Z (m)
HEAD		-7.667	10.408	-0.460
PT 01	HEDB05DP01	-6.372	10.405	-0.574
	HEDB05IN01			
	HEDB05TM01			
PT 02	HEDB05DP02	-5.376	10.404	-0.664
	HEDB05IN02			
	HEDB05TM02			
PT 03	HEDB05DP03	-4.380	10.403	-0.754
	HEDB05IN03			
	HEDB05TM03			
PT 04	HEDB05DP04	-3.384	10.401	-0.842
	HEDB05IN04			
	HEDB05TM04			
PT 05	HEDB05DP05	-2.388	10.399	-0.930
	HEDB05IN05			
	HEDB05TM05			
PT 06	HEDB05DP06	-1.392	10.397	-1.018
	HEDB05IN06			
	HEDB05TM06			
PT 07	HEDB05DP07	-0.396	10.394	-1.105
	HEDB05IN07			
	HEDB05TM07			

		X (m)	Y (m)	Z (m)
PT 08	HEDB05DP08	0.601	10.392	-1.190
	HEDB05IN08			
	HEDB05TM08			
PT 09	HEDB05DP09	1.597	10.389	-1.274
	HEDB05IN09			
	HEDB05TM09			
PT 10	HEDB05DP10	2.594	10.385	-1.357
	HEDB05IN10			
	HEDB05TM10			
PT 11	HEDB05DP11	3.590	10.382	-1.439
	HEDB05IN11			
	HEDB05TM11			
PT 12	HEDB05DP12	4.587	10.378	-1.519
	HEDB05IN12			
	HEDB05TM12			
PT 13	HEDB05DP13	5.584	10.374	-1.600
	HEDB05IN13			
	HEDB05TM13			

Appendix A-8 Instrumental layout of borehole BHE-D05 (source: ANDRA)

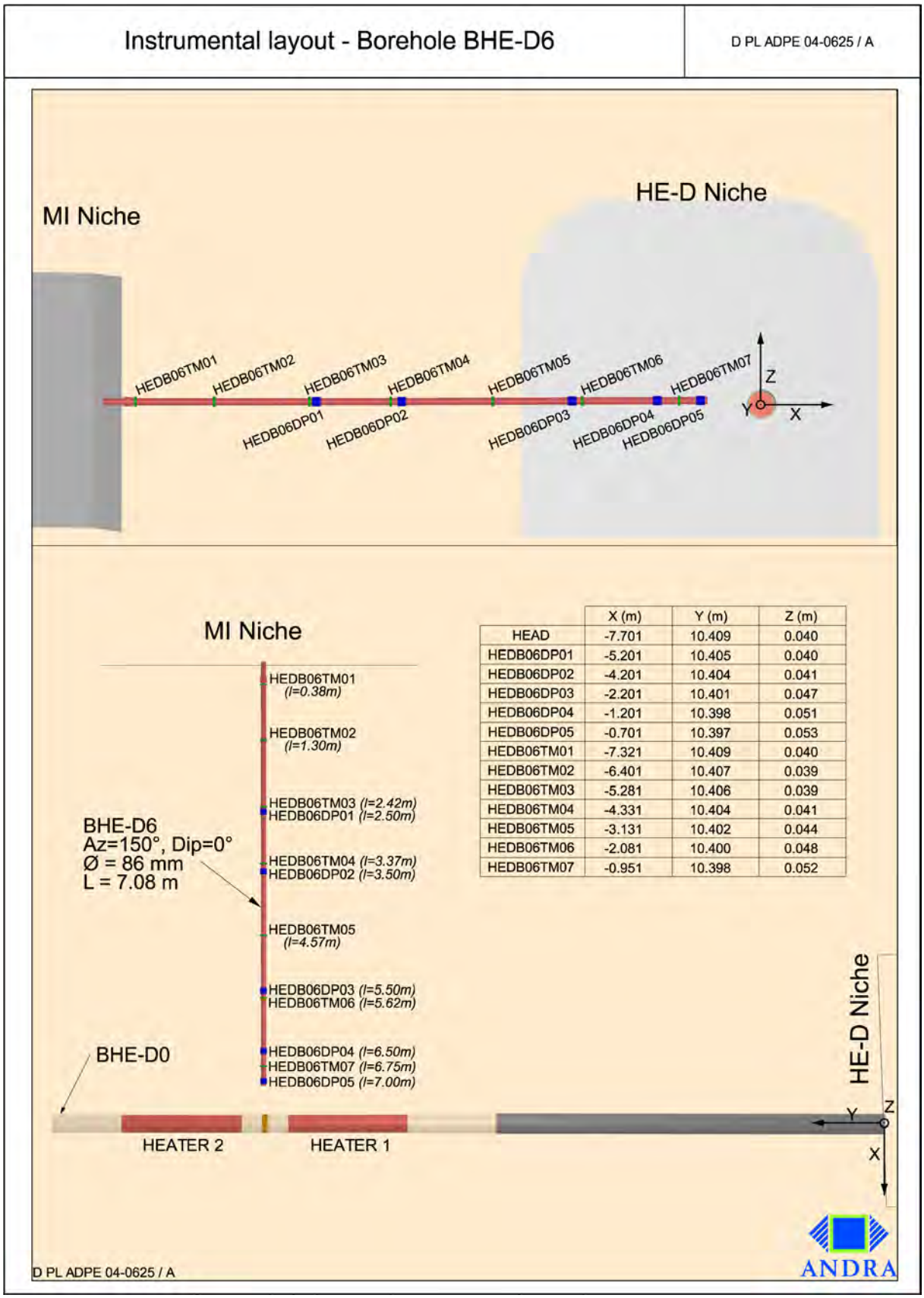

	X (m)	Y (m)	Z (m)
HEAD	-7.701	10.409	0.040
HEDB06DP01	-5.201	10.405	0.040
HEDB06DP02	-4.201	10.404	0.041
HEDB06DP03	-2.201	10.401	0.047
HEDB06DP04	-1.201	10.398	0.051
HEDB06DP05	-0.701	10.397	0.053
HEDB06TM01	-7.321	10.409	0.040
HEDB06TM02	-6.401	10.407	0.039
HEDB06TM03	-5.281	10.406	0.039
HEDB06TM04	-4.331	10.404	0.041
HEDB06TM05	-3.131	10.402	0.044
HEDB06TM06	-2.081	10.400	0.048
HEDB06TM07	-0.951	10.398	0.052

Appendix A-9 Instrumental layout of borehole BHE-D06 (source: ANDRA)

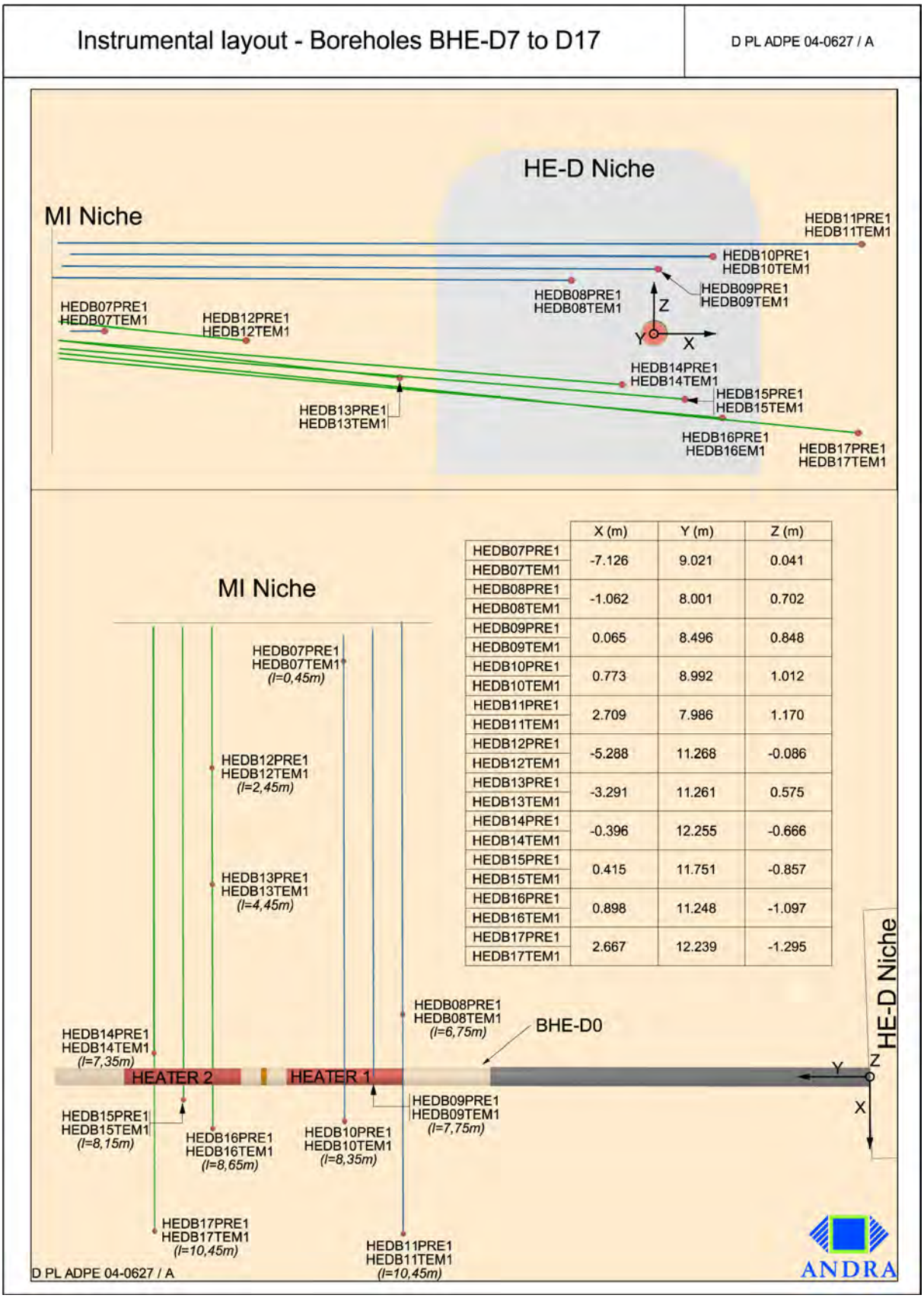

	X (m)	Y (m)	Z (m)
HEDB07PRE1 HEDB07TEM1	-7.126	9.021	0.041
HEDB08PRE1 HEDB08TEM1	-1.062	8.001	0.702
HEDB09PRE1 HEDB09TEM1	0.065	8.496	0.848
HEDB10PRE1 HEDB10TEM1	0.773	8.992	1.012
HEDB11PRE1 HEDB11TEM1	2.709	7.986	1.170
HEDB12PRE1 HEDB12TEM1	-5.288	11.268	-0.086
HEDB13PRE1 HEDB13TEM1	-3.291	11.261	0.575
HEDB14PRE1 HEDB14TEM1	-0.396	12.255	-0.666
HEDB15PRE1 HEDB15TEM1	0.415	11.751	-0.857
HEDB16PRE1 HEDB16TEM1	0.898	11.248	-1.097
HEDB17PRE1 HEDB17TEM1	2.667	12.239	-1.295

Appendix A-10 Instrumental layout of boreholes BHE-D07 to D17 (source: ANDRA)

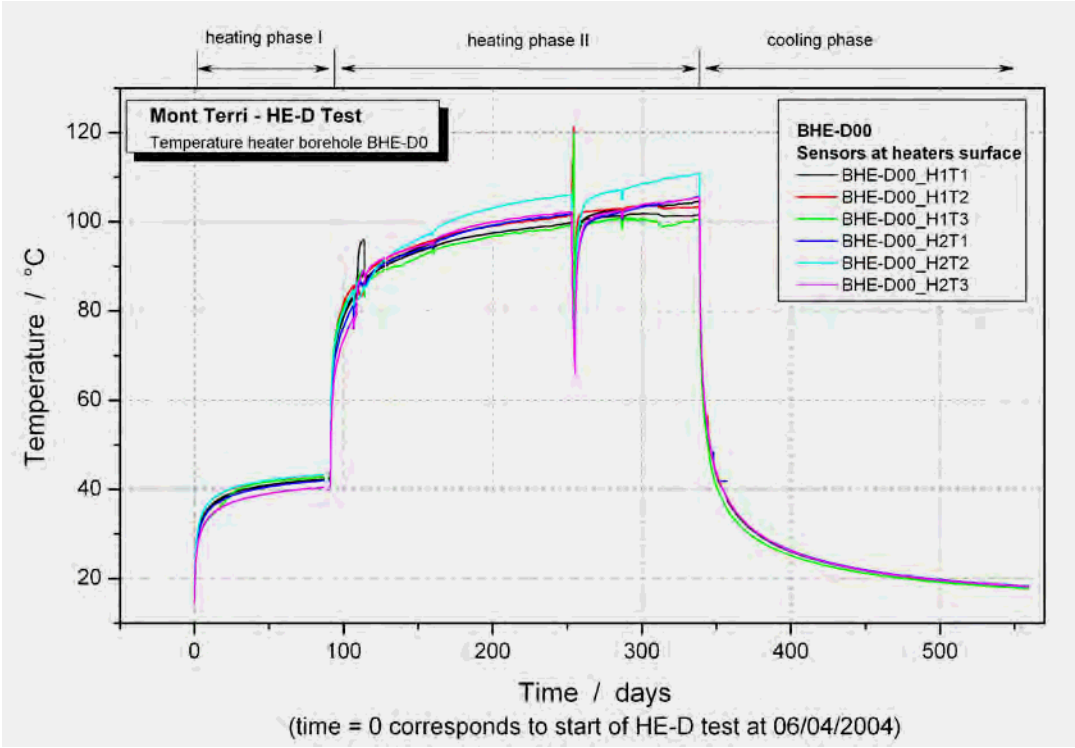

Appendix B-1 Temperature measurement in borehole BHE-D00

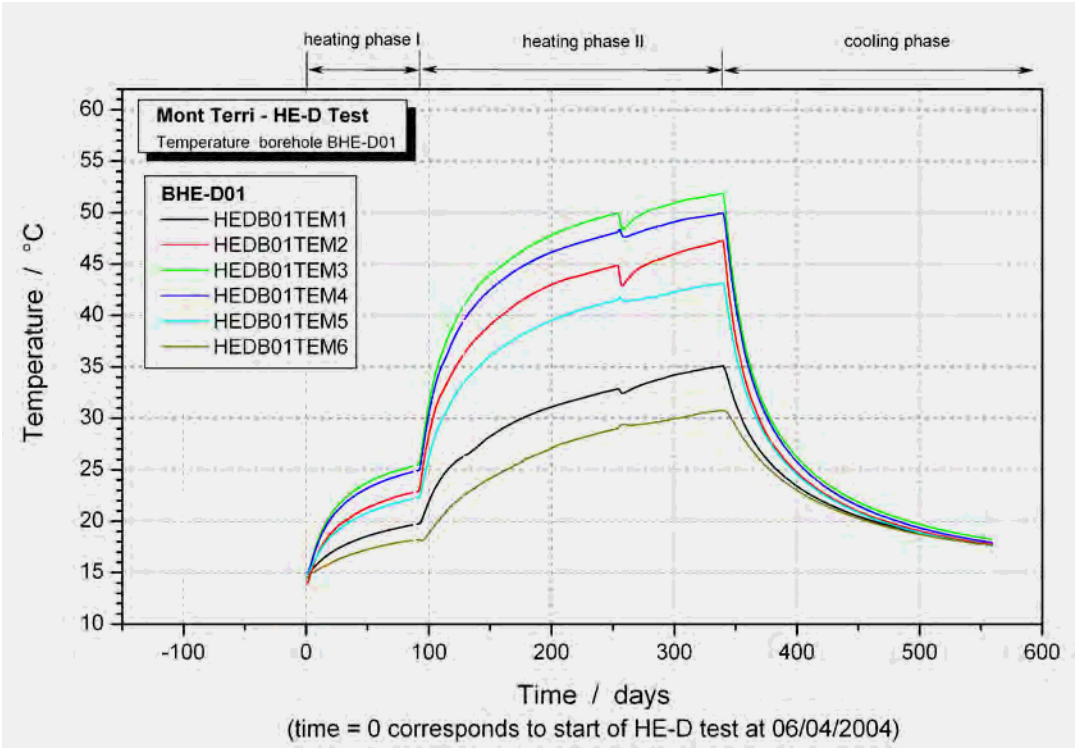

Appendix B-2 Temperature measurement in borehole BHE-D01

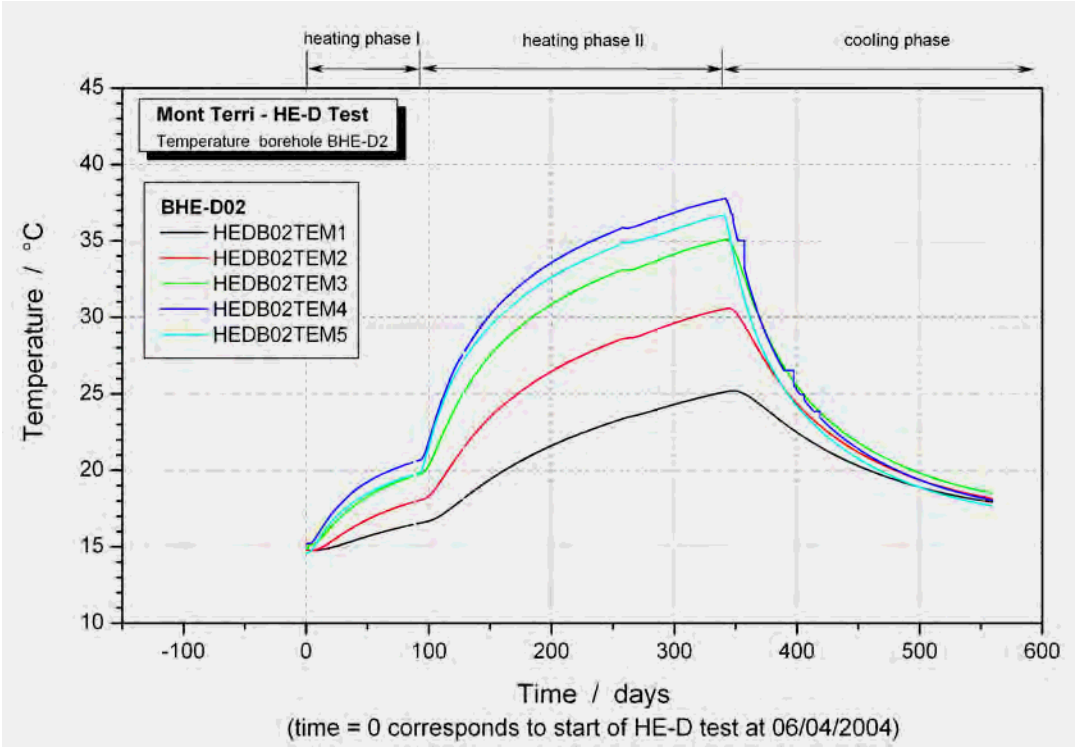

Appendix B-3 Temperature measurement in borehole BHE-D02

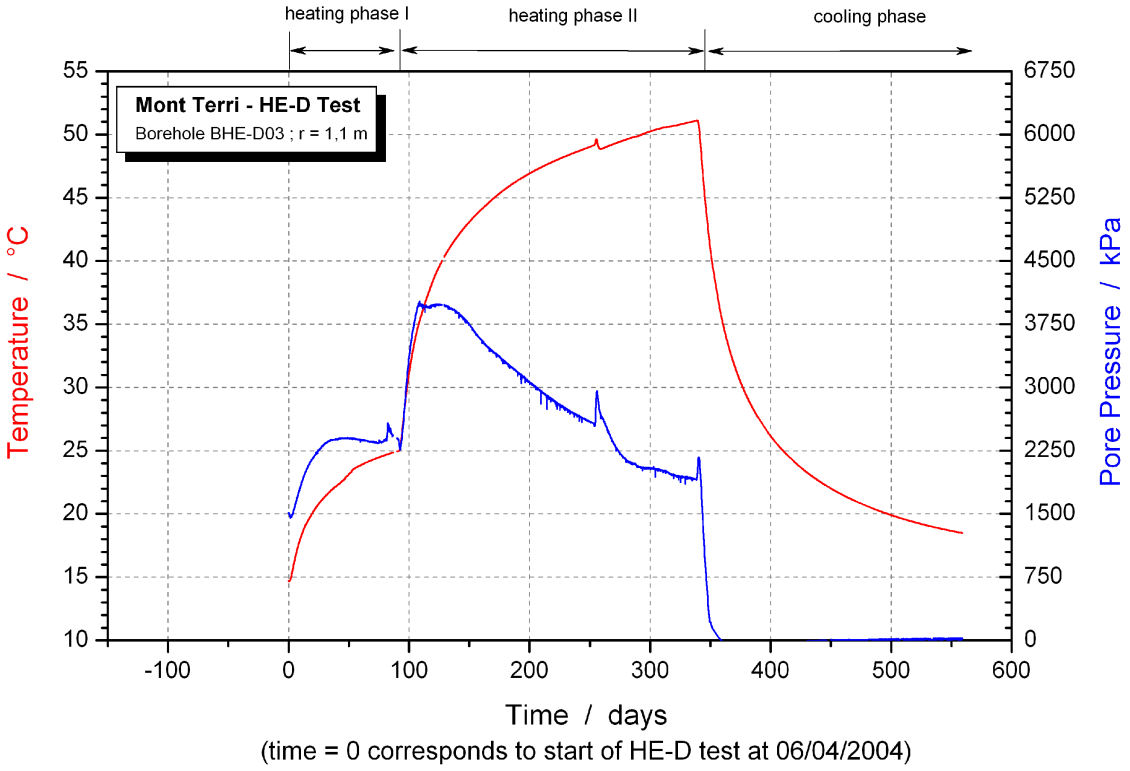

Appendix B-4 Temperature and pore pressure measurement in borehole BHE-D03

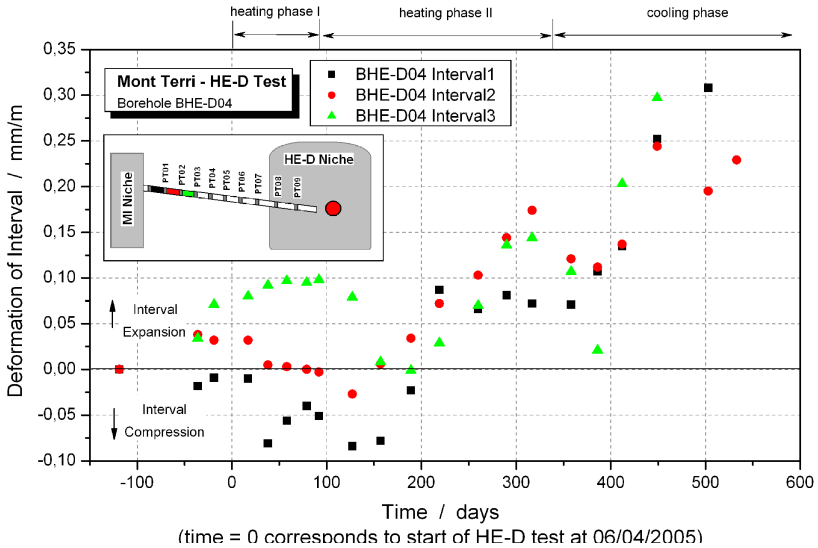

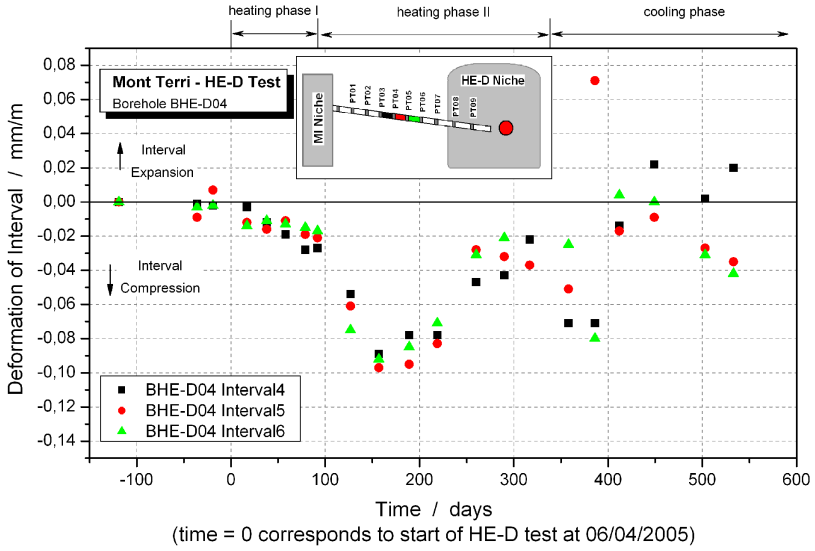

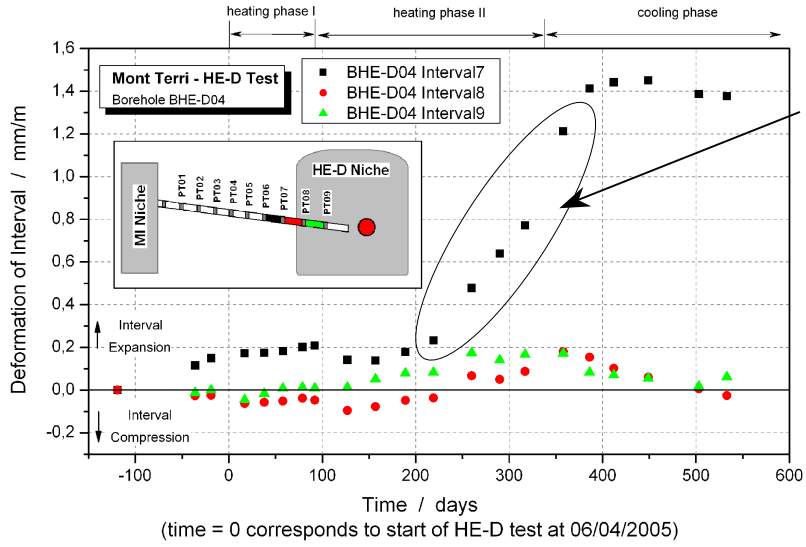

Interval-elongation in approx. 2–3 m distance to the heater (caused by shear-movement on joints due to thermal load and/or excavation work of Gallery04 ?)

Appendix B-5 Interval deformation of extensometer borehole BHE-D04

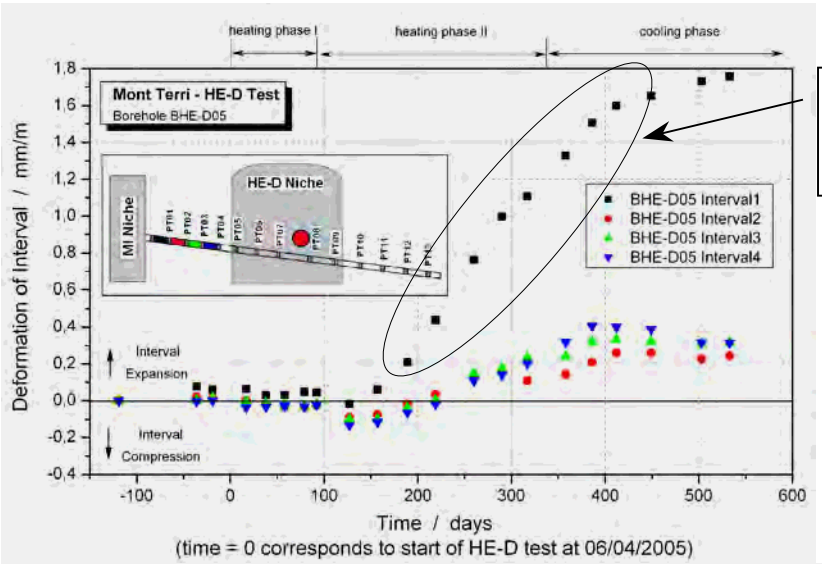

Convergence of MI-niche drift wall (caused by opening of joints in EDZ?)

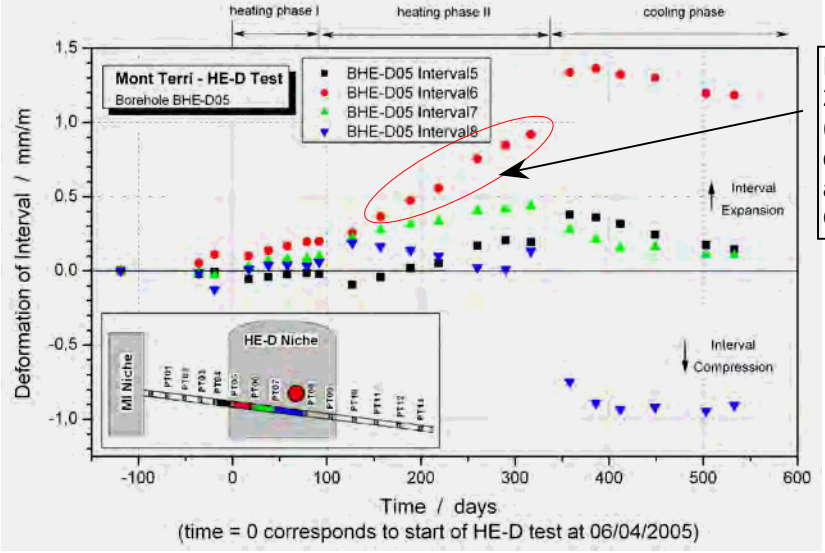

Interval-elongation in approx. 2–3 m distance to the heater (caused by shear-movement on joints due to thermal load and/or excavation work of Gallery04 ?)

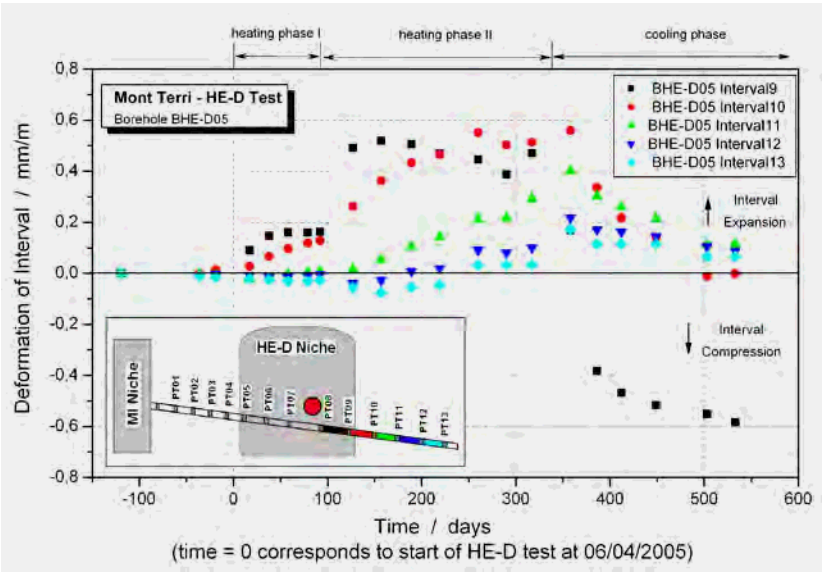

Appendix B-6 Interval deformation of extensometer borehole BHE-D05 (source: ANDRA)

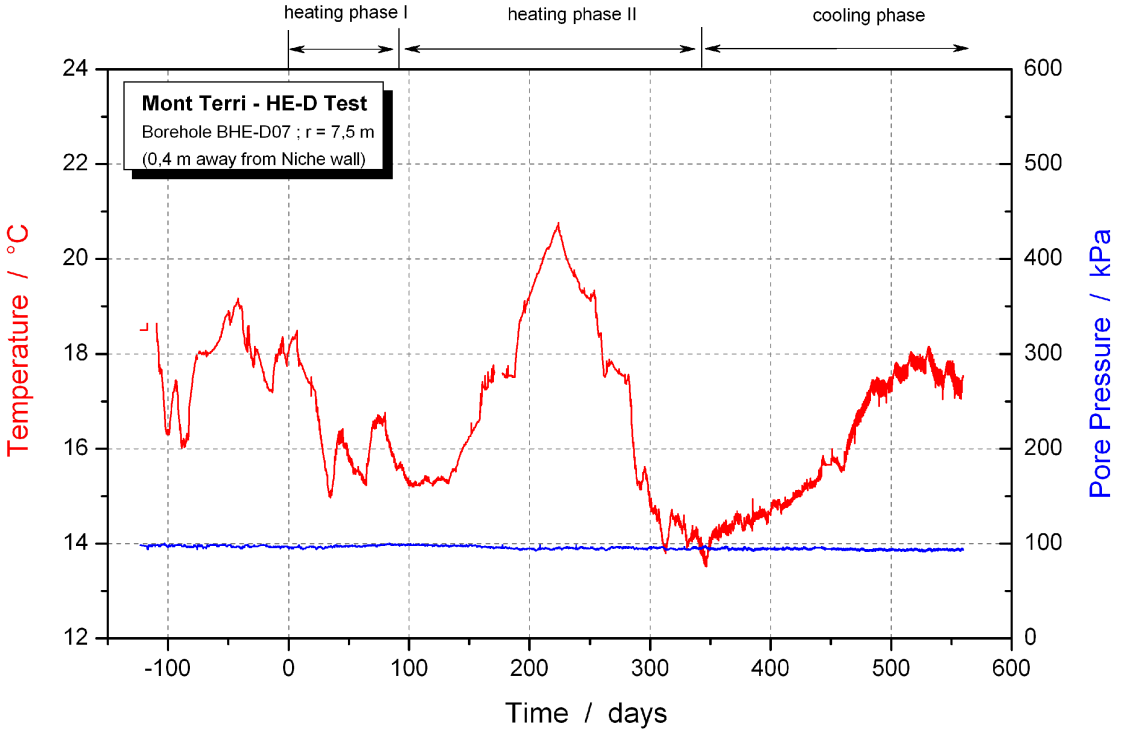

(time = 0 corresponds to start of HE-D test at 06/04/2004)

Appendix B-7 Temperature and pore pressure measurement in borehole BHE-D07

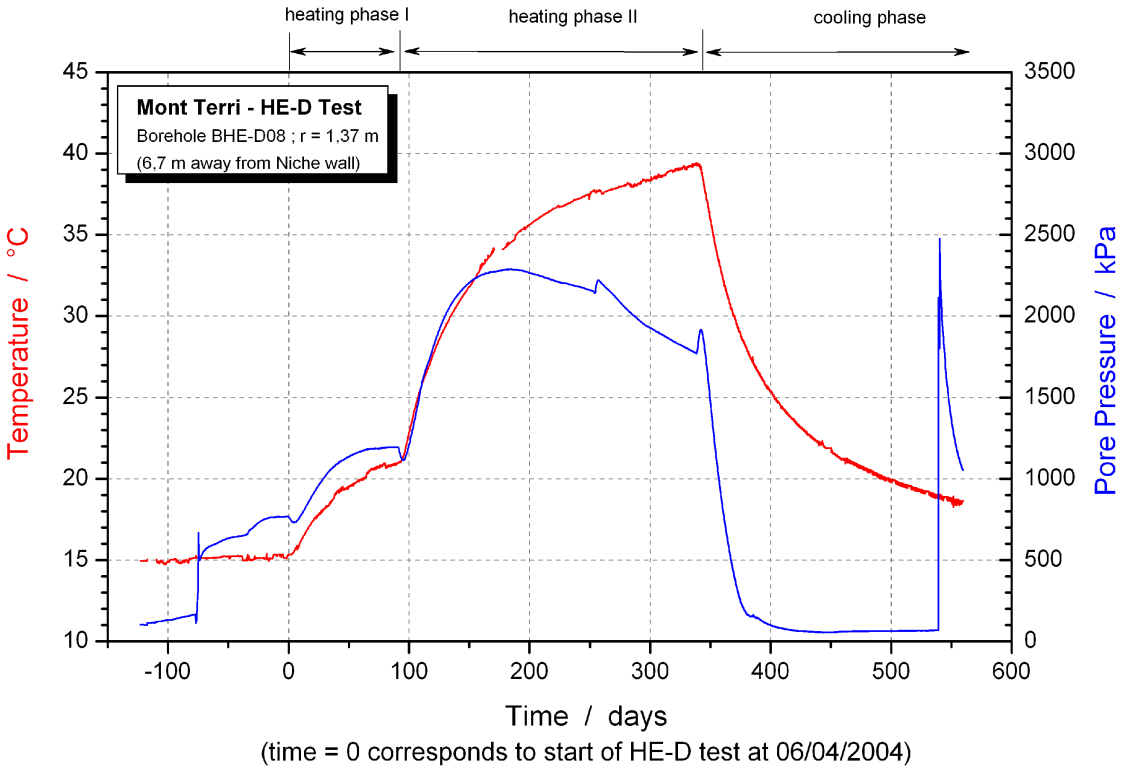

(time = 0 corresponds to start of HE-D test at 06/04/2004)

Appendix B-8 Temperature and pore pressure measurement in borehole BHE-D08

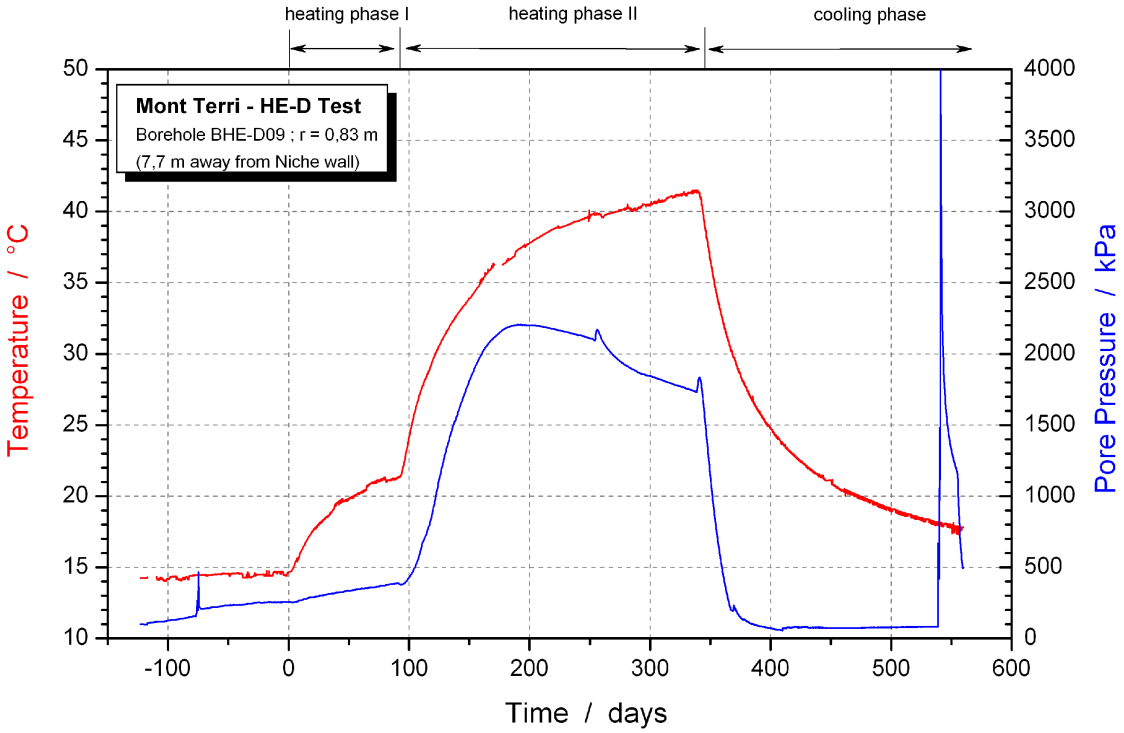

(time = 0 corresponds to start of HE-D test at 06/04/2004)

Appendix B-9 Temperature and pore pressure measurement in borehole BHE-D09

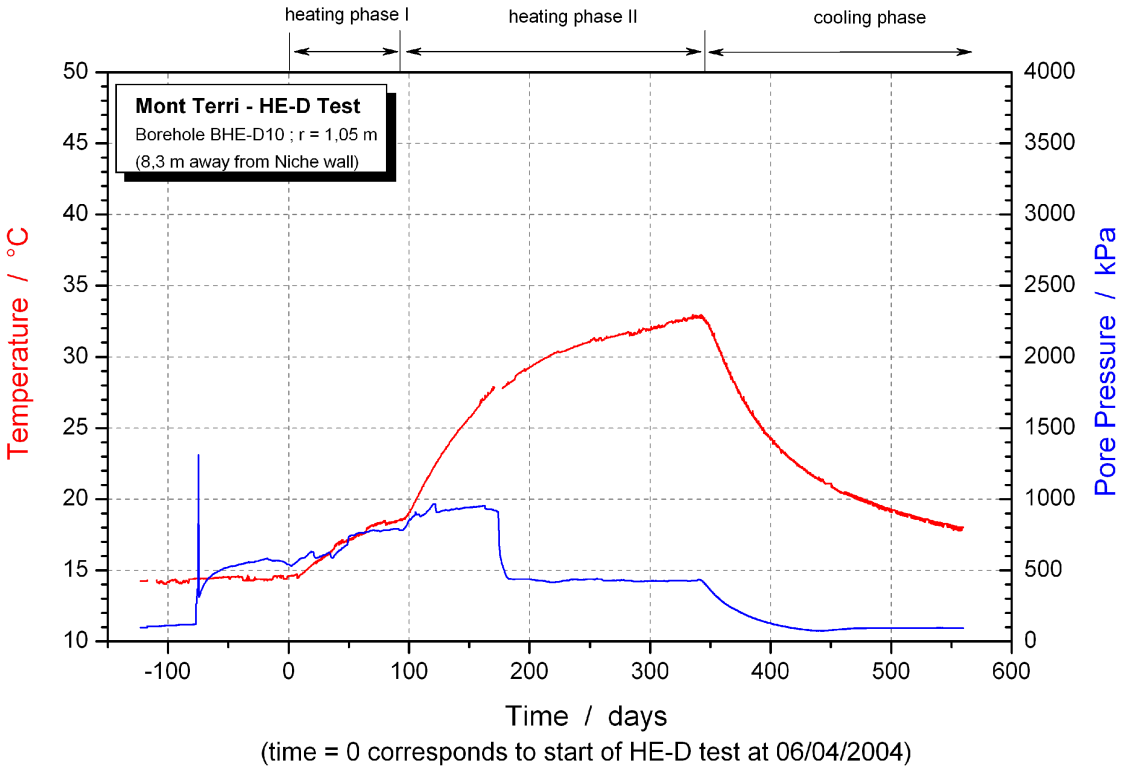

(time = 0 corresponds to start of HE-D test at 06/04/2004)

Appendix B-10 Temperature and pore pressure measurement in borehole BHE-D10

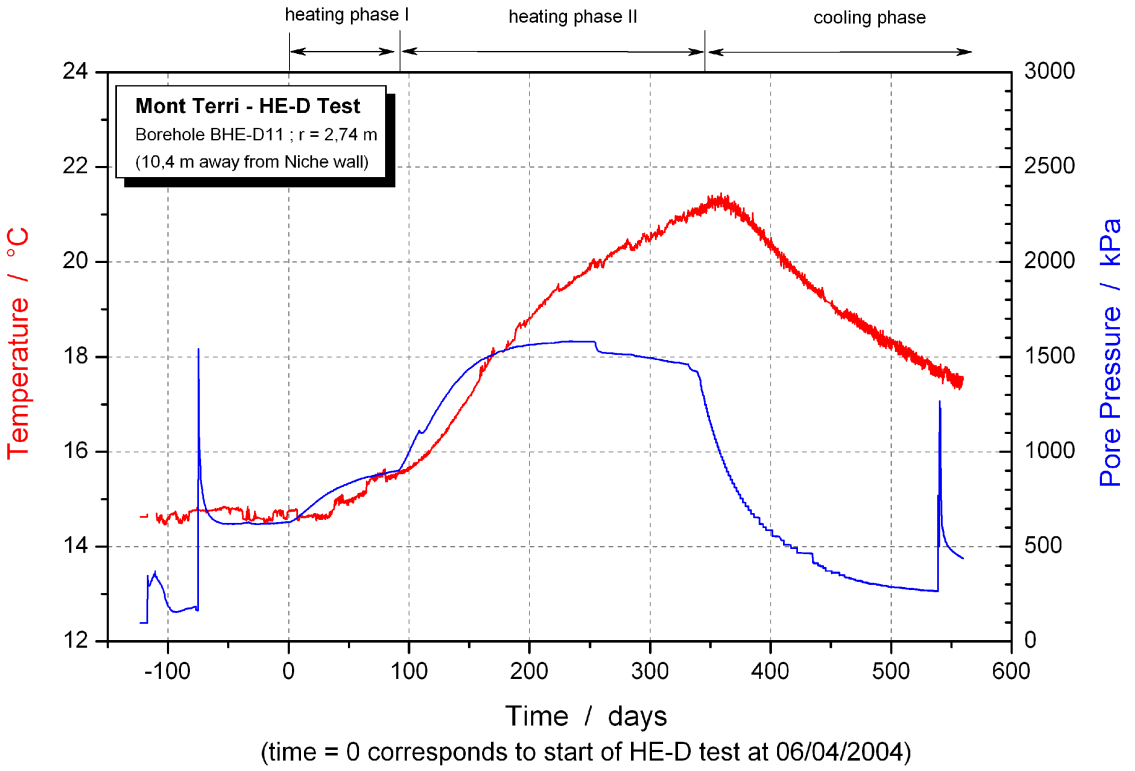

(time = 0 corresponds to start of HE-D test at 06/04/2004)

Appendix B-11 Temperature and pore pressure measurement in borehole BHE-D11

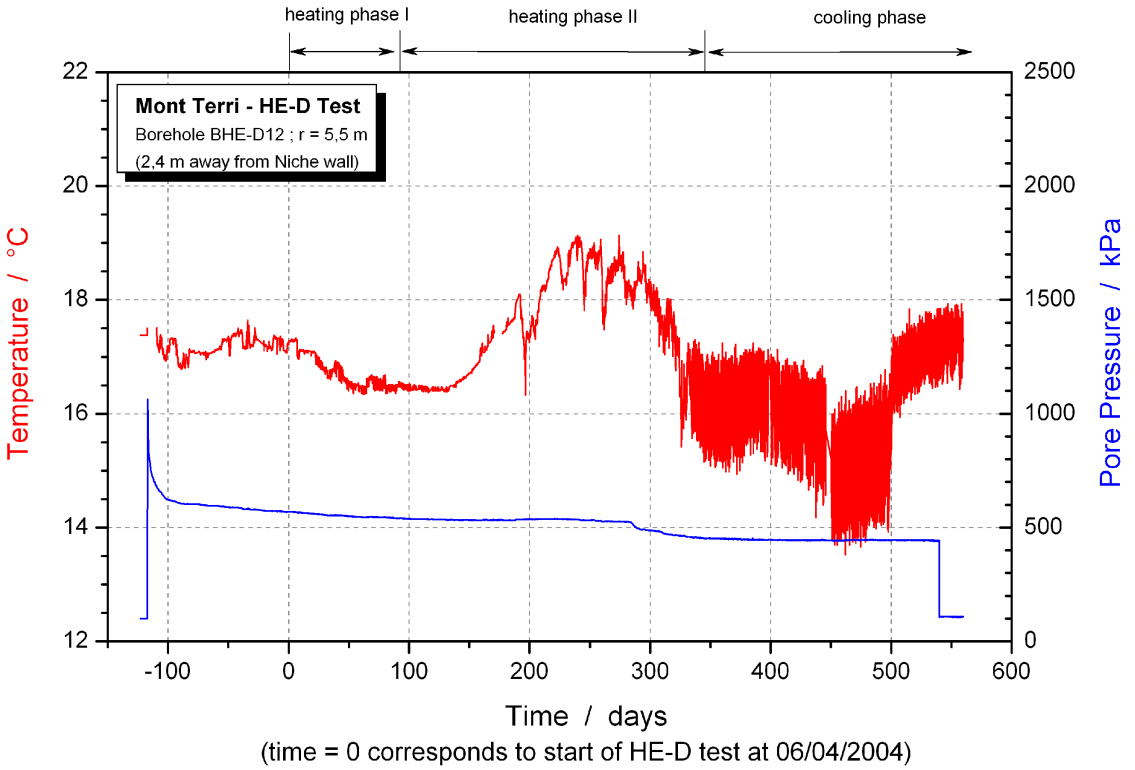

(time = 0 corresponds to start of HE-D test at 06/04/2004)

Appendix B-12 Temperature and pore pressure measurement in borehole BHE-D12

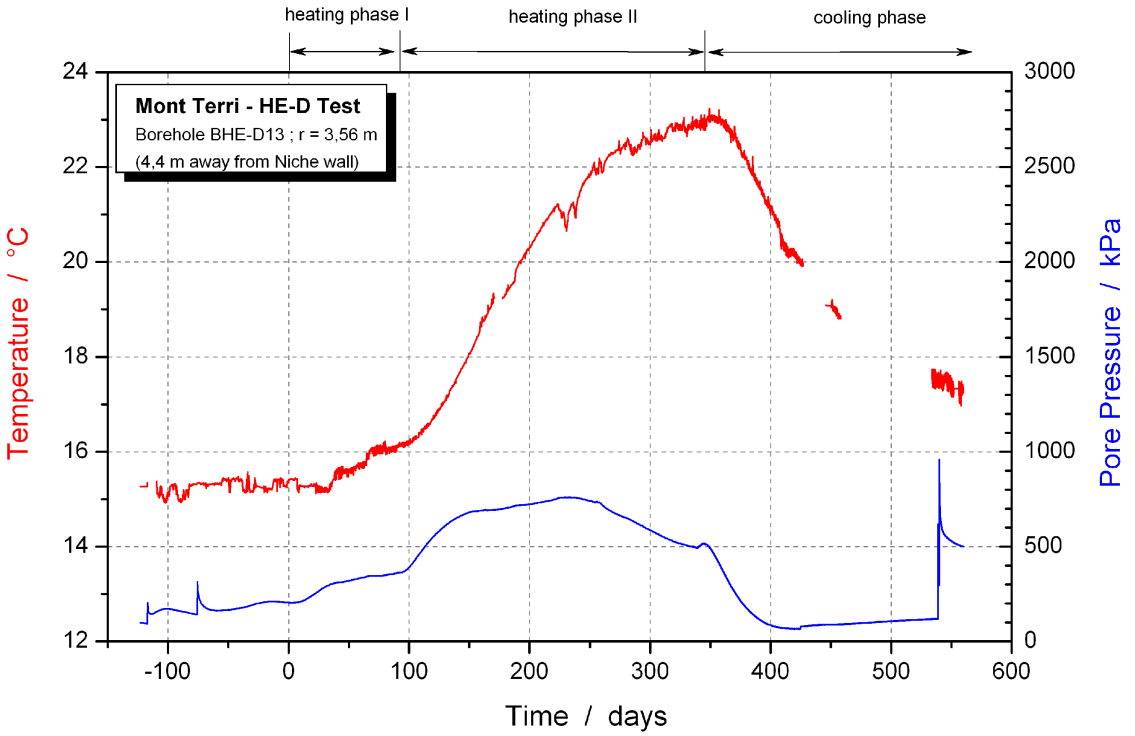

(time = 0 corresponds to start of HE-D test at 06/04/2004)

Appendix B-13 Temperature and pore pressure measurement in borehole BHE-D13

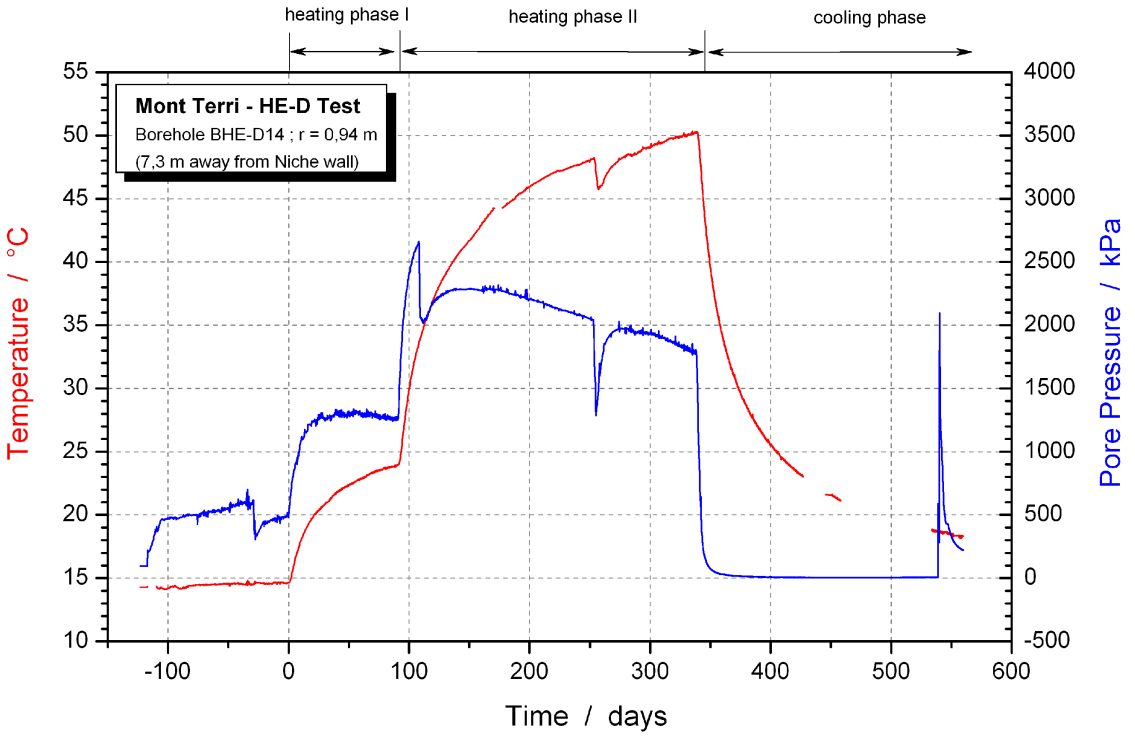

(time = 0 corresponds to start of HE-D test at 06/04/2004)

Appendix B-14 Temperature and pore pressure measurement in borehole BHE-D14

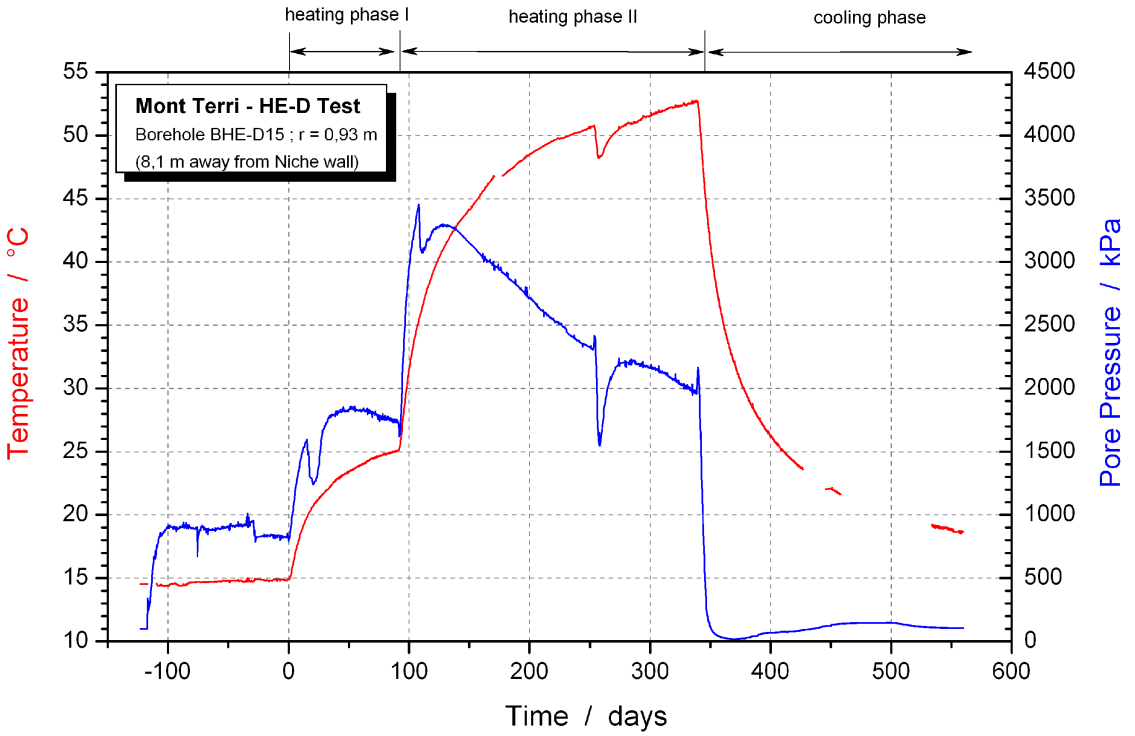

(time = 0 corresponds to start of HE-D test at 06/04/2004)

Appendix B-15 Temperature and pore pressure measurement in borehole BHE-D15

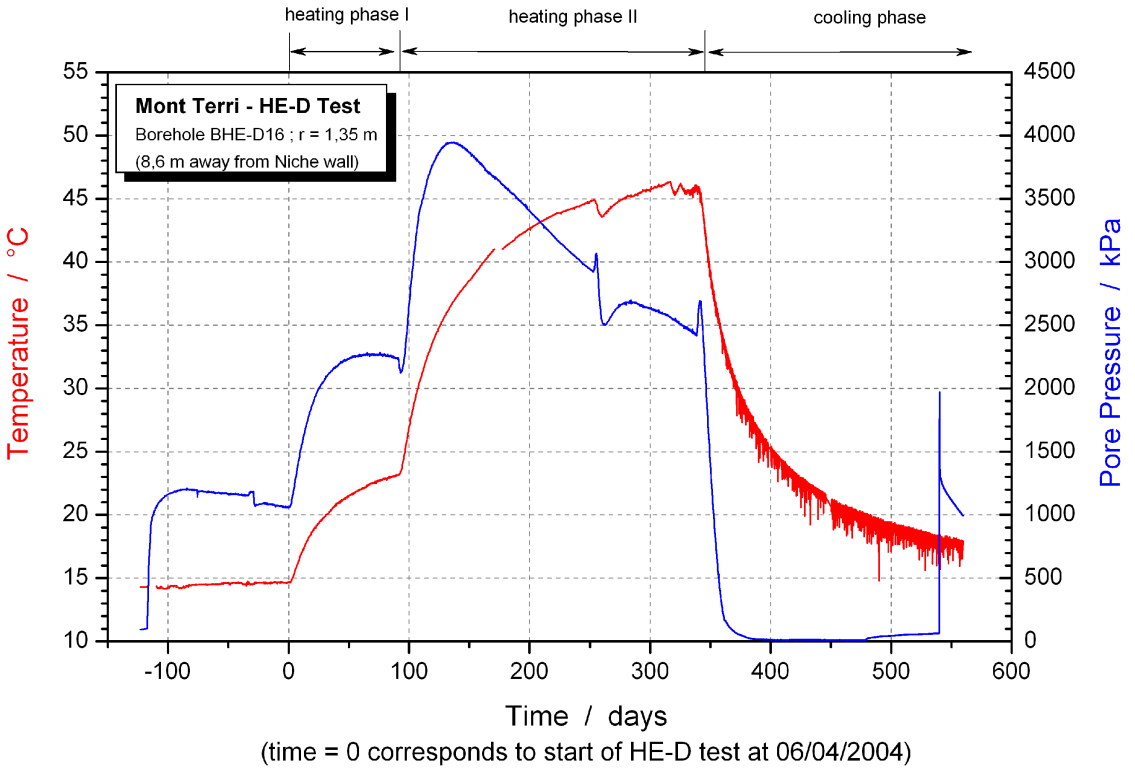

(time = 0 corresponds to start of HE-D test at 06/04/2004)

Appendix B-16 Temperature and pore pressure measurement in borehole BHE-D16

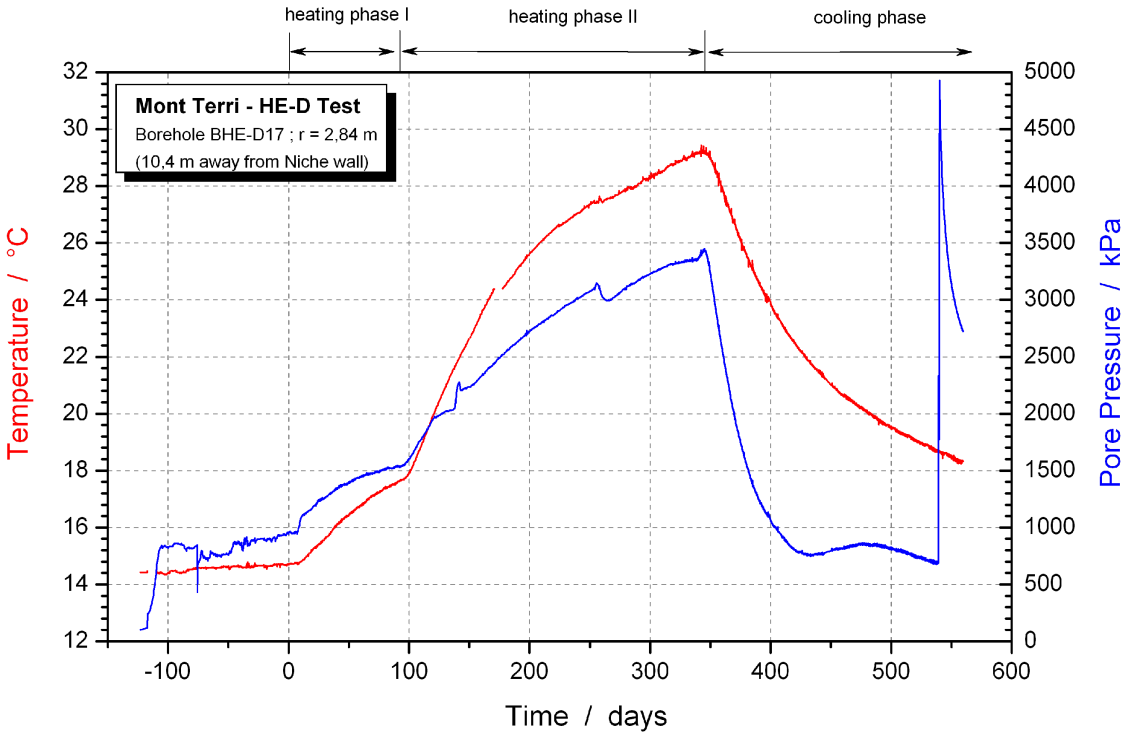

(time = 0 corresponds to start of HE-D test at 06/04/2004)

Appendix B-17 Temperature and pore pressure measurement in borehole BHE-D17

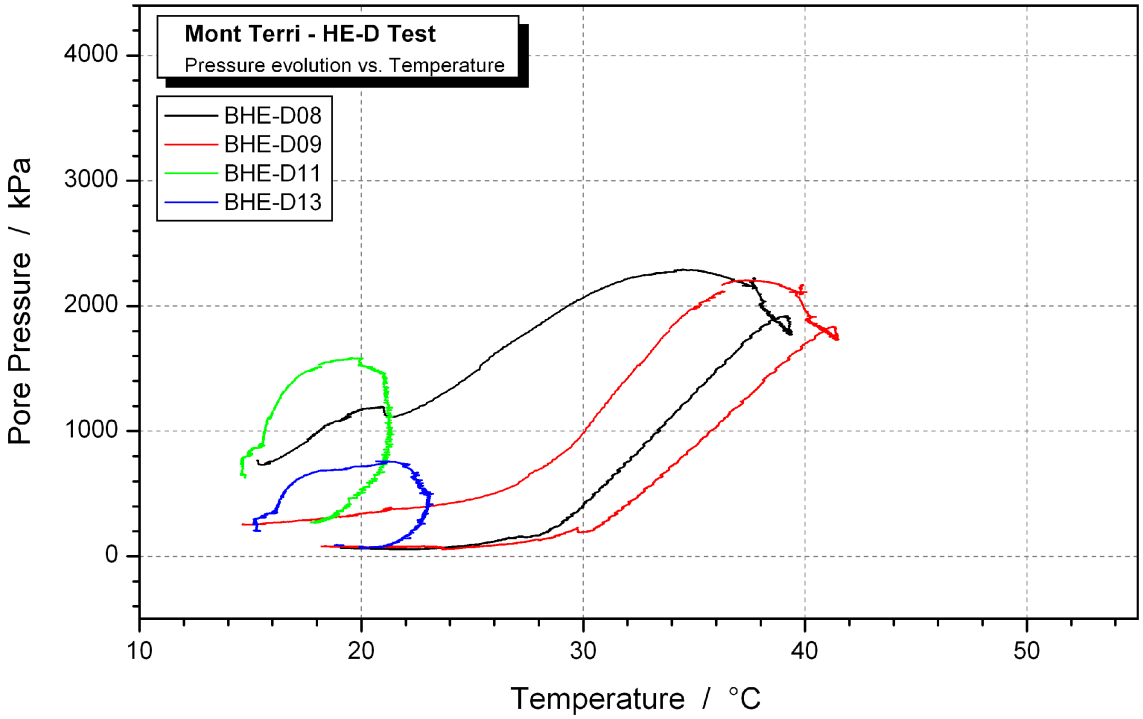

Appendix B-18 Pore pressure- vs. temperature evolution for sensors BHE-D08 – D13

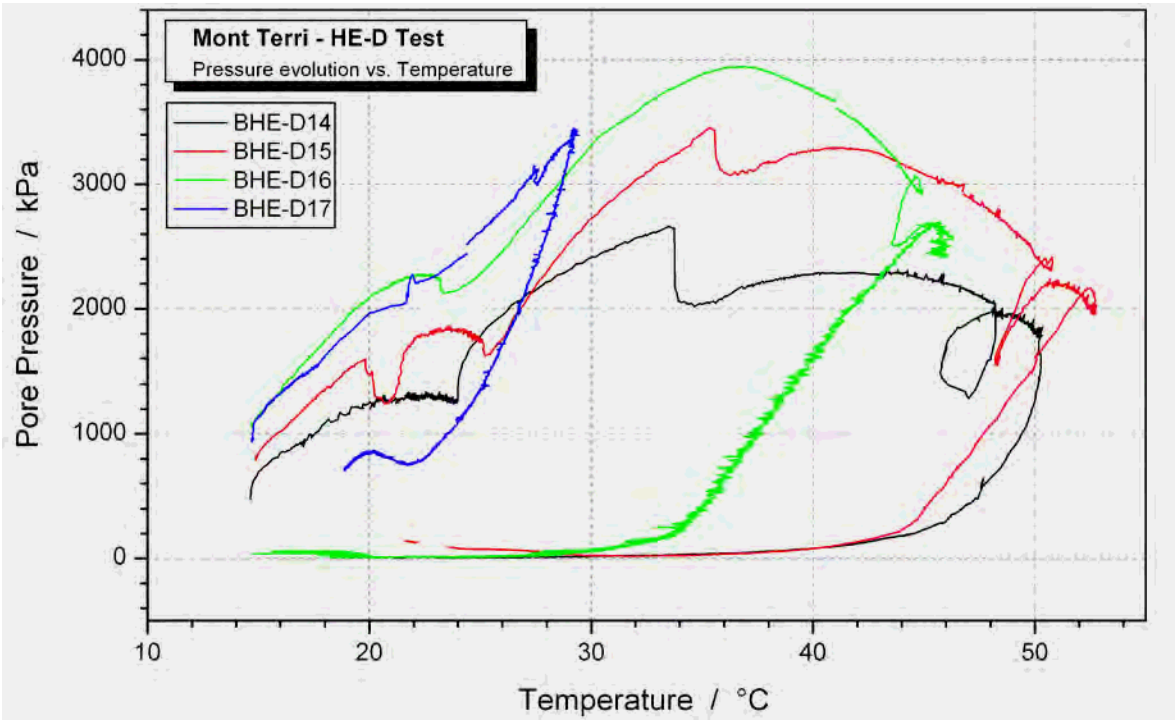

Appendix B-19 Pore pressure- vs. temperature evolution for sensors BHE-D14 – D17

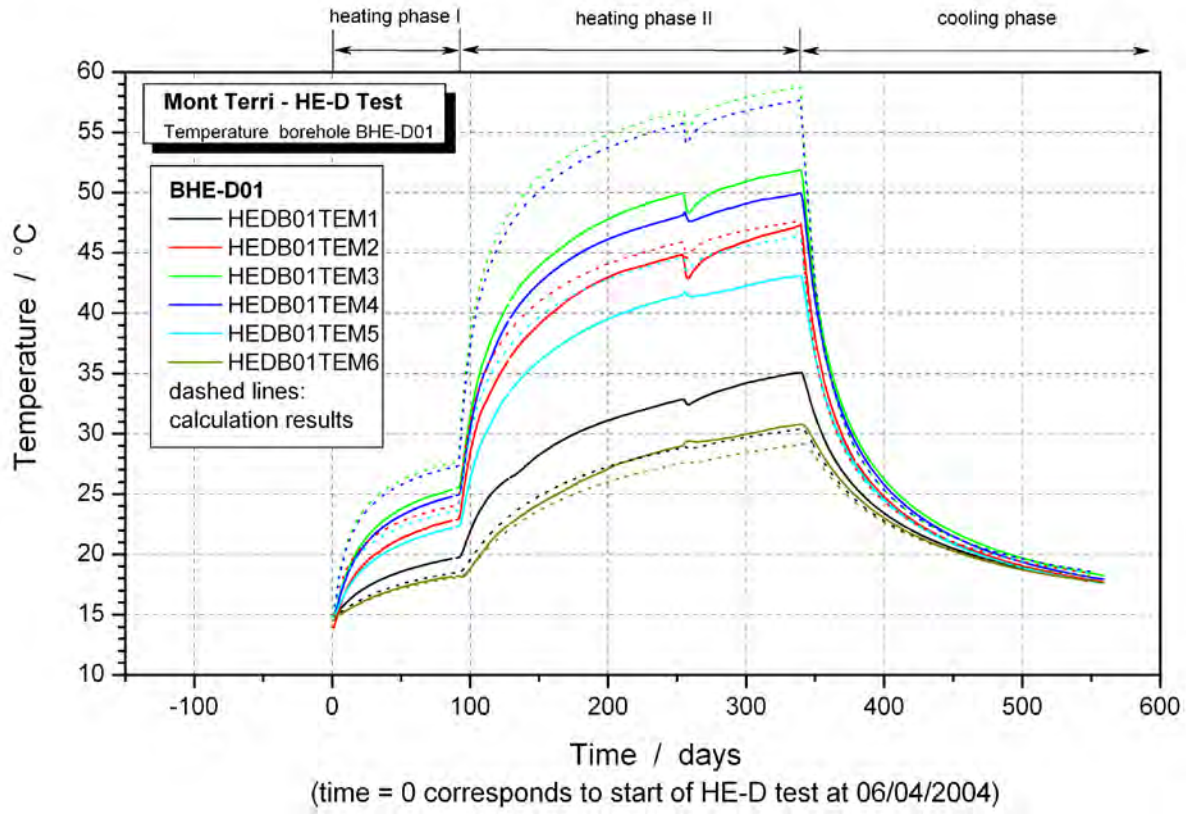

Appendix C-1 Comparison of measured and calculated temperatures for BHE-D01

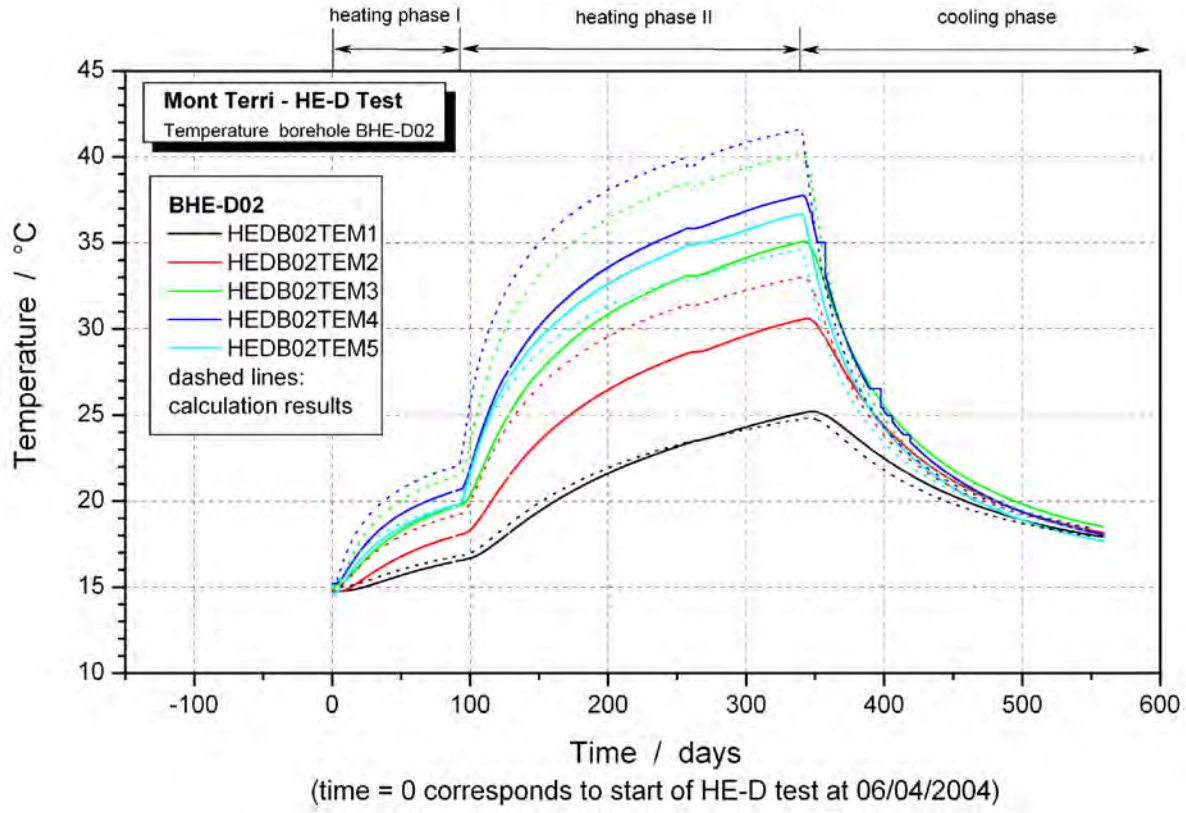

Appendix C-2 Comparison of measured and calculated temperatures for BHE-D02

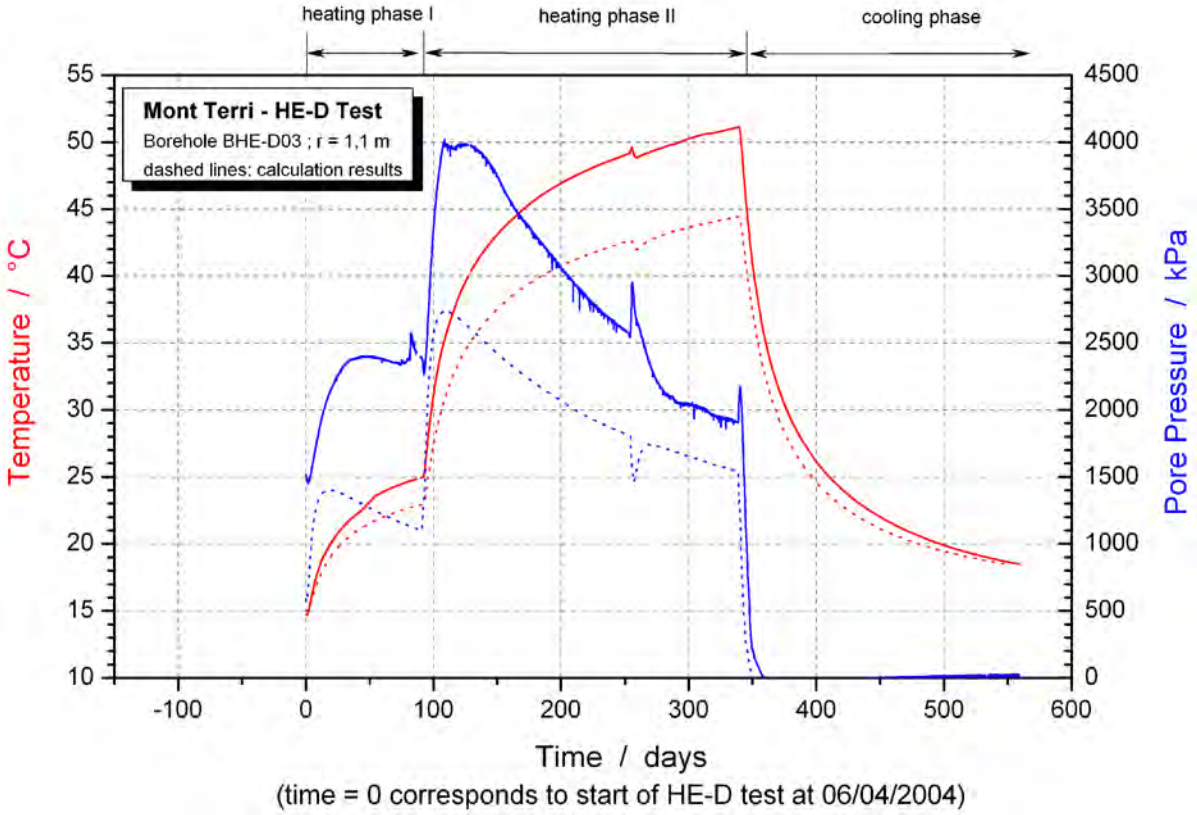

Appendix C-3 Comparison of measured and calculated temperatures and pore pressures for BHE-D03

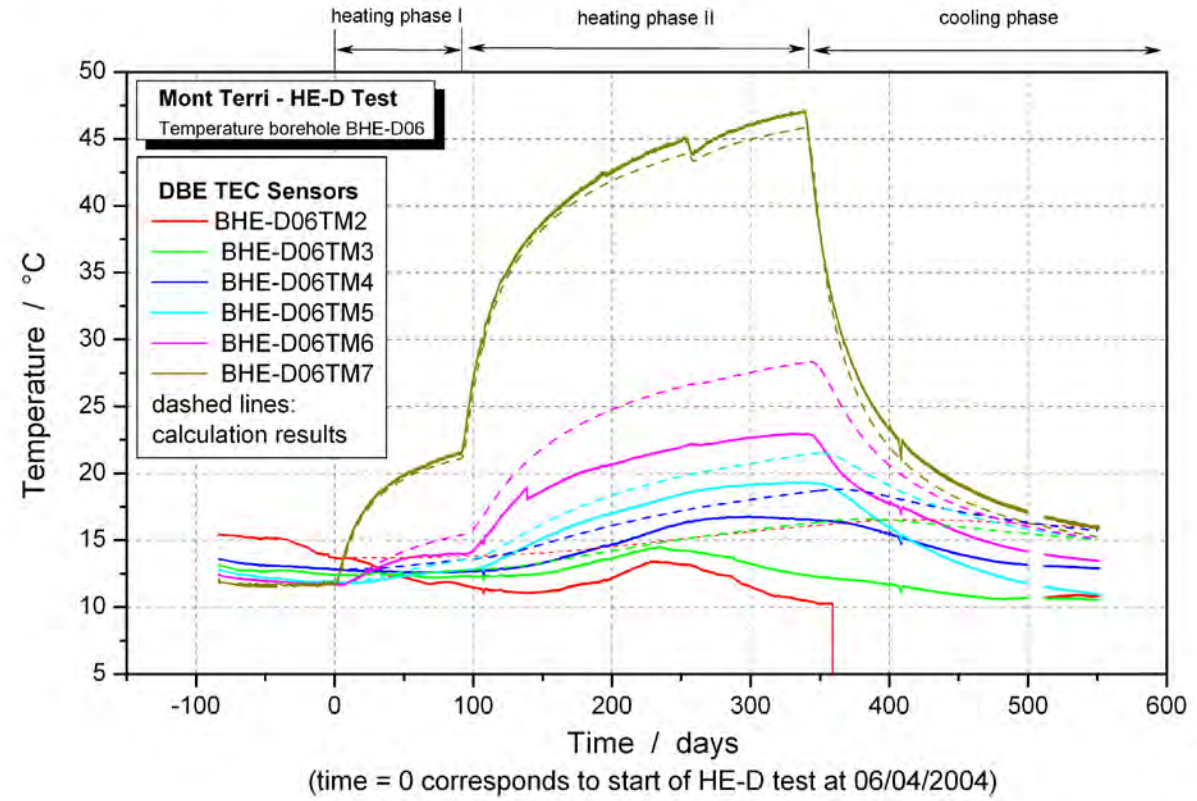

Appendix C-4 Comparison of measured and calculated temperatures for BHE-D06

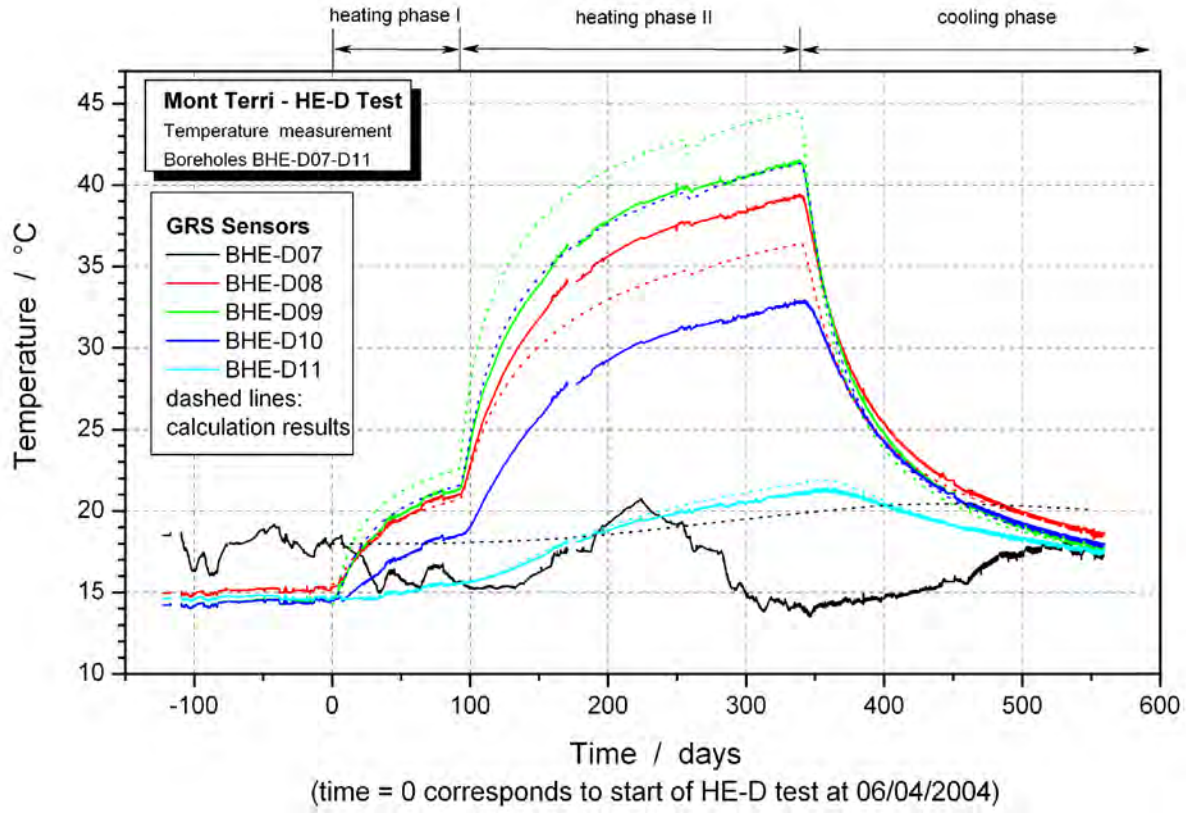

Appendix C-5 Comparison of measured and calculated temperatures for BHE-D07-D11

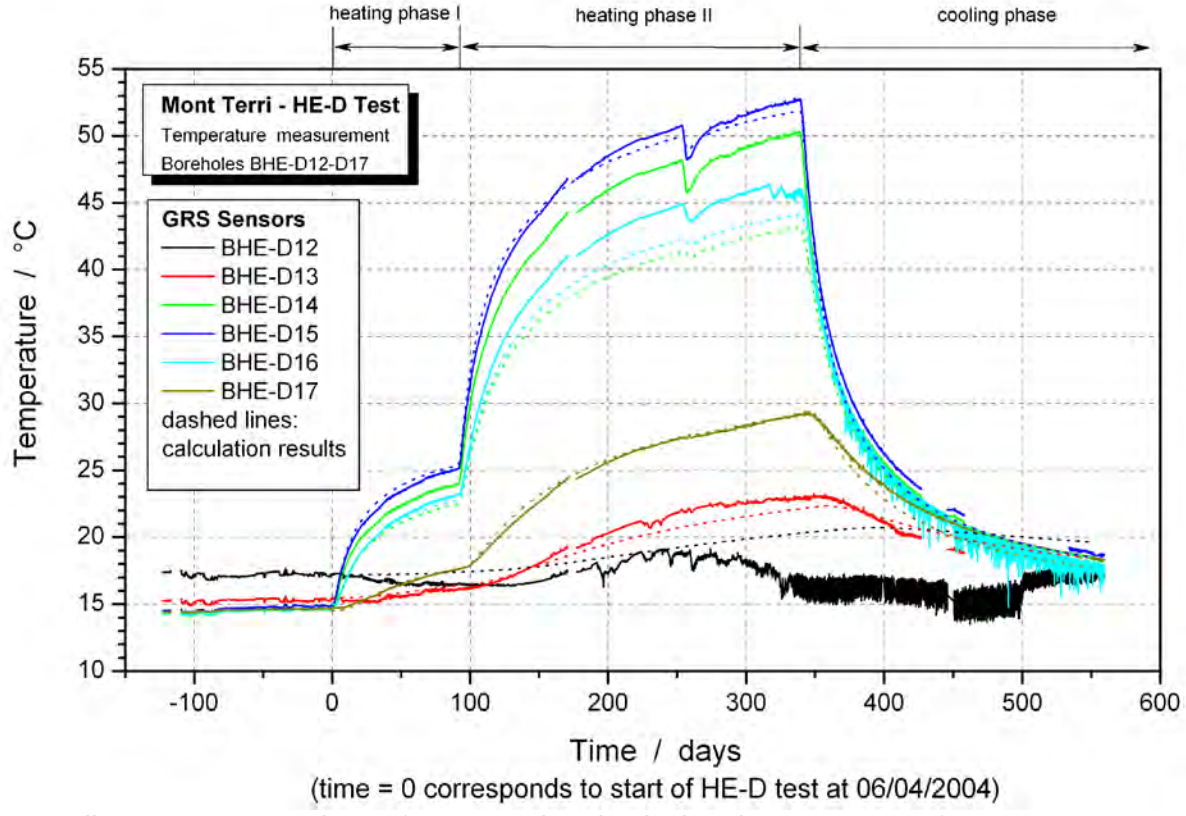

Appendix C-6 Comparison of measured and calculated temperatures for BHE-D12-D17

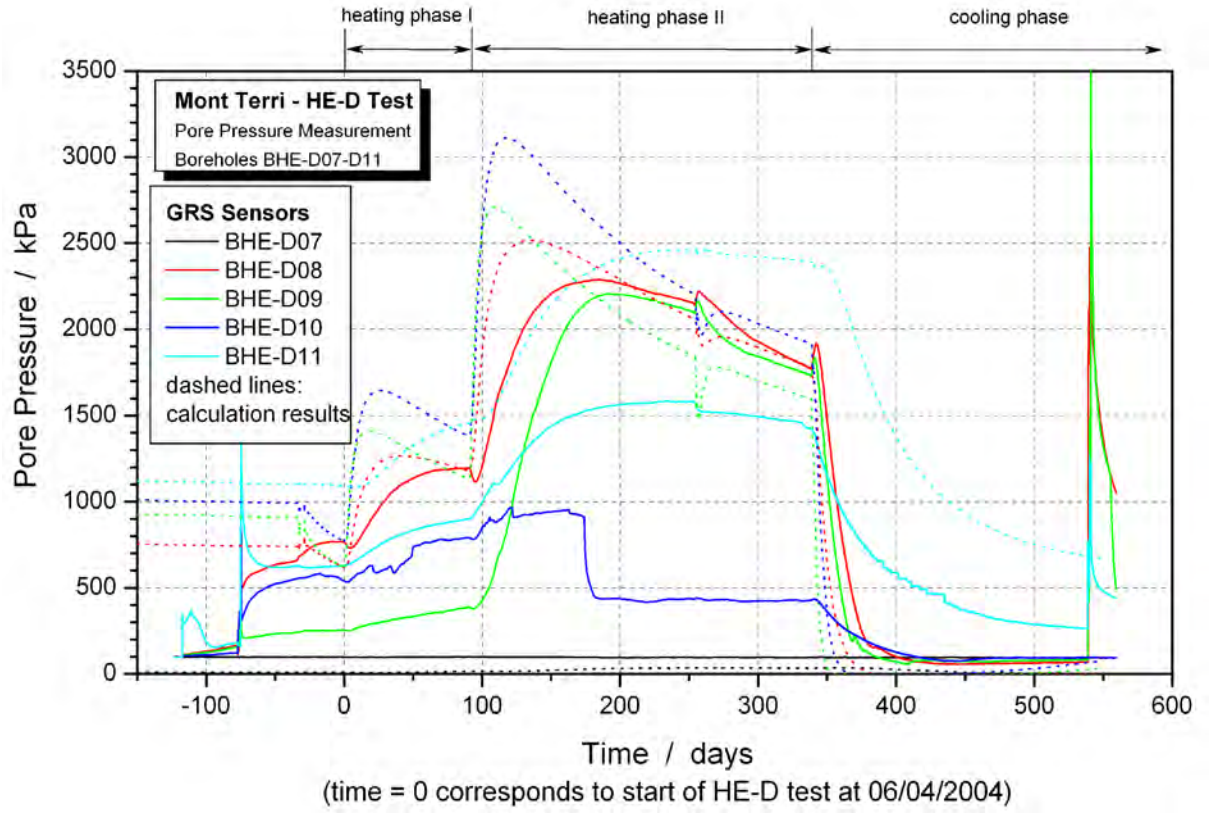

Appendix C-7 Comparison of measured and calculated pore pressures for BHE-D07-D11

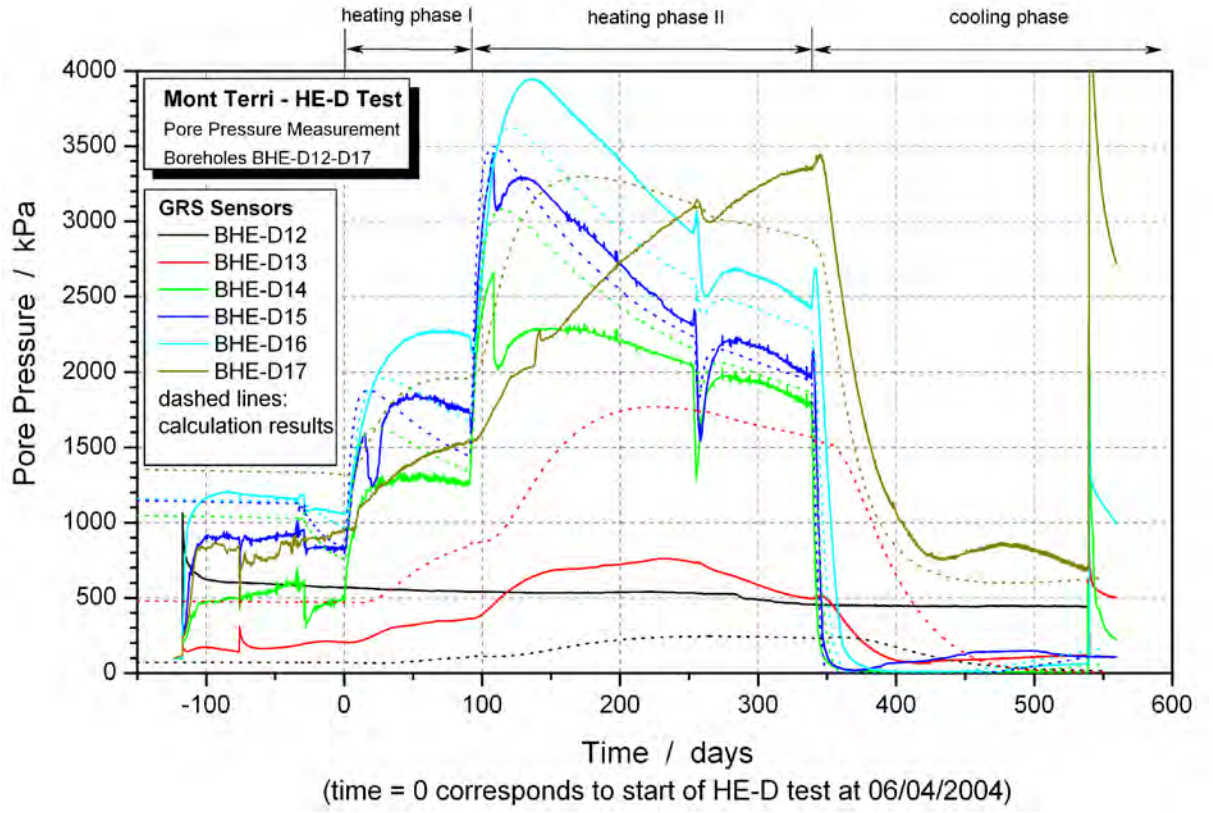

Appendix C-8 Comparison of measured and calculated pore pressures for BHE-D12-D17

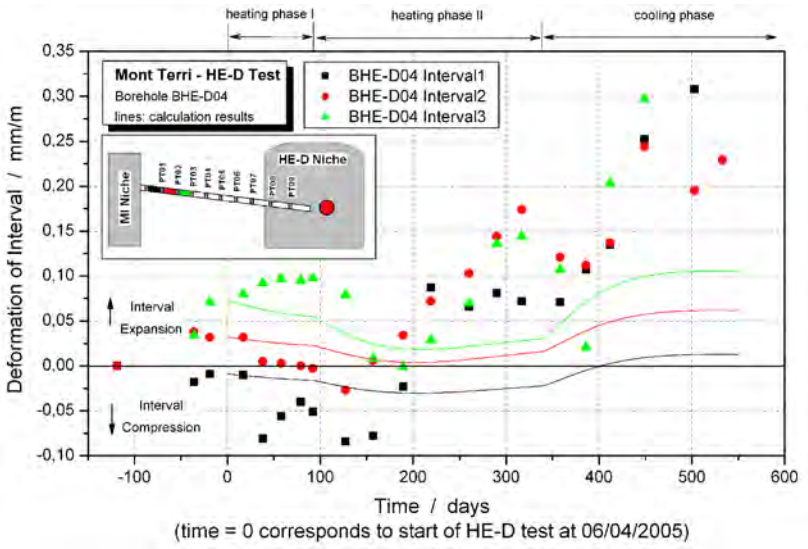

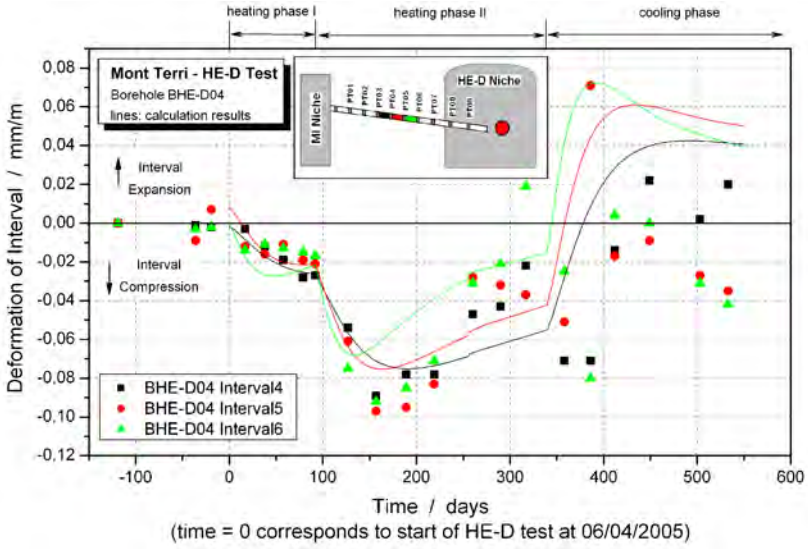

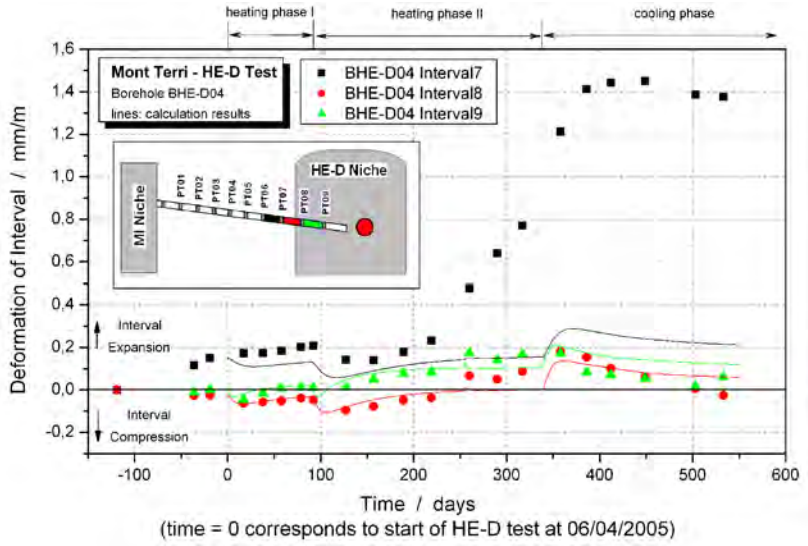

Appendix C-9 Comparison of measured and calculated deformations for BHE-D04

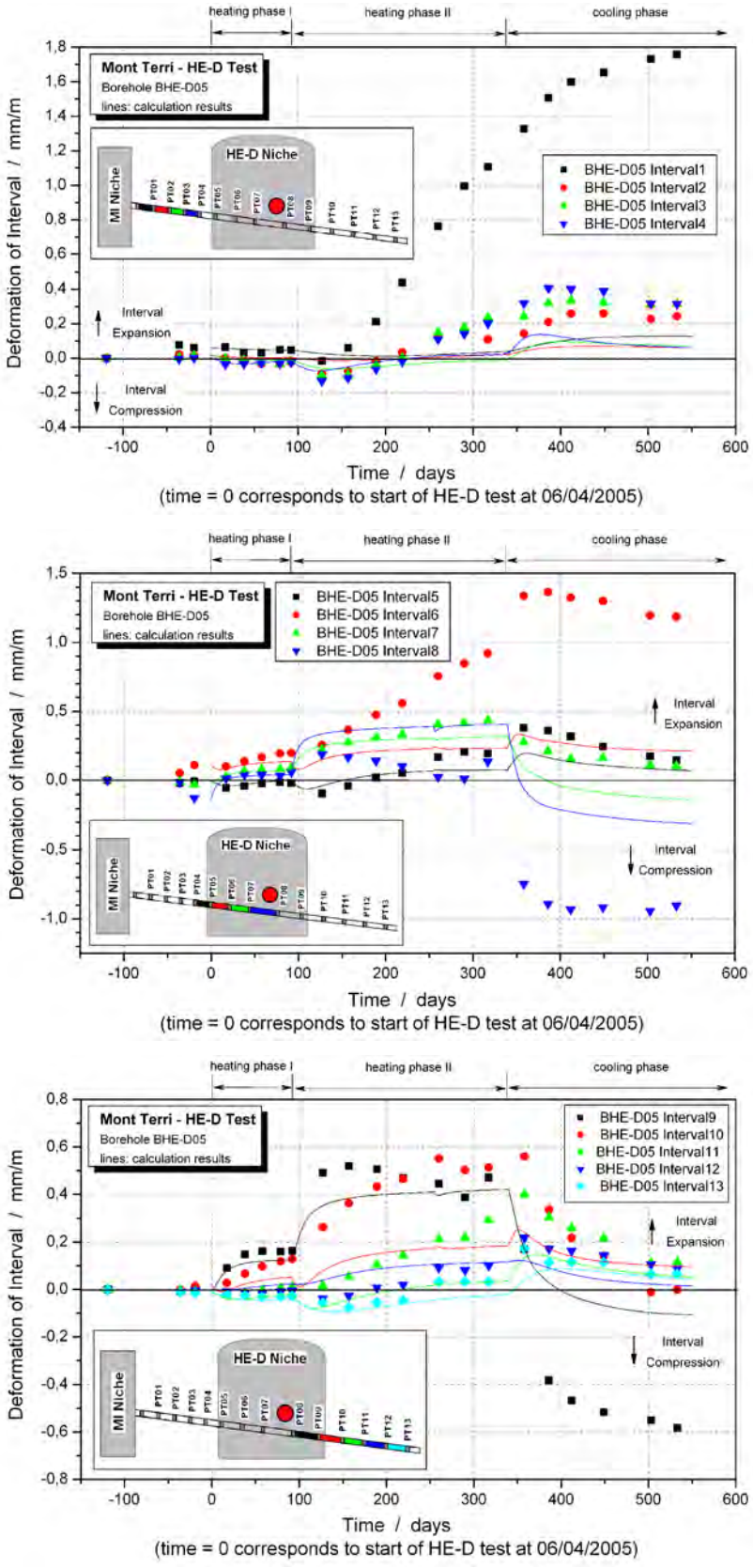

Appendix C-10 Comparison of measured and calculated deformations for BHE-D05

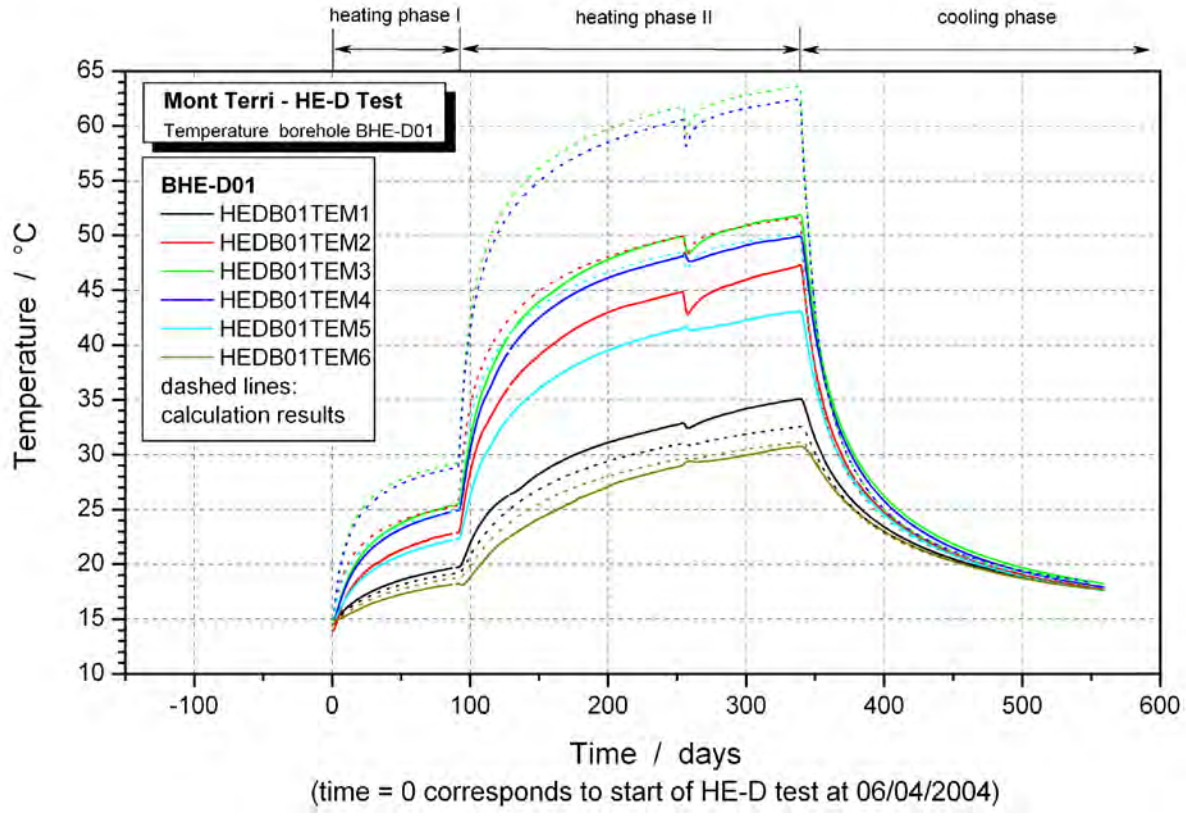

Appendix D-1 Comparison of measured and calculated temperatures for BHE-D01

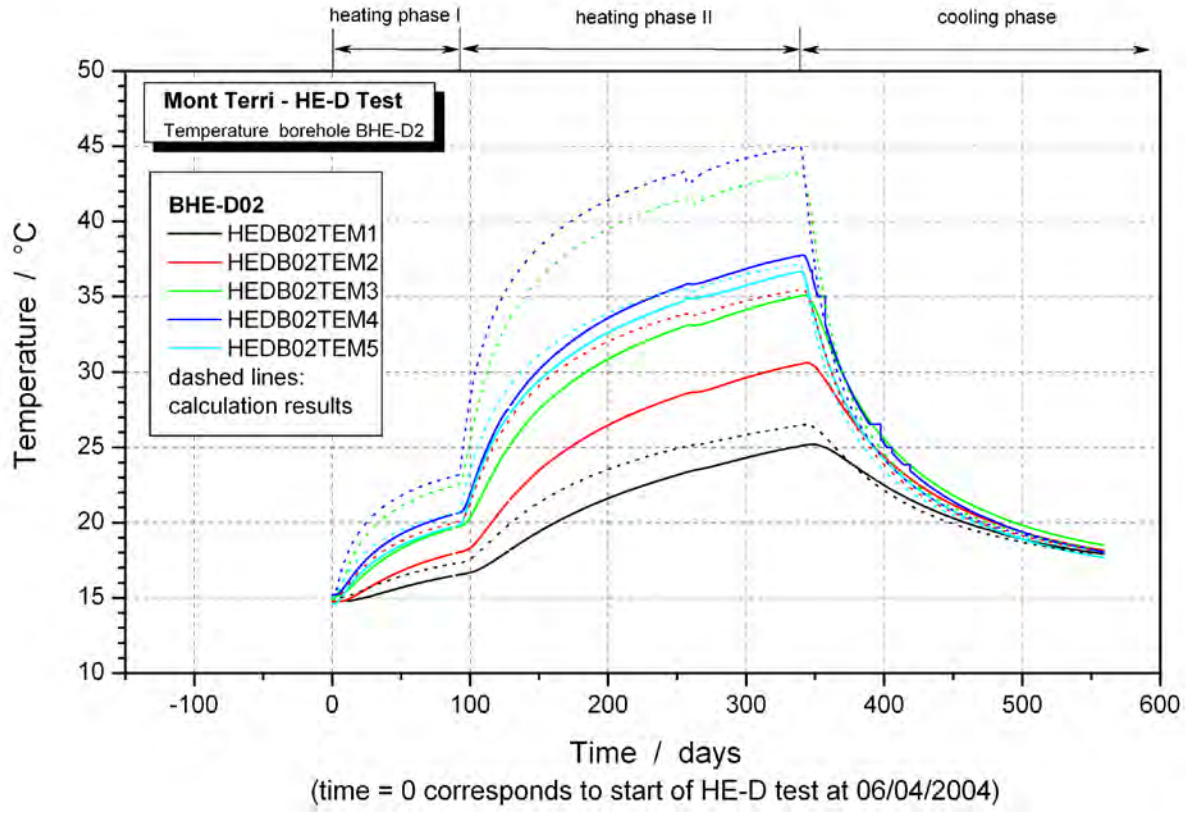

Appendix D-2 Comparison of measured and calculated temperatures for BHE-D02

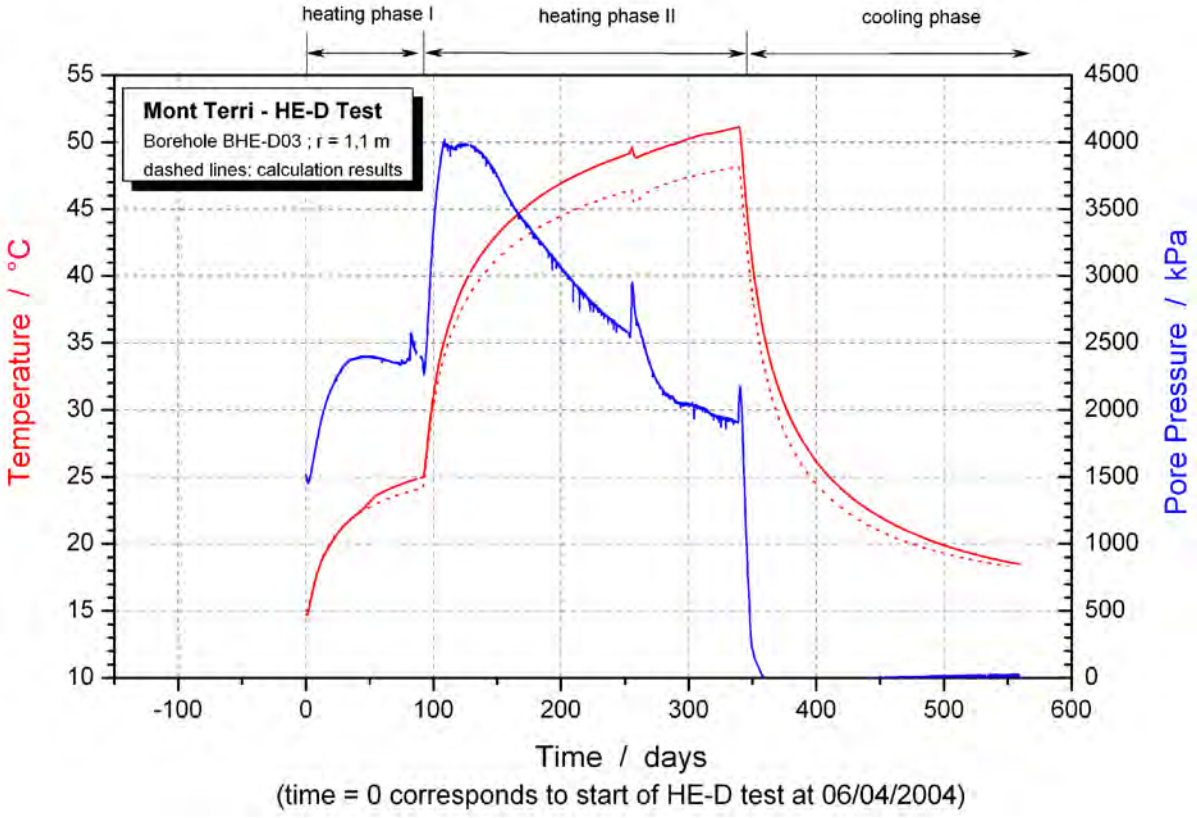

Appendix D-3 Comparison of measured and calculated temperatures and pore pressures for BHE-D03

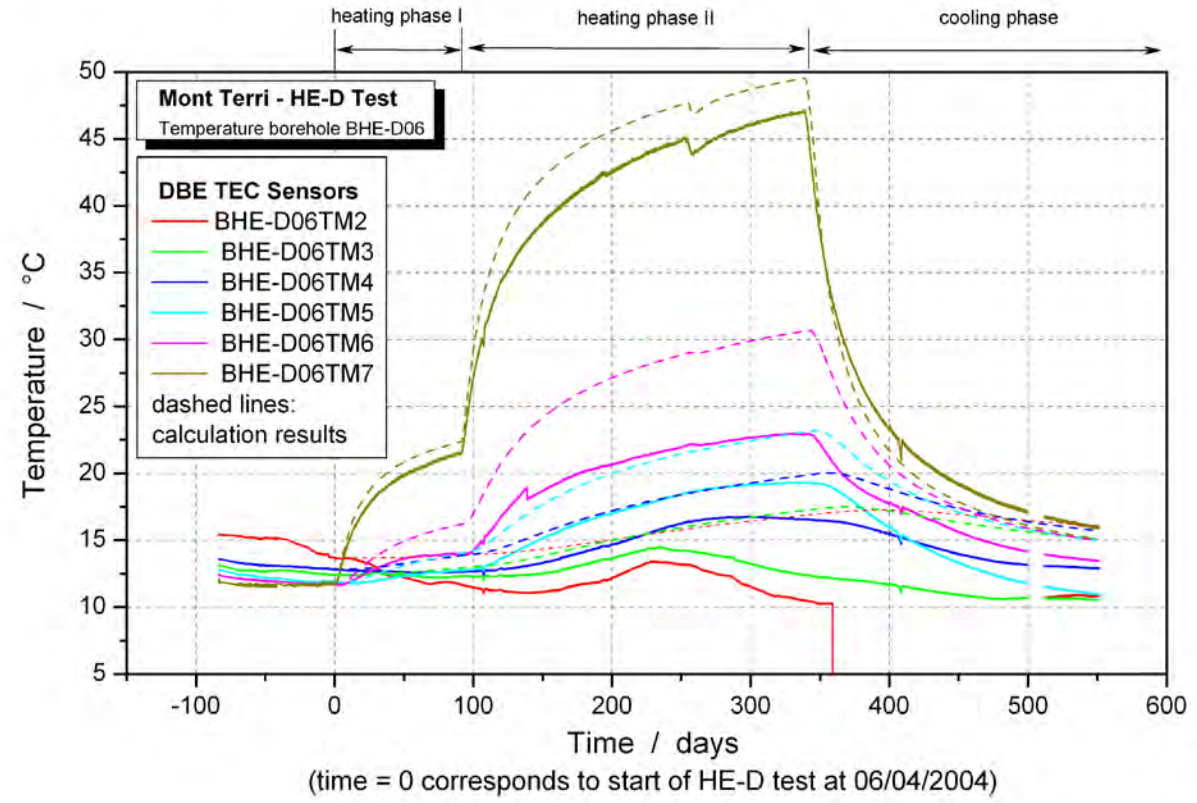

Appendix D-4 Comparison of measured and calculated temperatures for BHE-D06

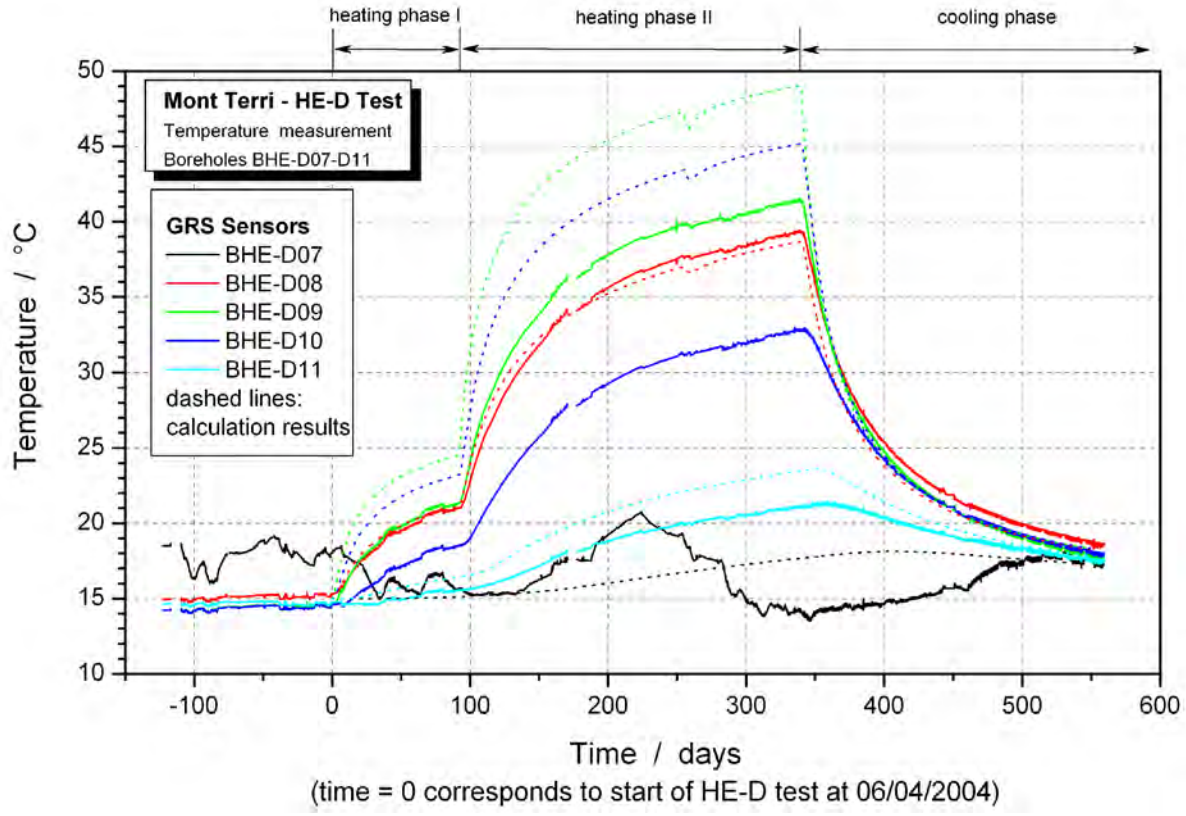

Appendix D-5 Comparison of measured and calculated temperatures for BHE-D07-D11

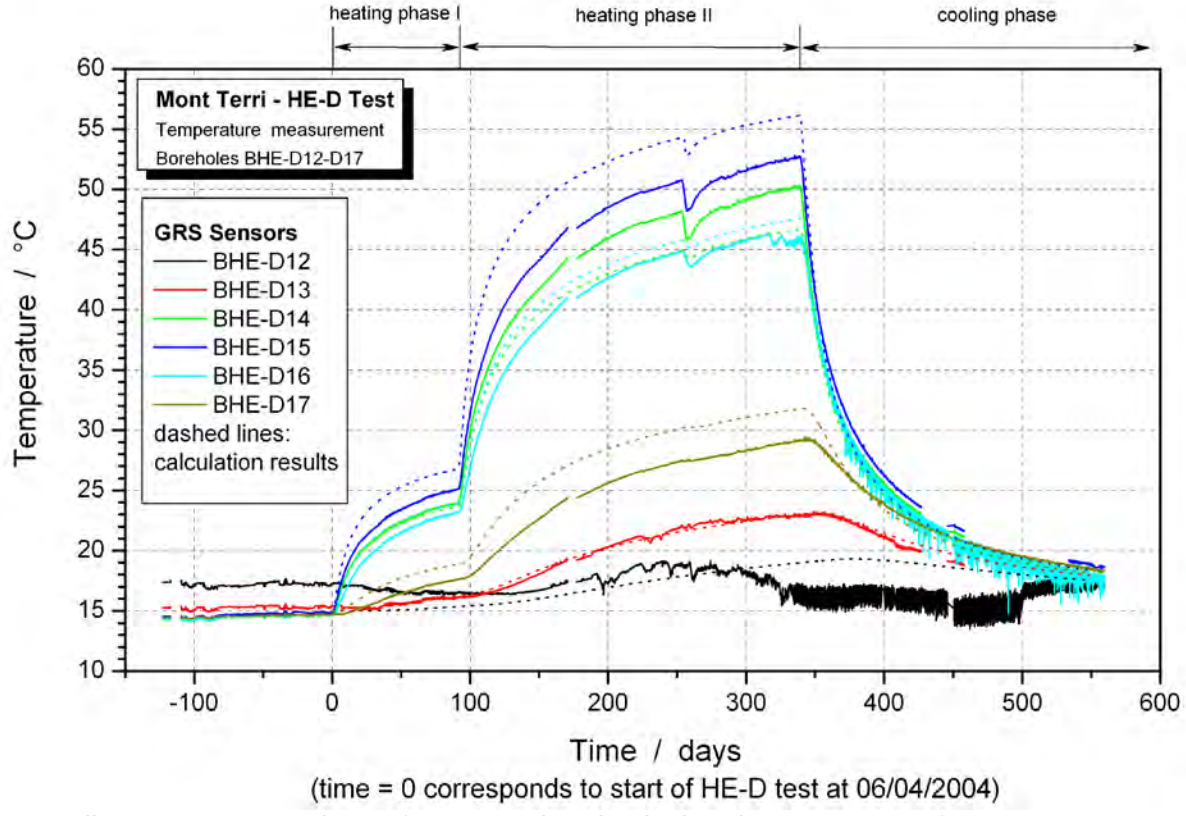

Appendix D-6 Comparison of measured and calculated temperatures for BHE-D12-D17

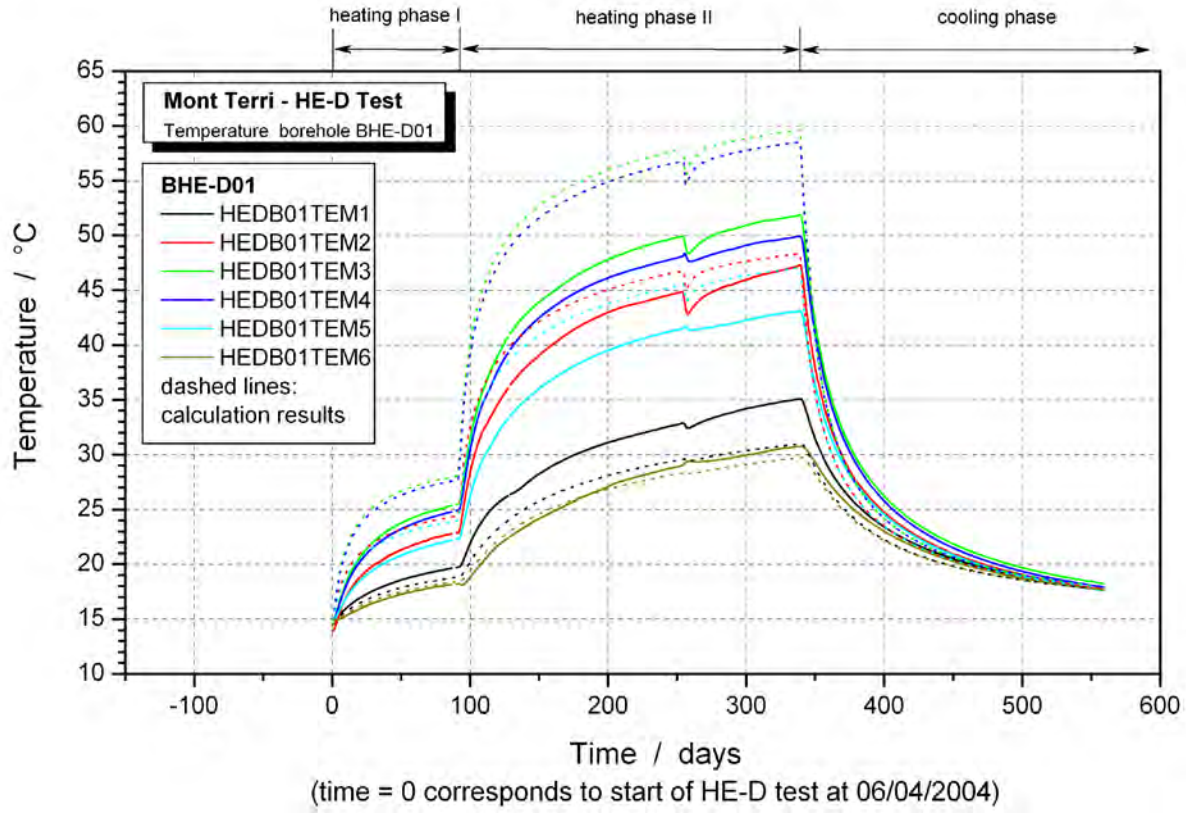

Appendix E-1 Comparison of measured and calculated temperatures for BHE-D01

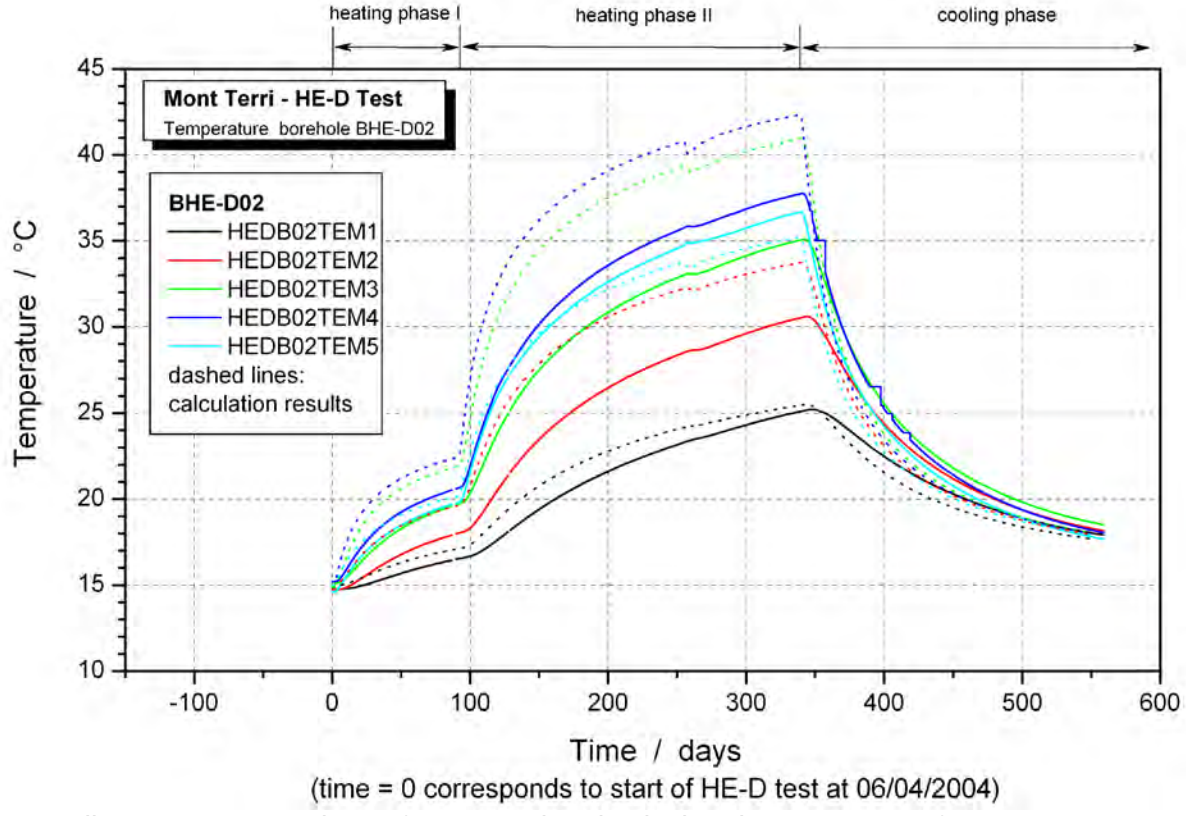

Appendix E-2 Comparison of measured and calculated temperatures for BHE-D02

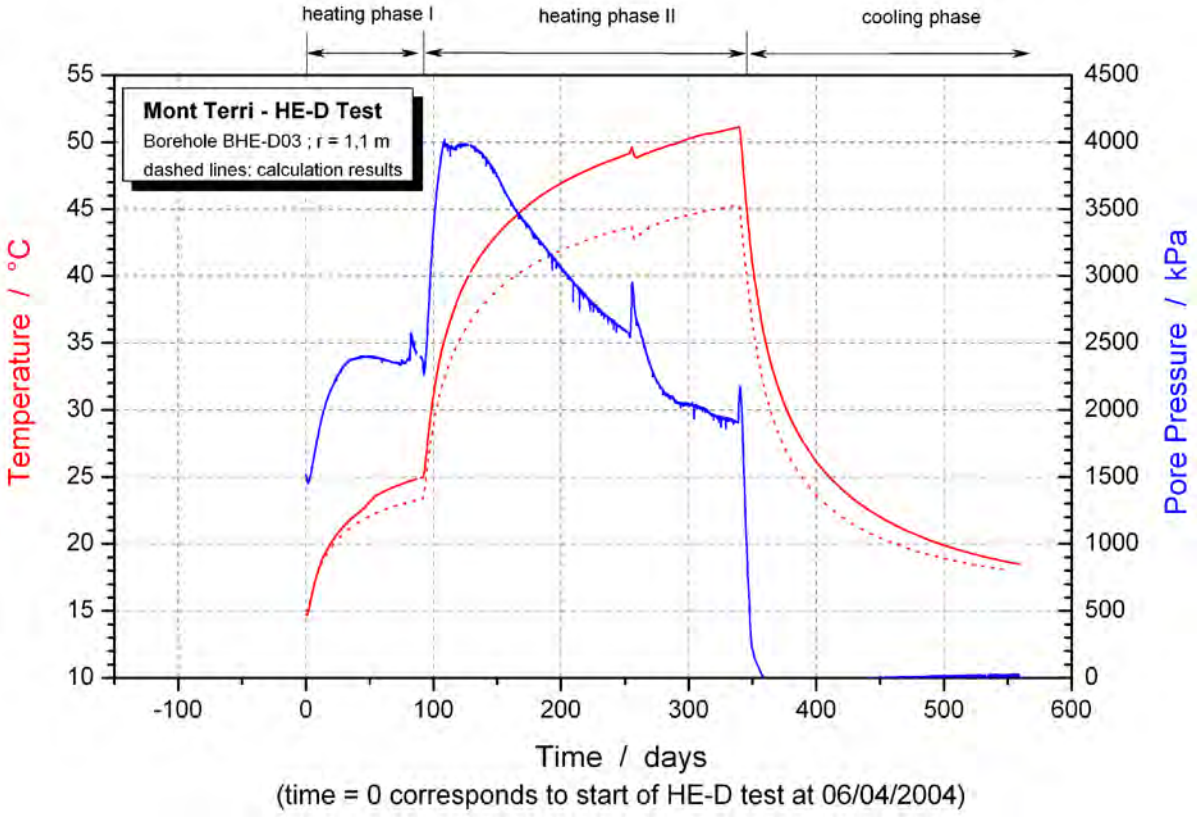

Appendix E-3 Comparison of measured and calculated temperatures and pore pressures for BHE-D03

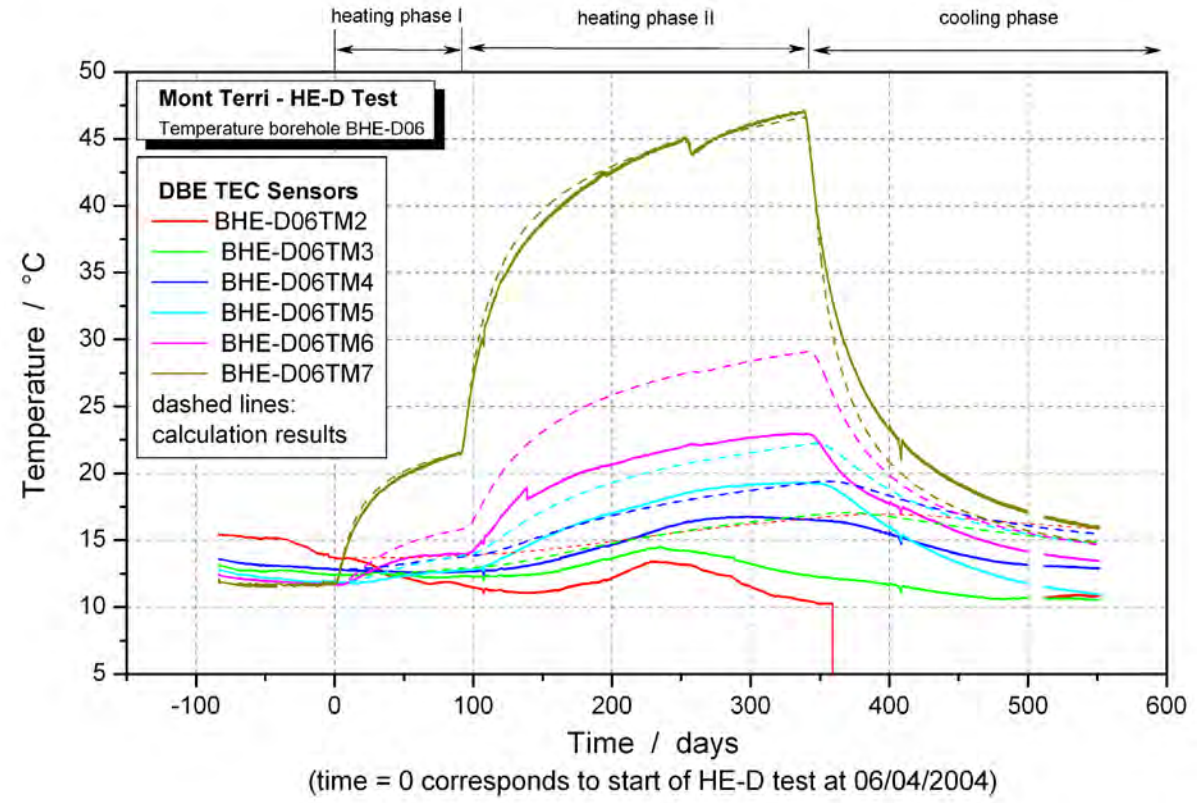

Appendix E-4 Comparison of measured and calculated temperatures for BHE-D06

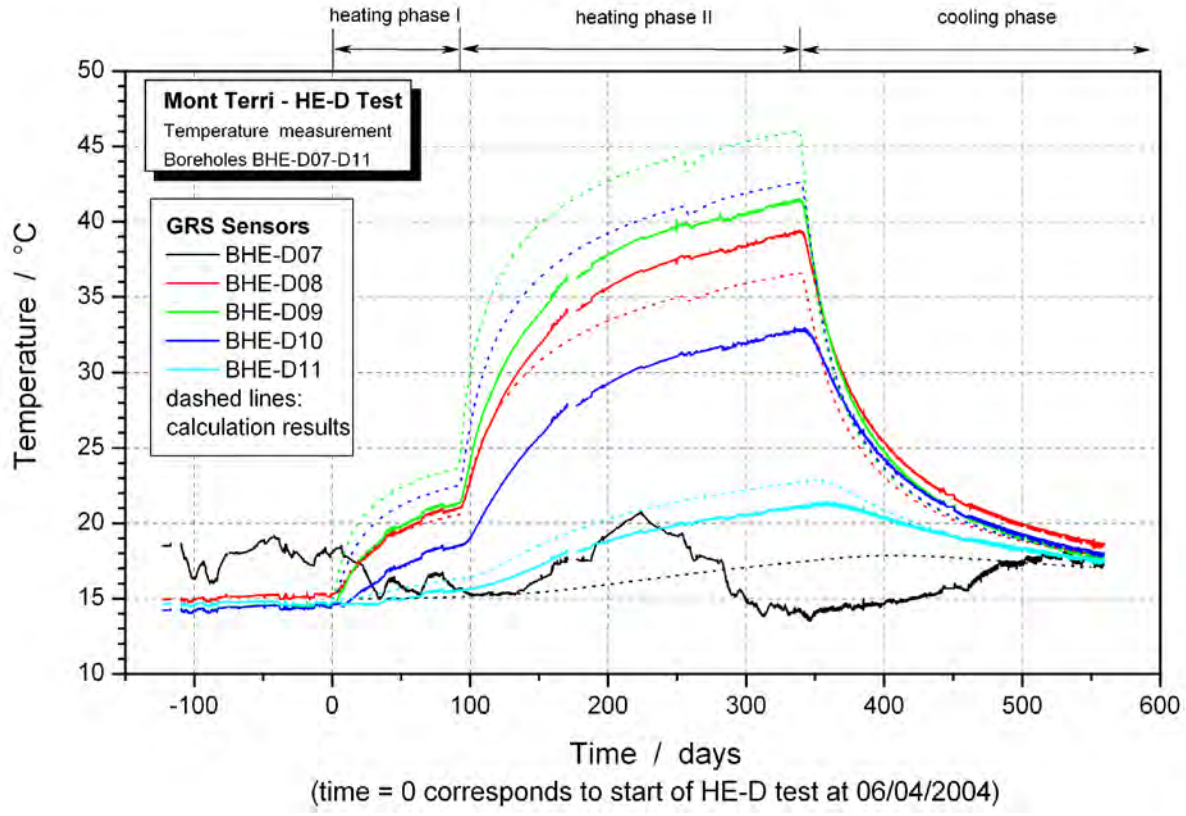

Appendix E-5 Comparison of measured and calculated temperatures for BHE-D07-D11

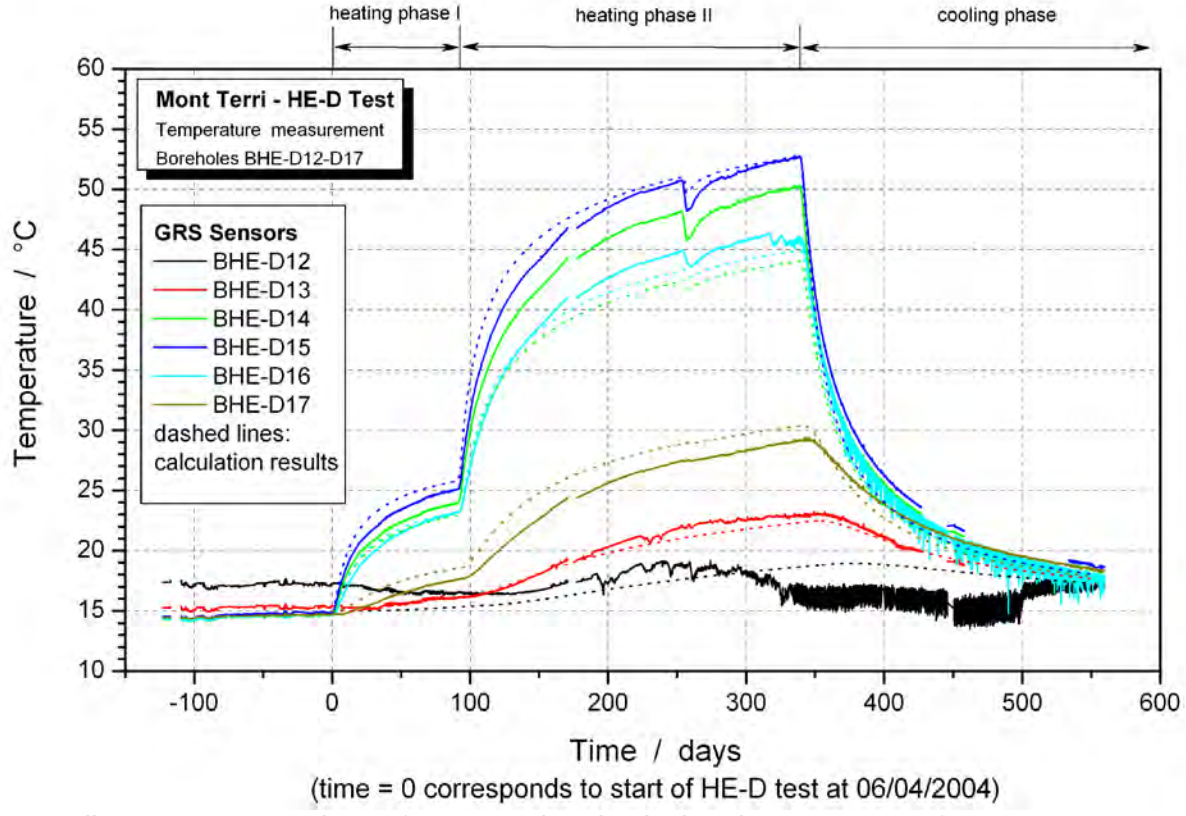

Appendix E-6 Comparison of measured and calculated temperatures for BHE-D12-D17

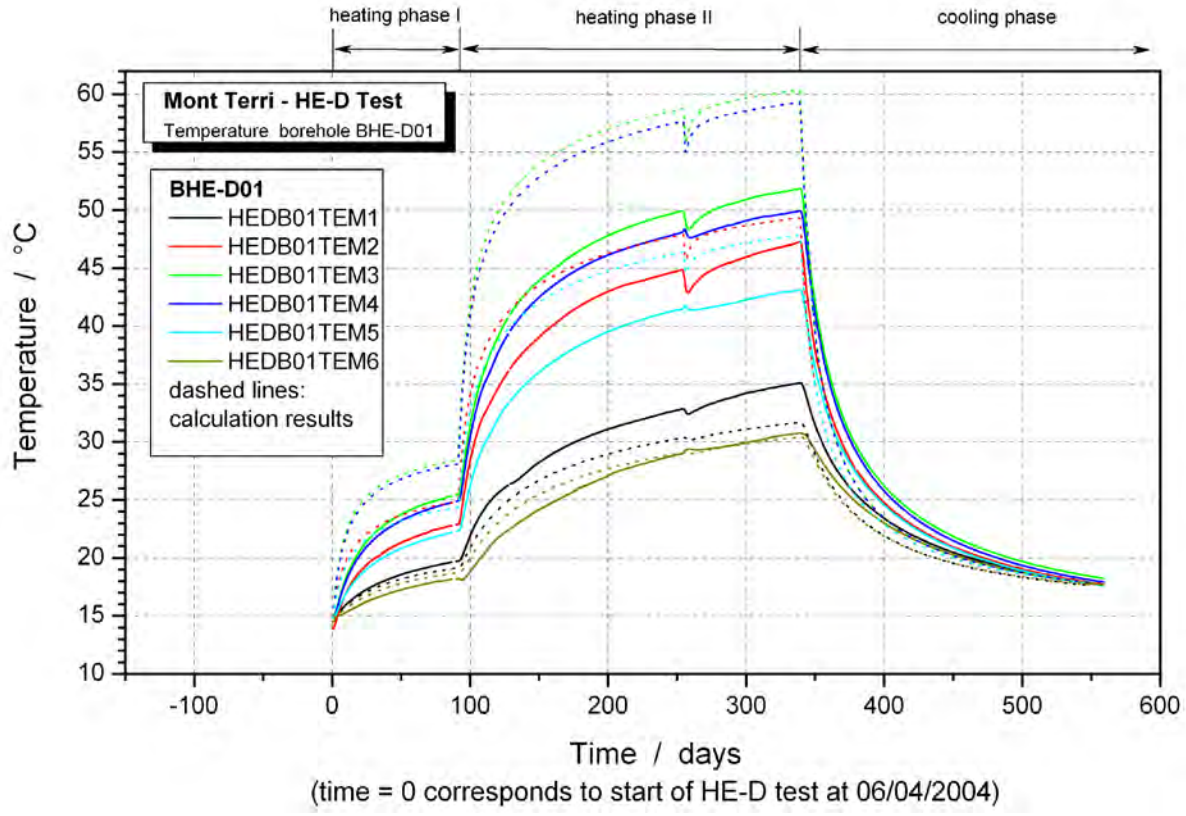

Appendix F-1 Comparison of measured and calculated temperatures for BHE-D01

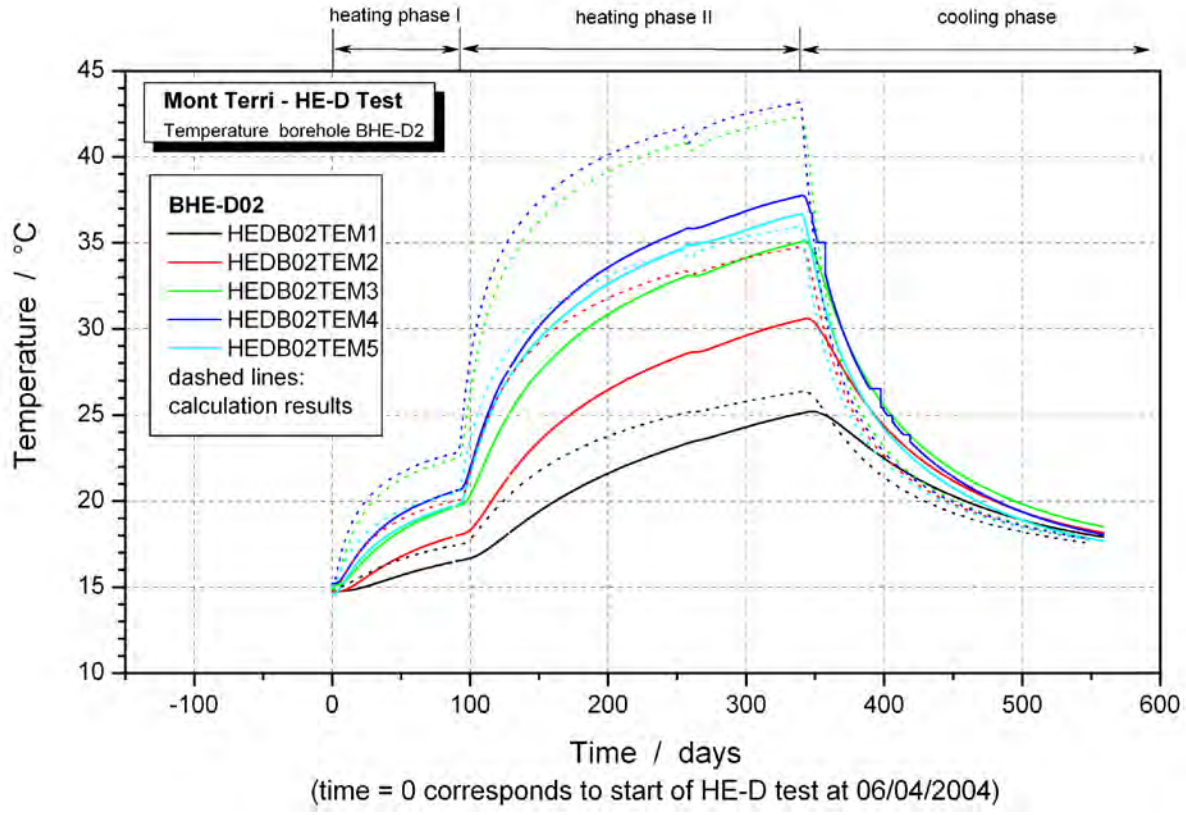

Appendix F-2 Comparison of measured and calculated temperatures for BHE-D02

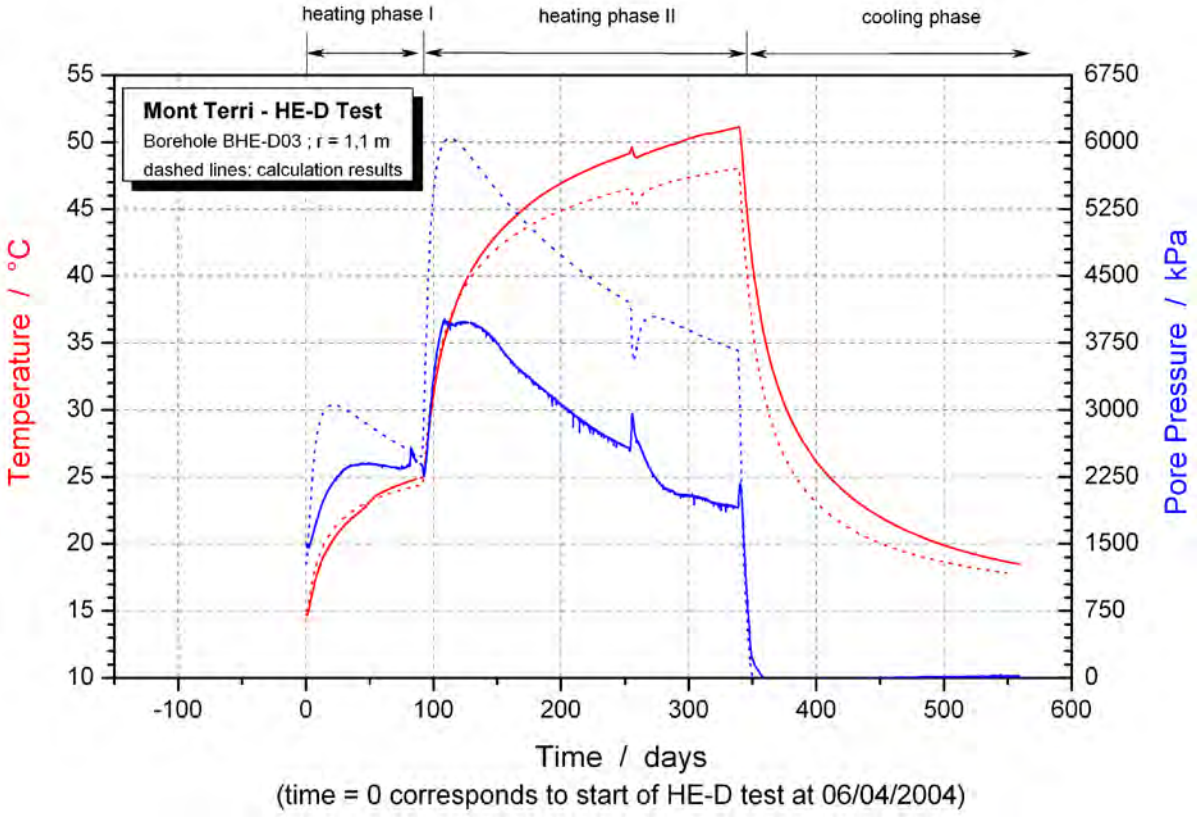

Appendix F-3 Comparison of measured and calculated temperatures and pore pressures for BHE-D03

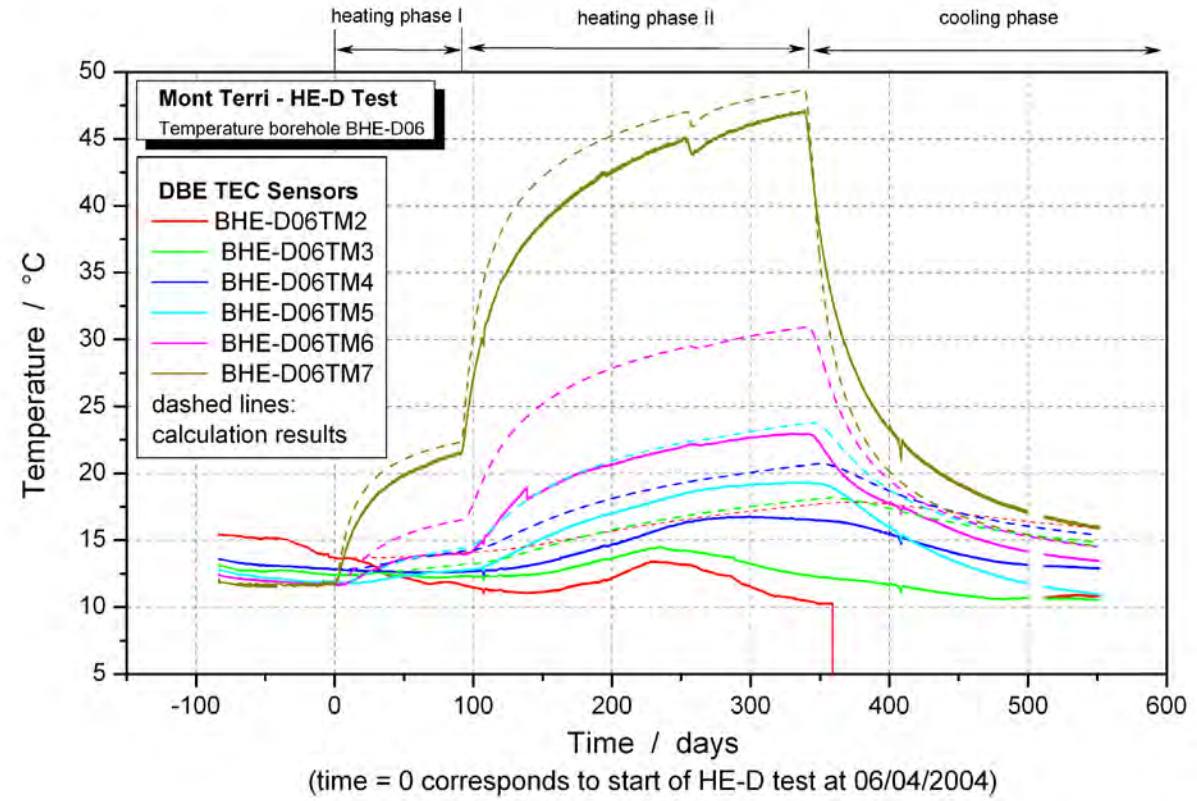

Appendix F-4 Comparison of measured and calculated temperatures for BHE-D06

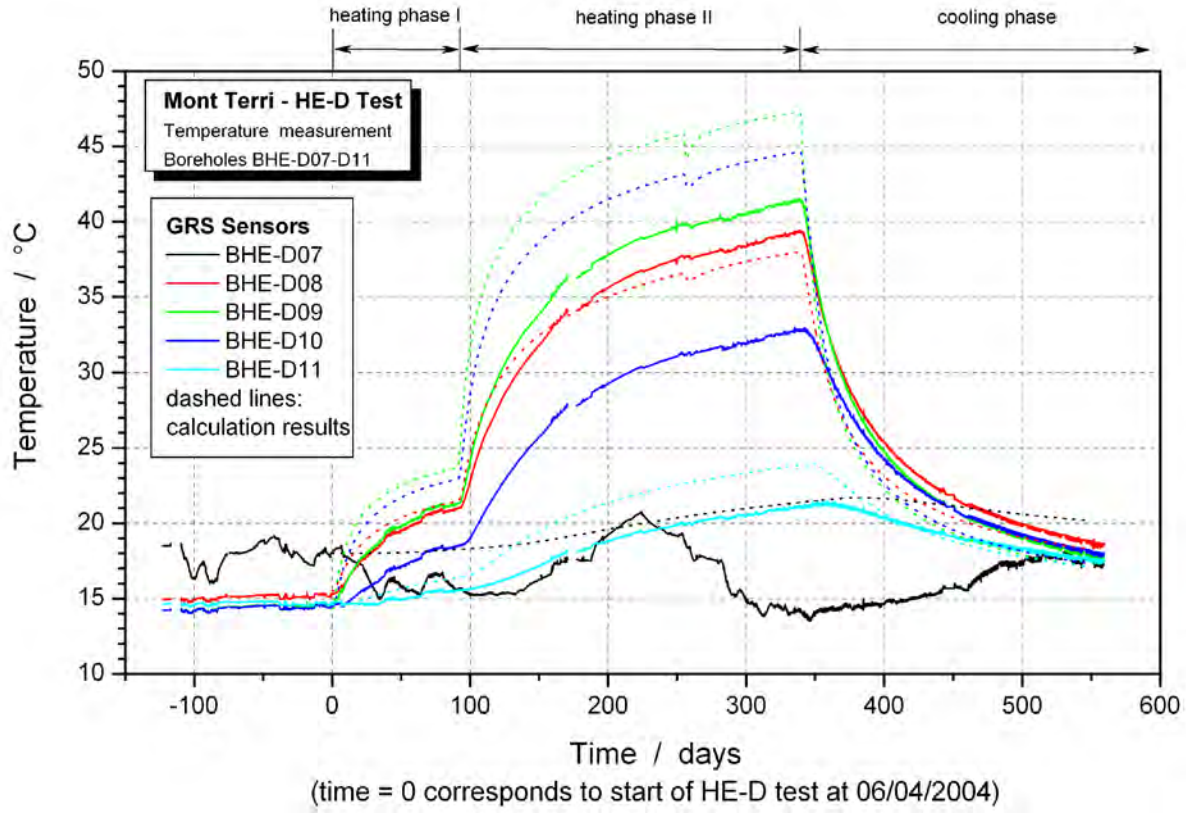

Appendix F-5 Comparison of measured and calculated temperatures for BHE-D07-D11

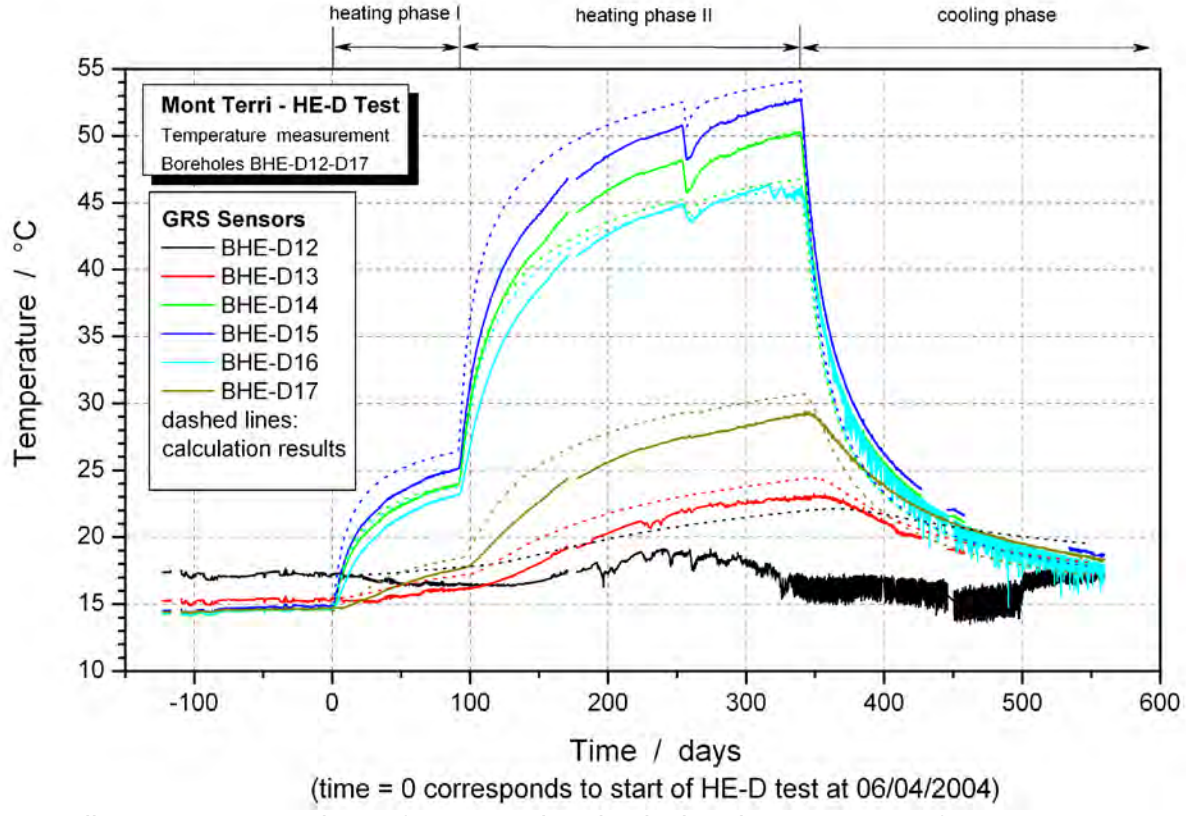

Appendix F-6 Comparison of measured and calculated temperatures for BHE-D12-D17

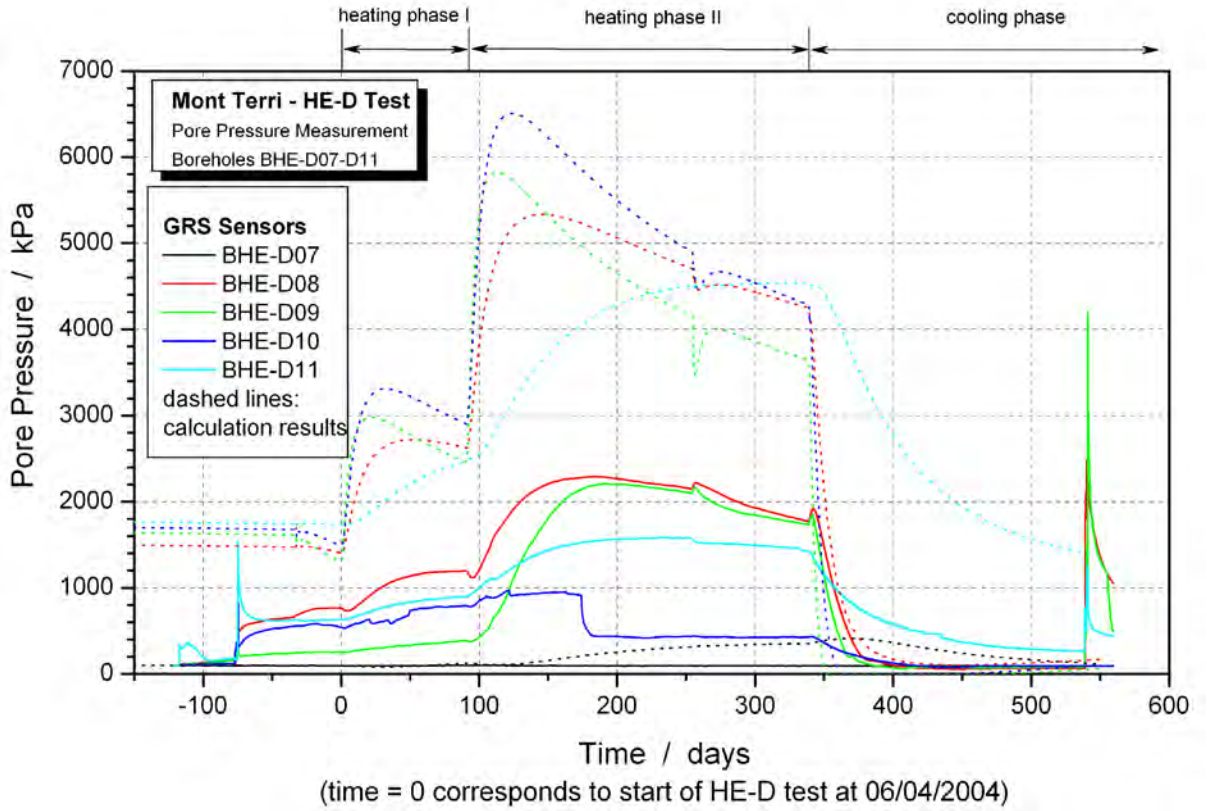

Appendix F-7 Comparison of measured and calculated pore pressures for BHE-D07-D11

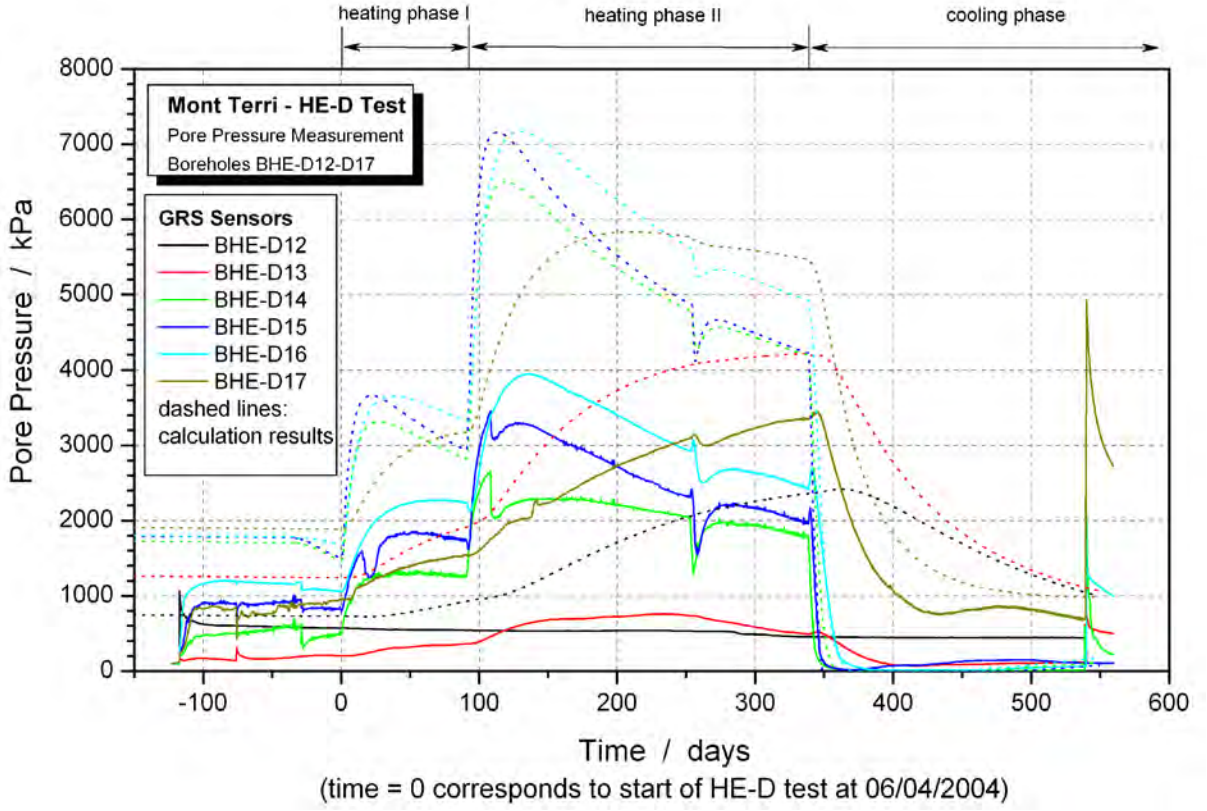

Appendix F-8 Comparison of measured and calculated pore pressures for BHE-D12-D17

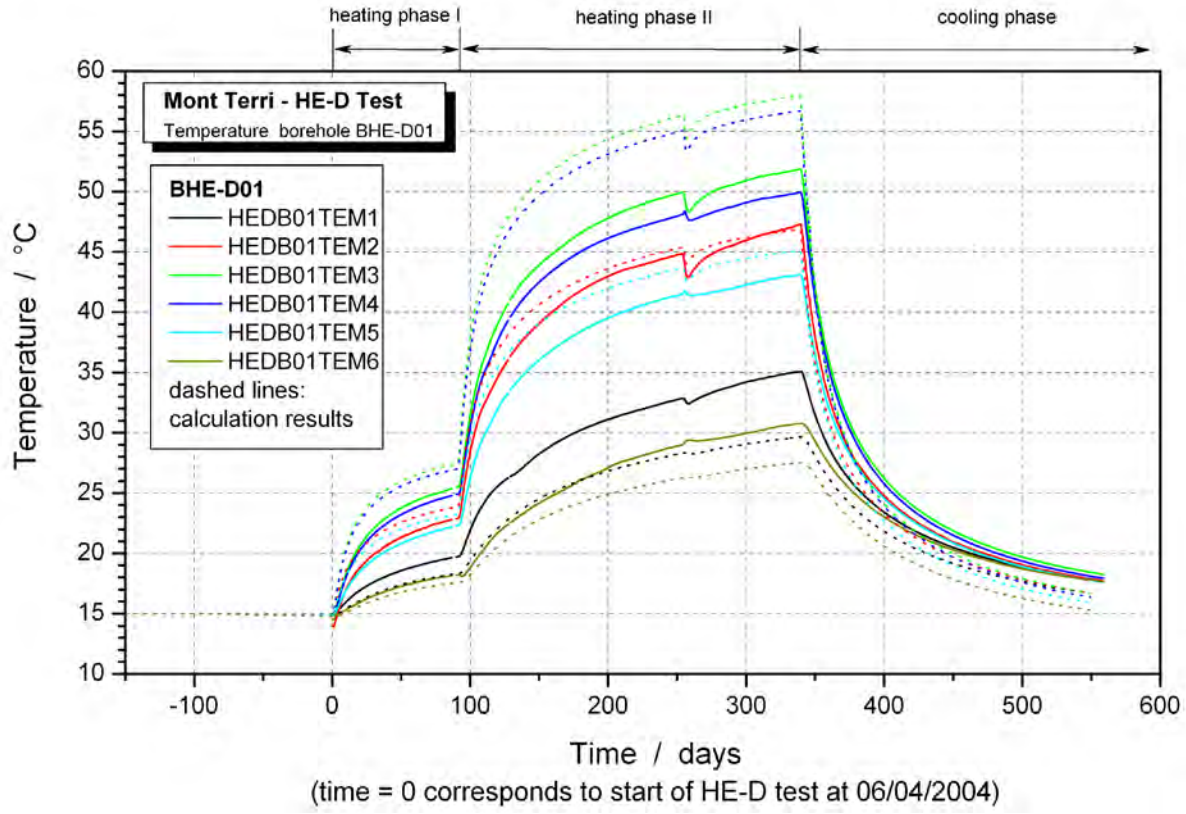

Appendix G-1 Comparison of measured and calculated temperatures for BHE-D01

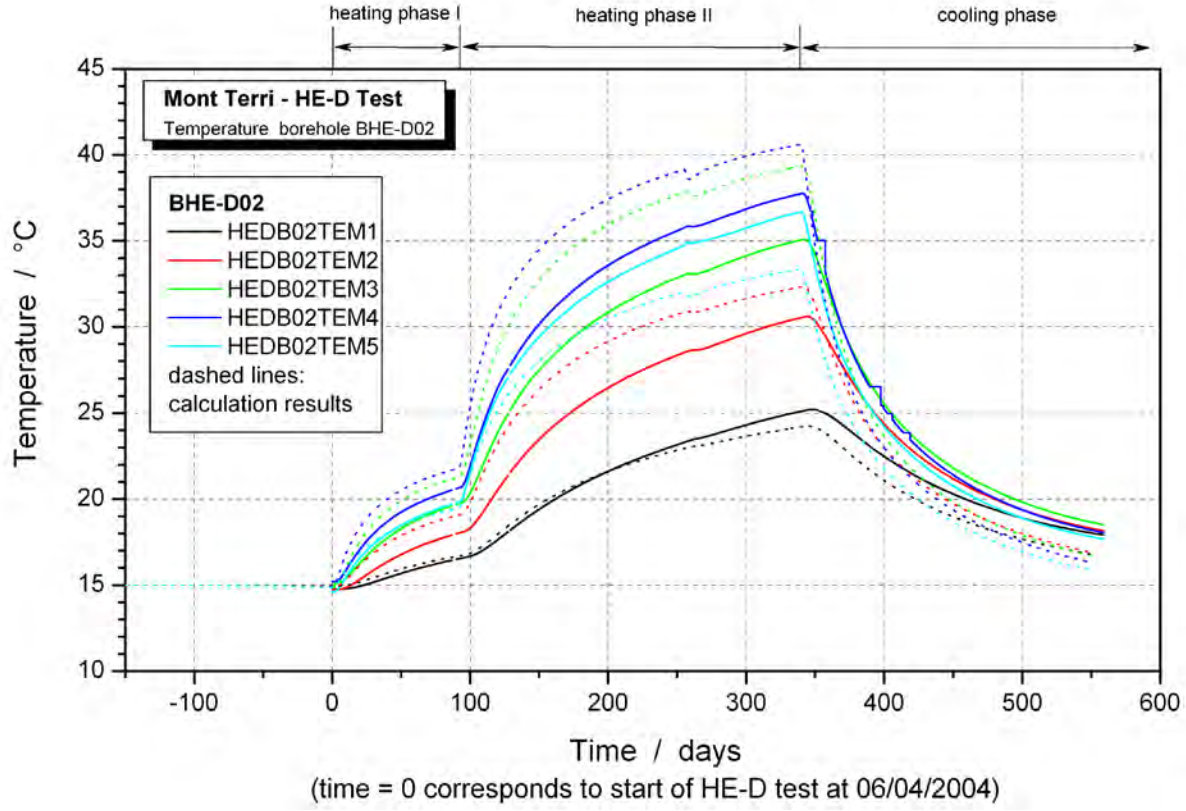

Appendix G-2 Comparison of measured and calculated temperatures for BHE-D02

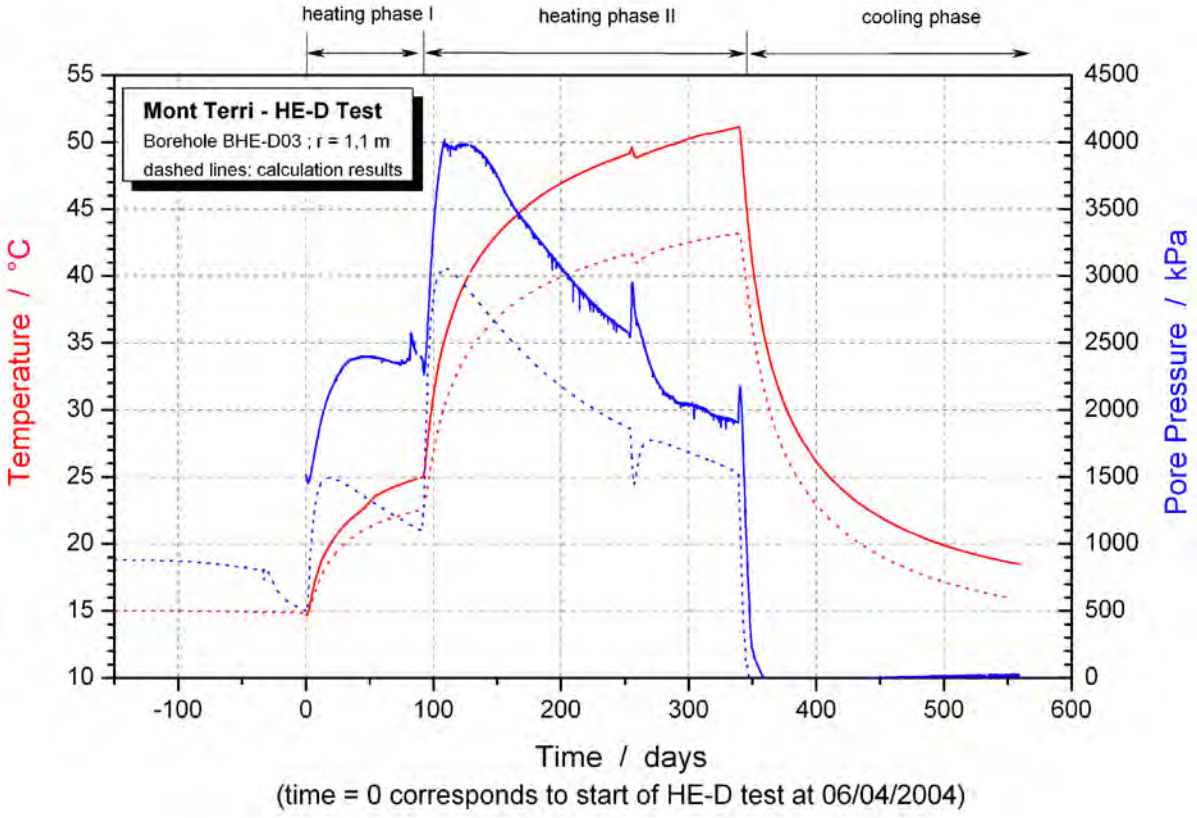

Appendix G-3 Comparison of measured and calculated temperatures and pore pressures for BHE-D03

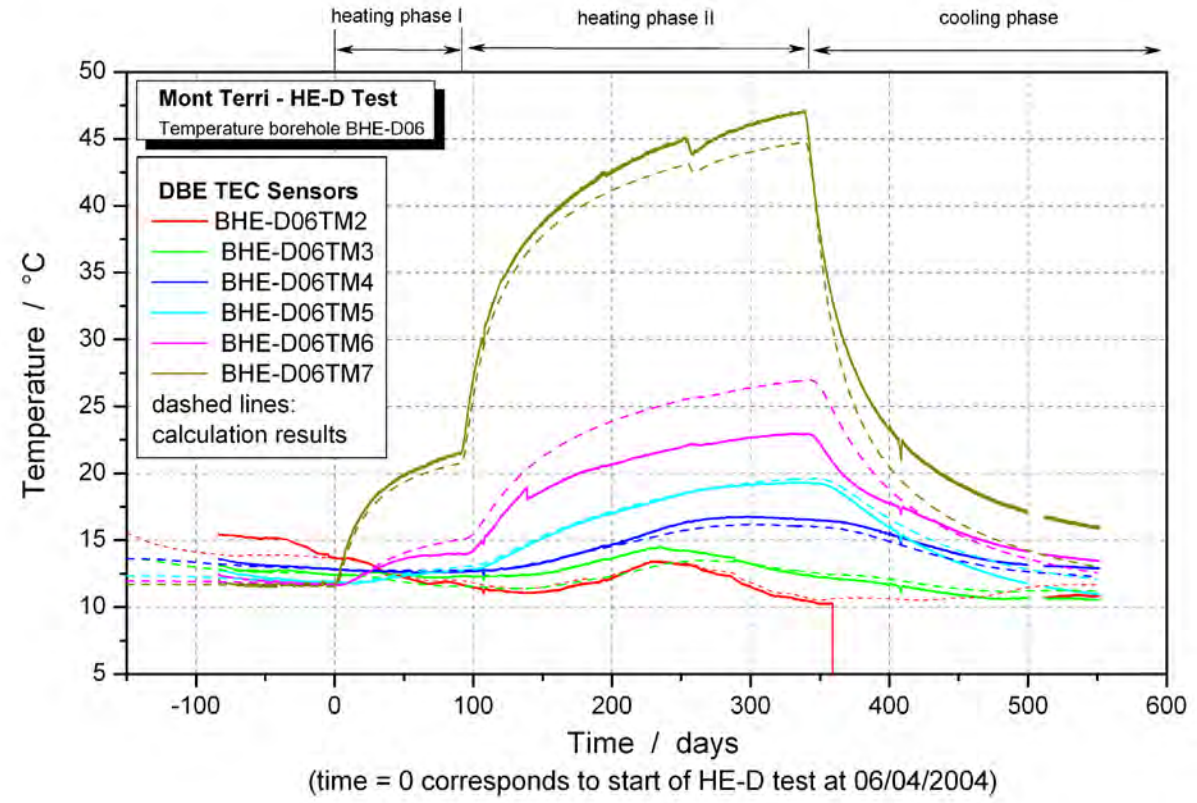

Appendix G-4 Comparison of measured and calculated temperatures for BHE-D06

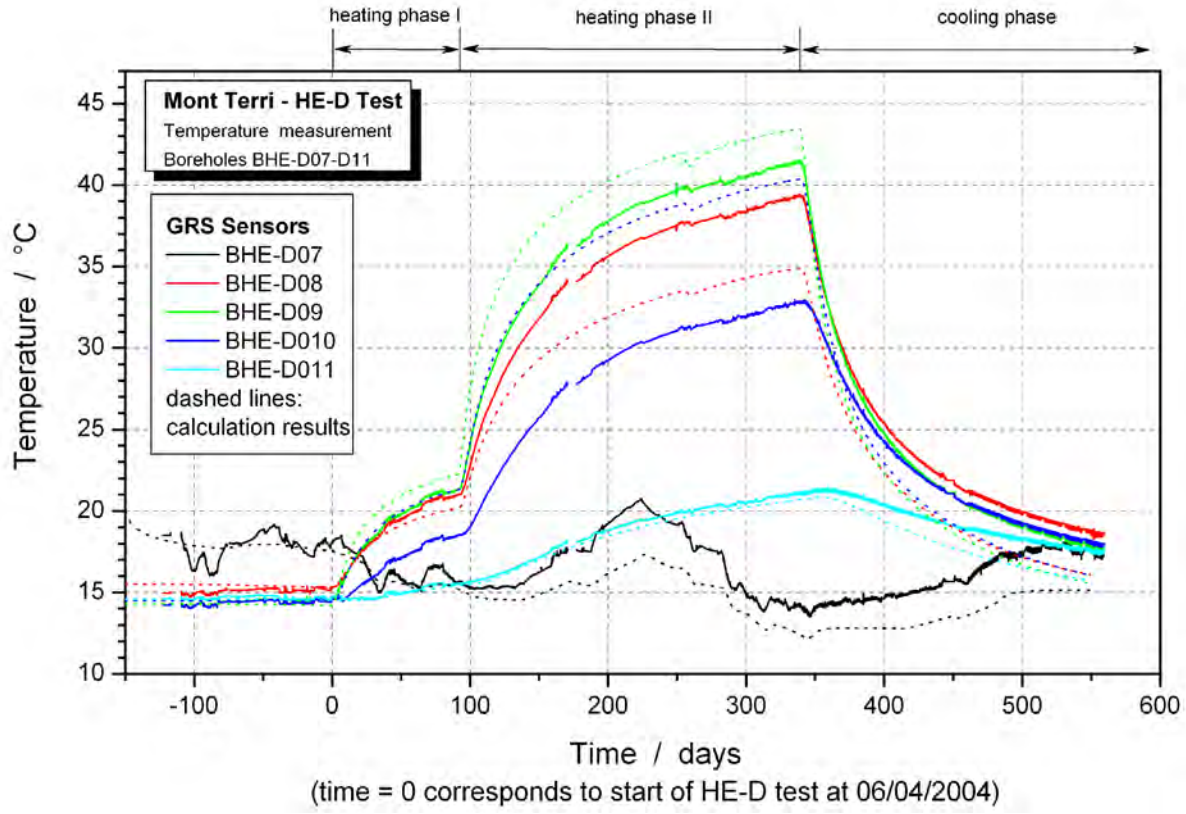

Appendix G-5 Comparison of measured and calculated temperatures for BHE-D07-D11

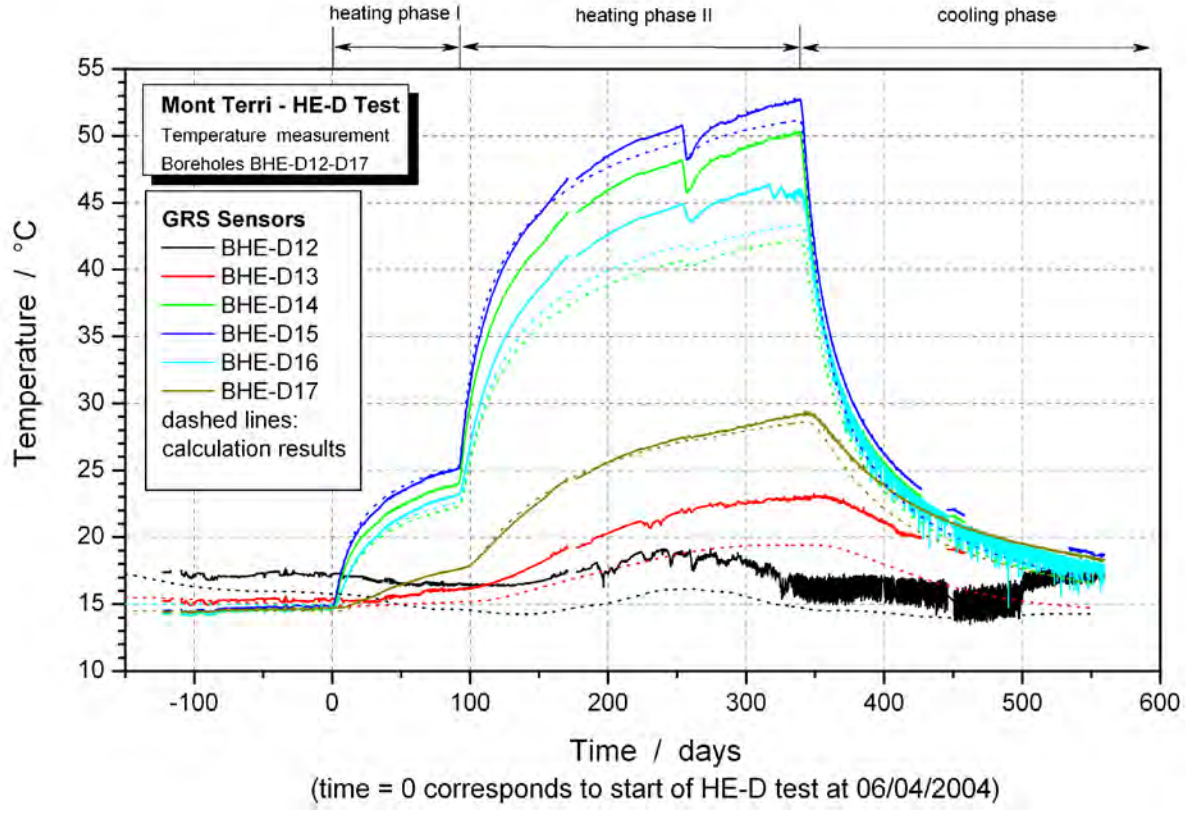

Appendix G-6 Comparison of measured and calculated temperatures for BHE-D12-D17

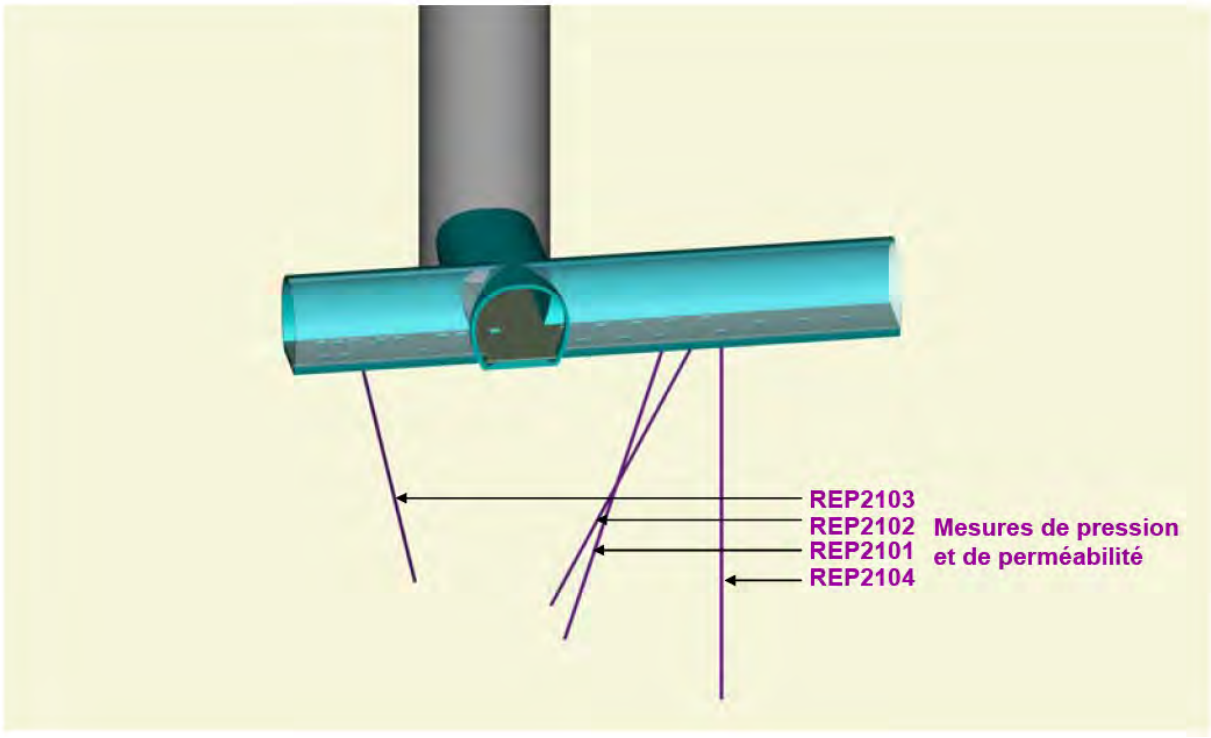

Appendix H-1 Location of boreholes for pore pressure measurement (*ANDRA, 2005d*)

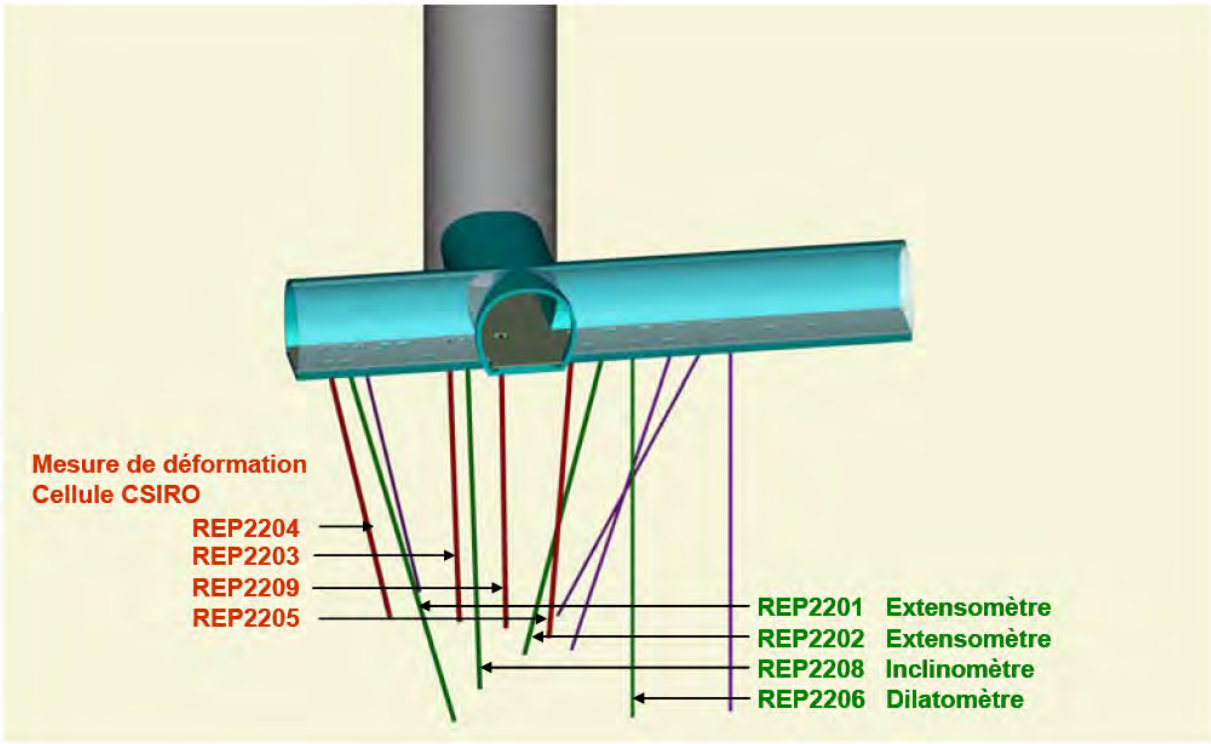

Appendix H-2 Location of boreholes for rock deformation measurement (*ANDRA, 2005d*)

Sensor	Location of sensor (corresponding to coordinate system of ANDRA)				
	x [m] in-situ	y [m] in-situ	z [m] in-situ	r [m] in-situ	difference in-situ – model (3D)
Pore pressure measurement					
REP2101_PRE_01	-5.80	5.45	-461.70	7.96	0.45
REP2101_PRE_03	-4.73	3.75	-466.72	6.04	0.34
REP2101_PRE_05	-4.06	2.67	-469.89	4.85	0.38
REP2102_PRE_03	-4.38	-0.44	-467.05	4.85	0.45
REP2102_PRE_05	-3.96	-2.01	-469.97	4.44	0.39
REP2103_PRE_01	5.09	-0.85	-462.45	5.16	0.17
REP2103_PRE_03	3.92	-4.38	-467.29	5.88	0.36
REP2103_PRE_05	3.25	-6.42	-470.08	7.20	0.54
REP2104_PRE_05	-11.27	12.73	-468.51	5.79	0.50
Displacement / Deformation between 2 points					
REP2201_DFO_06 REP2201_DFO_07	3.99 3.70	4.19 3.89	-468.51 -469.53	5.79 5.36	0.19 0.36
REP2201_DFO_09 REP2201_DFO_10	3.12 2.59	3.28 2.72	-471.56 -473.41	4.52 3.76	0.35 0.40
REP2202_DFO_06 REP2202_DFO_07	-2.10 -1.96	4.46 4.15	-465.47 -466.41	4.94 4.59	0.23 0.35
REP2202_DFO_09 REP2202_DFO_10	-1.64 -1.49	3.46 3.15	-468.47 -469.41	3.83 3.48	0.25 0.34
Convergence of shaft wall					
N60°E			-467.00	3.0	0.07
N150°E			-467.00	3.0	0.07

Appendix H-3 Locations of sensors used for comparison purpose
right figure: used coordinate system

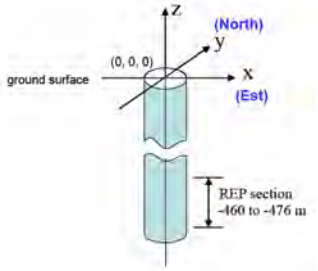

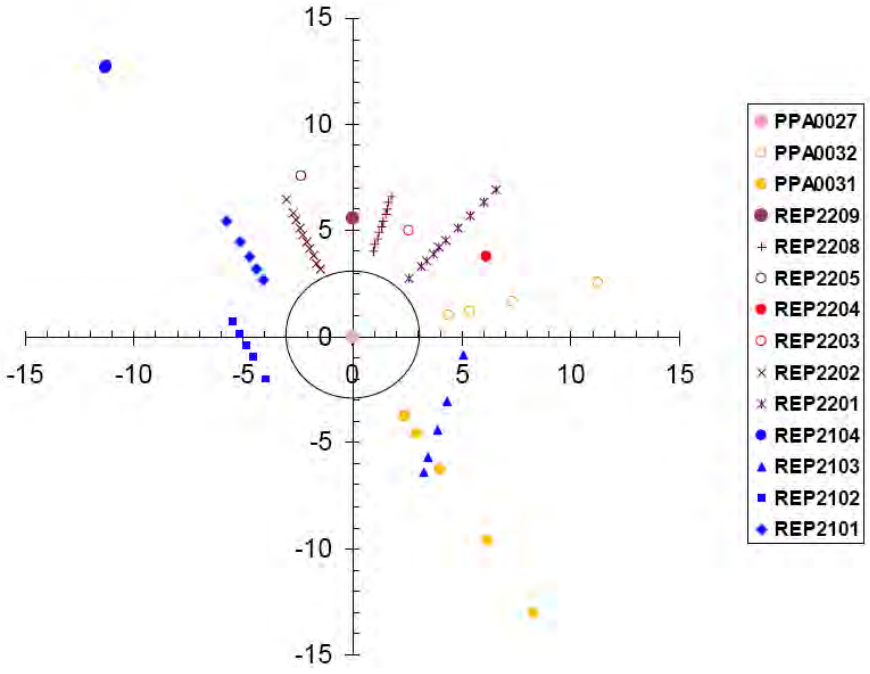

Appendix H-4 Locations of sensors in the rock mass (shown in a horizontal plane)

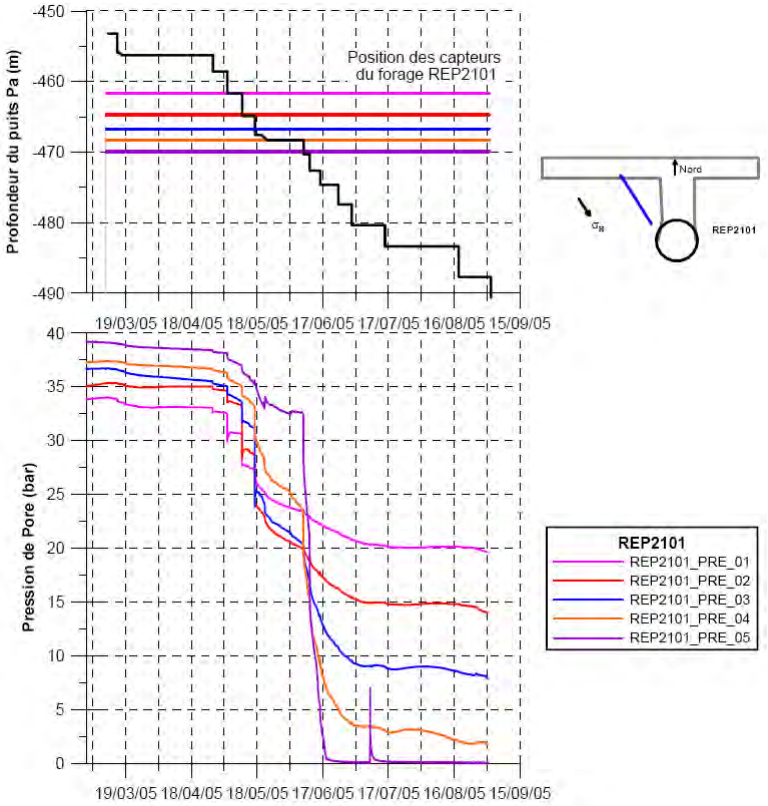

Appendix I-1 Pore pressure measurement in borehole REP2101 (*ANDRA, 2005d*)

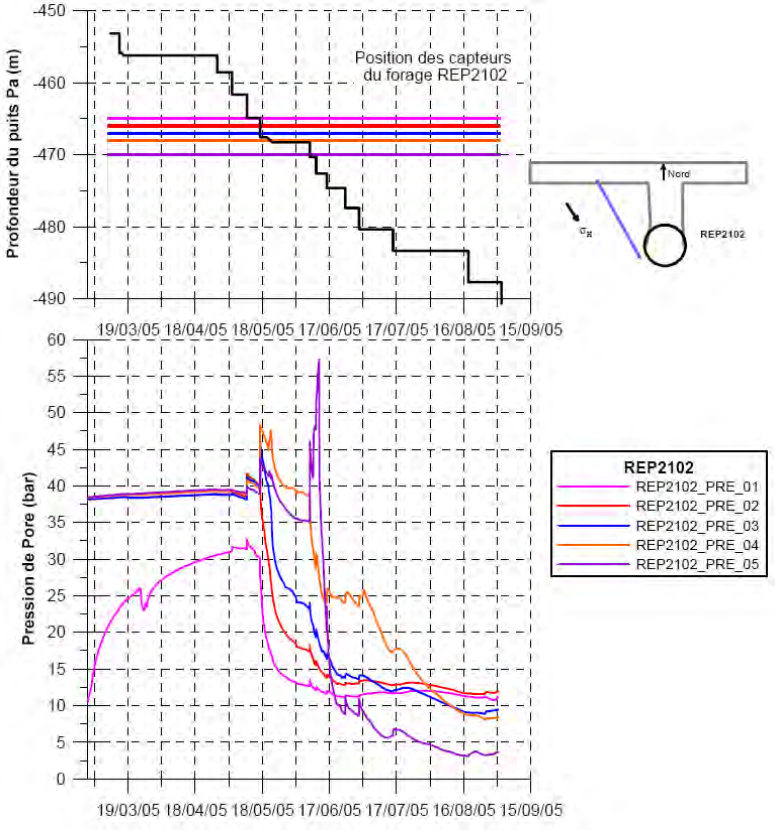

Appendix I-2 Pore pressure measurement in borehole REP2102 (*ANDRA, 2005d*)

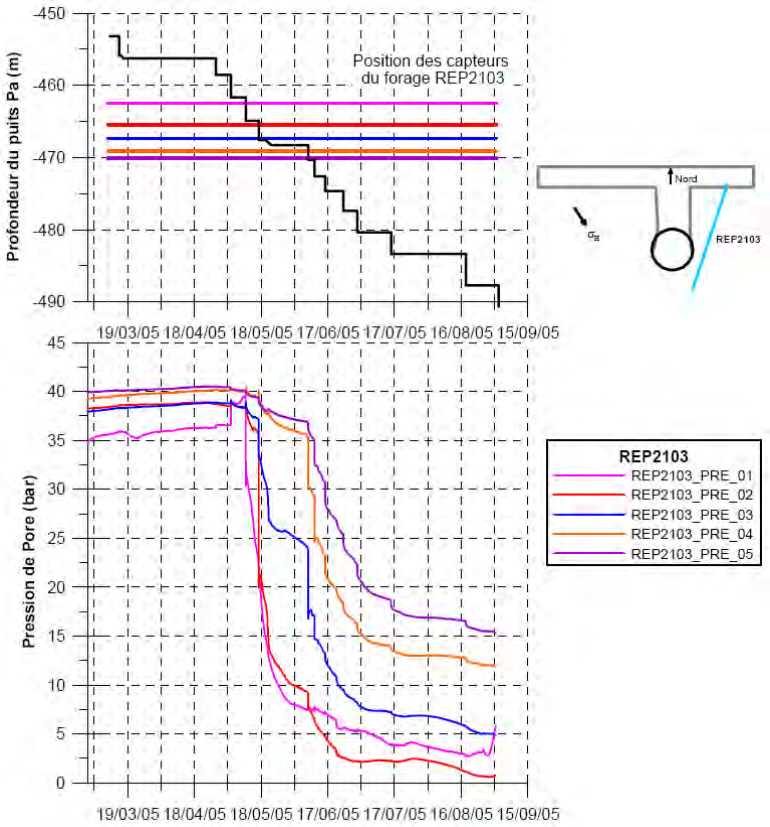

Appendix I-3 Pore pressure measurement in borehole REP2103 (*ANDRA, 2005d*)

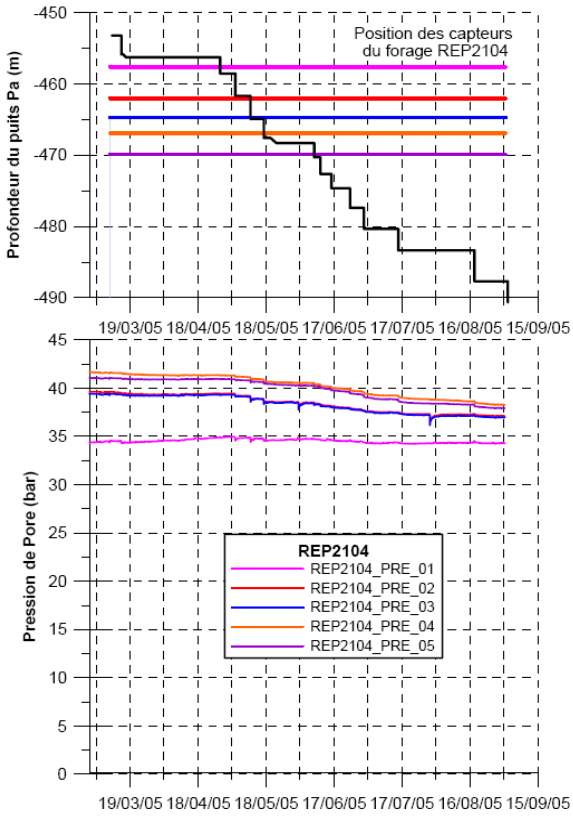

Appendix I-4 Pore pressure measurement in borehole REP2104 (*ANDRA, 2005d*)

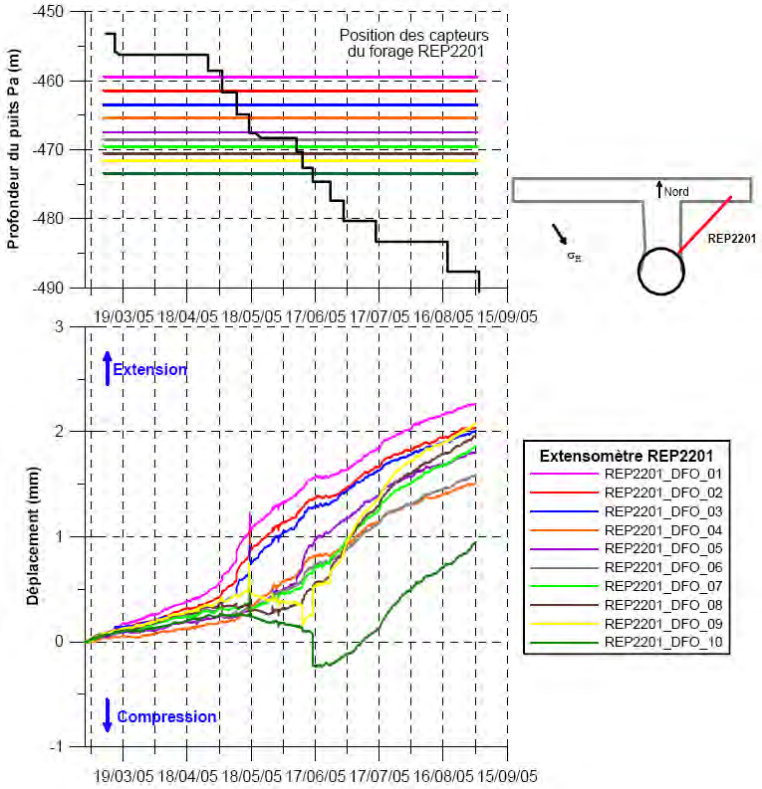

Appendix I-5 Extensometer measurement in borehole REP2201 (corrected by SUG2009 measurement, *ANDRA, 2005d*)

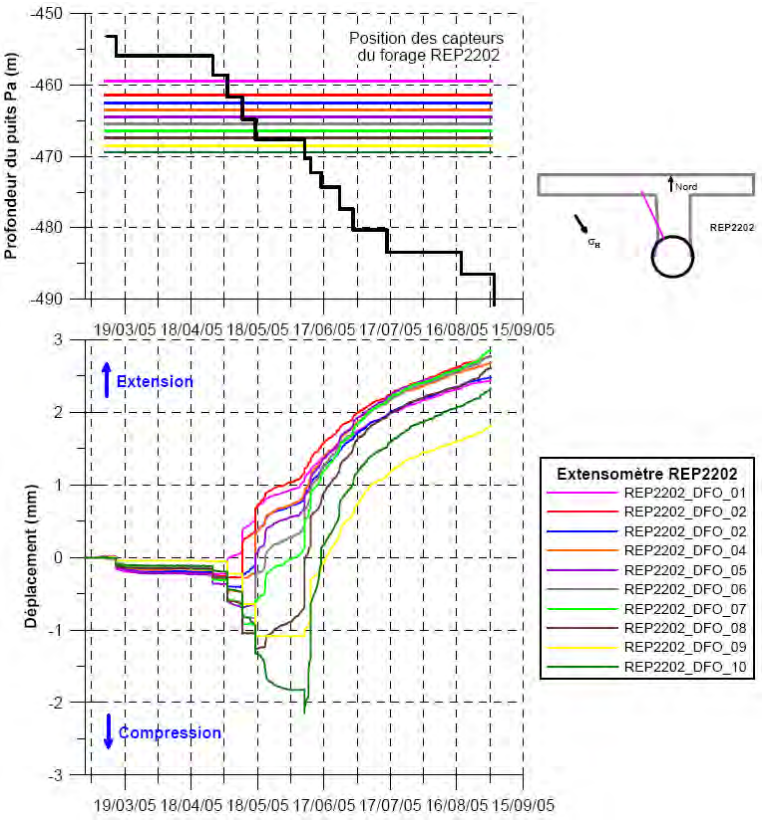

Appendix I-6 Extensometer measurement in borehole REP2202 (*ANDRA, 2005d*)

The argillites formation is 130m thick and is located at –418m to –548m [7] depth. The layer is subdivided into five geomechanical unites, but in terms of rheological model, we distinguish three zones with significant different mechanical behaviours (same constitutive model in the three layers but with different parameters) A', B', C'. The argillites layer is horizontal.

Table : Geomechanical units of the Callovo-Oxfordian argillites

Lithofacies	Rheological zone	Geomechanical units	Access shaft of the MHM-URL (based on the borehole EST204)
C2d	A' Upper zone	A	418 - 460
C2c			
C2b2	B' Middle zone	B	460 - 473,5
C2b1		C	473,5 – 515
	C' Lower zone	D	515 - 527
C2a		E	527 - 548

Appendix J-1 Geological and geomechanical units (Hypothesis H1, *ANDRA, 2005b*)

Table : In situ stress in the Meuse/Haute-Marne site

Stress	Orientation	Value
σ_v	Vertical	$= \gamma_1 Z$ for $Z > -417$ m with $\gamma_1 = 24700$ N/m^3 $= 417\,\gamma_1 + \gamma_2 (Z + 417)$ for $Z < -417$ m with $\gamma_2 = 24200$ N/m^3 (ground surface Z = 0)
σ_h	N62.5°	$K_h * \sigma_v$ with $K_h=1$
σ_H	N152.5°	$K_H * \sigma_v$ with $K_H=1,3$

Appendix J-2 In-situ stress orientation and values (Hypothesis H3, *ANDRA, 2005b*)

date	Blast level (m)	debris remove level (m)	Concreting level (m)	N° of blast	Hour	N° of sequence
10/03/05	-451,38	-451,38	-429	79	23:25	V 180
11/03/05	-453,2	-451,38	-429			
12/03/05	-453,2	-451,38	-429			
13/03/05	-453,2	-451,38	-429			
14/03/05	-453,2	-453,2	-429			
15/03/05	-455,9	-453,2	-429	80	03:25	V 181
16/03/05	-455,9	-453,2	-429			
17/03/05	-455,9	-453,2	-429			
18/03/05	-455,9	-456,3	-429			
19/03/05	-455,9	-456,3	-429			
20/03/05	-455,9	-456,3	-429			
21/03/05	-455,9	-456,3	-429			
22/03/05	-455,9	-456,3	-429			
23/03/05	-455,9	-456,3	-429			
24/03/05	-455,9	-456,3	-429			
25/03/05	-455,9	-456,3	-429			
26/03/05	-455,9	-456,3	-429			
27/03/05	-455,9	-456,3	-429			
28/03/05	-455,9	-456,3	-429			
29/03/05	-455,9	-456,3	-429			
30/03/05	-455,9	-456,3	-429			
31/03/05	-455,9	-456,3	-429			
01/04/05	-455,9	-456,3	-429			
02/04/05	-455,9	-456,3	-429			
03/04/05	-455,9	-456,3	-429			
04/04/05	-455,9	-456,3	-429			
05/04/05	-455,9	-456,3	-429			
06/04/05	-455,9	-456,3	-429			
07/04/05	-455,9	-456,3	-429			
08/04/05	-455,9	-456,3	-429			
09/04/05	-455,9	-456,3	-429			
10/04/05	-455,9	-456,3	-429			
11/04/05	-455,9	-456,3	-429			
12/04/05	-455,9	-456,3	-429			
13/04/05	-455,9	-456,3	-429			
14/04/05	-455,9	-456,3	-429			
15/04/05	-455,9	-456,3	-429			
16/04/05	-455,9	-456,3	-429			
17/04/05	-455,9	-456,3	-429			
18/04/05	-455,9	-456,3	-429			
19/04/05	-455,9	-456,3	-429			
20/04/05	-455,9	-456,3	-429			
21/04/05	-455,9	-456,3	-435			
22/04/05	-455,9	-456,3	-441			
23/04/05	-455,9	-456,3	-441			
24/04/05	-455,9	-456,3	-441			
25/04/05	-455,9	-456,3	-441			
26/04/05	-455,9	-456,3	-447			
27/04/05	-455,9	-456,3	-447	81	18:27	V 182
28/04/05	-458,6	-456,3	-447			
29/04/05	-458,6	-456,3	-447			
30/04/05	-458,6	-456,3	-447			

continuation:

01/05/05	-458,6	-456,3	-447			
02/05/05	-458,6	-456,3	-447			
03/05/05	-458,6	-456,3	-447			
04/05/05	-461,7	-458,6	-447	82	11:48	V 183
05/05/05	-461,7	-458,6	-447			
06/05/05	-461,7	-458,6	-447			
07/05/05	-461,7	-458,6	-447			
08/05/05	-461,7	-458,6	-447			
09/05/05	-461,7	-458,6	-447			
10/05/05	-461,7	-458,6	-447			
11/05/05	-464,77	-461,67	-447	83	04:40	V 184
12/05/05	-464,77	-461,67	-447			
13/05/05	-464,77	-461,67	-447			
14/05/05	-464,77	-461,67	-447			
15/05/05	-464,77	-461,67	-447			
16/05/05	-464,89	-464,89	-447			
17/05/05	-467,6	-464,89	-447	84	01:10	V 185
18/05/05	-467,6	-464,89	-447			
19/05/05	-467,6	-464,89	-447			
20/05/05	-467,6	-464,89	-447			
21/05/05	-467,6	-464,89	-447			
22/05/05	-467,6	-464,89	-447			
23/05/05	-467,6	-468,3	-447			
24/05/05	-467,6	-468,3	-447			
25/05/05	-467,6	-468,3	-447			
26/05/05	-467,6	-468,3	-447			
27/05/05	-467,6	-468,3	-447			
28/05/05	-467,6	-468,3	-447			
29/05/05	-467,6	-468,3	-447			
30/05/05	-467,6	-468,3	-447			
31/05/05	-467,6	-468,3	-447			
01/06/05	-467,6	-468,3	-447			
02/06/05	-467,6	-468,3	-447			
03/06/05	-467,6	-468,3	-447			
04/06/05	-467,6	-468,3	-447			
05/06/05	-467,6	-468,3	-447			
06/06/05	-467,6	-468,3	-453			
07/06/05	-467,6	-468,3	-453			
08/06/05	-467,6	-468,3	-453	85	07:15	V 186
09/06/05	-470,3	-468,3	-453			
10/06/05	-470,3	-468,3	-453			
11/06/05	-470,3	-468,3	-453	86	01:36	V 187
12/06/05	-472,3	-468,3	-453			
13/06/05	-472,3	-470,31	-453			
14/06/05	-472,3	-470,31	-453			
15/06/05	-472,3	-470,31	-453	87	21:30	V 188
16/06/05	-474,3	-472,31	-453			

Appendix J-3 Advancement of shaft sinking (Hypothesis H7, *ANDRA, 2005b*)

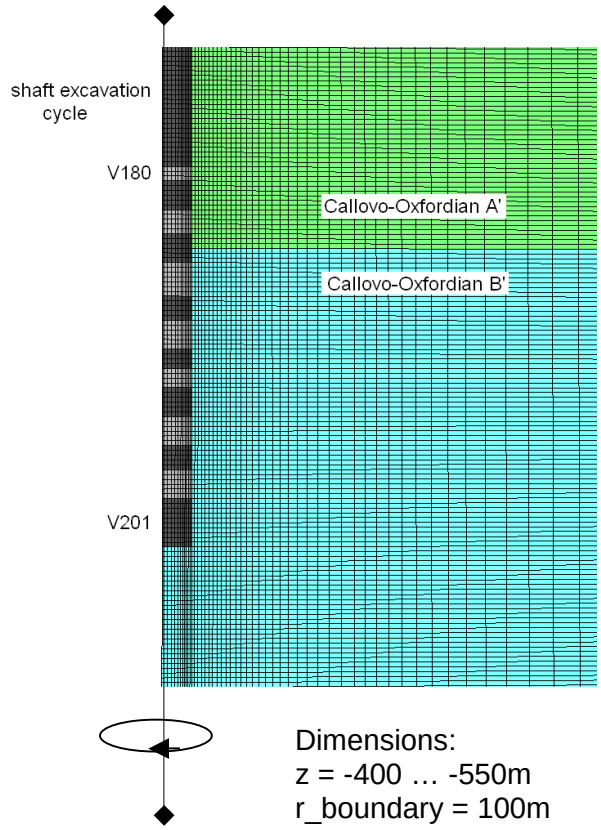

Appendix K-1 Detail of the axially-symmetric 2D-model (18.300 zones & 37.000 gridpoints)

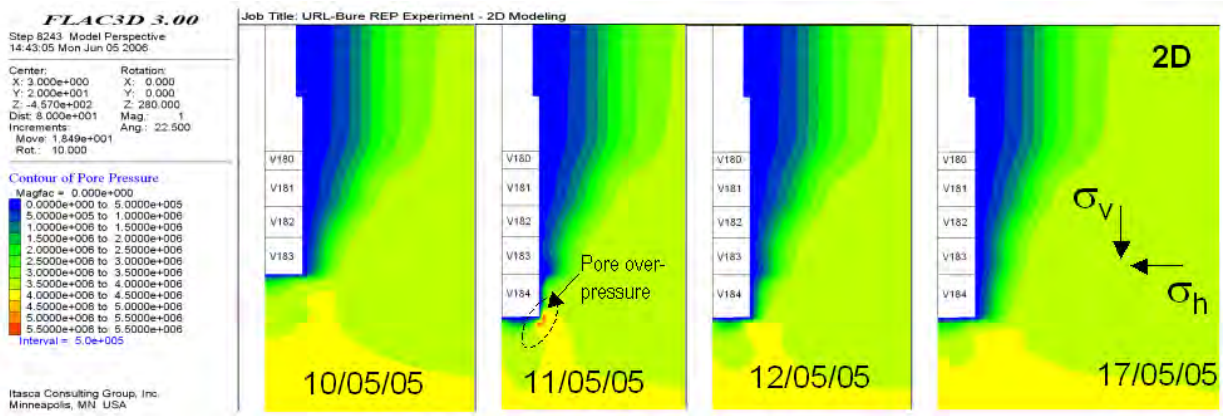

Appendix K-2 Pore pressure distribution before and after excavation cycle 184

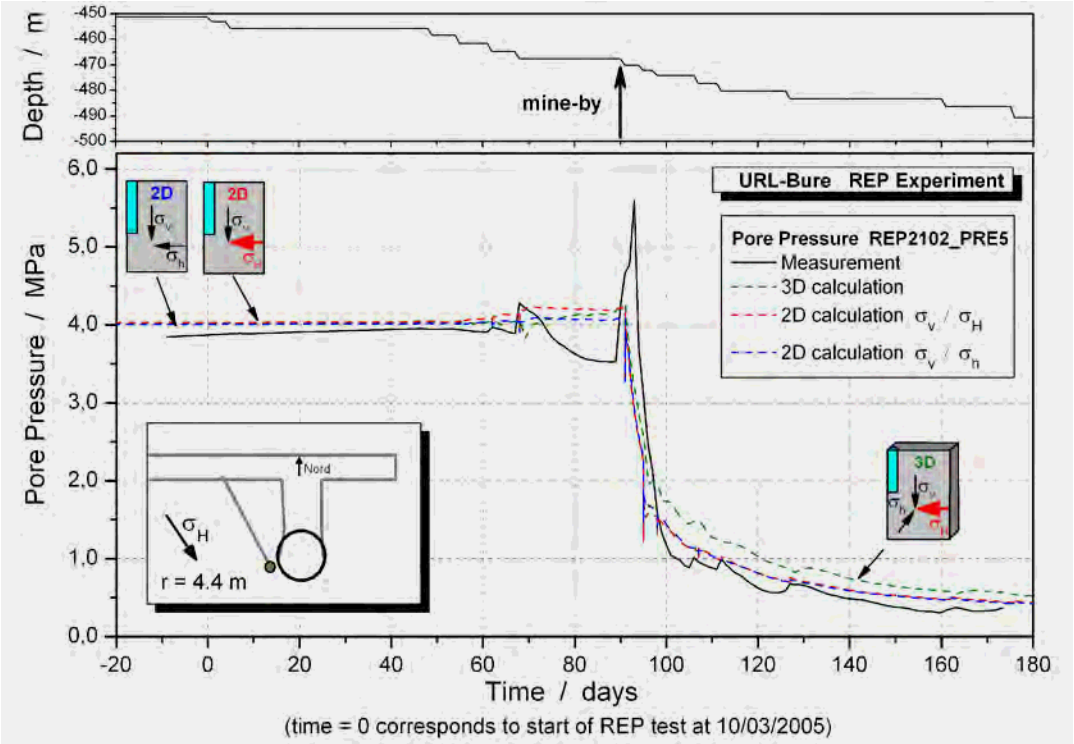

Appendix K-3 Comparison of measured and calculated pore pressures, interpretive modeling for sensor REP2102_PRE5

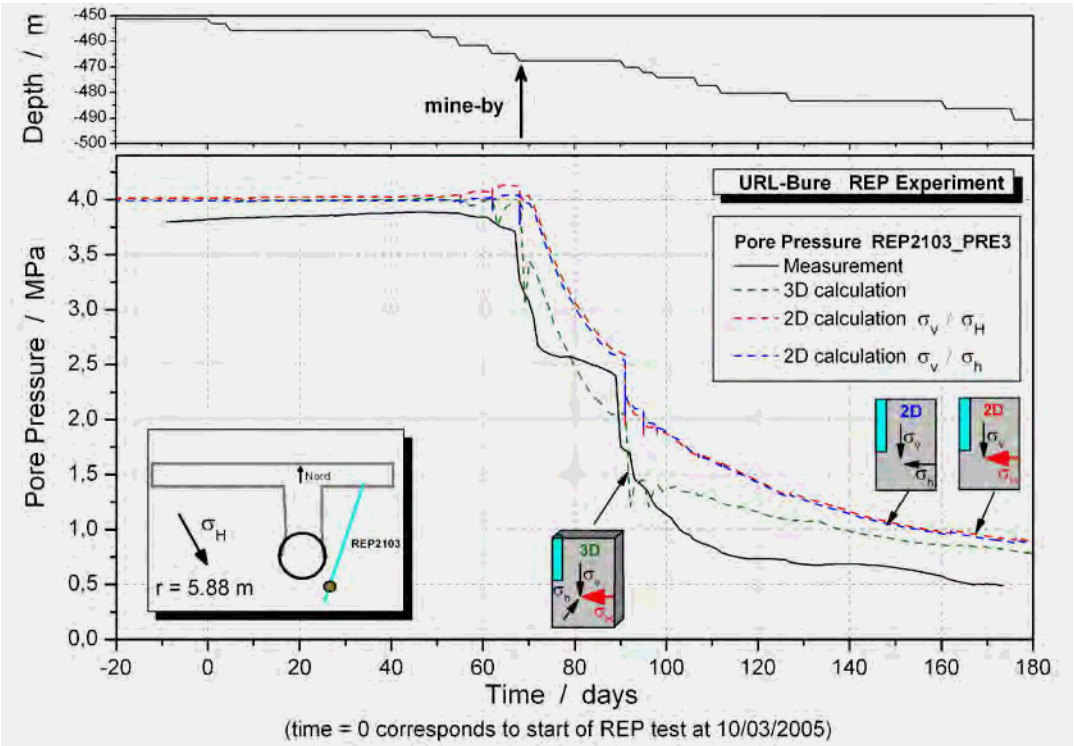

Appendix K-4 Comparison of measured and calculated pore pressures, interpretive modeling for sensor REP2103_PRE3

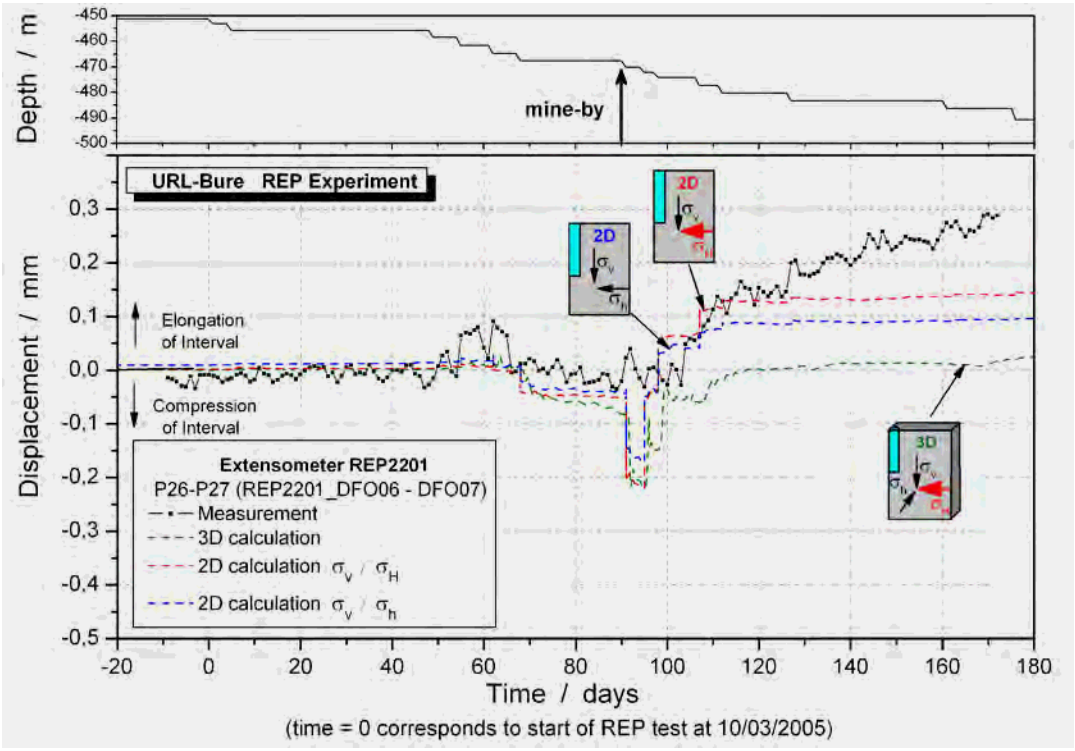

Appendix K-5 Comparison of measured and calculated displacements, extensometer REP2201_DFO06 – DFO07

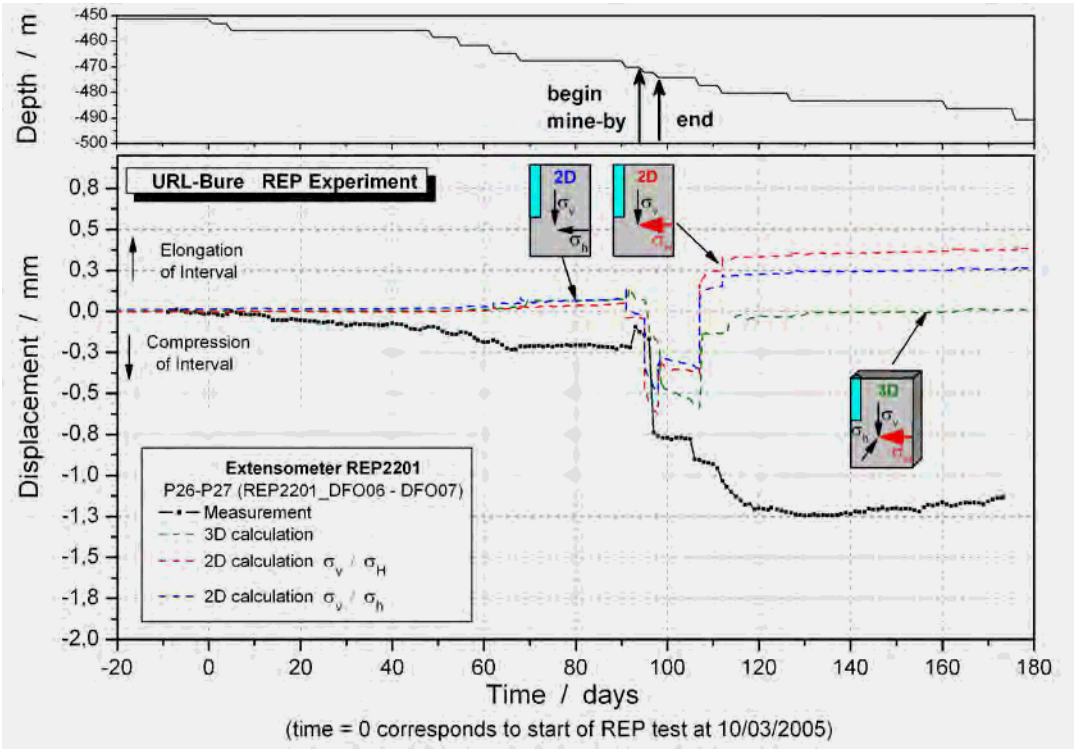

Appendix K-6 Comparison of measured and calculated displacements, extensometer REP2201_DFO09 – DFO10

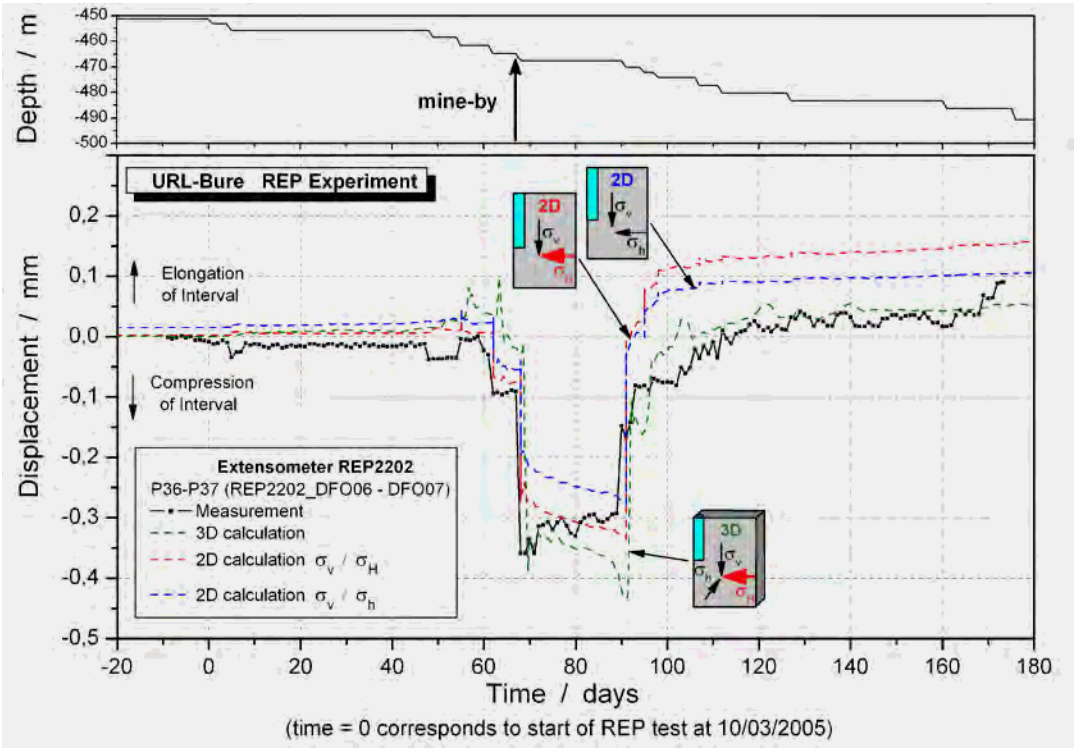

Appendix K-7 Comparison of measured and calculated displacements, extensometer REP2202_DFO06 – DFO07

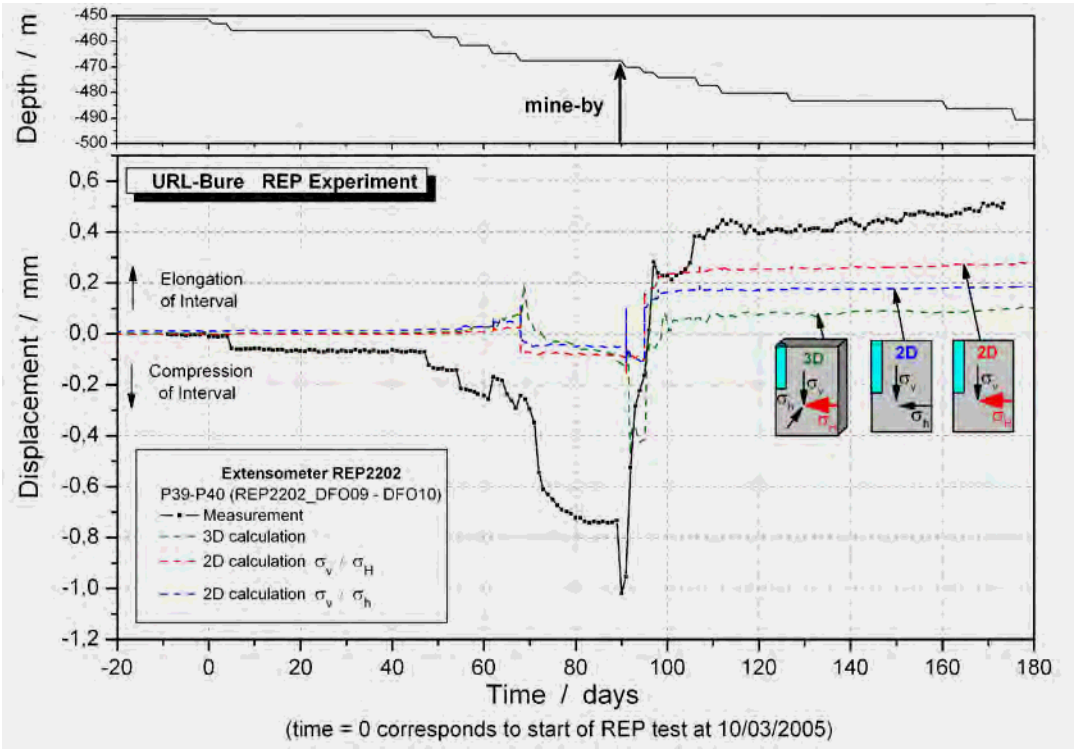

Appendix K-8 Comparison of measured and calculated displacements, extensometer REP2202_DFO09 – DFO10

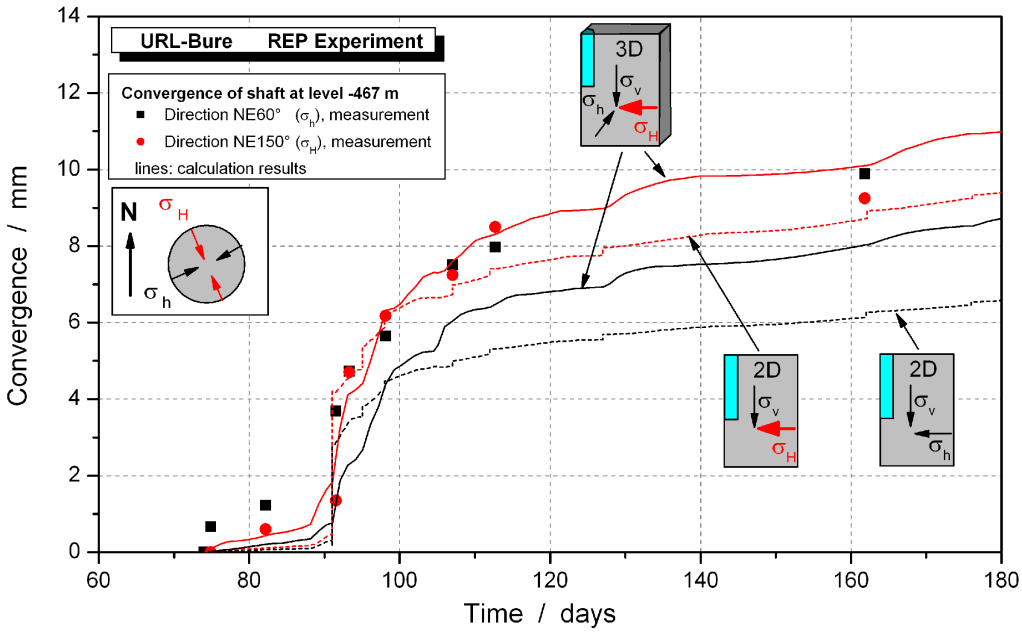

(time = 0 corresponds to start of REP test at 10/03/2005)

Appendix K-9 Comparison of measured and calculated convergences

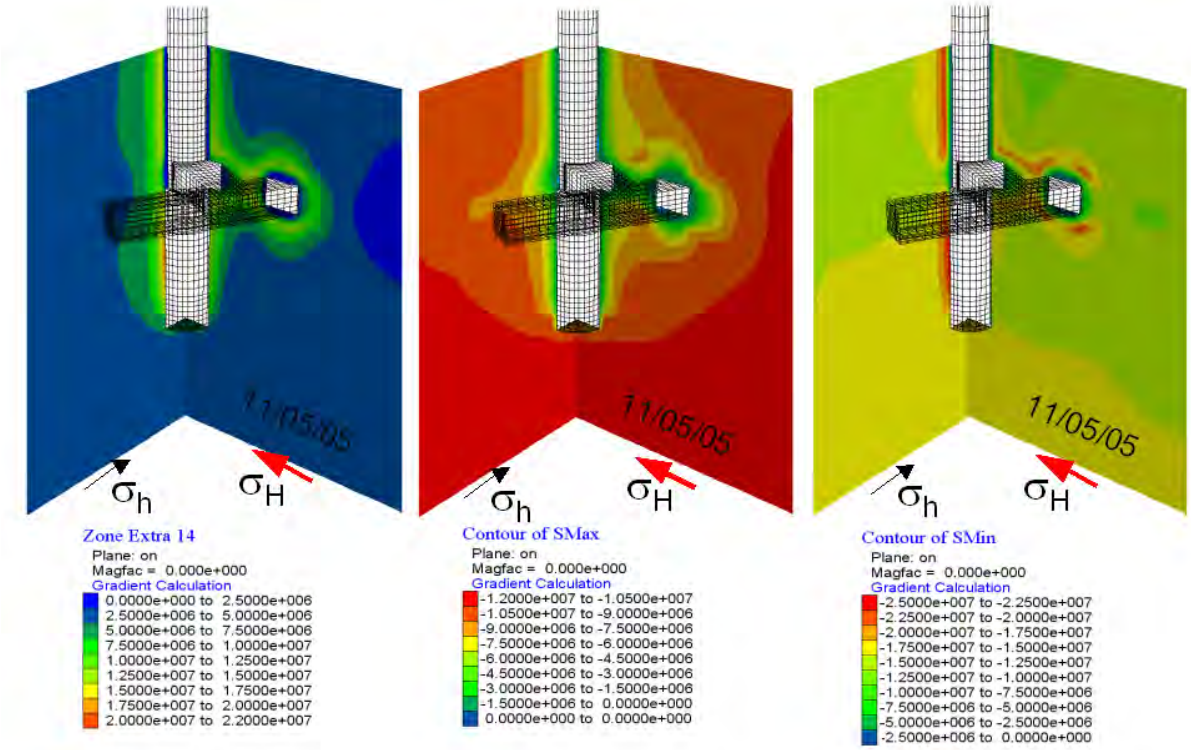

von Mises stress [Pa] σ_3 [Pa] σ_1 [Pa]

Appendix L-1 Stress field for cross section along initial principal stress planes; view from NNE (convention: compressive stresses are negative)

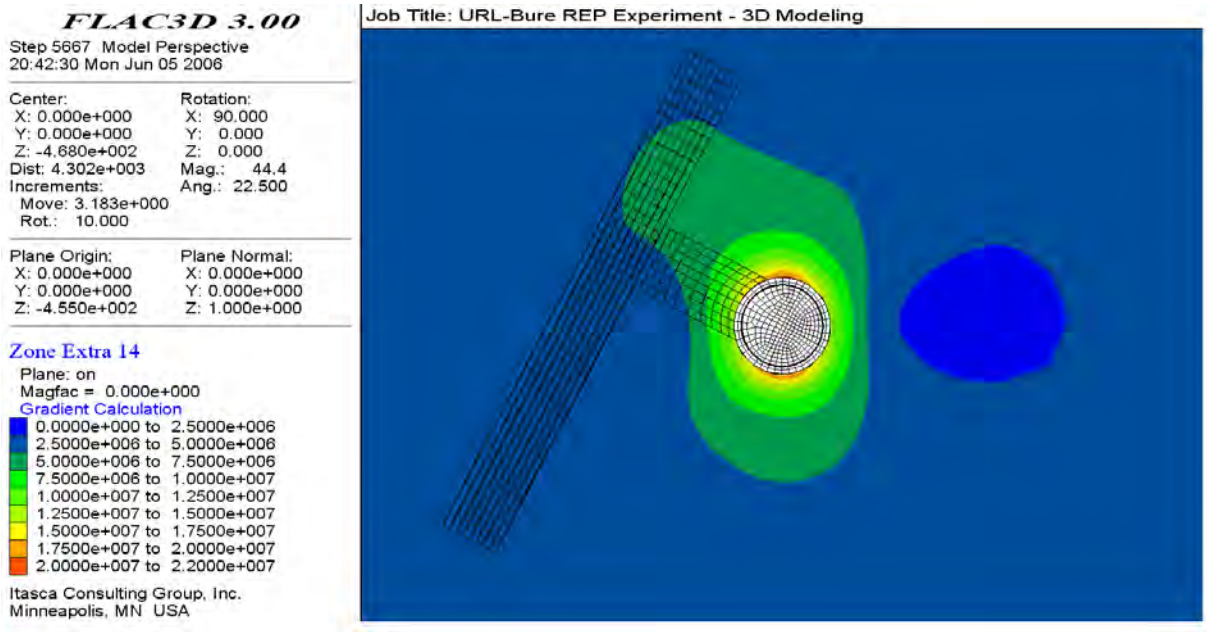

Appendix L-2 von Mises stress [Pa], horizontal cross section at –455 m

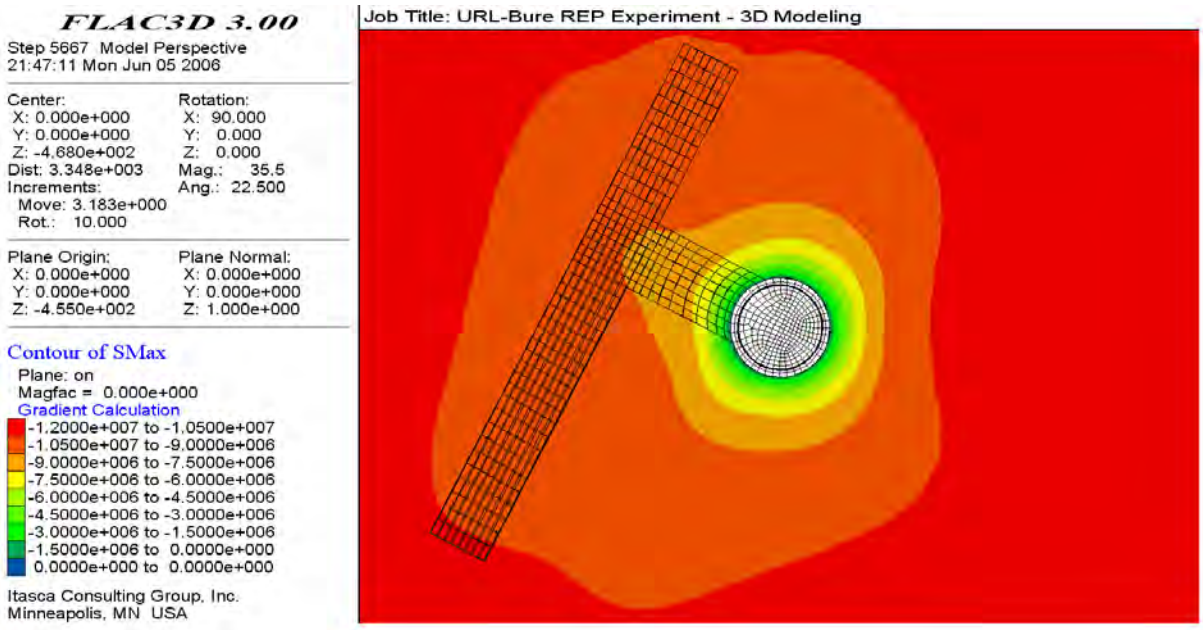

Appendix L-3 Minimum principle stress σ_3 [Pa], horizontal cross section at –455 m (convention: compressive stresses are negative)

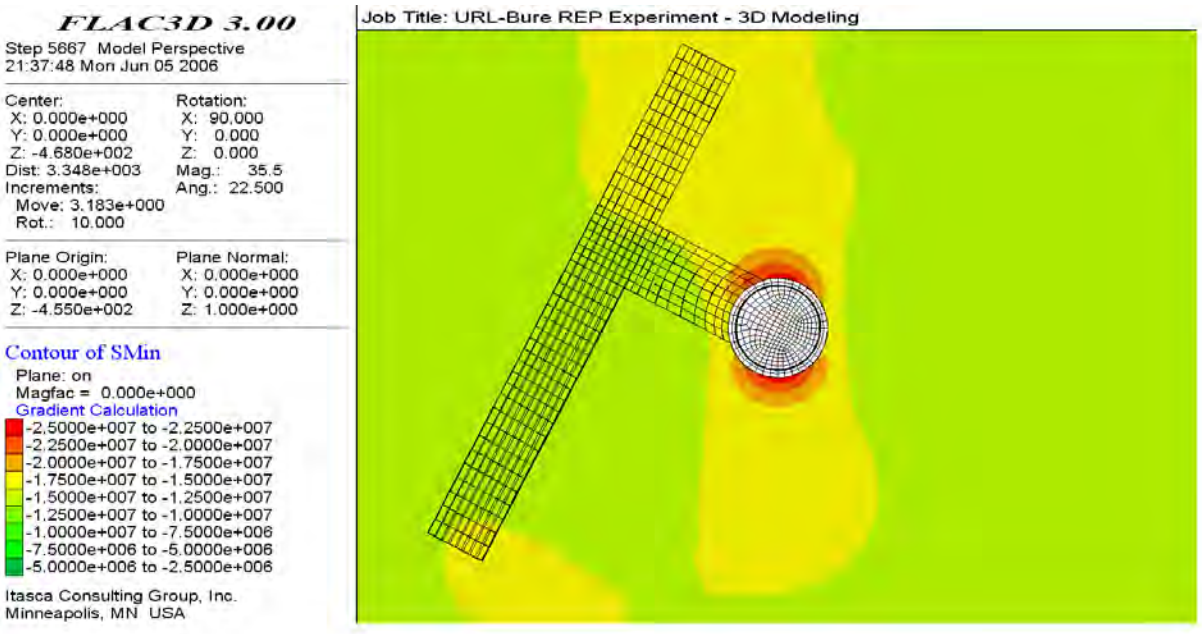

Appendix L-4 Maximum principle stress σ_1 [Pa], horizontal cross section at –455 m (convention: compressive stresses are negative)

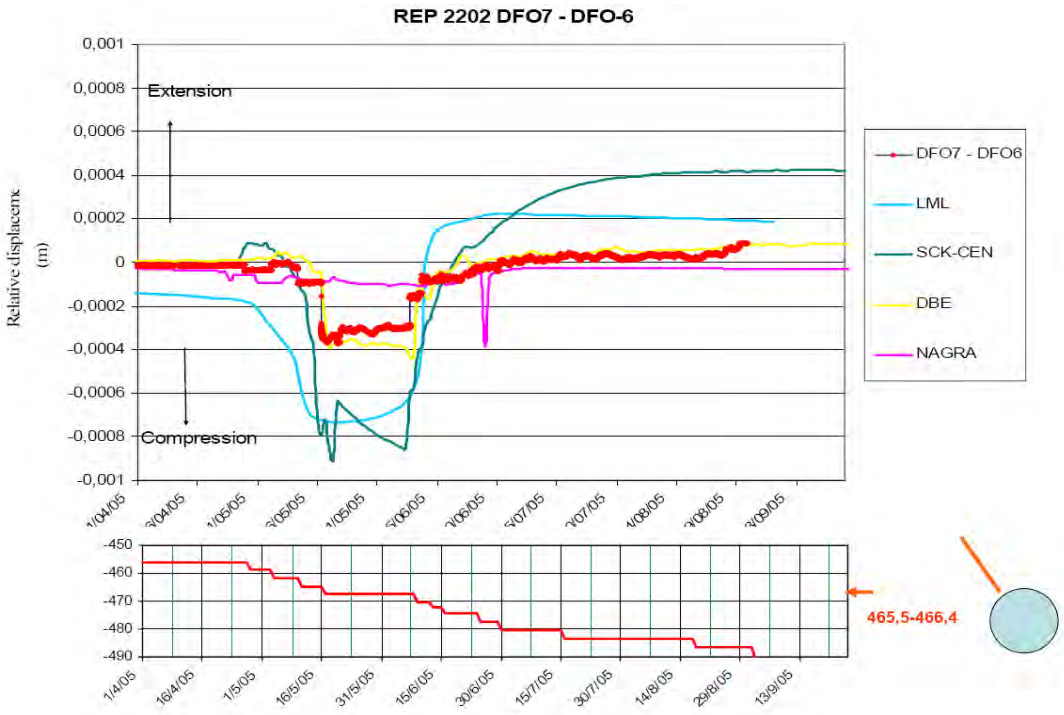

Appendix M-1 Interval deformation for extensometer REP 2202 DFO07 – DFO06 Comparison between measurement results and blind prediction results of various modeling teams (shaft far-field, *SU 2006b*)

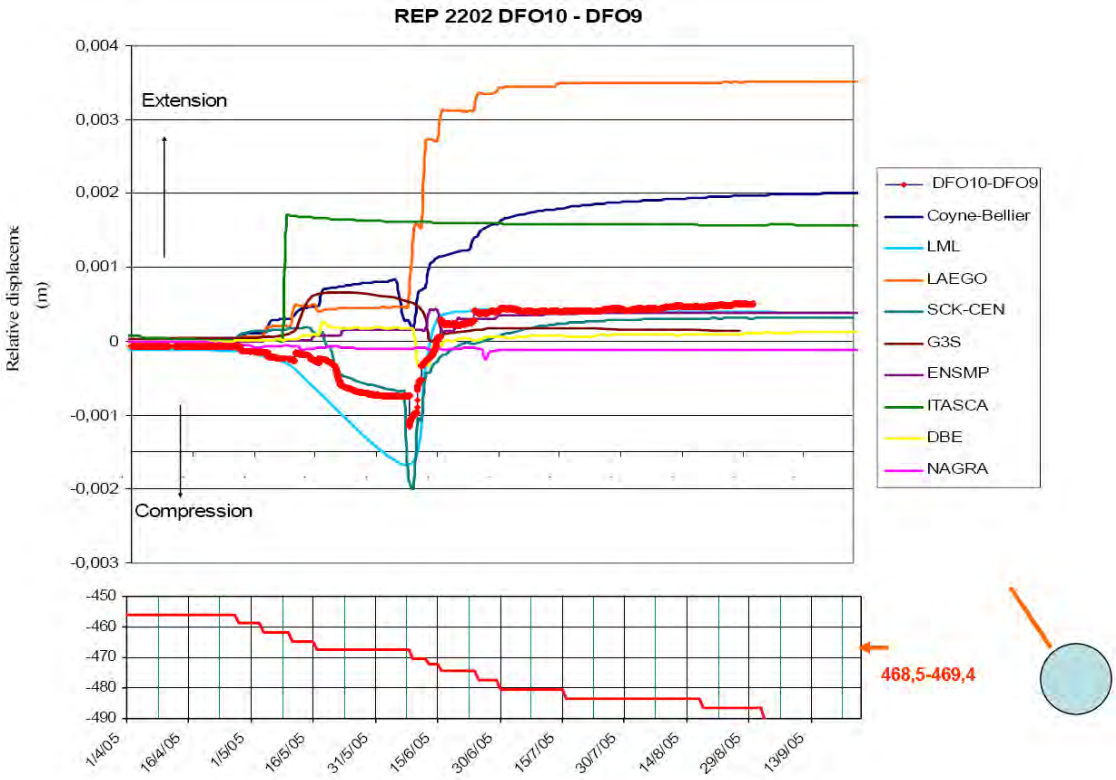

Appendix M-2 Interval deformation for extensometer REP 2202 DFO10 – DFO09 Comparison between measurement results and blind prediction results of various modeling teams (shaft near-field, *SU 2006b*)

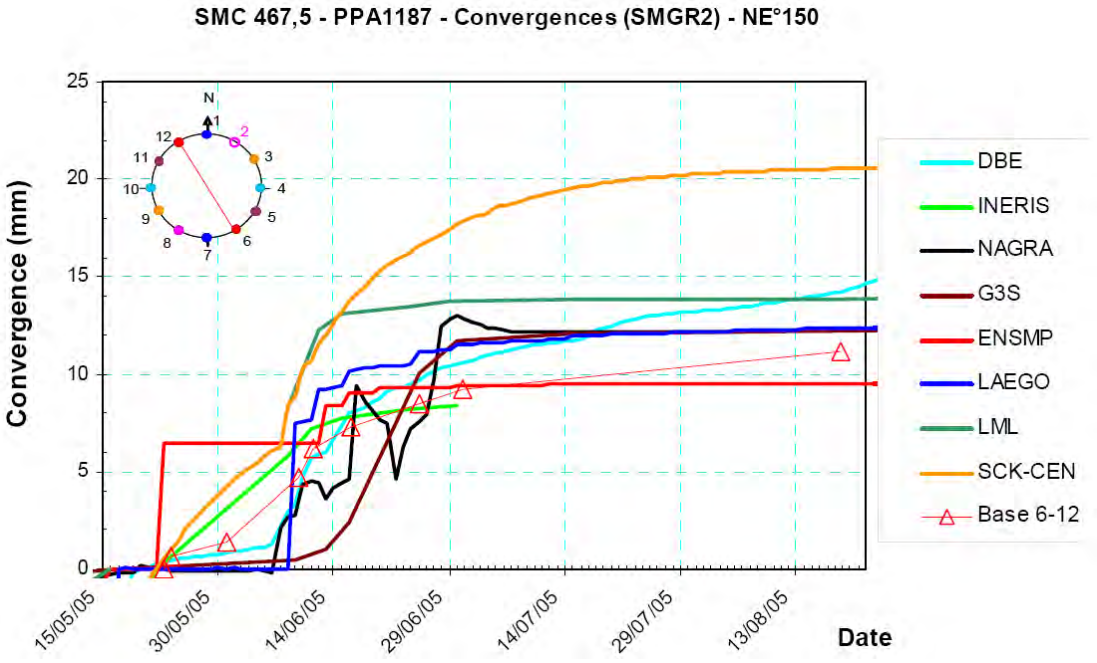

Appendix M-3 Shaft convergences, section SMGR2, -467,5 m ; Direction NE 150°
Comparison between measurement results and blind prediction results of various modeling teams (*SU 2006b*)

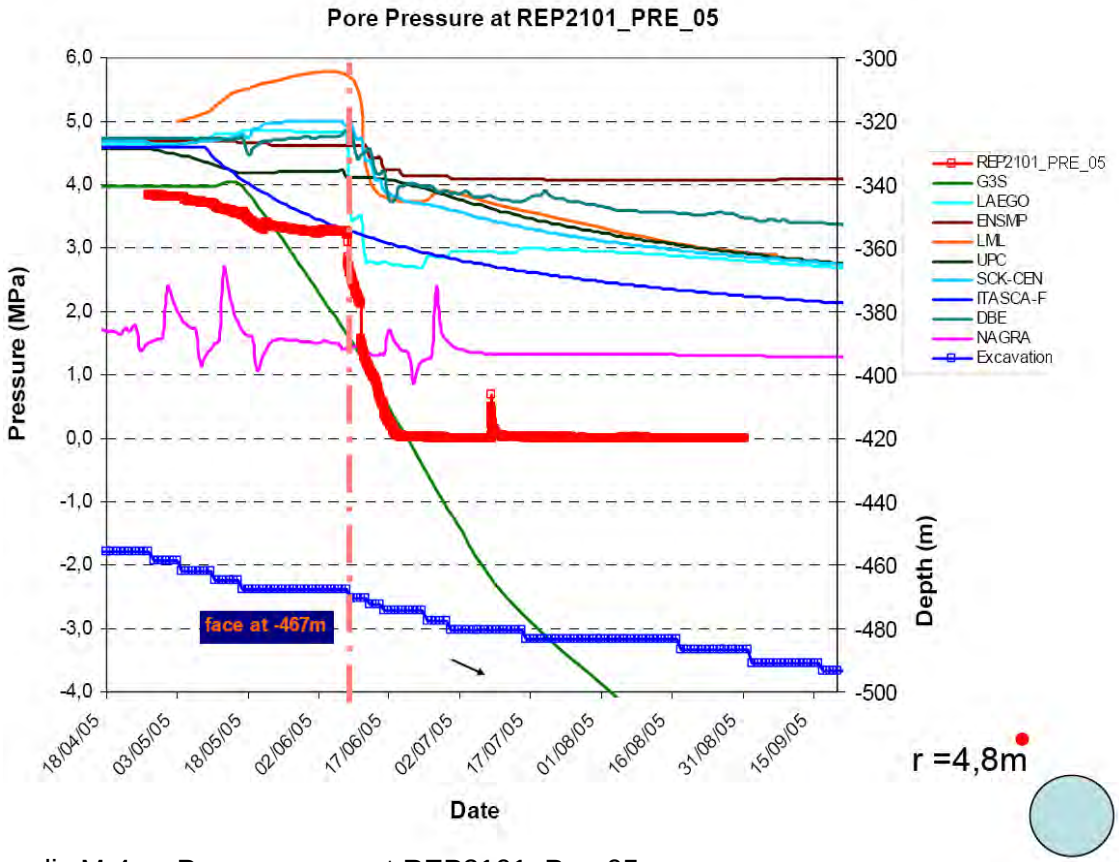

Appendix M-4 Pore pressure at REP2101_Pre_05
Comparison between measurement results and blind prediction results of various modeling teams (*SU 2006b*)